Modal Optical Studies of Multi-Moded Ultra-Low-Noise Detectors in Far-Infrared

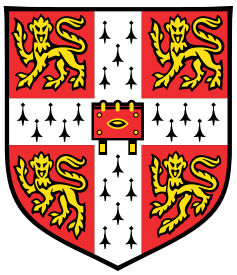

Jiajun Chen

Department of Physics, Cavendish Laboratory
University of Cambridge

This dissertation is submitted for the degree of
Doctor of Philosophy

Churchill College

December 2017

To my family . . .

Declaration

I hereby declare that except where specific reference is made to the work of others, the contents of this dissertation are original and have not been submitted in whole or in part for consideration for any other degree or qualification in this, or any other university. This dissertation is my own work carried out between April 2013 and February 2017 in the Quantum Sensors Group, Cavendish Laboratory, University of Cambridge. It contains nothing which is the outcome of work done in collabortion with others, except as specified in the text and Acknowledgements. This dissertation contains fewer than 60,000 words including appendices, bibliography, footnotes, tables and equations and has fewer than 150 figures.

Jiajun Chen
December 2017

Acknowledgements

It has been an incredible journey and by far, there are so many people to thank for helping me during the last four years. Firstly, I would like to express the gratitude to my supervisor, Professor Stafford Withington, for giving me the opportunity to work in his laboratory, and teaching me how world class research is done. He has always encouraged me to present my work at various conferences and meetings to help me build confidence and get over my shyness. He has not only taught me science, and also shown me how to grow as scientist. Without him, all the great things happened to me over the past four years would not exist. I would also like to thank him for being so kind and helpful in correcting my thesis.

I am also deeply grateful to Dr Chris Thomas, who has taught me so much. He guided me at every step of the way in getting my PhD degree. I cannot thank him enough for how much he has helped me. He has always comforted me and told me to not panic when things did not go greatly. I would like to thank him for providing remarkable solutions to the problems that I encountered.

I would like to thank Dr David Goldie, who has taught me so much about making experimental measurements, and providing fascinating discussions at the group meetings. I appreciate every member of Quantum Sensors Group for providing an supportive working environment. Thank Dr Dorota Glowacka and Michael Crane for fabricating the devices that I needed for testing. I also worked closely with Dennis Molloy and David Sawford, who were always there to help whenever I had problems in operating the test system or the cryogenic refrigerator.

Much of this work was carried out with colleagues in the Astronomy Instrumentation Group at the University of Cardiff, without the work of Professor Ade, Rashimi Sudiwala, Dmitry Mozorov and Ian Walker, much of the experimental work would not have being possible. The fabrication techniques for the few-mode lightpipes were developed by Richard Wylde at Thomas Keating Ltd. Without the support and help of Professor Ade, Richard Wylde and their teams, the experimental work would be not possible, and I am indebted to them.

I thank all my friends in the Quantum Sensors Group, Sarah Thompson, Djelal Osman, Tejas Guruswamy, Ankur Dhar, Max Schneidermann, Isabel Bonachera-Martin, Dan Moinar,

Zhengyuan Sun, and Emma Harwin, who have made the office a very enjoyable place to work. Thanks for their companionship. Outside of work, I have many people to thank for making the past four years beautiful. Thank all the friends I met at Churchill College and all around Cambridge. Thank for their friendship and companionship when life was not totally bright. Special thanks to Rebecca Sawalmeh, the graduate student administrator of Churchill College, who has been extremely kind and helpful to me over the past four year.

My deepest gratitude to my family, who have always supported me in every way that they could. This thesis is dedicated to my loving parents to express my thanks for their love and support throughout my life. Finally, I would like to thank my beloved husband, Deli Zhang, for making my life more meaningful. No words that could describe how grateful I am for who he is, and everything that he does.

Abstract

In this thesis, I have developed a range of theoretical and numerical techniques for modelling the behaviour of partially coherent optical systems and multi-mode detectors. The numerical simulations were carried out for the ultra-low-noise Transition Edge Sensors (TESs) being proposed for use on the SAFARI instrument on the cooled aperture infrared space telescope SPICA (34 - 210 μm). The optical behaviour of the SAFARI system is described in terms of the optical modes of the telescope, as distinct from the optical modes of the detector. The performance of the TESs were assessed in terms of signal power, background power and photon noise.

To establish a method for precisely characterising and calibrating ultra-low-noise TESs, a cryogenic test system was designed and engineered to measure the optical efficiencies of the SAFARI TESs. The multi-mode, partially coherent illumination conditions of the measurement system were engineered to be precisely the same as those of the telescope. A major difference between the test system and the telescope's optics is that the telescope will have focusing elements, but the test system was designed to avoid focusing elements in order to keep the optical path as clean as possible. The theoretical formalism and numerical models were adapted accordingly to address this difference. The numerical simulations show that the test system could provide near identical optical performance as that of the telescope system even though the focusing elements were absent. I also performed experimental measurements to investigate the optical efficiencies of the multi-mode TESs. The detectors worked exceedingly well in all respects with satisfactory optical efficiencies. In addition, it has been shown that the optical model provides a good description of the optical behaviour of the test system and detectors. Further modal analysis was developed to study losses in the multi-mode horns. The optical behaviour of the waveguide-mounted thin absorbing films in the far-infrared was modelled using a mode-matching method.

Table of contents

List of figures

List of tables

Chapter 1

Introduction

1.1 Astronomical Detectors For Far-Infrared Wavelengths

Astronomical observations in the far-infrared (30-450 μm) are of great importance for astrophysics. Many key questions can be only answered by making observations in this region of electromagnetic spectrum. The optical radiation from astronomical objects during the process of forming and evolving is obscured by gas and dust, and therefore they are only visible in the far-infrared [56]. The success of previous infrared satellites such as IRAS [33], IRTS [40], ISO [25], Spitzer Space Telescope [55] and AKARI [32] has revolutionised our understanding of the Universe.

Making observations in the far-infrared is challenging for a number of reasons [29]:

- Firstly, the Earth's atmosphere is opaque over most of far-infrared spectrum, this means many astronomical objects are not observable from the ground. To overcome this problem, the best way is to build space-borne observatories. The rapid development of space technology has made it possible to entirely avoid the atmosphere by launching telescopes into space.

- Secondly, radiation from objects with temperatures greater than a few Kelvins can add a large thermal background. Thus it is crucial to minimise the thermal emission from the telescope itself and all of its optical components. To maintain the telescope and the instruments at low temperatures, previous astronomical missions needed large volume of liquid He, which required large cryostats to carry the coolant. Because of this, aperture sizes of the telescopes were relatively small, which degrades the spatial resolution.

- Thirdly, the far-infrared radiation from astronomical sources can be low in intensity, so that the detectors must be highly sensitive and extremely low noise.

For astronomical observations in the far-infrared, imaging bolometers have been used widely. A typical bolometer has a metallic absorbing element, which absorbs the incident electromagnetic radiation. The incident energy is then converted to heat, and the resultant change in temperature of the absorber is measured by an electrical resistance thermometer. There is a wide range of materials that can be used as absorbers, depending on which part of the operating spectral range is required. An imaging system is usually presented in the form of array of individual bolometers at the focal plane of a telescope. Infrared bolometers have a wide variety of applications, and requirements such as responsivity, sensitivity, and saturation level can be very different. To observe faint and cold astronomical objects, cryogenically cooled bolometer arrays are needed [38]. Several types of detector are being studied, such as the Hot Electron Bolometer (HEB), Cold Electron Bolometer (CEB), Superconducting Tunnel Junctions (STJ), Superconducting Nanowire Single Photon Detector (SNSPD) [17]. For infrared astronomy, research on Kinetic Inductance Detectors (KID) and Transition Edge Sensors (TES) are being focused on. In this thesis, I concentrate on studying and modelling the optical, small signal and noise behaviour of cryogenic ultra-low-noise TESs in the far-infrared.

1.2 Transition Edge Sensors

The voltage biased TESs are currently the devices being actively developed for the purpose of astronomical observation [22].

1.2.1 Basic Operating Principle

A TES is composed of a superconducting thin-film absorber, a sensitive thermometer, and a weak thermal link of thermal conductance, G, to a thermal bath T_{bath}. β-phased Ta is a popular choice for making the thin absorbing films, its temperature increases when a tiny amount of power is absorbed by the thin films. The thermometer is a superconducting metal bilayer deposited onto a thin-film dielectric substrate. At temperatures lower than the critical temperature of the superconducting metal bilayer, the phase transition from normal to superconducting (zero resistance) state would occur over a narrow temperature range. The narrower the temperature range, the greater the rate of change in resistance with temperature. For example, good transition can be obtained by using materials such as Mo and Au in a bilayer [14].

Ultra-low-noise TESs are designed to have a transition temperature of approximately 100 mK. In order for a TES to operate as either a bolometer or a calorimeter, it must be voltage biased in its superconducting to normal state transition. This is achieved by connecting the TES to a heat bath that is cooler than its transition temperature. The cooler the bath, the greater the saturation power (bolometer) or energy (calorimeter) of the TES. Additionally, colder bath temperatures reduce the phonon noise contribution to the total noise in the measured signal from the device.

For TESs that transition at approximately 100 mK, typical bath temperatures that are currently used are those in the range of 50 to 70 mK. A typical TES is operated under constant bias voltage conditions. The voltage is raised until the current passing through the bilayer is equal to its superconducting critical current. Because the superconducting to normal state transition occurs over a finite temperature range, the device can be voltage biased such that its resistance is some small fraction of the normal state resistance. Typically, the lowest stable resistance achievable is approximately 10 - 30% of the normal-state resistance of the bilayer [1].

When the TES is illuminated by an external source of infrared radiation, the temperature of the bilayer will try to increase and its resistance will follow. Because the TES is voltage-biased, an increase in resistance acts to reduce the current passing through the TES, effectively cooling it back to its transition temperature. Provided the response time of the biasing circuit is faster than the thermal response time of the substrate, the temperature of the TES will not change, and the Joule power dissipated in the bilayer from the bias circuit will reduce. In this way, a drop in the biasing current of the TES becomes a direct measure of any external energy or power coupled to the device.

1.2.2 TES Applications

Owing to their high sensitivity, TESs have been widely used in detecting weakly interacting particles [3] and biomolecules [52]. They have also been developed for quantum information and communication [47], and astronomical detection. TESs are considered to be the primary candidate for the next generation of submillimetre-wave and far-infrared space imaging arrays. Many low-noise TES imaging arrays have been used on numerous ground-based and balloon-borne astronomical telescopes, such as SCUBA-2 [54] on the James Clerk Maxwell Telescope (JCMT); the Millimetre Bolometer Array Camera on the Atacama Cosmology Telescope (ACT); the POLABEAR-1 and POLARBEAR-2 spectrometers, for searching for B-Modes in the Cosmic Microwave Background (CMB) [2]; the E and B Experiment (EBEX), which measures the polarisation state of the CMB radiation using a balloon based telescope; and more recently, the Spider polarimeter which searched for primordial gravity

waves also using a balloon telescope [5]. There are also some future space-borne telescopes such as COrE+ [37] and SPICA [23] which will use TESs as the focal plane imaging arrays. For the upcoming far-infrared missions, a new generation of cryogenic ultra-low-noise TESs with Noise-Equivalent-Power (NEP) of approximately 0.2 aW$/\sqrt{\text{Hz}}$ are needed.

1.3 SAFARI TESs

In this thesis, the described TESs were developed as prototypes for the Spica far-infrared Instrument (SAFARI) on the proposed Space Infrared Telescope for Cosmology and Astrophysics (SPICA). SPICA has been proposed as an astronomical mission with a cryogenically cooled 3.2 m telescope optimised for mid- and far-infrared astronomy. Unlike the previous missions such as IRAS, IRTS, ISO, Spitzer Space Telescope and AKARI, which carried liquid He to cool the instrument, SPICA carries no coolants, so that the telescope aperture size does not need to be reduced as that of the previous missions. Hence, its spatial resolution and sensitivity in MIF and FIR astronomy is optimised as the cryogenically cooled 3.2 m telescope is employed. The telescope will be cooled to below 5 K, and designed to be diffraction limited at a wavelength of 30 μm, to give extraordinary levels of performance. The large aperture will enable astrophysicists to address a number of key problems in current astrophysics, such as planetary system formation, the life cycle of dust and gas in the galaxy, and the formations of stars and galaxies [12, 26].

SAFARI was initially proposed to be a far-infrared imaging Fourier Transform Spectrometer on the SPICA spacecraft. The original concept of SAFARI was designed to be operated over 34 μm to 210 μm. 3 arrays of ultra-low-noise TESs were planning to be used to cover the wavelength range L-Band 210-110 μm (324 pixels), M-Band 110-60 μm (1156 pixels) and S-Band 60-34 μm (1849 pixels). The side lengths of the L-, M- and S-Band pixels were 1600 μm, 812 μm and 68 μm, respectively [23, 64]. The pixels were designed to be small to enable Nyquist sampled mapping, and thus the optical throughput of each pixel is small. The effective area of a single pixel is small as the Point Spread Function (PSF) is much larger than a single pixel. A 1.7 K cooled aperture stop was placed inside the cryostat at an image of the primary mirror to minimise the background load on the detectors.

To evaluate the optical performance of the SAFARI detectors, I developed a single partially coherent optical model to give all of the required performance information. The optical performances of the SAFARI detectors were characterised using the natural modes of the telescope and the natural modes of the detector. Many other aspects of optical behaviour of the system were determined through this method. To determine the optical behaviour of this optical system, developing partially coherent models and having a clear understanding of

the physical interpretations of the equations are fundamental. Using this method, the optical throughput when the telescope observes a sky having uniform brightness, the effective area of the telescope when a number of pixels are combined to collect the flux from point source, the mapping characteristics for nonuniform extended sources, and the power couple to the 1.7 K aperture stop, were determined.

To measure the optical efficiencies of the SAFARI TESs, a cryogenic optical system has been designed and engineered. A series of ultra-low-noise TESs have been designed and fabricated as prototypes of the SAFARI instrument. The target noise equivalent powers for the devices are 0.2 aW$/\sqrt{\text{Hz}}$ for SAFARI L- and M-Band, and 0.25 aW$/\sqrt{\text{Hz}}$ for SAFARI S-Band [13]. The TESs were fabricated from Mo/Au bilayers, and used superconducting β-phase Ta films as absorbers. A variable-temperature load was designed as a blackbody source to illuminate the detectors, and an aperture was used to limit the optical throughput. The test system was designed to reproduce the partially coherent illumination condition of the SAFARI telescope when it observes a uniform sky having temperature T_S. In the test system, the radiation from the blackbody source at temperature T_B passes through an aperture and is incident on the device plane, and then couples to a multi-mode lightpipe and it is eventually detected by the TESs. The geometrical requirements of the test system were made the same as that of the telescope system. The major difference was that the focusing elements of the telescope was replaced simply with an circular aperture. Figure 1.1 shows the simplified drawing of the optics of the SPICA telescope and the test system.

The thin lens in Figure 1.1(a) represents the primary mirror of the telescope, and only an circular aperture is present in the test system, which is illustrated in Figure 1.1(b). Each TES is coupled to a multi-mode lightpipe (shown as yellow triangles in the diagrams). A large number of simulations have been performed both on the telescope and the test system. It has been found that the test system could provide near identical optical behaviour as that of the telescope system, which was what we would expect. The absence of the focusing elements should not alter the transformation of the blackbody sources. Because the thin lens transforms the phase of the radiation, while the phases of the blackbody field are essentially random, at least over distances of greater than a wavelength.

The major results obtained from the numerical model including the power loading of the detector by the source, and the associated photon noise from the source were extremely important because they could be used to predict the optical behaviour of detectors and provide a good estimate for the experimental measurements. The main concept for building the optical models will be introduced in the next section.

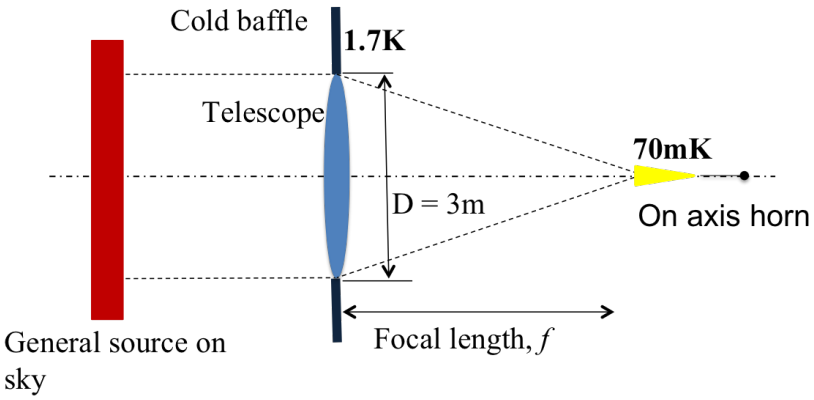

(a) Reduced model of SPICA/SAFARI optics

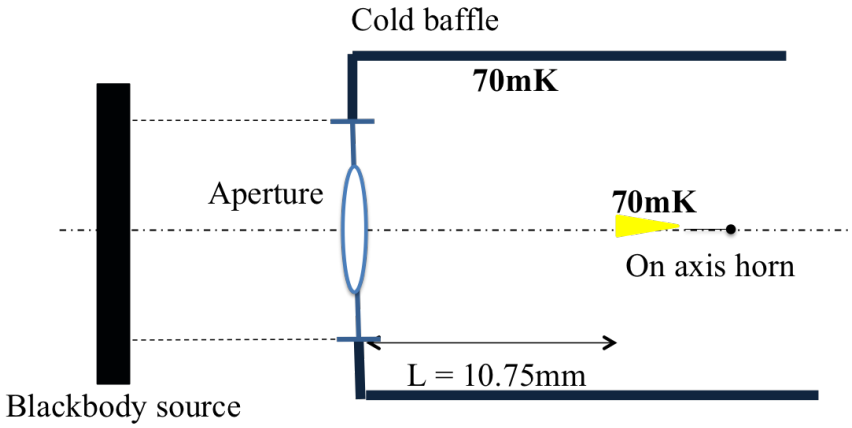

(b) Cryogenic test system optics

Fig. 1.1 Simplified drawing of the optics of the SPICA/SAFARI system and the optical test system.

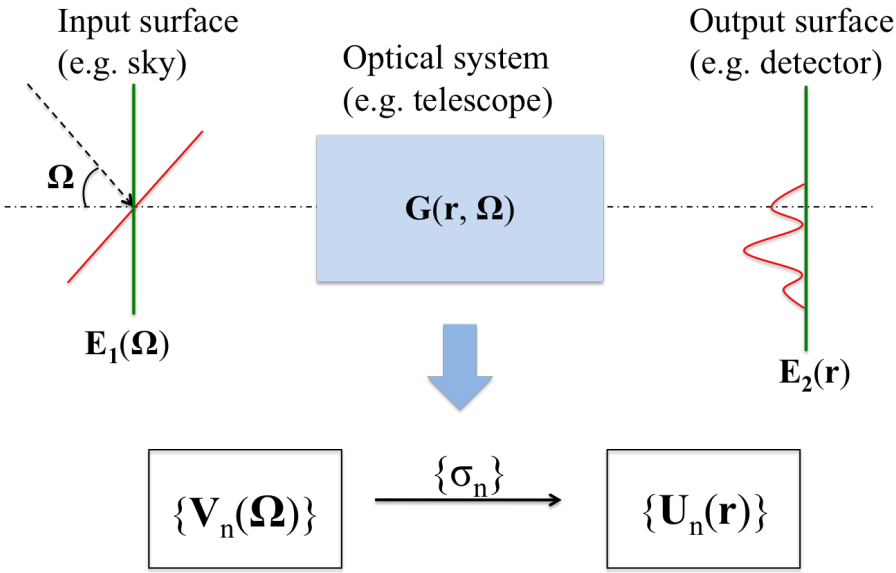

Fig. 1.2 Hilbert Schmidt Decomposition of operator $\overline{\overline{\mathbf{G}}}(\mathbf{r},\mathbf{\Omega})$.

1.4 Multi-Mode Optical Modelling

The optical modelling of the ultra-low-noise TESs for both the telescope system and the test system were based on the coupled mode theory [44]. We can think of an astronomical instrument to be mainly comprised of two components: an optical system, such as a telescope; and a detector, such as a bolometer. For detection in the far-infrared, multi-mode detectors are widely used. For a multi-mode detector, the reception field is only partially spatially coherent. In this thesis, by expressing the partially coherent source in terms of a superposition of transverse coherent modes with orthogonal polarisations [16], the behaviour of waveguide-mounted detectors will be studied in terms of the state of spatial coherence of the electromagnetic field to which the detector is sensitive. In other words, the optical behaviour will be described in terms of a set of natural modes of the optical system, and a set detector modes which are responsive to power. The SAFARI TES pixels will be used as the baseline for numerical modelling and experimental measurements.

The definitions of the natural modes of an optical system, and the natural modes of a detector in this context were firstly developed by Withington and Saklatvala in [44] and [58]. The different sets of modes have their own physical significance. The natural modes of an optical system can be simply seen as the field distributions that can pass through the optical system with the spatial forms unchanged. The modes of the detector are a set of spatially coherent waveguide modes that the detector is sensitive to.

Previously, Saklatvala has presented a thorough discussion of the theory and method for modal analysis in the multi-mode limit [43]. The basic technique of finding the fields on the sky and the field on the detectors is through singular value decomposition. The key is to establish an operator, $\overline{\overline{\mathbf{G}}}(\mathbf{r},\mathbf{\Omega})$, which maps all possible electromagnetic field distributions from the input surface to the output surface, as illustrated in Figure 1.2. The two sets of field are vector spaces, and each of the input field maps to an output field. Thus the optical system is represented in terms of a mapping between two vector spaces. The operator, $\mathbf{G}(\mathbf{r},\mathbf{\Omega})$, can be written in terms of Hilbert-Schmidt decomposition [66] as

$$\mathbf{G}(\mathbf{r},\mathbf{\Omega}) = \sum_n \mathbf{U}_n(\mathbf{r})\sigma_n\mathbf{V}_n(\mathbf{\Omega}), \tag{1.1}$$

where $\{\sigma_n\}$ are known as the singular values, $\{\mathbf{U}_n(\mathbf{r})\}$ and $\{\mathbf{V}_n(\mathbf{\Omega})\}$ are the left and right singular vectors. The singular vectors are the natural modes of the optical system. The equation above describes that the fields on the input surface, which are spanned by singular vectors $\{\mathbf{U}_n(\mathbf{r})\}$ are mapped to a set of fields on the output surface, which are spanned by $\{\mathbf{V}_n(\mathbf{\Omega})\}$, and $\{\sigma_n\}$ are weighting coefficients which represent the relative transmission amplitudes of the modes. This method is powerful in modelling the behaviour of multimode optical systems.

Figure 1.3 illustrates that each of the natural modes of the illuminating field couples into each of the natural modes of the detector. The coupling efficiency can be determined from the projection of the incoming field onto the reception pattern. Mathematically it takes the form of an inner product in the vector space of the square integrable functions. In the case of multi-mode structures, the coupling efficiency can be calculated from the projection of the state of coherence of the incoming fields, onto the state of coherence to which the structure is maximally sensitive.

The coupled mode theory is extremely generic and can be applied to detectors of any kind. In this thesis, I will explicitly show its application in modelling the optical behaviour of the TESs on the SAFARI space telescope, and an optical test system in the far-infrared.

1.5 Thesis Outline

Given the importance of ultra-low-noise TES imaging arrays for the next generation of astronomical missions in the far-infrared, such as SPICA/SAFARI, the optical performance of TESs in astronomical telescope-like optical systems should be assessed. The theory and numerical techniques for analysing the optical behaviour of the multi-mode detectors were developed previously. In this thesis, the theoretical and the numerical model that is based

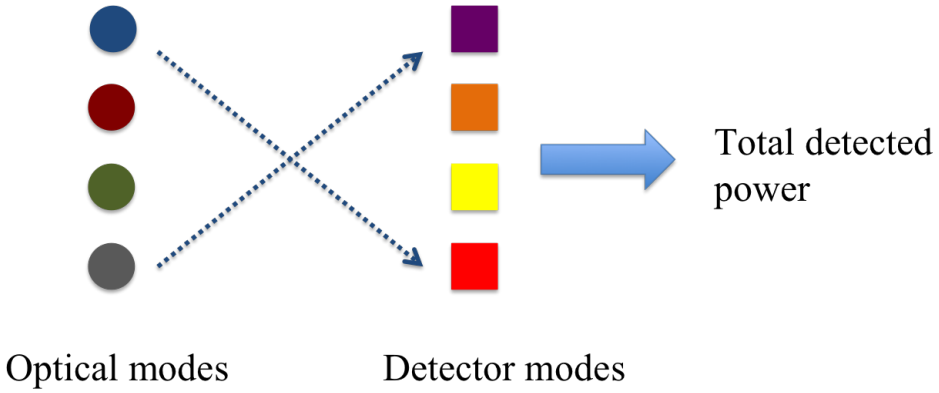

Fig. 1.3 Coupled-mode model of power detection, each natural mode of the radiation field couples into each natural absorption mode of the structure.

on the natural modes of the illuminating field and the optical modes of the detectors was adapted to investigate the optical behaviour of the TESs in real optical systems. An outline of each chapter is as follows:

- Chapter 2 describes the theory and the numerical methods used for modelling the ultra-low-noise TESs being developed for the infrared space telescope, SPICA. The optical performance of a far-infrared imaging FTS, SAFARI, on SPICA are fully assessed. SAFARI uses three sets of TES arrays to cover wavelength range 34-210 μm. The formalisms for investigating the effects of including of a subreflector and arbitrary number of support legs are developed. The optics of the SPICA/SAFARI detectors are studied using paraxial optics. The theory and methods used for determining the natural modes of the illuminating field and the natural modes of the detectors are described. Using the information of the modal contents and modal throughputs of the natural modes, and their coupling to the detector modes in multi-mode waveguides, a thorough discussion of the optical behaviour of the multi-mode, partially coherent illumination is described. The results of power loading to the detectors, aperture efficiencies for point sources, and spillover loading are presented.

- In Chapter 3, the mode coupled theory is used to investigate the classical and quantum noise (shot noise) for multi-mode systems. The specifications of the SAFARI detectors are used to produce results such as the average powers, power fluctuations, and correlations between power fluctuations at the output of detectors.

- In Chapter 4, the design of a cryogenic optical test system for the SAFARI TESs is described. The TESs are illuminated through an aperture by a variable-temperature blackbody source, which is made of a blackened copper-load. The system can be

considered as a scaled-down version of the SPICA telescope, except without having a focusing element. The formalism for modelling the test system is developed. The multi-mode optical model is adapted so that it can be used to study the optical behaviour of the test system. The cryogenic test system is also characterised in terms of a set of optical modes and detector modes. The power loading and the associated noise to the detectors are calculated. The optical behaviour of the test system is compared to that of the telescope system.

- In Chapter 5, optical efficiency and saturation power measurements performed on the SAFARI L-Band TES pixels using the cryogenic optical test system are presented. The operating principles of the relevant devices and the experimental methods are explicitly explained. The results of the detected power are presented as a function of the temperature of the blackbody source. The experimental results are compared to the theoretical results estimated from the optical model. The experimental results are interpreted in terms of effective number of detected modes by comparing the actual detected power to the power for a single mode.

- In Chapter 6, the optical performance of the multi-mode lightpipes and waveguide are studied. The optical model is extended to include the reflections due to waveguide impedance mismatch at the exit aperture of the waveguide. The Ohmic losses due to waveguide walls itself are also investigated.

- In Chapter 7, a mode-matching method to study the optical behaviour of waveguide-mounted thin films is developed. The formalisms of numerically calculating the scattering parameters of a thin resistive film placed within a waveguide are developed. The scheme is valid for films which are larger than a wavelength in size, and patterned absorbers, provided they are positioned within the waveguide. Waveguide modes are used as the basis functions to expand the current and field. The analytical expressions for evaluating the overlap integrals of the basis functions over a finite size are developed, which provides an efficient numerical method to calculate the currents induced on the waveguide-mounted finite sized thin films.

Chapter 2

Modal Optical Modelling of a Far-Infrared Telescope

2.1 Optics of the SAFARI System

In this Chapter, a numerical method for modelling few-mode optical systems will be presented. The optical behaviour of an imaging instrument comprising a telescope and an array of few-mode lightpipe detectors can be analysed using this model. In this model, the optical system was characterised by a set of optical modes. The power is only traced in the direction from the sky to the detector. The optical performance of the far-infrared instrument SAFARI on space telescope SPICA was studied to illustrate this method. The optics of the SAFARI optical system was studied in the paraxial approximation, the method can be used to analyse a more general non-paraxial model. A schematic diagram of this simplified version of SAFARI optics is shown in Figure 2.1.

The SAFARI optics is analysed in terms of plane waves radiated by the source on sky, pass through the telescope, and then arrive at the TES absorber. The source can have any brightness distribution. Examining this scheme enables us to understand how the optical modes couple power from the sky onto the footprint of a pixel in the focal plane, the forms of the waveguide modes, and how efficient the optical modes couple to each of the waveguide modes.

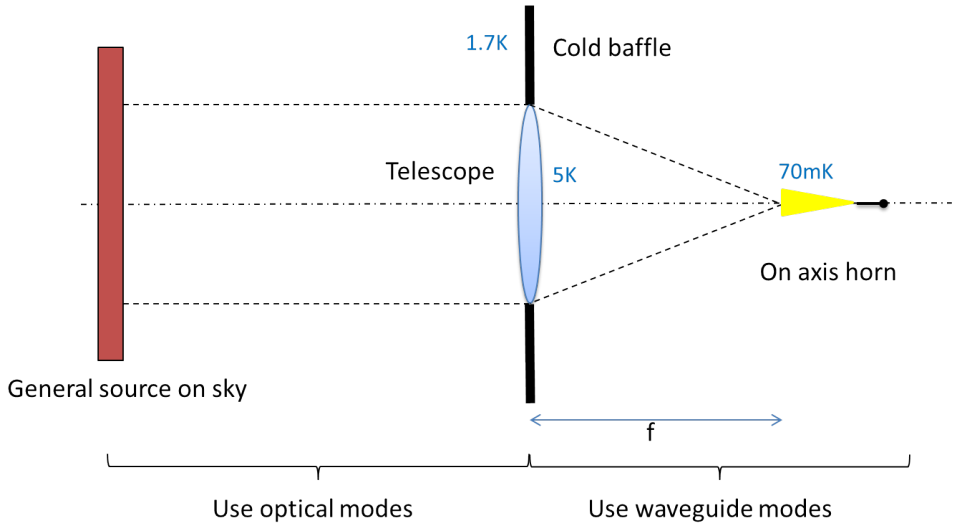

Fig. 2.1 A simplified representation of the SAFARI optics, f is the effective focal length, and the telescope is indicated with a thin lens.

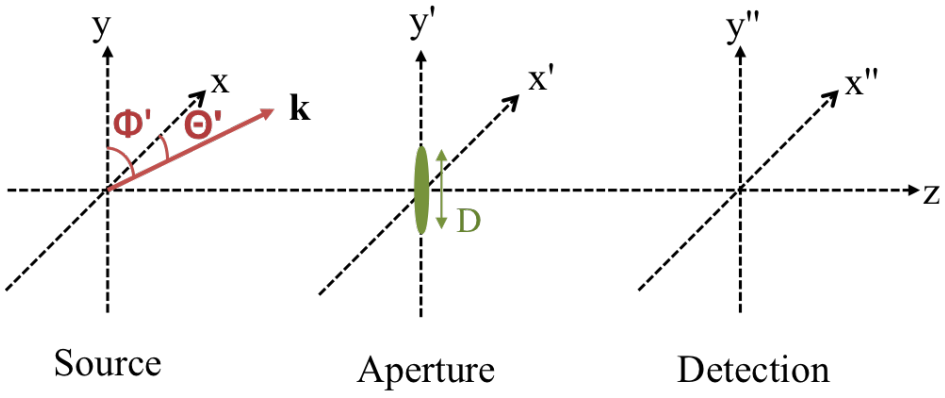

Fig. 2.2 Cartesian coordinates for the optical system.

2.2 Theoretical Formalism

2.2.1 Optical Modes of the Telescope

The coherent field, $\mathbf{E}(\mathbf{r}_t)$, which is associated with a single realisation of the source, can be expressed as a linear superposition of plane waves:

$$\mathbf{E}(\mathbf{r}_t) = \frac{1}{2\pi}\int \sum_i a(\mathbf{k}_t)\hat{\boldsymbol{\varepsilon}}_i(\mathbf{k}_t)\exp(i\mathbf{k}_t\cdot\mathbf{r}_t)\exp(ik_z z)\mathrm{d}^2\mathbf{k}_t, \tag{2.1}$$

where $\mathbf{k}_t$ is the transverse wavevector, $\mathbf{r}_t$ is the position vector, $a(\mathbf{k}_t)$ is the complex amplitude, and $\hat{\boldsymbol{\varepsilon}}(\mathbf{k}_t)$ is the associated unit polarisation vector; i denotes a sum over polarisation basis states; $\exp(i\mathbf{k}_t\cdot\mathbf{r}_t)$ and $\exp(ik_z z)$ are plane waves which are perpendicular to and along the propagation direction. Note that the time-dependent phase term, $\exp(-i\omega t)$, has not been shown explicitly. As the studies of the SAFARI optics are carried out under the assumption of paraxial approximation, certain of the parameters in Eq.(2.1) can be written as follows:

$$\begin{aligned} k_x &= k\sin\theta \approx k\theta \\ k_y &= k\sin\phi \approx k\phi \\ k_z &\approx k. \end{aligned} \tag{2.2}$$

θ and ϕ denote the propagation angles are very small, which are given by $\theta = \pi/2 - \theta'$ and $\phi = \pi/2 - \phi'$, as shown in Figure 2.2, with θ' and ϕ' being the angle to the x- and y-axis, respectively. For paraxial propagations, $\theta' \approx \pi/2$ and $\phi' \approx \pi/2$. Figure 2.2 also shows a thin lens, which according to paraxial optics, θ and ϕ can be used to represent the telescope. The diameter of the telescope is D.

The transverse wavevector $\mathbf{k}_t$ can be approximately written as

$$\mathbf{k}_t \approx k(\theta\hat{\mathbf{i}} + \phi\hat{\mathbf{j}}) \approx k\boldsymbol{\Omega}, \tag{2.3}$$

where $\boldsymbol{\Omega}$ is the solid angle, such that, $\mathrm{d}^2k_t \approx k^2\mathrm{d}\theta\mathrm{d}\phi \approx k^2\mathrm{d}\Omega$. The polarisation vectors can be approximated by $\hat{\boldsymbol{\varepsilon}}_i(\mathbf{r}_t) = \hat{\boldsymbol{\varepsilon}}_i$. Thus, the expression for the coherent field becomes

$$\mathbf{E}(\mathbf{r}_t) = \frac{k^2}{2\pi}\exp(ikz)\int \sum_i a_i(\boldsymbol{\Omega})\hat{\boldsymbol{\varepsilon}}_i\exp(ik_i\boldsymbol{\Omega}\cdot\mathbf{r}_t)\mathrm{d}\boldsymbol{\Omega}. \tag{2.4}$$

The power flowing per unit area across a far-field surface is given by

$$\begin{aligned} W &= \frac{\langle \mathbf{E}(\mathbf{r}_t) \cdot \mathbf{E}^*(\mathbf{r}_t) \rangle}{2Z_0} \\ &= \frac{k^4}{2Z_0 4\pi^2} \iint \sum_i \langle a_i(\mathbf{\Omega}) a_i^*(\mathbf{\Omega'}) \rangle \exp[ik(\mathbf{\Omega} - \mathbf{\Omega'}) \cdot \mathbf{r}_t] \mathrm{d}\mathbf{\Omega} \mathrm{d}\mathbf{\Omega'}, \end{aligned} \tag{2.5}$$

where Z_0 is the impedance of free space, the Dirac brackets denote the ensemble average, which is the mean of the products of all possible incoming fields within the bracket, and i denotes a sum over all polarisation basis states. Astronomical sources, which are usually thermal in all region, are assumed to be uncorrelated in the k-domain, and thus we write

$$\langle a_i(\mathbf{\Omega}) a_i^*(\mathbf{\Omega'}) \rangle = S_i(\mathbf{\Omega}) \delta(\mathbf{\Omega} - \mathbf{\Omega'}), \tag{2.6}$$

and therefore Eq.(2.5) becomes

$$W = \frac{k^4}{2Z_0 4\pi^2} \int \sum_i S_i(\mathbf{\Omega}) \mathrm{d}\mathbf{\Omega}, \tag{2.7}$$

where the sum is taken across all transverse polarisations. By definition, the brightness of polarisation i is then

$$B_i(\mathbf{\Omega}) = \frac{k^4}{2Z_0 4\pi^2} S_i(\mathbf{\Omega}). \tag{2.8}$$

By re-arranging Eq.(2.8) and using Eq.(2.6) gives an expression for $\langle a_i(\mathbf{\Omega}) a_i^*(\mathbf{\Omega'}) \rangle$, which is

$$\langle a_i(\mathbf{\Omega}) a_i^*(\mathbf{\Omega'}) \rangle = \frac{2Z_0 4\pi^2}{k^4} B_i(\mathbf{\Omega}) \delta(\mathbf{\Omega} - \mathbf{\Omega'}). \tag{2.9}$$

Following Eq.(2.9), the angular correlation function of the incoming plane waves can be calculated in terms of the sky brightness distribution. Following Eq.(2.4), the expression for a single coherent plane wave in polarisation i at the aperture of the telescope becomes

$$\mathbf{E}_a(\mathbf{r}'_t) = \frac{k^2}{2\pi} \exp(ikz') a_i(\mathbf{\Omega}) \hat{\boldsymbol{\epsilon}}_i \exp(ik_i \mathbf{\Omega} \cdot \mathbf{r}'_t) \mathrm{d}\mathbf{\Omega}, \tag{2.10}$$

where z' is the position of the aperture, and $\mathbf{r}'_t$ is the transverse wavevector at the aperture of the telescope. After passing through the telescope, which is represented by a thin lens in Figure (2.2), an additional phase change is accumulated, and the coherent field is truncated

by the aperture with the top-hat function $L(D)$,

$$\mathbf{E}_a(\mathbf{r}_t') = \frac{k^2}{2\pi}\exp(ikz')a_i(\mathbf{\Omega})\hat{\boldsymbol{\varepsilon}}_i\exp(ik_i\mathbf{\Omega}\cdot\mathbf{r}_t')L(D)\exp\left(\frac{-ik|\mathbf{r}_t'|^2}{2f}\right)\mathrm{d}\mathbf{\Omega}, \tag{2.11}$$

where f is the effective focal length, as shown in Figure 2.1. According to paraxial optics, the phase transformation at the telescope is represented by the parabolic phase front, $\exp\left(\frac{-ik|\mathbf{r}_t'|^2}{2f}\right)$. Diffraction theory can be used to map the field represented by Eq.(2.11) onto the focal plane using the diffraction integral [15],

$$\mathbf{E}_f(\mathbf{r}_t'') = -\frac{i}{\lambda}\int\frac{1}{|\mathbf{r}_t''-\mathbf{r}_t'|}\exp(ik|\mathbf{r}_t''-\mathbf{r}_t'|)\mathbf{E}_a(\mathbf{r}_t')\mathrm{d}^2\mathbf{r}_t'. \tag{2.12}$$

It is considered that the detector is in the far-field of the aperture, which means the effective focal length, f, is much larger than the diameter of the aperture, D. So $|\mathbf{r}_t''-\mathbf{r}_t'|$ can be expanded and approximated to

$$\begin{aligned}|\mathbf{r}_t''-\mathbf{r}_t'| &= [(x''-x')^2+(y''-y')^2+(z''-z')^2]^{1/2}\\ &\approx (z''-z')+\frac{1}{2}\frac{(x''-x')^2}{z''-z'}+\frac{1}{2}\frac{(y''-y')^2}{z''-z'},\end{aligned} \tag{2.13}$$

with $z''-z'=f$. Then the diffraction integral becomes

$$\begin{aligned}\mathbf{E}_f(\mathbf{r}_t'') = &-\frac{i}{\lambda}\frac{1}{f}\frac{k^2}{2\pi}\exp(ikz'')\hat{\boldsymbol{\varepsilon}}_i a_i(\mathbf{\Omega})\mathrm{d}^2\mathbf{\Omega}\\ &\times\int_A\exp\left[\frac{ik}{2f}[(x''-x')^2+(y''-y')^2-(x'^2+y'^2)\right]\mathrm{d}^2\mathbf{r}_t'.\end{aligned} \tag{2.14}$$

In the first instance, consider a single incoming on-axis plane wave, i.e. $\mathbf{\Omega}=\mathbf{0}$. Expanding the bracket inside of the exponential term, we have

$$\begin{aligned}\mathbf{E}_f(\mathbf{r}_t'') = &-\frac{i}{\lambda}\frac{1}{f}\frac{k^2}{2\pi}\exp(ikz'')\hat{\boldsymbol{\varepsilon}}_i a_i(0)\mathrm{d}^2\mathbf{\Omega}\exp\left[\frac{ik}{2f}(x''+y'')^2\right]\\ &\times\int_A\exp\left\{-\frac{ik}{f}[(x''x'+y''y')]\right\}\mathrm{d}^2\mathbf{r}_t',\end{aligned} \tag{2.15}$$

The detectors are placed in the detection plane, as shown in Figure 2.2. Because the side length of the pixel in the focal plane is much smaller than the effective focal length, i.e $(x'^2+y'^2)\ll f$, the term $\exp\left[\frac{ik}{2f}\left(x'^2+y'^2\right)\right]$ is approximated to unity. A simplification can

then be made to the expression of the field:

$$\mathbf{E}_f(\mathbf{r}_t'') = -\frac{i}{\lambda}\frac{1}{f}\frac{k^2}{2\pi}\exp(ikz'')\hat{\boldsymbol{\varepsilon}}_i a_i(0)\mathrm{d}^2\boldsymbol{\Omega}\int_A \exp\left[-\frac{ik}{f}(x''x'+y''y')\right]\mathrm{d}^2\mathbf{r}_t'. \tag{2.16}$$

To evaluate Eq.(2.16), the surface integral must be known. The integral can be evaluated in polar coordinates with substitutions

$$\begin{aligned} x' &= r'\cos\theta \\ y' &= r'\sin\theta \\ x'' &= r''\cos\theta \\ y'' &= r''\sin\theta, \end{aligned} \tag{2.17}$$

note that these are not in spherical polar coordinates. Thus the integral is written as

$$\int_A \exp\left[-\frac{ik}{f}(x''x'+y''y')\right]\mathrm{d}^2\mathbf{r}_t' = \int_0^{D/2}\int_0^{2\pi}\exp\left[-\frac{ik}{f}r''r'\cos(\theta''-\theta')\right]r'\mathrm{d}r'\mathrm{d}\theta'. \tag{2.18}$$

Using the identities

$$\begin{aligned} \mathrm{J}_0(r) &= \frac{1}{2\pi}\int_0^{2\pi}\exp(ir\cos\theta)\mathrm{d}\theta \\ \int r\mathrm{J}_0(r)\mathrm{d}r &= r\mathrm{J}_1(r), \end{aligned} \tag{2.19}$$

to evaluate the integrals in θ' and r' respectively, results in

$$\mathbf{E}_f(\mathbf{r}_t'') = -\frac{i}{\lambda}\frac{\pi^2}{f}\left(\frac{D}{\lambda}\right)^2\exp[ikz'']\frac{\mathrm{J}_1(u)}{u}\hat{\boldsymbol{\varepsilon}}_i a_i(0)\mathrm{d}\boldsymbol{\Omega}, \tag{2.20}$$

where

$$u = \frac{\pi}{\lambda F_\#}|r_t''|, \tag{2.21}$$

is a dimensionless coordinate in the focal plane. Thus, equivalently the field from an on-axis incoming wave at the focal plane can be written as

$$\mathbf{E}_f(\mathbf{r}_t'') = -\frac{i}{\lambda}\frac{\pi^2}{F_\#\lambda}\left(\frac{D}{\lambda}\right)\exp[ikz'']\frac{\mathrm{J}_1(u)}{u}\hat{\boldsymbol{\varepsilon}}_i a_i(0)\mathrm{d}\boldsymbol{\Omega}. \tag{2.22}$$

The electric field increases with increasing diameter because the collecting area is increased, and the focal ratio is reduced.

We now consider an incoming wave having direction $\mathbf{\Omega}$. The position of centre of the PSF will be shifted by $f\mathbf{\Omega}$, and thus the electric field on the focal plane becomes

$$\mathbf{E}_f(\mathbf{r}_t'') = -\frac{i}{\lambda}\frac{\pi^2}{F_\#\lambda}\left(\frac{D}{\lambda}\right)\exp(ikz'')\frac{\mathrm{J}_1(u)}{u}\hat{\boldsymbol{\varepsilon}}_i a_i(\mathbf{\Omega})\mathrm{d}\mathbf{\Omega}, \tag{2.23}$$

where

$$u = \frac{\pi}{\lambda F_\#}|\mathbf{r}_t'' - f\mathbf{\Omega}|. \tag{2.24}$$

To this point, we have just calculated the coherent field of a single realisation in the focal plane, then the total field in the focal plane is derived by summing the field over all polarisations

$$\mathbf{E}_f(\mathbf{r}_t'') = -\frac{i}{\lambda}\frac{\pi^2}{F_\#\lambda}\left(\frac{D}{\lambda}\right)\exp[ikz'']\sum_i\int\frac{\mathrm{J}_1(u)}{u}\hat{\boldsymbol{\varepsilon}}_i a_i(\mathbf{\Omega})\mathrm{d}\mathbf{\Omega}. \tag{2.25}$$

The field at the focal plane can be expressed with the relationship of the angular spectrum of incoming plane waves,

$$\mathbf{E}_f(\mathbf{r}_t'') = \int\overline{\overline{\mathbf{G}}}(\mathbf{r}_t|\mathbf{\Omega})\cdot\mathbf{a}(\mathbf{\Omega})\mathrm{d}\mathbf{\Omega}, \tag{2.26}$$

where the dyadic tensor, $\overline{\overline{\mathbf{G}}}(\mathbf{r}_t|\mathbf{\Omega})$, is given by

$$\overline{\overline{\mathbf{G}}}(\mathbf{r}_t|\mathbf{\Omega}) = \frac{\pi^2}{\lambda f}\left(\frac{D}{\lambda}\right)^2\frac{\mathrm{J}_1(u)}{u}\overline{\overline{\mathbf{I}}}, \tag{2.27}$$

and $\overline{\overline{\mathbf{I}}}$ the unit dyad, which is a second order tensor with rank one, with $\overline{\overline{\mathbf{I}}}\cdot\mathbf{a} = \mathbf{a}$, for any vector $\mathbf{a}$. A dyadic tensor is a second order tensor, written in a notation that fits in with vector algebra. Note that in the above equation, I have dropped the constant phase factor $-i$, since it has no influence on power calculations. For a source in any general state of angular coherence, the spatial states of coherence in the focal plane is given by

$$\overline{\overline{\mathbf{E}}}(\mathbf{r}_{t1},\mathbf{r}_{t2}) = \langle\mathbf{E}_f(\mathbf{r}_{t1})\mathbf{E}_f^*(\mathbf{r}_{t2})\rangle. \tag{2.28}$$

Using Eq.(2.26), we may write

$$\overline{\overline{\mathbf{E}}}(\mathbf{r}_{t1},\mathbf{r}_{t2}) = \iint\overline{\overline{\mathbf{G}}}(\mathbf{r}_{t1}|\mathbf{\Omega}_1)\cdot\overline{\overline{\mathbf{A}}}(\mathbf{\Omega}_1,\mathbf{\Omega}_2)\cdot\overline{\overline{\mathbf{G}}}^{\dagger}(\mathbf{\Omega}_2|\mathbf{r}_{t2})\mathrm{d}\mathbf{\Omega}_1\mathrm{d}\mathbf{\Omega}_2, \tag{2.29}$$

with

$$\overline{\overline{\mathbf{A}}}(\mathbf{\Omega}_1,\mathbf{\Omega}_2) = \langle\mathbf{a}(\mathbf{\Omega}_1)\mathbf{a}^*(\mathbf{\Omega}_2)\rangle, \tag{2.30}$$

which describes the angular state of coherence in the far field. To calculate the throughput over some region, F, of the focal plane, the total power passing through region, F, needs to be determined. When the system is illuminated by a source having angular state of coherence $\overline{\overline{\mathbf{A}}}(\mathbf{\Omega}_1,\mathbf{\Omega}_2)$, according to Poynting theorem, the total power is

$$\begin{aligned} P &= \frac{1}{2Z_0}\int_F \bar{\bar{\mathbf{I}}}\cdot\cdot\,\overline{\overline{\mathbf{E}}}(\mathbf{r}_{t1},\mathbf{r}_{t2})\mathrm{d}\mathbf{r}_{t1}\mathrm{d}\mathbf{r}_{t2} \\ &= \frac{1}{2Z_0}\int_F\iint \bar{\bar{\mathbf{I}}}\cdot\cdot\,\overline{\overline{\mathbf{G}}}(\mathbf{r}_{t1}|\mathbf{\Omega}_1)\cdot\overline{\overline{\mathbf{A}}}(\mathbf{\Omega}_1,\mathbf{\Omega}_2)\cdot\overline{\overline{\mathbf{G}}}^{\dagger}(\mathbf{\Omega}_2|\mathbf{r}_{t2})\mathrm{d}\mathbf{\Omega}_1\mathrm{d}\mathbf{\Omega}_2\mathrm{d}\mathbf{r}_{t1}\mathrm{d}\mathbf{r}_{t2}, \end{aligned} \tag{2.31}$$

where $\mathbf{r}_{t1}=\mathbf{r}_{t2}=\mathbf{r}_t$ the double dot notation denotes contracting the dyads to a scalar value, and the double-dot product is commutative. The result of the double dot product is invariant under cyclic permutations, the quantity inside of the integral is in fact the Trace of $\overline{\overline{\mathbf{E}}}(\mathbf{r}_1,\mathbf{r}_2)$, which gives

$$\begin{aligned} P &= \frac{1}{2Z_0}\int_F \bar{\bar{\mathbf{I}}}\cdot\cdot\,\overline{\overline{\mathbf{E}}}(\mathbf{r}_{t1},\mathbf{r}_{t2})\mathrm{d}\mathbf{r}_{t1}\mathrm{d}\mathbf{r}_{t2} \\ &= \iint\left[\frac{1}{2Z_0}\int_F \overline{\overline{\mathbf{G}}}^{\dagger}(\mathbf{\Omega}_2|\mathbf{r}_{t2})\cdot\overline{\overline{\mathbf{G}}}(\mathbf{r}_{t1}|\mathbf{\Omega}_1)\mathrm{d}\mathbf{r}_{t1}\mathrm{d}\mathbf{r}_{t2}\right]\cdot\cdot\,\overline{\overline{\mathbf{A}}}(\mathbf{\Omega}_1,\mathbf{\Omega}_2)\mathrm{d}\mathbf{\Omega}_1\mathrm{d}\mathbf{\Omega}_2. \end{aligned} \tag{2.32}$$

As stated earlier, most astronomical sources are usually spatially incoherent in the k-domain, and so for incoherent source. Using Eq.(2.8), Eq.(2.32) becomes

$$P = \int\left[\frac{4\pi^2}{k^4}\int_F \overline{\overline{\mathbf{G}}}^{\dagger}(\mathbf{\Omega}_2|\mathbf{r}_{t2})\cdot\overline{\overline{\mathbf{G}}}(\mathbf{r}_{t1}|\mathbf{\Omega}_1)\mathrm{d}\mathbf{r}_{t1}\mathrm{d}\mathbf{r}_{t2}\right]\cdot\cdot\,\overline{\overline{\mathbf{B}}}(\mathbf{\Omega})\mathrm{d}\mathbf{\Omega}, \tag{2.33}$$

where $\mathbf{\Omega}_1=\mathbf{\Omega}_2=\mathbf{\Omega}$, with $\overline{\overline{\mathbf{B}}}(\mathbf{\Omega})$ being a sky brightness tensor. Define a dimensionless quantity $\overline{\overline{\mathbf{T}}}(\mathbf{r}|\mathbf{\Omega})$ which is closely related to throughput as

$$\overline{\overline{\mathbf{T}}}(\mathbf{r}_t|\mathbf{\Omega}) = \frac{2\pi}{k^2}\overline{\overline{\mathbf{G}}}(\mathbf{r}_t|\mathbf{\Omega}) = \frac{\pi}{2}\frac{D}{\lambda}\frac{1}{F_{\#}}\frac{\mathrm{J}_1(u)}{u}, \tag{2.34}$$

which gives

$$P = \int\left[\int_F \overline{\overline{\mathbf{T}}}^{\dagger}(\mathbf{\Omega}_2|\mathbf{r}_{t2})\cdot\overline{\overline{\mathbf{G}}}(\mathbf{r}_{t1}|\mathbf{\Omega}_1)\mathrm{d}\mathbf{r}_{t1}\mathrm{d}\mathbf{r}_{t2}\right]\cdot\cdot\,\overline{\overline{\mathbf{B}}}(\mathbf{\Omega})\mathrm{d}\mathbf{\Omega}. \tag{2.35}$$

The normalised dyadic power pattern of a completely incoherent power absorber over the region F is given by the tensor in brackets. The total power is the contraction of the dyadic power pattern with the brightness tensor of the source. In the case of uniform sky brightness,

$$\overline{\overline{\mathbf{B}}}(\mathbf{\Omega}) = \bar{\bar{\mathbf{I}}}B_0, \tag{2.36}$$

and Eq.(2.35) becomes

$$P = B_0 \iint_F \overline{\overline{\mathbf{T}}}^{\dagger}(\mathbf{\Omega}_2|\mathbf{r}_{t2}) \cdot \cdot \overline{\overline{\mathbf{T}}}(\mathbf{r}_{t1}|\mathbf{\Omega}_1) \mathrm{d}\mathbf{r}_{t1} \mathrm{d}\mathbf{r}_{t2} \mathrm{d}\mathbf{\Omega}, \tag{2.37}$$

The dyadic operator $\overline{\overline{\mathbf{T}}}(\mathbf{r}_t|\mathbf{\Omega})$ admits a Hilbert-Schmidt (singular value) decomposition

$$\overline{\overline{\mathbf{T}}}(\mathbf{r}_t|\mathbf{\Omega}) = \sum_n \sigma_n \mathbf{u}_n(\mathbf{r}_t) \mathbf{v}_n^*(\mathbf{\Omega}). \tag{2.38}$$

where $\{\mathbf{u}_n(\mathbf{r}_t)\}$ and $\{\mathbf{v}_n(\mathbf{\Omega})\}$ are orthonormal sets of basis states and $\{\sigma_n\}$ is the set of real singular values of the operator. Eq.(2.38) describes that a set of angular beam pattern on the sky, $|\mathbf{v}_n(\mathbf{\Omega})|^2$, that maps on to a set of fields over region F in the focal plane, $|\mathbf{u}_n(\mathbf{r}_t)|^2$, with one-to-one corresponding weighting factors, $|\sigma_n|^2$, which can be solved numberically. In simpler words, $\{\mathbf{u}_n(\mathbf{r}_t)\}$ and the corresponding $\{\mathbf{v}_n(\mathbf{\Omega})\}$ are associated with the optical modes of the system on the detector plane and the sky. The functional forms of the optical modes can be obtained by numerically calculating $|\mathbf{u}_n(\mathbf{r}_t)|^2$ and $|\mathbf{v}_n(\mathbf{\Omega})|^2$.

In the case of a uniform sky, substituting Eq.(2.38) into Eq.(2.37), and using the orthogonality of $\mathbf{v}_n(\mathbf{\Omega})$ and $\mathbf{u}_n(\mathbf{r}_t)$, gives

$$P = \sum_n \sigma_n^2 B_0, \tag{2.39}$$

where B_0 is the single-polarisation brightness and the sum includes modes of both polarisations. The total optical throughput is defined geometrically as

$$\eta_0 = \frac{A\Theta}{\lambda^2}, \tag{2.40}$$

where A is the effective area in the focal plane, and Θ is the effective solid angle. Likewise, according to the multimode calculations, the total throughput must be

$$\eta_0 = \frac{1}{\lambda^2} \sum_n \sigma_n^2. \tag{2.41}$$

Hence, the total throughput is determined and also the spatial-spectral form of throughput is determined. For a surface having a uniform single polarisation brightness at temperature T_s, using Planck's Law for the brightness,

$$B_0 = \frac{h\nu}{\lambda^2} \frac{1}{\exp\left(\frac{h\nu}{k_b T_s}\right) - 1}, \tag{2.42}$$

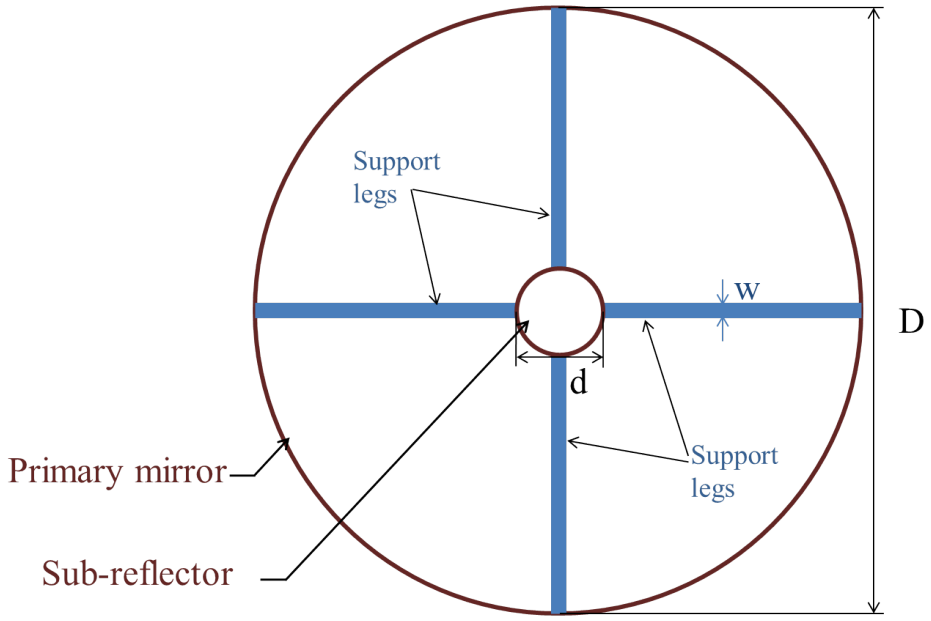

Fig. 2.3 The primary mirror of the telescope, and its sub-reflector with 4 support legs.

where k_b is the Boltzmann constant, the mixing with wavelength and frequency in the equation is for the convenience of express the throughput in the form of $1/\lambda^2$. Eq.(2.39) can be written as

$$P = \frac{h\nu}{\lambda^2}\frac{1}{\exp\left(\frac{h\nu}{k_b T_s}\right)-1}\sum_n \sigma_n^2 = \frac{h\nu}{\exp\left(\frac{h\nu}{k_b T_s}\right)-1}\eta_0. \tag{2.43}$$

Thus, the normalised spectrum is

$$\eta_n = \frac{\sigma_n^2}{\lambda^2}, \tag{2.44}$$

which can be plotted easily once the singular values of $\overline{\overline{\mathbf{T}}}(\mathbf{r}_t|\mathbf{\Omega})$ are determined.

2.2.2 Optical Modes with Sub-Reflector Blockage

A real telescope also has a sub-reflector, which is suspended by legs and which leads to blockage. We will use d to denote the diameter of the sub-reflector, and w, the width of the legs, as shown in Figure 2.3. These two factors cause blockage effects on the optical modes. The electric field over the focal plane must be modified as

$$\mathbf{E}_f(\mathbf{r}_t'') = -\frac{i}{\lambda}\frac{\pi^2}{f}\left(\frac{D}{\lambda}\right)^2 \exp[ikz'']F(u,v)\hat{\boldsymbol{\varepsilon}}_i a_i(\mathbf{\Omega})\mathrm{d}\mathbf{\Omega}, \tag{2.45}$$

where $F(u,v)$ characterises the diffraction pattern of the telescope in the focal plane, and must have the form

$$F(u,v) = \left\{ \frac{\mathrm{J}_1(u)}{u} - \rho \frac{\mathrm{J}_1(v)}{v} - F_{sl}(x'',y'';\theta,\phi) \right\}, \tag{2.46}$$

with ρ is the ratio of the diameters of the subreflector and the primary mirror $\rho = d/D$, and $v = \rho u$, where u is given by Eq.(2.24). $F_{sl}(x'',y'';\theta,\phi)$ corresponds to the diffraction pattern produced by the 4 support legs, which is given by

$$\begin{aligned} F_{sl}(x'',y'';\theta,\phi) = & \frac{w(D-d)}{\lambda f} \left\{ \mathrm{sinc}\left[\frac{kw}{2f}(x-f\theta)\right] \mathrm{sinc}\left[\frac{k(D-d)}{4f}(y-f\phi)\right] \cos\left[\frac{k(D+d)}{4f}(y-f\phi)\right] \right. \\ & \left. + \mathrm{sinc}\left[\frac{kw}{2f}(y-f\phi)\right] \mathrm{sinc}\left[\frac{k(D-d)}{4f}(x-f\theta)\right] \cos\left[\frac{k(D+d)}{4f}(x-f\theta)\right] \right\}. \end{aligned} \tag{2.47}$$

The dimensionless quantity $\overline{\overline{\mathbf{T}}}(\mathbf{r}_t|\mathbf{\Omega})$, is now given by

$$\overline{\overline{\mathbf{T}}}(\mathbf{r}_t|\mathbf{\Omega}) = \frac{\pi}{2}\frac{D}{\lambda}\frac{1}{F_\#}F(u,v), \tag{2.48}$$

and the optical modes and modal spectra with a subreflector and support legs can be calculated.

2.2.3 Waveguide Modes of the Detector

We have shown how to calculate the forms of the optical modes, that can propagate through the optical system in the previous section; a perfect absorber was assumed to determine focal-plane throughput. In this section, we will introduce how to determine the forms of the waveguide modes. In the case of SAFARI, square waveguide modes are used. The detector comprises a lightpipe, which are profiled with a sine squared form, and couples into a sheet-resistive absorber. Figure 2.4(a) illustrates the geometry of the lightpipe, and (b) shows a 4×4 prototype array. The transverse electric (TE) and transverse magnetic (TM) waves propagate in a rectangular waveguide with inner dimensions a, b have the spatially normalised forms $\mathbf{F}_n(\mathbf{r}'')$ [24]:

$$\mathbf{F}^{TE}_{mn}(\mathbf{r}''_t) = \frac{\sqrt{2}}{\sqrt{ab(n^2+m^2)}} \left[n\cos\left(\frac{m\pi x}{a}\right) \sin\left(\frac{n\pi y}{b}\right) \hat{\mathbf{i}} - m\sin\left(\frac{m\pi x}{a}\right) \cos\left(\frac{n\pi y}{b}\right) \hat{\mathbf{j}} \right], \tag{2.49}$$

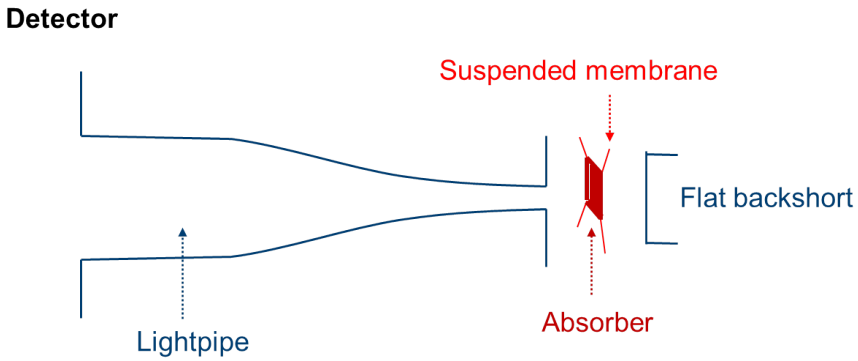

(a) Geometry of a detector;

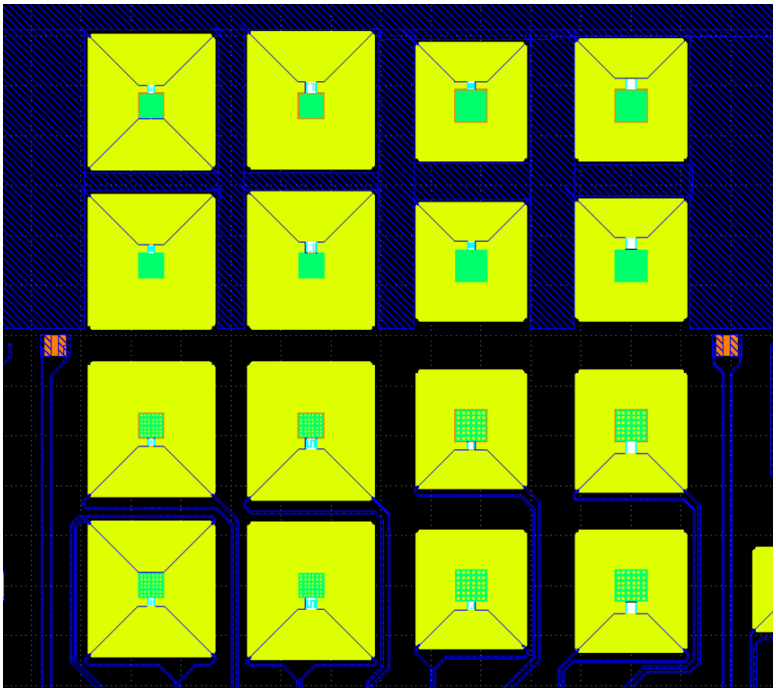

(b) Prototype detector array.

Fig. 2.4 (a) Drawing of a detector which comprises a lightpipe, a suspended absorber and a backshort; (b) an image of a 4×4 prototype detector array: the larger squares show the size of the entrance aperture of the lightpipes, and the absorbers are suspended at the centre.

for TE types, and

$$\mathbf{F}_{mn}^{TM}(\mathbf{r}_t'') = \frac{\sqrt{2}}{\sqrt{ab(n^2+m^2)}}\left[m\cos\left(\frac{m\pi x}{a}\right)\sin\left(\frac{n\pi y}{b}\right)\hat{\mathbf{i}} + n\sin\left(\frac{m\pi x}{a}\right)\cos\left(\frac{n\pi y}{b}\right)\hat{\mathbf{j}}\right], \quad (2.50)$$

for TM modes. m and n are two integers that identify each waveguide mode. The equations of the field have been normalised to unit power in the case where $m = 0$ and $n = 0$. For $m \neq 0$ and $n \neq 0$, an additional $\sqrt{2}$ needs to be multiplied to these equations.

The above equations assume a very small phase error across the horn aperture. The electric field at the entrance aperture must end normally on the walls of the lightpipe. Thus, the radius of curvature of the phase front is given by the side length of the horns, which is large. The flare angle of the lightpipe is designed to be small, the horns are nearly diffraction limited, and so the phase difference between bore site and the edge of the horn is very small. It is common practice to model small-flare angle antennas in this way, even at microwave frequencies. It is a standard assumption in microwave antenna design, an is valid here also.

Define a tensor, $\overline{\overline{\mathbf{D}}}(\mathbf{r}_{t2}'', \mathbf{r}_{t1}'')$, such that

$$\overline{\overline{\mathbf{D}}}(\mathbf{r}_{t2}'', \mathbf{r}_{t1}'') = \sum_{mn} \alpha_{mn}\mathbf{F}_{mn}(\mathbf{r}_{t2}'')\mathbf{F}_{mn}^{*}(\mathbf{r}_{t1}''), \quad (2.51)$$

which characterises the ability of the detector to absorb power from a field in any state of spatial coherence, where α_{mn} is the corresponding efficiency with which the detector absorbs power in waveguide mode mn, which is given by

$$\alpha_{mn} = \frac{1}{2Z_0}\left(1 - |\Gamma_{mn}|^2\right), \quad (2.52)$$

where Z_0 is the wave impedance of plane waves in free space, and $(1 - |\Gamma_{mn}|^2)$ is the absorption efficiency with which the power in the waveguide mode is absorbed by the sheet absorber. Γ_{mn} is given by

$$\Gamma_{mn} = \frac{Z_t - Z_{mn}}{Z_t + Z_{mn}}, \quad (2.53)$$

where Z_{mn} is the waveguide modal impedance, and Z_t is the sheet resistance Z_s in parallel with a backshort impedance Z_b at distance l. The backshort impedance Z_b is given by

$$Z_b = iZ_{mn}\tan(\beta l), \quad (2.54)$$

where β is the propagation constant for waveguide, which is given by

$$\beta = k\left[1-\left(\frac{k_c}{k}\right)^2\right]^{1/2}, \tag{2.55}$$

where k_c is the cut-off wavenumber. The wave impedance of a traveling wave is dependent on the frequency, but is the same throughout the waveguide. For TE modes of propagation the wave impedance is

$$Z^{\mathrm{TE}} = Z_0\left[1-\left(\frac{k_c}{k}\right)^2\right]^{-1/2}, \tag{2.56}$$

and for TM modes,

$$Z^{\mathrm{TM}} = Z_0\left[1-\left(\frac{k_c}{k}\right)^2\right]^{1/2}. \tag{2.57}$$

k_c is given by relation

$$k_c^2 = \left(\frac{m\pi}{a}\right)^2 + \left(\frac{n\pi}{b}\right)^2; \tag{2.58}$$

in this case, $a = b$, re-arranging the above relation gives

$$\frac{a}{\lambda_c} = \frac{1}{2}(m^2+n^2)^{1/2}. \tag{2.59}$$

The power absorbed by the detector when the aperture is illuminated by some incoming radiation field in some general state of coherence, can be determined by calculating the contraction of tensor $\overline{\overline{\mathbf{D}}}(\mathbf{r}''_{t2},\mathbf{r}''_{t1})$ and tensor, $\overline{\overline{\mathbf{E}}}(\mathbf{r}_{t2},\mathbf{r}_{t1})$, which describes the state of coherence of the incoming field. Using Eq.(2.29) together with (2.9), we obtain an expression for $\overline{\overline{\mathbf{E}}}(\mathbf{r}_{t2},\mathbf{r}_{t1})$:

$$\overline{\overline{\mathbf{E}}}(\mathbf{r}_{t1},\mathbf{r}_{t2}) = \frac{2Z_0 4\pi^2}{k^4}\int \overline{\overline{\mathbf{G}}}(\mathbf{r}_{t1}|\boldsymbol{\Omega})\cdot\overline{\overline{\mathbf{B}}}(\boldsymbol{\Omega})\cdot\overline{\overline{\mathbf{G}}}^{\dagger}(\boldsymbol{\Omega}|\mathbf{r}_{t2})\mathrm{d}\boldsymbol{\Omega}. \tag{2.60}$$

Finally, the power absorbed by the waveguide detector for any brightness distribution is determined through equation

$$P = \int_F\int_F\left[\sum_{mn}\alpha_{mn}\mathbf{F}_{mn}(\mathbf{r}''_{t2})\mathbf{F}^*_{mn}(\mathbf{r}''_{t1})\right]\cdot\cdot\,\overline{\overline{\mathbf{E}}}(\mathbf{r}_{t2},\mathbf{r}_{t1})\mathrm{d}^2\mathbf{r}_{t1}\mathrm{d}^2\mathbf{r}_{t2}, \tag{2.61}$$

where F denotes that the integrals extend over the entrance pupil of the lightpipe [51].

2.2.4 Full Optical System

Now we can consider the full optical system, including the waveguide detector. Substitute Eq.(2.60) into Eq.(2.61) to calculate the power absorbed by a pixel,

$$P = \frac{2Z_0 4\pi^2}{k^4} \int\int_F \int_F \overline{\overline{\mathbf{D}}}(\mathbf{r}''_{t2}, \mathbf{r}''_{t1}) \cdot\cdot \overline{\overline{\mathbf{G}}}(\mathbf{r}_{t1}|\mathbf{\Omega}) \cdot \overline{\overline{\mathbf{B}}}(\mathbf{\Omega}) \cdot \overline{\overline{\mathbf{G}}}^{\dagger}(\mathbf{\Omega}|\mathbf{r}_{t2}) \mathrm{d}\mathbf{r}_{t1} \mathrm{d}\mathbf{r}_{t2} \mathrm{d}\mathbf{\Omega}, \tag{2.62}$$

then substituting Eq.(2.34) into equation (2.62), we have

$$P = \int 2Z_0 \int_F \int_F \overline{\overline{\mathbf{D}}}(\mathbf{r}''_{t2}, \mathbf{r}''_{t1}) \cdot\cdot \overline{\overline{\mathbf{T}}}(\mathbf{r}_{t1}|\mathbf{\Omega}) \cdot \overline{\overline{\mathbf{B}}}(\mathbf{\Omega}) \cdot \overline{\overline{\mathbf{T}}}^{\dagger}(\mathbf{\Omega}|\mathbf{r}_{t2}) \mathrm{d}\mathbf{r}_{t1} \mathrm{d}\mathbf{r}_{t2} \mathrm{d}\mathbf{\Omega}. \tag{2.63}$$

Following the cyclic permutations for double dot product, we can express the total power P as the contraction of a power reception dyadic, $\overline{\overline{\mathbf{P}}}(\mathbf{\Omega})$, with the brightness tensor, $\overline{\overline{\mathbf{B}}}(\mathbf{\Omega})$, of the source.

$$\begin{aligned} P &= \int 2Z_0 \int_F \int_F \overline{\overline{\mathbf{T}}}^{\dagger}(\mathbf{\Omega}|\mathbf{r}_{t2}) \cdot \overline{\overline{\mathbf{D}}}(\mathbf{r}''_{t2}, \mathbf{r}''_{t1}) \cdot \overline{\overline{\mathbf{T}}}(\mathbf{r}_{t1}|\mathbf{\Omega}) \cdot\cdot \overline{\overline{\mathbf{B}}}(\mathbf{\Omega}) \mathrm{d}\mathbf{r}_{t1} \mathrm{d}\mathbf{r}_{t2} \mathrm{d}\mathbf{\Omega} \\ &= \int \overline{\overline{\mathbf{P}}}(\mathbf{\Omega}) \cdot\cdot \overline{\overline{\mathbf{B}}}(\mathbf{\Omega}) \mathrm{d}\mathbf{\Omega}. \end{aligned} \tag{2.64}$$

The power reception dyadic for the system is then

$$\overline{\overline{\mathbf{P}}}(\mathbf{\Omega}) = 2Z_0 \int_F \int_F \overline{\overline{\mathbf{T}}}^{\dagger}(\mathbf{\Omega}|\mathbf{r}_{t2}) \cdot \overline{\overline{\mathbf{D}}}(\mathbf{r}''_{t2}, \mathbf{r}''_{t1}) \cdot \overline{\overline{\mathbf{T}}}(\mathbf{r}_{t1}|\mathbf{\Omega}) \mathrm{d}\mathbf{r}_{t1} \mathrm{d}\mathbf{r}_{t2}. \tag{2.65}$$

Use Eq.(2.38) to write the power reception dyadic as the summation,

$$\overline{\overline{\mathbf{P}}}(\mathbf{\Omega}) = 2Z_0 \sum_i \alpha_i \sum_{mn} \sigma_n \sigma_m S^*_{in} S^*_{im} \mathbf{v}_n(\mathbf{\Omega}) \cdot \mathbf{v}^*_m(\mathbf{\Omega}), \tag{2.66}$$

where i denotes a sum over waveguide modes, and mn denotes a sum over optical modes. S_{in} is the field coupling between the focal plane field of the telescope and the aperture field of the waveguide, which is given by

$$S_{in} = \int \mathbf{F}^*_i(\mathbf{r}''_t) \cdot \mathbf{u}_n(\mathbf{r}'') \mathrm{d}\mathbf{r}''_t. \tag{2.67}$$

For an unpolarised, uniform source $\overline{\overline{\mathbf{B}}}(\mathbf{\Omega}) = \bar{\bar{\mathbf{I}}} B_0$,

$$P = \int \overline{\overline{\mathbf{P}}}(\mathbf{\Omega}) \cdot\cdot \bar{\bar{\mathbf{I}}} \mathrm{d}\mathbf{\Omega} B_0, \tag{2.68}$$

it can be written as

$$\begin{aligned} P &= 2Z_0 \sum_i \alpha_i \sum_{mn} \sigma_n \sigma_m S_{in}^* S_{im}^* \int \mathbf{v}_n(\mathbf{\Omega}) \cdot \mathbf{v}_m^*(\mathbf{\Omega}) \mathrm{d}\mathbf{\Omega} B_0 \\ &= 2Z_0 \sum_i \alpha_i \sum_m |S_{im}^*|^2 \sigma_m^2 B_0, \end{aligned} \tag{2.69}$$

where the sum over m includes the different polarisations. Using the Planck expression for the single mode brightness, Eq.(2.69) becomes

$$P = 2Z_0 \sum_i \alpha_i \sum_m |S_{im}^*|^2 \frac{\sigma_m^2}{\lambda^2} \frac{h\nu}{\exp\left(\frac{h\nu}{k_b T_s}\right) - 1}. \tag{2.70}$$

and including the expression for the absorption coefficient α

$$P = \sum_i (1 - |\Gamma_i|^2) \sum_i \alpha_i \sum_m |S_{im}^*|^2 \left(\frac{\sigma_m}{\lambda}\right)^2 \frac{h\nu}{\exp\left(\frac{h\nu}{k_b T_s}\right) - 1}. \tag{2.71}$$

The $|S_{in}|^2$ are the power coupling efficiencies between the natural modes of the telescope and those of the detector. From Eq.(2.71), we can see that the power per natural mode of the optical system on the sky is determined by multiplying the spectral throughput of the mode $\eta_n = \left(\frac{\sigma_m}{\lambda}\right)^2$, the power coupling factor into each waveguide mode $|S_{in}|^2$, and then the fraction of power in the waveguide mode which is absorbed by the absorber.

In the case of a point source having direction $\mathbf{\Omega}_0$, the brightness tensor is

$$\overline{\overline{\mathbf{B}}}(\mathbf{\Omega}) = \overline{\overline{\mathbf{I}}} S_0 \delta(\mathbf{\Omega} - \mathbf{\Omega}_0), \tag{2.72}$$

where S_0 is the flux density in Jy (Jansky). Then the power detected becomes

$$P = S_0 \int \overline{\overline{\mathbf{P}}}(\mathbf{\Omega}) \cdot \cdot \, \overline{\overline{\mathbf{I}}} \delta(\mathbf{\Omega} - \mathbf{\Omega}_0) \mathrm{d}\mathbf{\Omega}. \tag{2.73}$$

Expand this equation, and manipulate algebraic expression, we get

$$P = \sum_i (1 - |\Gamma_i|^2) \sum_{mn} \sigma_n \sigma_m S_{in}^* S_{im}^* \mathbf{v}_n(\mathbf{\Omega}_0) \cdot \mathbf{v}_m^*(\mathbf{\Omega}_0) S_0. \tag{2.74}$$

This is the power detected from a fully coherent field of the point source on the sky. Then the effective area of the aperture, $A_e(\mathbf{\Omega}_0)$as a function of direction becomes

$$A_e(\mathbf{\Omega}_0) = P/S_0 = \sum_i (1 - |\Gamma_i|^2) \sum_{mn} \sigma_n \sigma_m S_{in}^* S_{im}^* \mathbf{v}_n(\mathbf{\Omega}_0) \cdot \mathbf{v}_m^*(\mathbf{\Omega}_0). \tag{2.75}$$

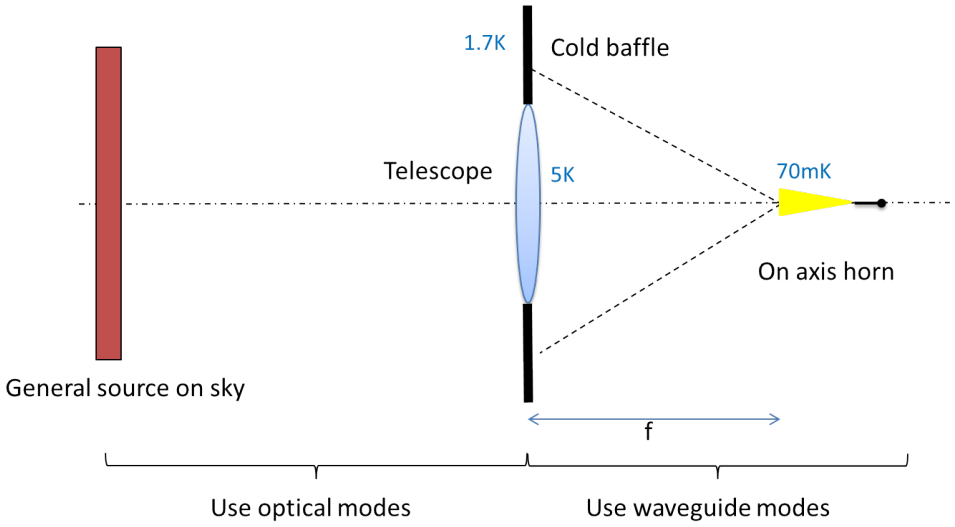

Fig. 2.5 Illustration of power coupling to the cold baffles.

Define the aperture efficiency as

$$\eta_{\rm ap} = \frac{A_e(\mathbf{\Omega}_0)}{A}, \tag{2.76}$$

where A is the physical area of the primary mirror, which has been introduced at an earlier stage. The effective number of modes are determined by integrating Eq.(2.75) over the whole sky,

$$\begin{aligned} N &= \frac{1}{\lambda^2}\int A_e(\mathbf{\Omega}_0)\mathrm{d}\mathbf{\Omega}_0 \\ &= \sum_i (1-|\Gamma_i|^2)\sum_n |S_{in}|^2\eta_n. \end{aligned} \tag{2.77}$$

2.2.5 Spillover Loading

We now consider the power loading from the cold baffle. Figure 2.5 shows how power couples to the surrounding baffle. The transmission efficiency of optical mode n is η_n, and the power coupling factor from optical mode n to waveguide mode m is $|S_{mn}|^2$. If the sky is a uniform blackbody at radiometric temperature T_s then the total power traveling along the waveguide in waveguide mode m is

$$P_m = \sum_n |S_{mn}|^2\eta_n \frac{h\nu}{\exp\left(\frac{h\nu}{k_b T_s}\right)-1} + N_m, \tag{2.78}$$

where N_m is the power coupled into waveguide mode m from the baffle surrounding the aperture. If the temperature of the aperture is T_a, the power in waveguide mode m is then

given by

$$P_m = \frac{h\nu}{\exp\left(\frac{h\nu}{k_b T_a}\right) - 1}. \tag{2.79}$$

If the temperature of the aperture, T_a, is the same as the sky, that $T_s = T_a$, then substituting Eq.(2.79) to the left side of Eq.(2.78) gives

$$\frac{h\nu}{\exp\left(\frac{h\nu}{k_b T_a}\right) - 1} = \sum_n |S_{mn}|^2 \eta_n \frac{h\nu}{\exp\left(\frac{h\nu}{k_b T_a}\right) - 1} + N_m. \tag{2.80}$$

Re-arrange the above equation for N_m, we get

$$N_m = \frac{h\nu}{\exp\left(\frac{h\nu}{k_b T_a}\right) - 1} \left[1 - \sum_n |S_{mn}|^2 \eta_n\right]. \tag{2.81}$$

Write the quantity in brackets: which is the coupling efficiency of waveguide mode m to the cold stop, χ_m, as

$$\chi_m = 1 - \sum_n |S_{mn}|^2 \eta_n. \tag{2.82}$$

Finally, the total power absorbed by the detector due to the presence of the cold stop is

$$P = \sum_m (1 - |\Gamma_m|^2) \chi_m \frac{h\nu}{\exp\left(\frac{h\nu}{k_b T_a}\right) - 1}. \tag{2.83}$$

which shows the coupled power is determined by two processes: the transmission efficiency of the optical modes, and the coupling of the optical modes to the waveguide modes.

2.3 Numerical Considerations

I wrote a large package of computer code to enable the modal optical behaviour of SAFARI to be simulated. The code was written in MatLab, and the key point of using MatLab is to evaluate the above numerically by converting the expressions into matrix algebra. A list of the parameters that were used are listed in Table 2.1.

The diameter of the primary mirror, D, and the diameter of the subreflector, d, were set to 3m and 1.06 m. It is assumed that a support leg with a width of 0.1m is sufficient to support the subreflector.

To calculate the optical modes of the telescope, a matrix $\mathbf{T}$ was made to represent the dyadic propagator described in Eq.(2.38). Each column of the matrix $\mathbf{T}$ contains the sampled

Table 2.1 Simulation parameters of the original SAFARI design, with $\lambda_{\max}$, λ_{cen}, and $\lambda_{\min}$ the maximal, central and minimal wavelengths of the bands; f the effective focal length; $F_{\#}$ the focal ratio; Pixel size denotes the side length of each pixel.

Waveband	L-Band	M-Band	S-Band
$\lambda_{\max}$ (μm)	210	110	60
λ_{cen} (μm)	160	85	47
$\lambda_{\min}$ (μm)	110	60	34
f (m)	49.5	60	60
$F_{\#}$	16.5	20	20
Pixel size (μm)	1600	1026	812

PSF across the footprint of a pixel. 80×80 of sample points were chosen for a square pixel. The different columns in the matrix correspond to the point source being moved from sample point to sample point over the sky, covering the whole field of view of the pixel. Matrix SVD (Singular Value Decomposition) was used to implement the HS decomposition described in Eq.(2.38), it gives [57]

$$\mathbf{T} = \mathbf{u}\Sigma\mathbf{v}. \tag{2.84}$$

The sample step size Δx, Δy in the focal plane and $\Delta\theta$, $\Delta\phi$ on the sky are needed to be taken into account. In Eq.(2.38), $\mathbf{u}(\mathbf{r})$ is a continuous function, whereas $\mathbf{u}$ from Eq.(2.84) is a numerical vector. The relationship between $\mathbf{u}(\mathbf{r})$ and $\mathbf{u}$ needs to be understood. If $\mathbf{u}(\mathbf{r})$ is sampled according to $u_t(r\Delta x, s\Delta y)$, where t spans the vector components, and r, s the sample points in the x and y directions with differential intervals Δx and Δy respectively, then

$$\int \mathbf{u}^*(\mathbf{r}) \cdot \mathbf{u}(\mathbf{r}) \mathrm{d}^2\mathbf{r} = 1. \tag{2.85}$$

Writing it in the form of summations, we get

$$\sum_{r,s,t} u_t^*(r\Delta x, s\Delta y) u_t(r\Delta x, s\Delta y) \Delta x \Delta y = 1, \tag{2.86}$$

and the result numerically obtained from SVD gives

$$\sum_m u_m^* u_m = 1, \tag{2.87}$$

where m spans the sample points and vector components. Equating Eq.(2.86) and (2.87) gives

$$\mathbf{u}(\mathbf{r}) = \frac{\mathbf{u}}{\sqrt{\Delta x \Delta y}}, \tag{2.88}$$

a factor of $\sqrt{(\Delta x \Delta y)}$ needs to be divided when we calculate the optical modes. Likewise,

$$\mathbf{v}(\mathbf{\Omega}) = \frac{\mathbf{v}}{\sqrt{\Delta\theta\Delta\phi}}. \tag{2.89}$$

The overlap integral between the optical and waveguide modes across the waveguide aperture, as shown in Eq.(2.67),

$$\int \mathbf{f}(\mathbf{r}^*) \cdot \mathbf{u}(\mathbf{r}) \mathrm{d}^2\mathbf{r}, \tag{2.90}$$

can be written as summations, as

$$\sum_{r,s,t} f_t^*(r\Delta x, s\Delta y) u_t(r\Delta x, s\Delta y) \Delta x \Delta y. \tag{2.91}$$

Substituting Eq.(2.88) into the above equation, it becomes

$$\sum_m f_m^* u_m \frac{1}{\sqrt{\Delta x \Delta y}} \Delta x \Delta y, \tag{2.92}$$

which is

$$\sum_m f_m^* u_m \sqrt{\Delta x \Delta y}. \tag{2.93}$$

Therefore the power coupling factor becomes

$$\eta_{cpl} = \left| \sum_m f_m^* u_m \right|^2 \Delta x \Delta y. \tag{2.94}$$

Similarly, it can be shown that the relationship between the HS singular value σ_n and the SVD singular values Σ_n is

$$\sigma_n = \Sigma_n \sqrt{\Delta x \Delta y \Delta\theta \Delta\phi}. \tag{2.95}$$

From Eq.(2.44), we can thus obtain the throughput between a sample solid angle on the sky and a sample area in the focal plane by

$$\left(\frac{\sigma_n}{\lambda}\right)^2 = \left[\frac{\Sigma_n \sqrt{\Delta x \Delta y \Delta\theta \Delta\phi}}{\lambda}\right]^2. \tag{2.96}$$

2.4 Simulations and Analysis

By numerically simulating the behaviour of the full SAFARI system, a large number of results and plots were obtained. The calculations were carried out over the required range of wavelengths, from 34 μm to 210 μm. In this section, only the results that were calculated at

the maximal, central and minimal wavelengths of the SAFARI bands will be shown. The optical modes of the telescope, and those included a subreflector and support legs were first calculated. Then the total optical throughput of the modes, and the modal throughputs of each mode were obtained. The composite beam pattern, which is the incoherent sum of all the optical modes weighted by the throughputs of each mode, and the summed intensity in the focal plane across the footprint of a pixel were also plotted. These two plots provide a good test of whether the beam patterns and modal spectra are correct. Then a number of rectangular waveguide modes were calculated. The coupling efficiency between the optical modes and waveguide modes were determined, which enables us to work out how many waveguide modes are required to achieve the best performance. After that, the effective area of the instrument for point sources were calculated. The aperture efficiencies for single pixels are small because the pixel size is chosen to enable Nyquist sampled mapping [35], thus a number of pixels are combined to increase the aperture efficiencies. The co-added beam patterns and enhanced aperture efficiencies were also determined.

2.4.1 Optical Modes

The natural modes of the optical systems are introduced in this section. The throughputs of the optical modes of the L-, M- and S-Band at different wavelengths were obtained.

Optical Modes of the Telescope

Figure 2.6 shows an example of the simulations of the optical modes at 210 μm of L-Band: (a) shows the optical modes, (b) shows the associated spatial spectral throughputs and (c) shows the composite beam pattern (top) and focal plane intensity (bottom).

Figure 2.6(a) shows the intensities of the first, second and fourth optical modes of SAFARI L-Band at 210 μm left to right. Each mode propagates independently of each other. The second and the third modes are degenerate, the other is identical but rotated through 90°. The first 4 optical modes contribute most to the throughput. The top row shows the intensity beam patterns on the sky, and the bottom row shows the corresponding intensity modes in the focal plane. Plot (b) in Figure 2.6 shows the optical throughputs associated with each of these modes. The total optical throughput, 0.171, was calculated by summing optical modal throughputs. A simple check of the results can be made by calculating the total optical throughput geometrically, as shown in Eq.(2.40), where the effective solid angle is taken to be the physical solid angle calculated from the geometry of the telescope. The total optical throughput was calculated to be 0.167 using the later method. It seems that for a wavelength of 210 μm in L-Band, the two results of optical throughput match very well. The composite

beam pattern and focal plane intensity plot are shown in Figure 2.6(c), the top plot is the beam pattern that would result if a perfect square absorber were used as the detector, and the bottom plot is the intensity across the footprint of a pixel when the telescope observes a uniform sky, the uniform intensity pattern across the footprint is what we would expected when a perfect square absorber is used for observing a uniform sky. It can be produced from relation $\sum_n \eta_n |\mathbf{v}_n|^2$.

The optical modes, the spectra and the summed beam patterns at other wavelengths of the SAFARI bands were also determined. Figure 2.6 to 2.14 summarises results at the maximal, central and minimal wavelengths of the wavebands. The optical modes for different wavelengths in other wavebands have the similar modal forms. It is fascinating to notice that the modes in the focal plane look the same as the modes on the sky when they are truncated in the central region.

Table 2.2 Total throughput, η_{cal}, and geometrical throughput, η_{geo}, for the maximal, central and minimal wavelengths of the SAFARI L-, M- and S-Band.

Waveband	λ (μm)	η_{cal}	η_{geo}	$\eta_{\text{cal}}/\eta_{\text{geo}}$
L-Band	210	0.171	0.168	1.018
	160	0.295	0.289	1.021
	110	0.623	0.610	1.021
M-Band	110	0.175	0.171	1.023
	85	0.292	0.286	1.021
	60	0.587	0.574	1.023
S-Band	60	0.367	0.360	1.019
	47	0.599	0.586	1.022
	34	1.140	1.120	1.018

Within the same waveband, the optical throughput increases as wavelength decreases. In each case, the total throughput is almost the same as the geometrical throughput, the results of the throughputs are tabulated in Table 2.2. η_{cal} denotes the total throughput calculated by summing all of the optical modal throughputs, and η_{geo} denotes the throughputs calculated geometrically. The results given by the modal calculation and the approximate geometrical calculation are in pleasing agreement. The numerical calculations are slightly larger than the geometrical throughput by about 2%. It also shows that in different wavebands, even for the same scaled wavelengths, the optical throughputs are different because that the optical designs for each band are slightly different.

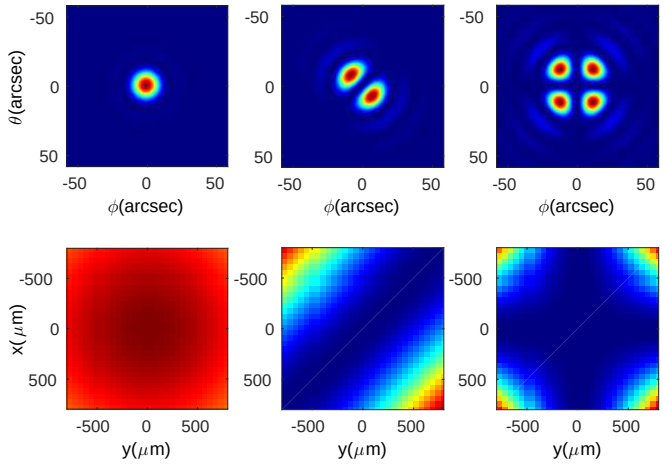

(a) Optical modes.

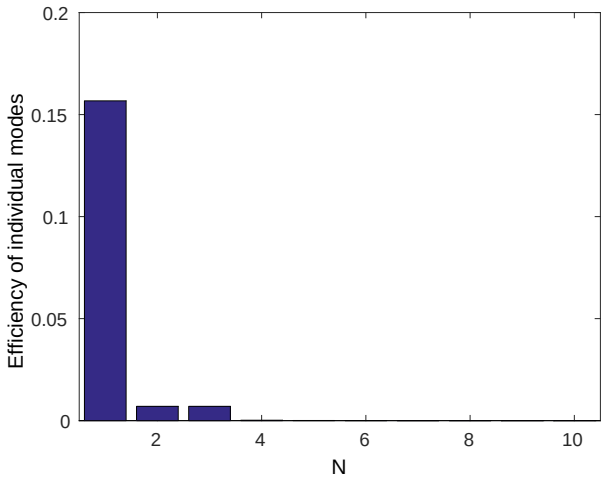

(b) Optical throughput spectral.

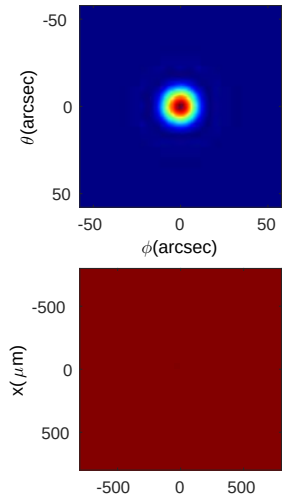

(c) Incoherent sum of the optical modes.

Fig. 2.6 Optical modes for 210 μm of L-Band: (a) first, second and fourth optical modes shown from left to right; (b) spectral throughputs show the efficiencies of each individual modes; (c) incoherent sum of the optical modes weighted by the spectral throughputs.

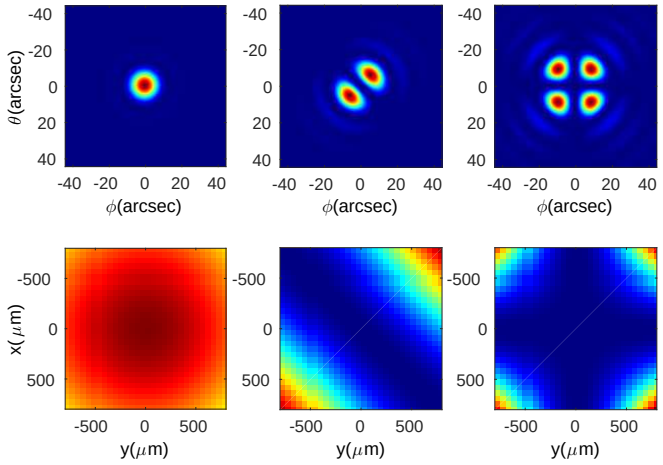

(a) Optical modes.

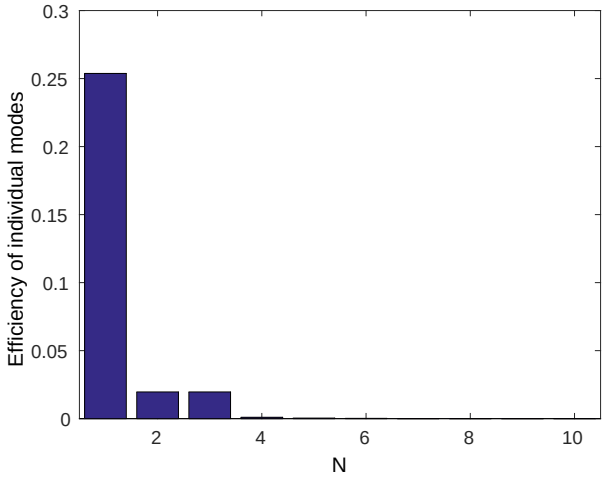

(b) Optical throughput spectral.

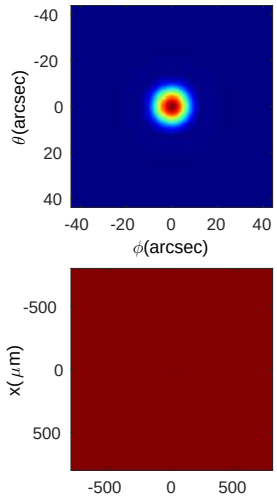

(c) Incoherent sum of optical modes.

Fig. 2.7 Optical modes for 160 μm of L-Band: (a) first, second and fourth optical modes shown from left to right; (b) spectral throughputs show the efficiencies of each individual modes; (c) incoherent sum of the optical modes weighted by the spectral throughputs.

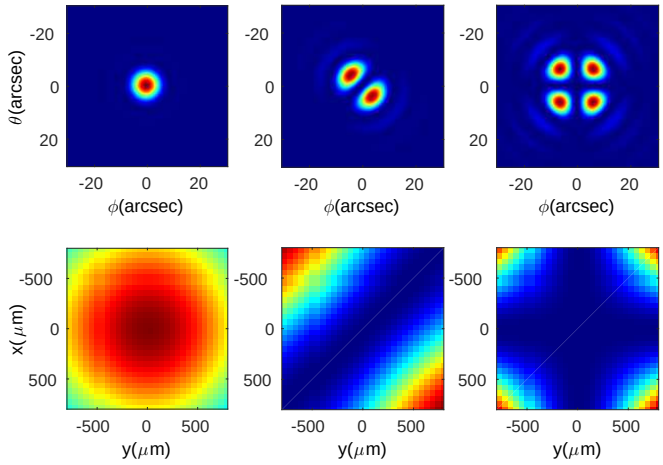

(a) Optical modes.

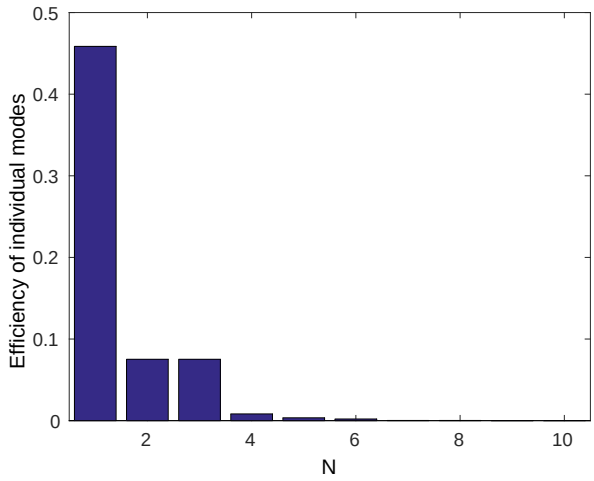

(b) Optical throughput spectral.

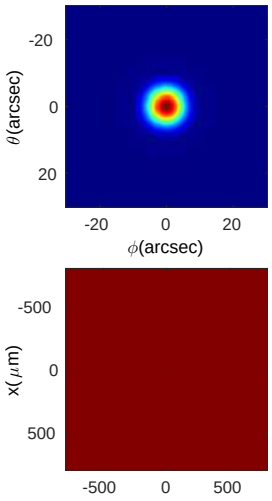

(c) Incoherent sum of optical modes.

Fig. 2.8 Optical modes for 110 μm of L-Band: (a) first, second and fourth optical modes shown from left to right; (b) spectral throughputs show the efficiencies of each individual modes; (c) incoherent sum of the optical modes weighted by the spectral throughputs.

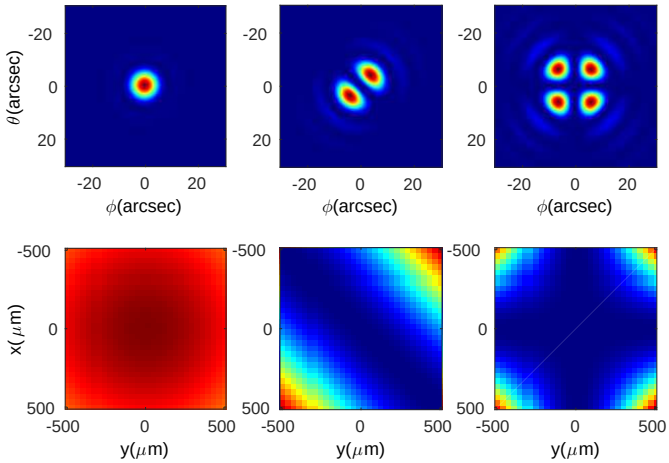

(a) Optical modes.

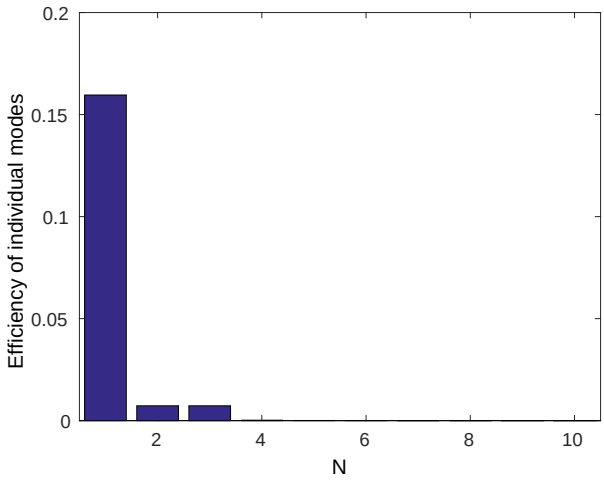

(b) Optical throughput spectral.

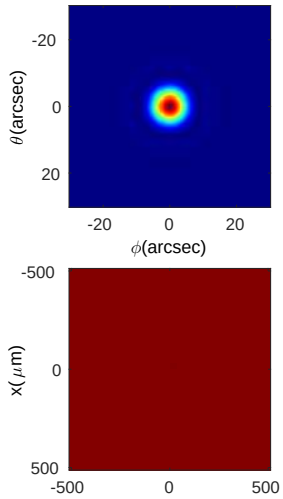

(c) Incoherent sum of optical modes.

Fig. 2.9 Optical modes for 110 μm of M-Band: (a) first, second and fourth optical modes shown from left to right; (b) spectral throughputs show the efficiencies of each individual modes; (c) incoherent sum of the optical modes weighted by the spectral throughputs.

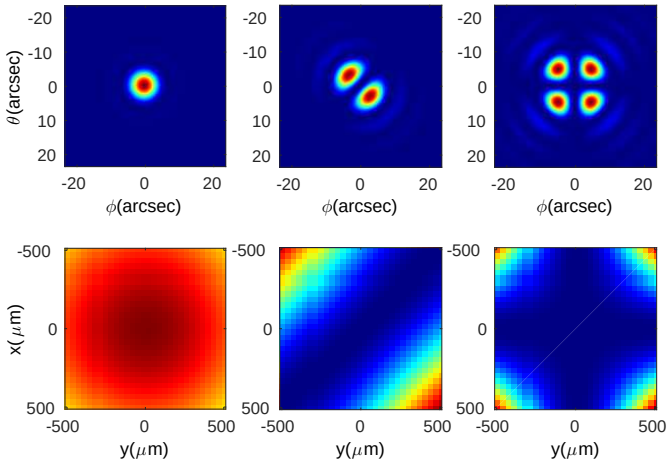

(a) Optical modes.

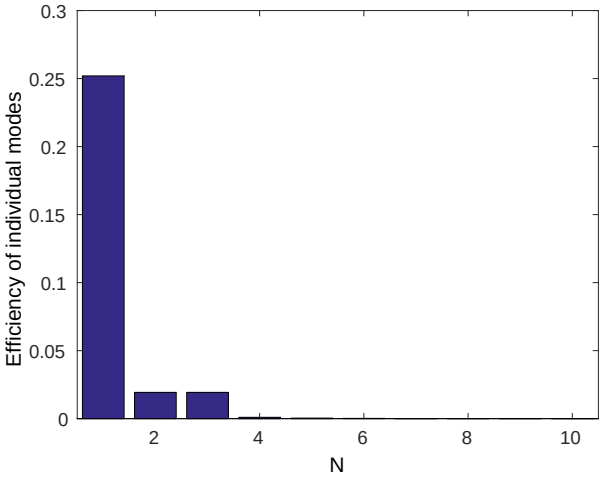

(b) Optical throughput spectral.

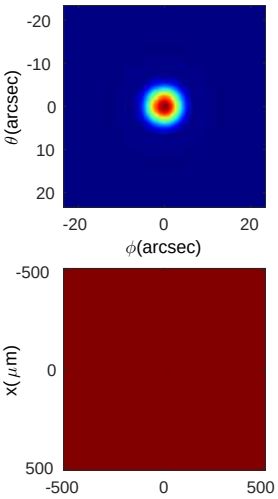

(c) Incoherent sum of optical modes.

Fig. 2.10 Optical modes for 85 μm of M-Band: (a) first, second and fourth optical modes shown from left to right; (b) spectral throughputs show the efficiencies of each individual modes; (c) incoherent sum of the optical modes weighted by the spectral throughputs.

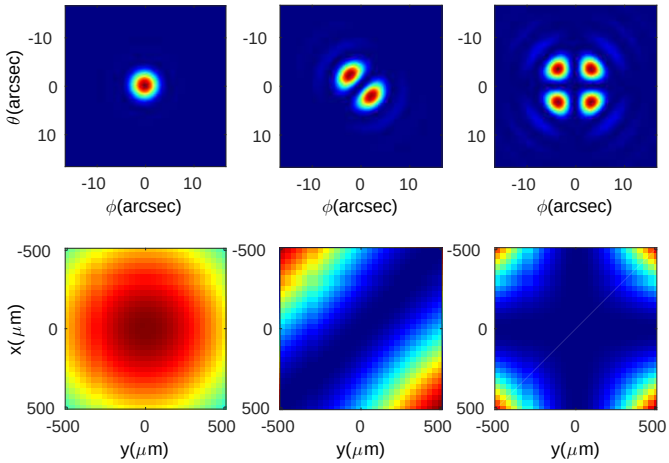

(a) Optical modes.

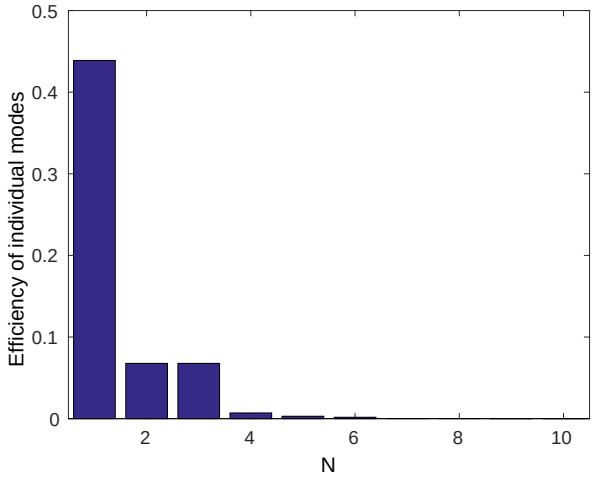

(b) Optical throughput spectral.

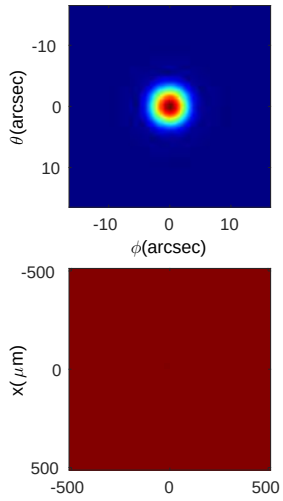

(c) Incoherent sum of optical modes.

Fig. 2.11 Optical modes for 60 μm of M-Band: (a) first, second and fourth optical modes shown from left to right; (b) spectral throughputs show the efficiencies of each individual modes; (c) incoherent sum of the optical modes weighted by the spectral throughputs.

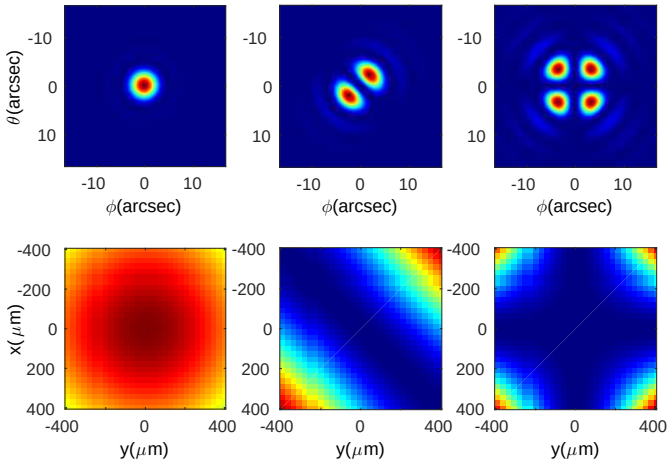

(a) Optical modes.

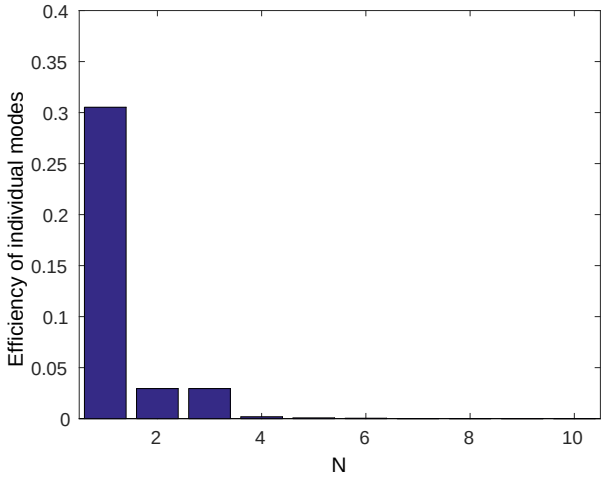

(b) Optical throughput spectral.

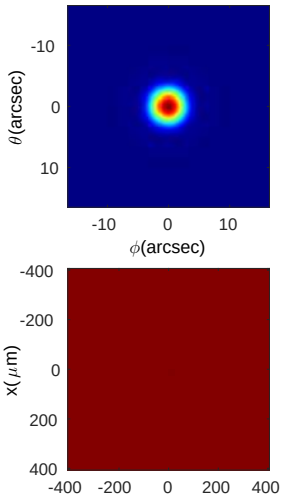

(c) Incoherent sum of optical modes.

Fig. 2.12 Optical modes for 60 μm of S-Band: (a) first, second and fourth optical modes shown from left to right; (b) spectral throughputs show the efficiencies of each individual modes; (c) incoherent sum of the optical modes weighted by the spectral throughputs.

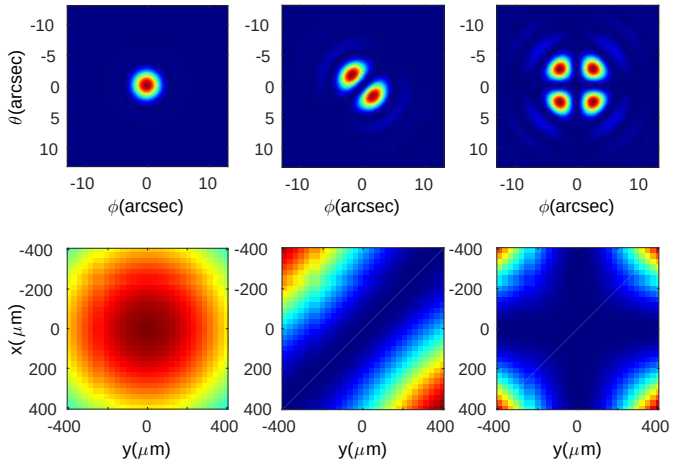

(a) Optical modes.

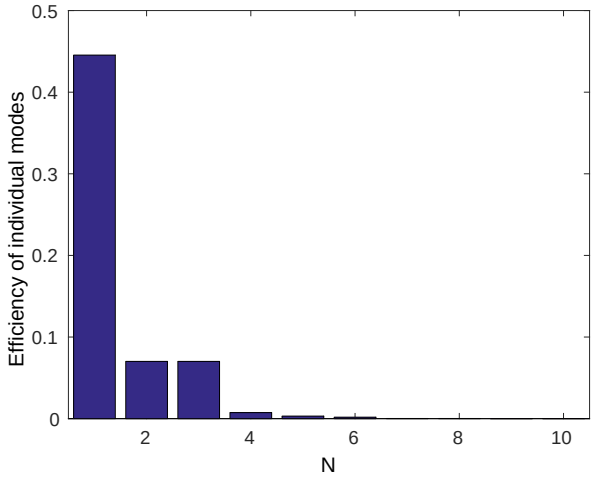

(b) Optical throughput spectral.

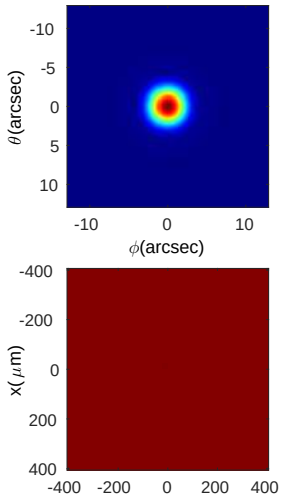

(c) Incoherent sum of optical modes.

Fig. 2.13 Optical modes for 47 μm of S-Band: (a) first, second and fourth optical modes shown from left to right; (b) spectral throughputs show the efficiencies of each individual modes; (c) incoherent sum of the optical modes weighted by the spectral throughputs.

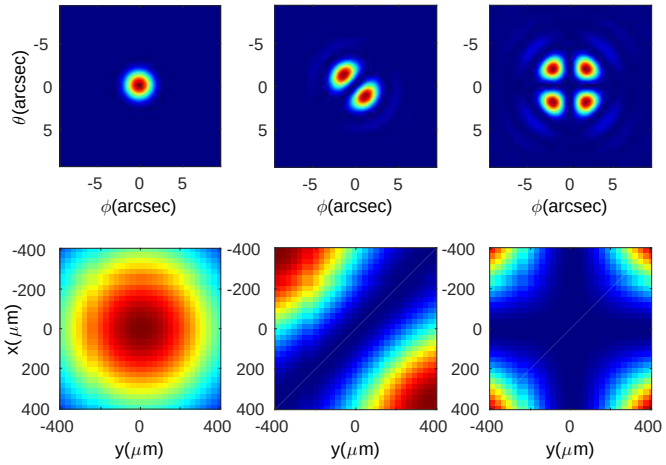

(a) Optical modes.

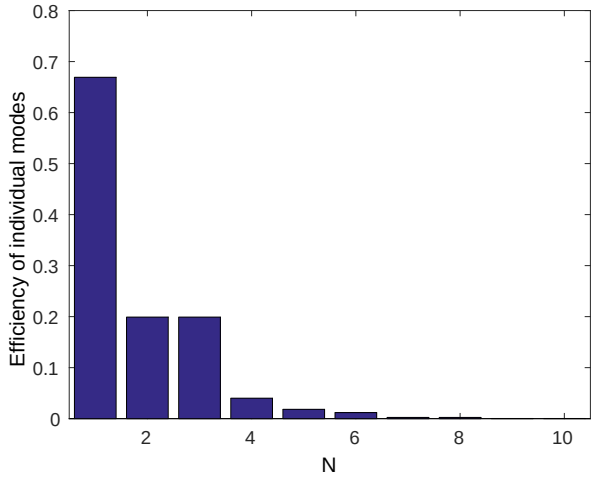

(b) Optical throughput spectral.

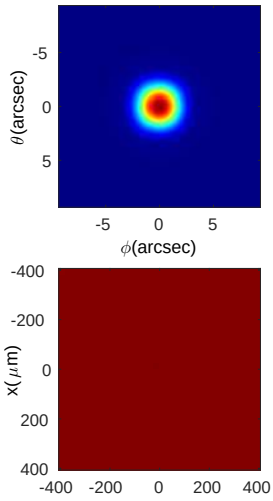

(c) Incoherent sum of optical modes.

Fig. 2.14 Optical modes for 34 μm of S-Band: (a) first, second and fourth optical modes shown from left to right; (b) spectral throughputs show the efficiencies of each individual modes; (c) incoherent sum of the optical modes weighted by the spectral throughputs.

Optical Modes of An Off-axis Pixel

In order to examine if the optical modes are the same for off-axis pixels, the optical modes of a pixel that neighbours the central pixel were calculated, so that the spectral throughput can be determined. The optical modes, the modal spectrum and the composite beam patterns of an off-axis pixel for L-Band at 160 μm are plotted in Figure 2.15.

The spectral throughputs are identical as compared to the on-axis case, which shows that off-axis pixels have the same throughput, as would be predicted by paraxial optics. Also as expected, the optical modes on the sky are shifted. It seems that the optical modes and modal spectrum of an off-axis pixel are the same as those of the on-axis pixel.

Optical Modes with Subreflector and Support Legs Blockage

By considering the effect of the blockage of the subreflector and support legs, the optical modes and the associated efficiencies were calculated. The modal forms were expected to be almost identical, but the beam patterns should then show the effect of diffraction around the subreflector and support legs. The optical modes shown in Figure 2.16 to 2.18 are essentially the same as those shown earlier, but with the effects of blockage included. The plots of the central wavelengths in each waveband are shown.

The optical modes on the sky show the effects of diffraction around the subreflector and along the support legs. But the form of optical modes are largely unaltered, and the spectral throughputs are decreased as including the subreflector and support legs blockage decreases the effective telescope area. The reduced sum of the throughputs $\eta'_{\rm cal}$, geometrical throughputs $\eta'_{\rm geo}$ for the central wavelengths in the 3 bands are shown in Table 2.3. To check how the throughputs changed with blockage, the values of total throughputs and geometrical throughputs without blockage are also tabulated in the table.

Table 2.3 Overall throughputs calculated by summing the modal efficiencies, $\eta'_{\rm cal}$, and the throughputs calculated geometrically $\eta'_{\rm geo}$ for the situation that subreflector and support legs blockage are included at the central wavelengths of the SAFARI bands.

Waveband	λ (μm)	$\eta'_{\rm cal}$	$\eta'_{\rm geo}$	$\eta'_{\rm cal}/\eta_{\rm cal}$	$\eta'_{\rm geo}/\eta_{\rm geo}$
L-Band	160	0.242	0.237	0.820	0.834
M-Band	85	0.240	0.235	0.822	0.834
S-Band	47	0.491	0.481	0.820	0.834

The results calculated numerically and geometrically are essentially equal. The ratio between $\eta'_{\rm cal}$ and $\eta_{\rm cal}$ shows that the loss in throughputs when sub-reflector and support legs are included, is about 18%. The throughputs calculated geometrically has dropped by about 17%.

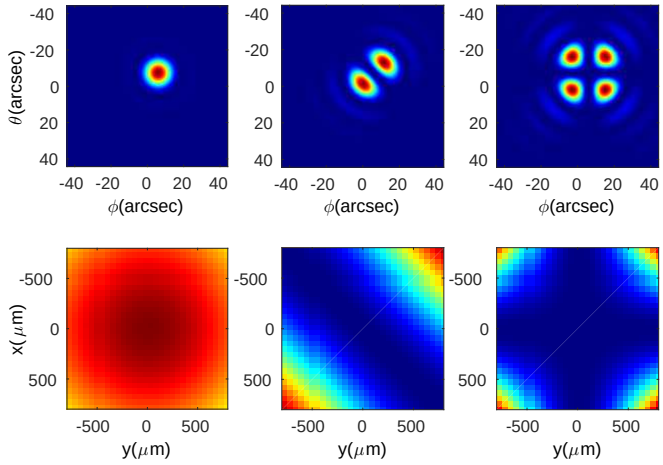

(a) Optical modes.

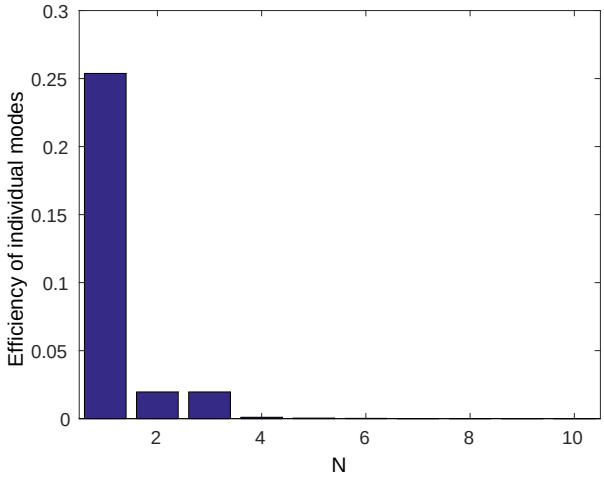

(b) Optical throughput spectral.

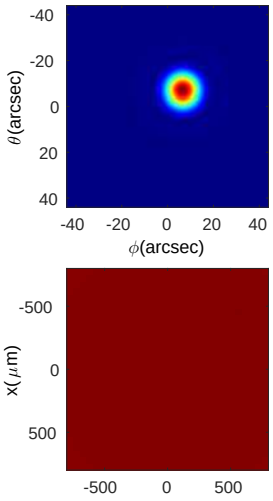

(c) Incoherent sum of optical modes.

Fig. 2.15 Optical modes of an off-axis pixel for SAFARI L-Band of 160 μm: (a) first, second and fourth optical modes shown from left to right; (b) spectral throughputs show the efficiencies of each individual modes; (c) incoherent sum of the optical modes weighted by the spectral throughputs.

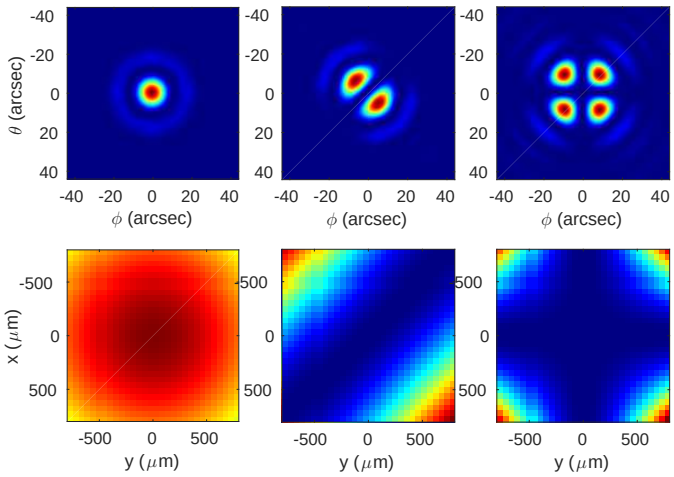

(a) Optical modes.

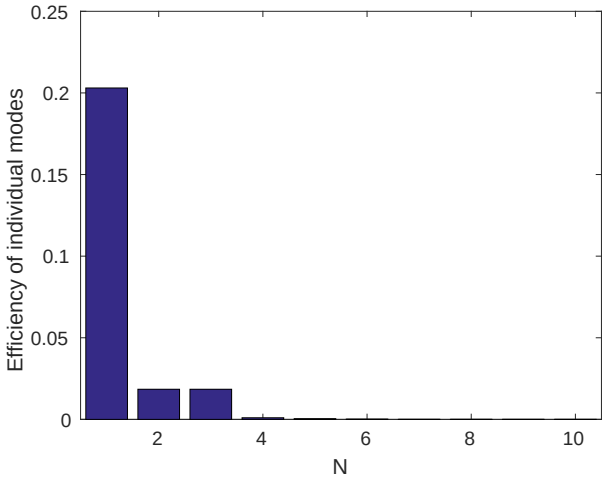

(b) Optical throughput spectral.

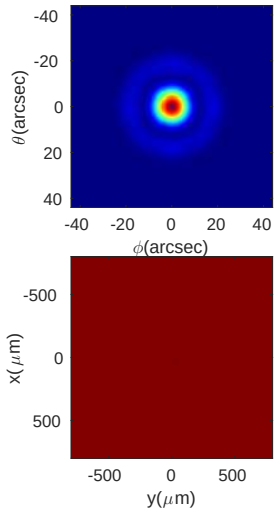

(c) Incoherent sum of optical modes.

Fig. 2.16 Optical modes with subreflector and support legs blockage included at 160 μm of L-Band: (a) first, second and fourth optical modes shown from left to right; (b) spectral throughputs show the efficiencies of each individual modes; (c) incoherent sum of the optical modes weighted by the spectral throughputs.

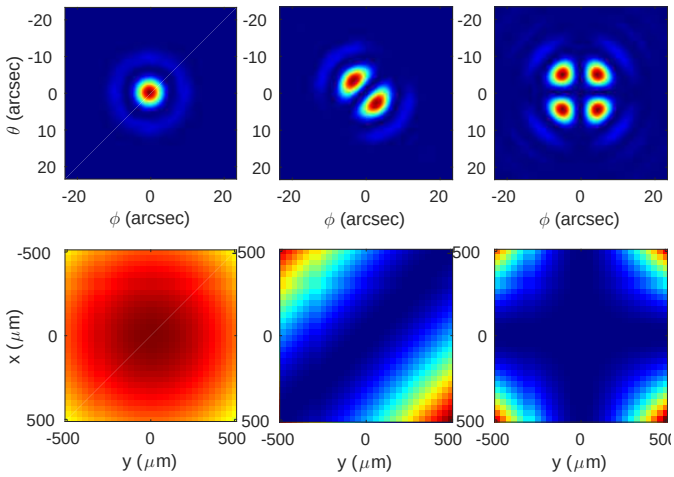

(a) Optical modes.

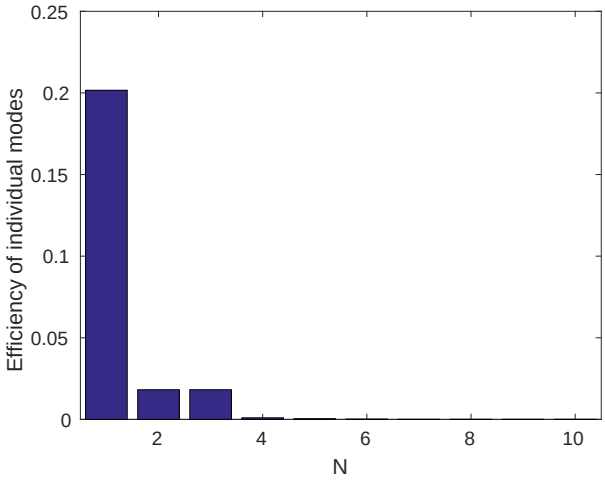

(b) Optical throughput spectral.

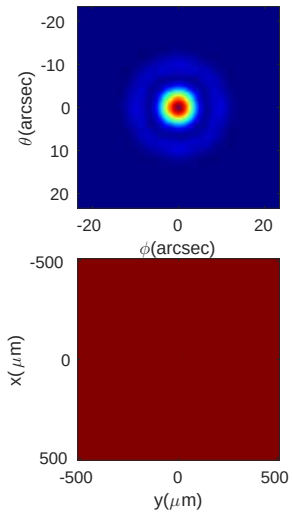

(c) Incoherent sum of optical modes.

Fig. 2.17 Optical modes with subreflector and support legs blockage included at 85 μm of M-Band: (a) first, second and fourth optical modes shown from left to right; (b) spectral throughputs show the efficiencies of each individual modes; (c) incoherent sum of the optical modes weighted by the spectral throughputs.

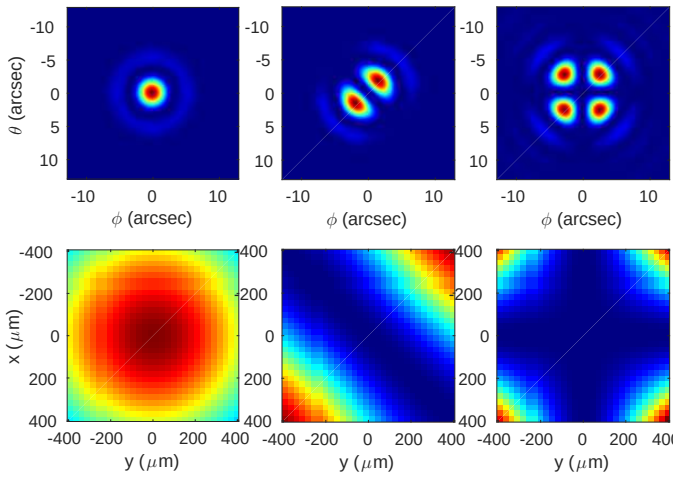

(a) Optical modes.

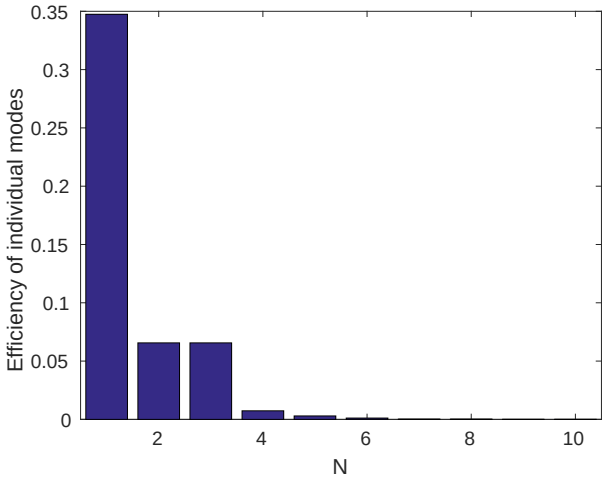

(b) Optical throughput spectral.

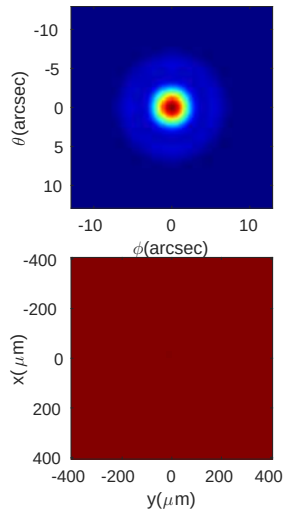

(c) Incoherent sum of optical modes.

Fig. 2.18 Optical modes with subreflector and support legs blockage included at 47 μm of S-Band: (a) first, second and fourth optical modes shown from left to right; (b) spectral throughputs show the efficiencies of each individual modes; (c) incoherent sum of the optical modes weighted by the spectral throughputs.

2.4.2 Waveguide Modes

A crucial question is how well the focal plane fields of the optical modes are spanned by the waveguide modes of the input aperture of the lightpipe. As stated in earlier sections, the majority of the throughput is accounted by the first 4 optical modes, the needed number of waveguide modes are needed to be determined. A set of 24 square waveguide modes having the size of the pixel footprint are considered. The indicies of the modes are ordered in certain ways that TE and TM modes with the same indices cut on at the same wavelength. The modes are given in Table 2.4.

Table 2.4 The indices of the square waveguide modes.

Mode Index	**1**	**2**	**3**	**4**	**5**	**6**	**7**	**8**
TE_{mn}	10	01	11	20	02	21	12	22
TM_{mn}	-	-	11	-	-	21	12	22
Mode Index	**9**	**10**	**11**	**12**	**13**	**14**	**15**	**16**
TE_{mn}	30	03	31	13	32	23	40	04
TM_{mn}	-	-	31	13	32	23	-	-

The images in Figure 2.19-2.21 are showing these TE types and TM types waveguide modes for the 3 wavebands at their central wavelengths.

2.4.3 Coupling between Optical Modes & Waveguide Modes

The efficiencies with which the waveguide modes can couple to those optical modes that carry power were then considered. The first 4 optical modes were considered for the calculation as that the majority of power are carried by them.

The histograms in Figure 2.22, 2.23 and 2.24 show the coupling efficiencies of the first 4 optical modes to a set of 24 square waveguide modes having the size of the pixel footprint for the SAFARI wavebands at their central wavelengths.The coupling efficiencies to TE type modes are show in blue, and the coupling efficiencies to TM type modes are shown in red. It can be seen that the first optical mode only couples to TE_{10}, TE_{01}, TE_{30} and TE_{03}; the seccond and the third optical modes are degenerate, they couple to the same waveguide modes TE_{11}, TM_{11}, TE_{20}, TE_{02}, TE_{31}, TE_{13}, TE_{40}, and TE_{04}, with the same efficiencies; the fourth optical mode mainly couples to waveguide modes TE_{21}, TM_{21}, TE_{12} and TM_{12}.

The coupling efficiencies of each optical mode to a full set of square waveguide modes, η_{cpl}, at the extreme and central wavelengths of the wavebands are shown in Table 2.5, together with the values of optical throughput in one polarisation of the optical mode, η_{opt}.

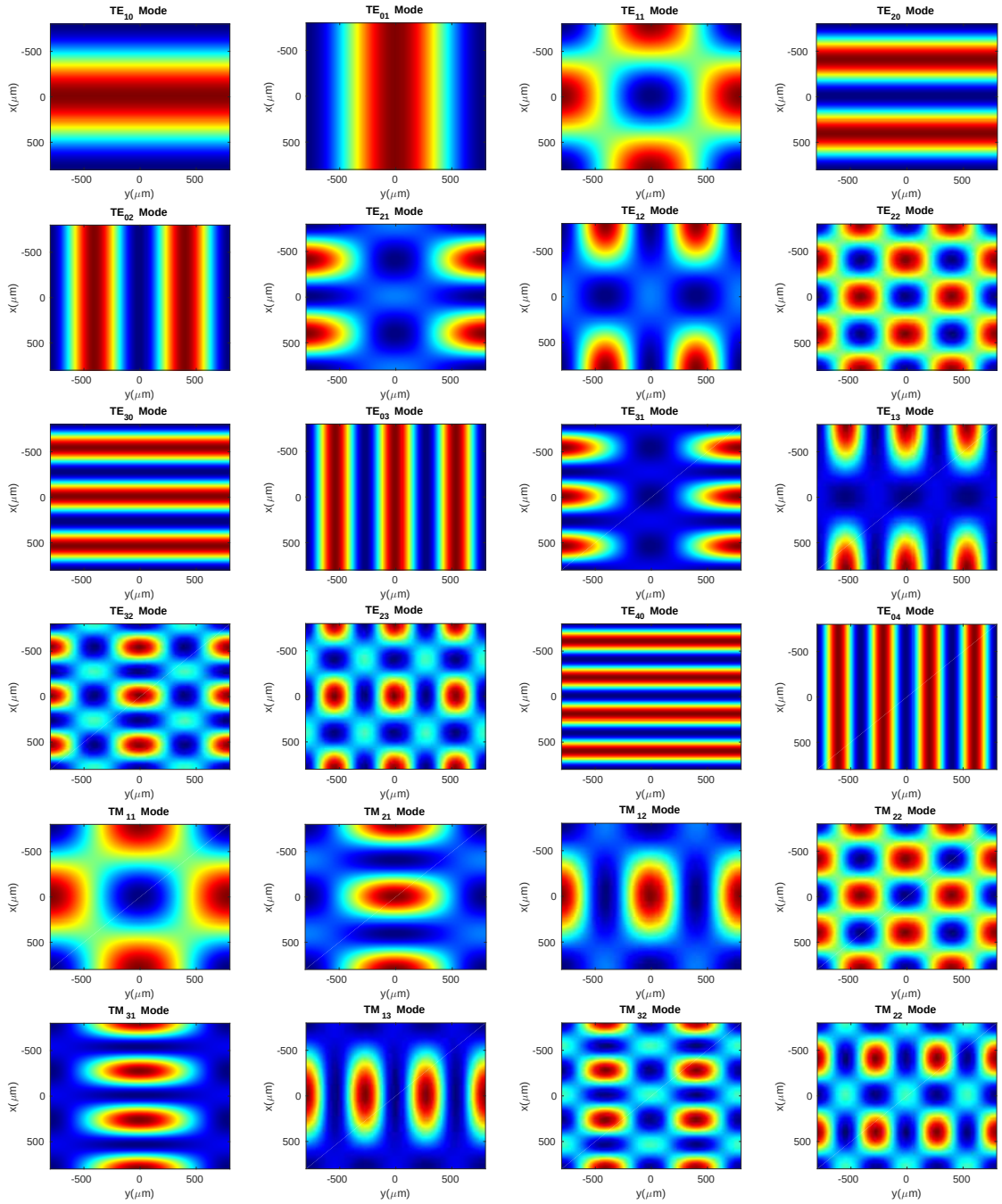

Fig. 2.19 TE and TM waveguide modes for L-Band at 160 μm.

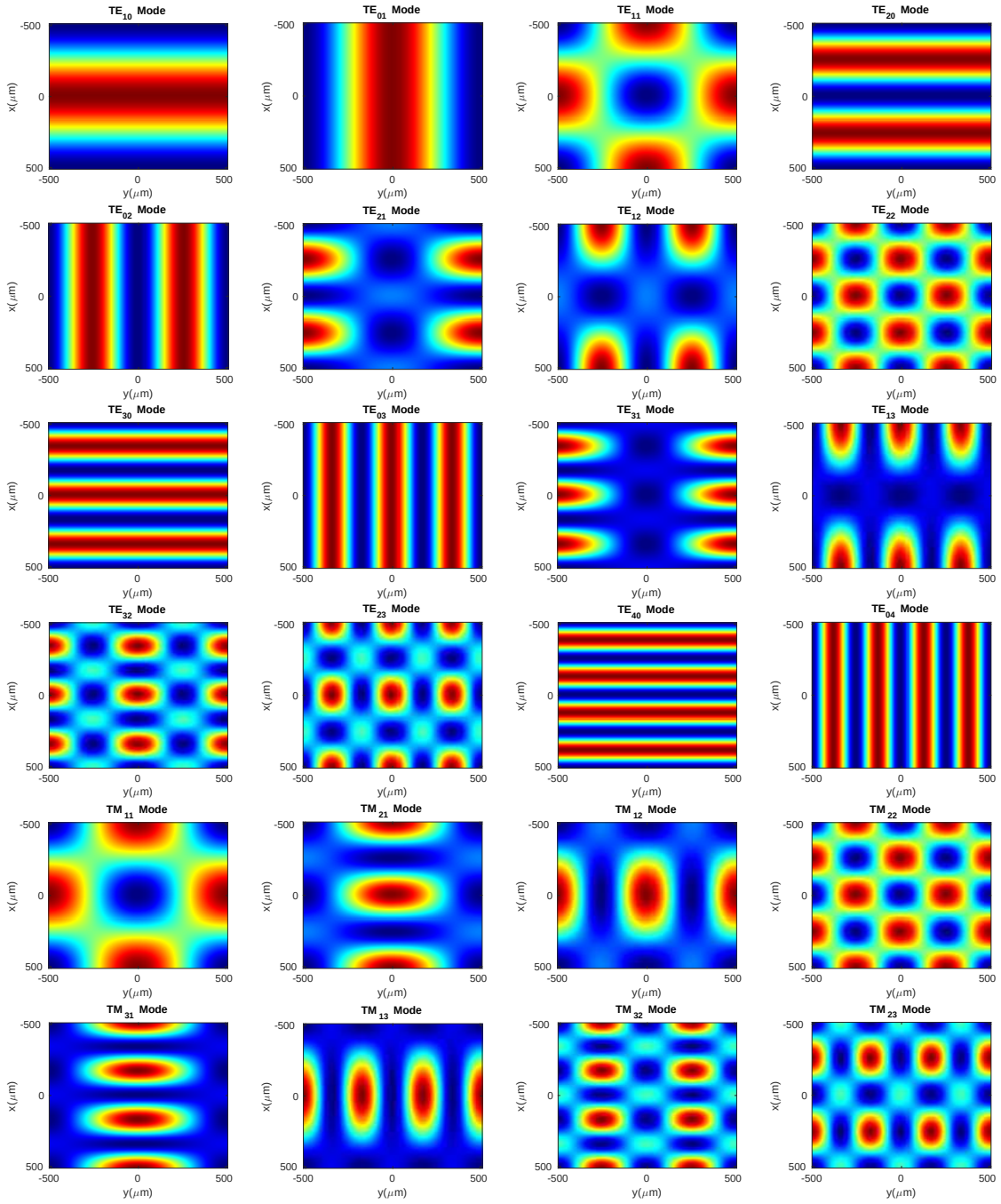

Fig. 2.20 TE and TM waveguide modes for M-Band at 85 μm.

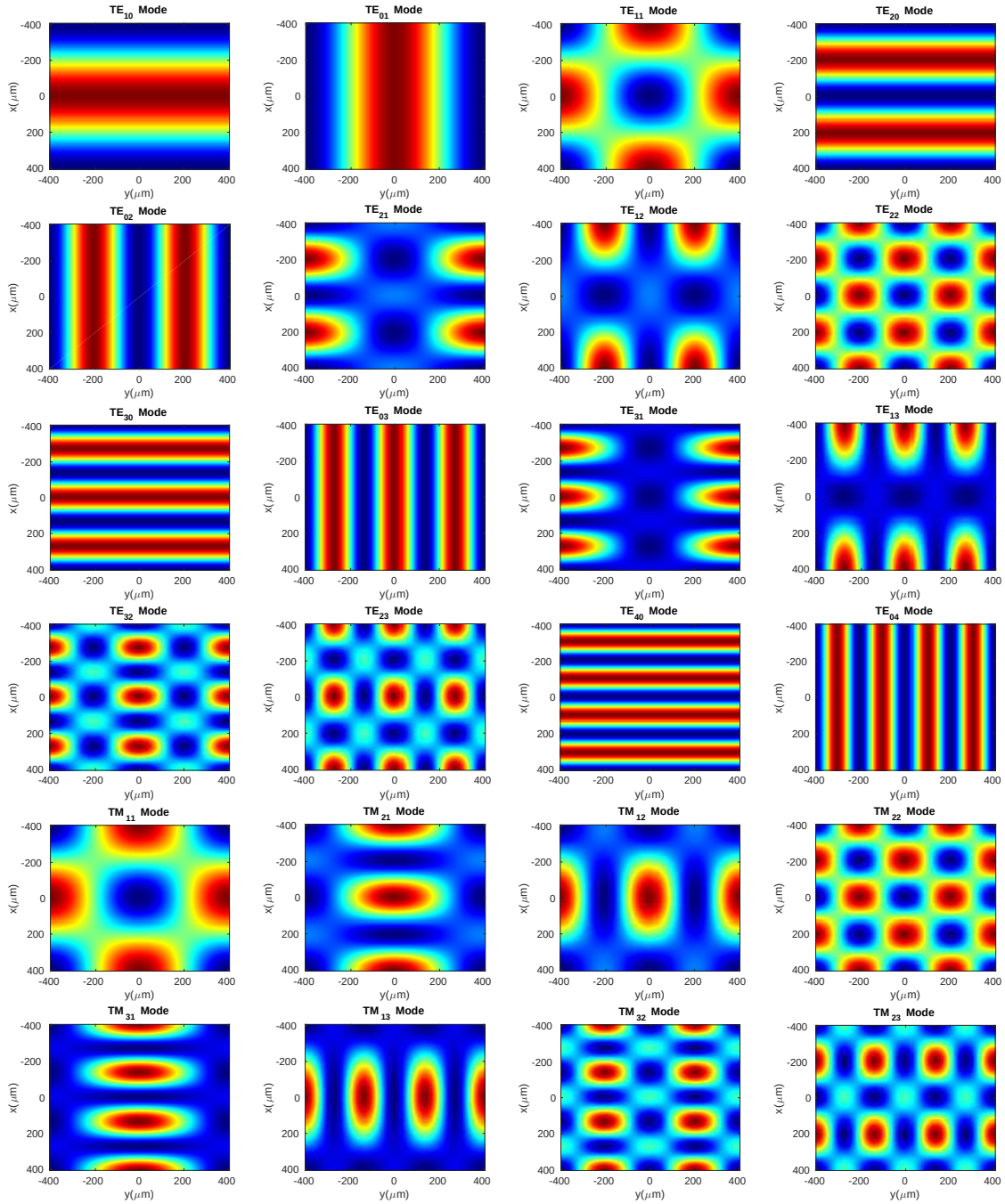

Fig. 2.21 TE and TM waveguide modes for S-Band at 47 μm.

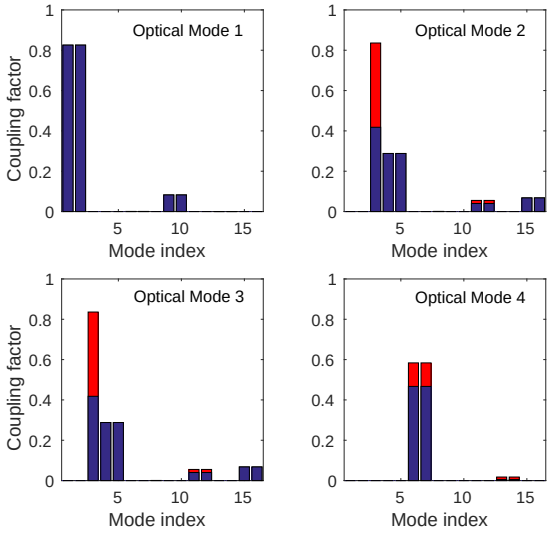

(a) 210 μm of L-Band,

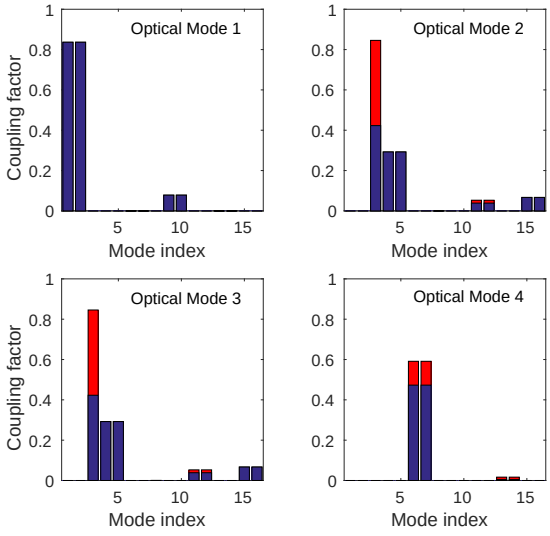

(b) 160 μm of L-Band,

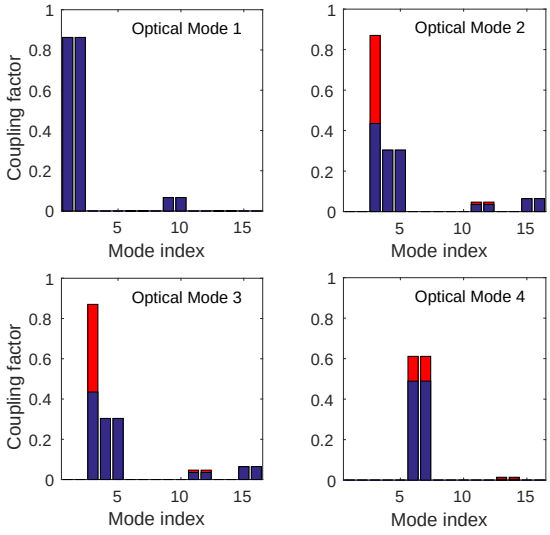

(c) 110 μm of L-Band;

Fig. 2.22 Histograms of the coupling efficiencies of the first 4 optical modes of the telescope to a full set of square waveguide modes for the maximal, central and minimal wavelengths of the SAFARI L-Band. The blue bars correspond to TE modes, and the red bars to TM modes.

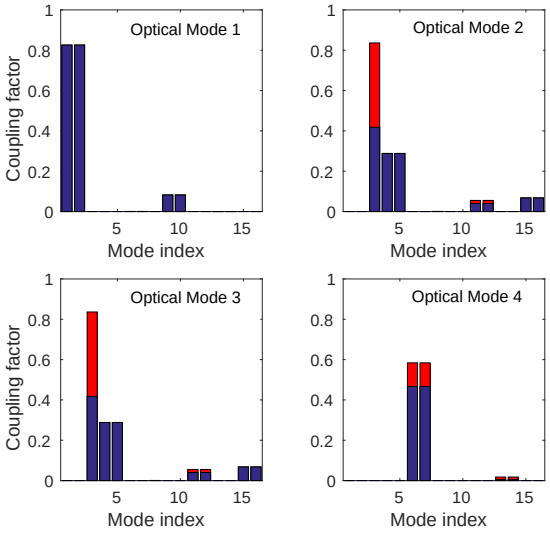

(a) 110 μm of M-Band,

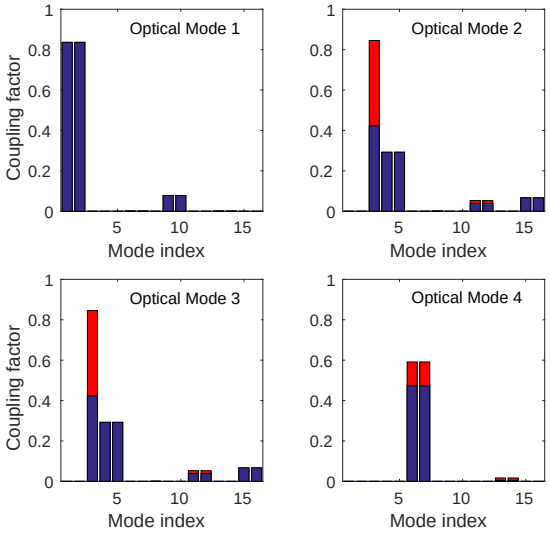

(b) 85 μm of M-Band,

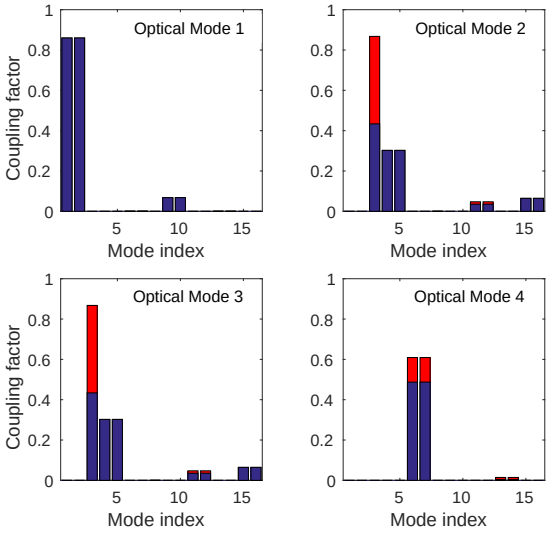

(c) 60 μm of M-Band;

Fig. 2.23 Histograms of the coupling efficiencies of the first 4 optical modes of the telescope to a full set of square waveguide modes for the maximal, central and minimal wavelengths of the SAFARI M-Band. The blue bars correspond to TE modes, and the red bars to TM modes.

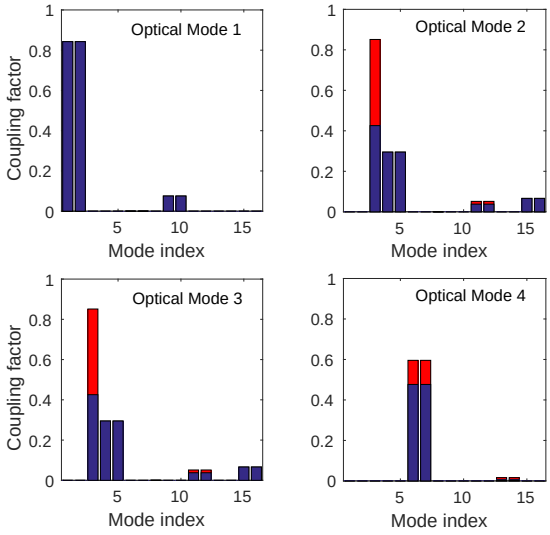

(a) 60 μm of S-Band,

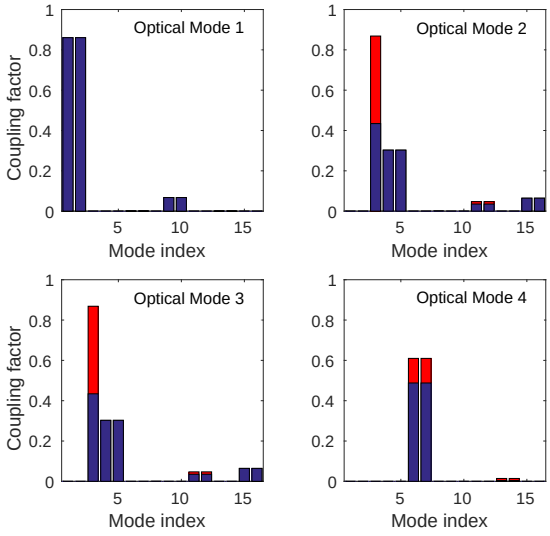

(b) 47 μm of S-Band,

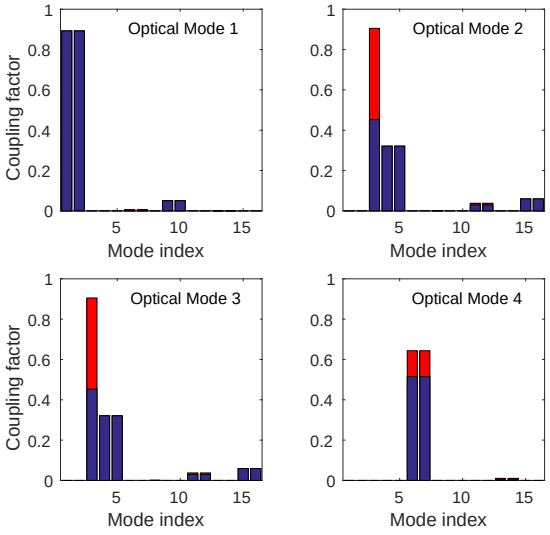

(c) 34 μm of S-Band.

Fig. 2.24 Histograms of the coupling efficiencies of the first 4 optical modes of the telescope to a full set of square waveguide modes for the maximal, central and minimal wavelengths of the SAFARI S-Band. The blue bars correspond to TE modes, and the red bars to TM modes.

Table 2.5 Optical throughput in one polarisation of the optical mode, $\eta_{\rm opt}$; coupling efficiency of the optical mode to all of the waveguide modes, $\eta_{\rm cpl}$; and total throughput to an ideal waveguide absorber in one polarisation $\eta_{\rm det} = \eta_{\rm opt} \times \eta_{\rm cpl}$.

Waveband	λ (μm)	Optical Mode 1			Optical Mode 2			Optical Mode 4		
		$\eta_{\rm opt}$	$\eta_{\rm cpl}$	$\eta_{\rm det}$	$\eta_{\rm opt}$	$\eta_{\rm cpl}$	$\eta_{\rm det}$	$\eta_{\rm opt}$	$\eta_{\rm cpl}$	$\eta_{\rm det}$
L-Band	210	0.157	0.908	0.143	0.007	0.829	0.006	0.0002	0.601	0.0001
	160	0.254	0.915	0.232	0.020	0.835	0.017	0.001	0.608	0.001
	110	0.459	0.929	0.426	0.075	0.849	0.064	0.008	0.626	0.005
M-Band	110	0.160	0.909	0.145	0.007	0.829	0.006	0.0002	0.602	0.0001
	85	0.252	0.914	0.230	0.019	0.835	0.016	0.001	0.608	0.001
	60	0.439	0.928	0.407	0.068	0.848	0.058	0.007	0.624	0.004
S-Band	60	0.305	0.918	0.280	0.030	0.838	0.025	0.002	0.612	0.001
	47	0.445	0.928	0.413	0.070	0.848	0.059	0.007	0.624	0.004
	34	0.670	0.948	0.635	0.199	0.871	0.173	0.040	0.654	0.026

The total throughput to an ideal waveguide absorber in one polarisation, $\eta_{\rm det}$, are determined and also tabulated in Table 2.5.

2.4.4 Power Loading from the Source

Once the optical throughputs of the optical modes, and the coupling efficiencies between the individual optical modes and the waveguide modes are known, we can then calculate the integrated power loading from the source to a single detector as a function of temperature, from relation

$$P(T) = \sum_i \sum_n \int_{\nu_{\rm min}}^{\nu_{\rm max}} \eta_n^{\rm opt}(\nu)\eta_n^{\rm cpl}(\nu)\frac{2h\nu}{\exp(\frac{h\nu}{k_bT})-1}{\rm d}\nu, \tag{2.97}$$

where i denotes the index of the waveguide modes. Figure 2.25 shows the estimated power for L-, M- and S-Band. Detected power increases as temperature, as expected. The power levels vary for different bands, because the wavelengths fall at different region of the blackbody spectrum, which indicates that for shorter wavelength bands, only little power can be seen by the detector if the temperature of the source is low.

2.4.5 Aperture Efficiency

Figure 2.26 shows the beam patterns that would be measured when the telescope is being scanned of a point source when the complete set of 24 waveguide modes was used are shown in the top row for the 3 SAFARI wavebands at their central wavelengths. The bottom row shows the power cuts in the θ and ϕ directions. The plots on the left are for a θ-polarised source, and the middle plots for a ϕ-polarised source, and the right plots for an unpolarised

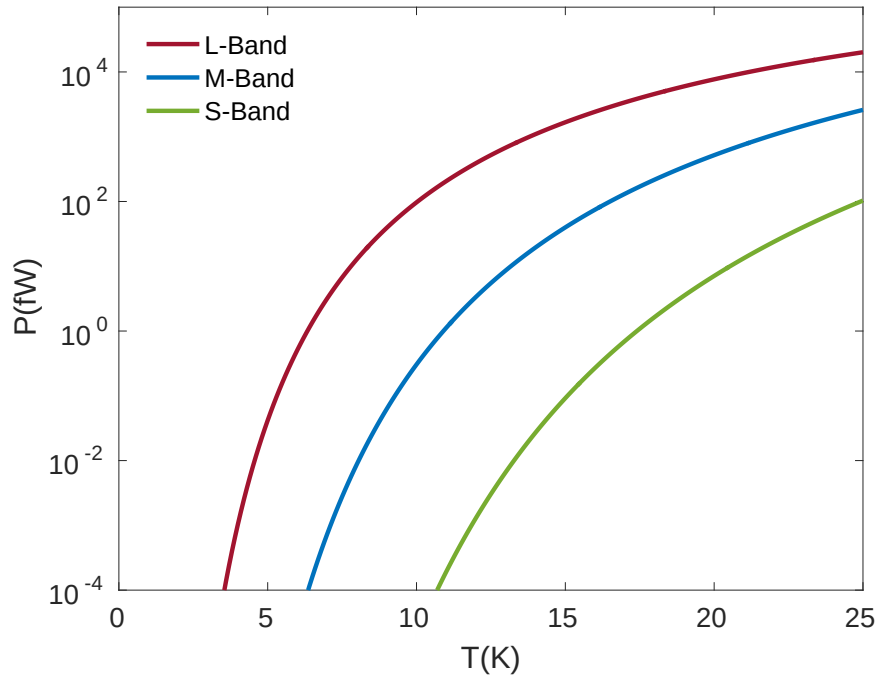

Fig. 2.25 Power seen by a single detector, assuming a perfect square absorber are used, for the L-, M-, and S-Band.

source. For an unpolarised source, the cuts in θ and ϕ directions are identical and thus the green and red lines are indistinguishable. The vertical blue lines correspond to the diffraction limits, $\pm\lambda/2D$, where D is the diameter of the primary mirror.

The 3 plots shown in Figure 2.26 are essentially the same. The plots in the bottom row are the effective area as a function of point source direction, expressed in dB's, and normalised to the maximum value, which were calculated from Eq.(aper). The effect on the beam shape of using a reduced set of waveguide modes was examined. The plots in Figure 2.27 show the beam patterns of an L-Band waveguide detector at the central wavelength, 160μm, when an unpolarised source is swept across the sky.

It seems that almost no differences can be observed in the beam patterns, but the effective area increases left to right. The effective area of the whole optical system for an on-axis source were determined from Eq.(2.76), selected results over a range of wavelength in the 3 wavebands are listed in Table 2.6. The shorter the wavelength in the same waveband, the higher the aperture efficiency can be achieved, this is because for the shorter wavelength, more modes can be recovered.

In the case of a complete set of 24 waveguide modes, the on-axis aperture efficiency varies between 0.148 to 0.629. The effective area falls further when the waveguide mode set is

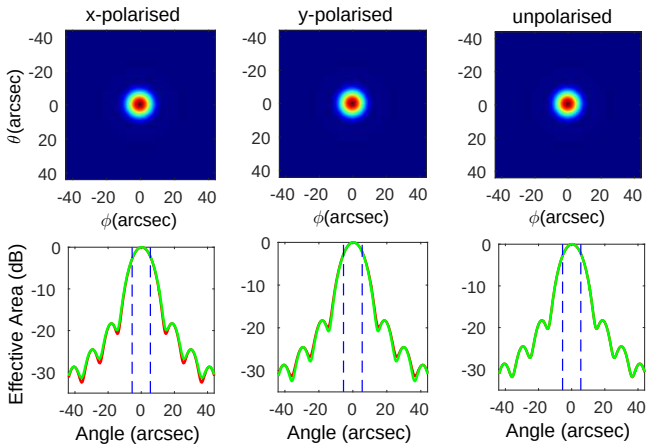

(a) 160 μm of L-Band;

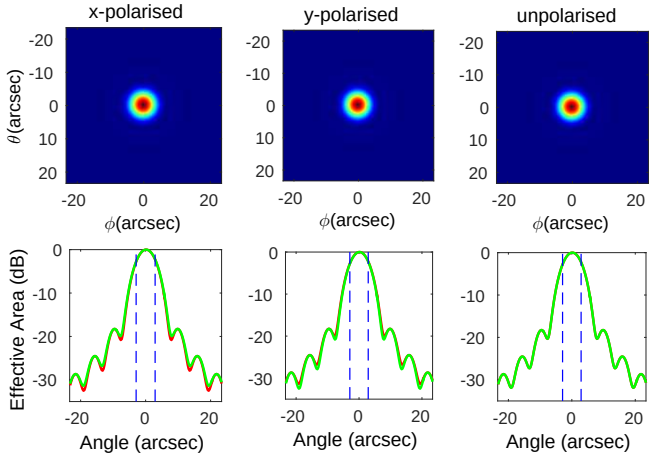

(b) 85 μm of M-Band;

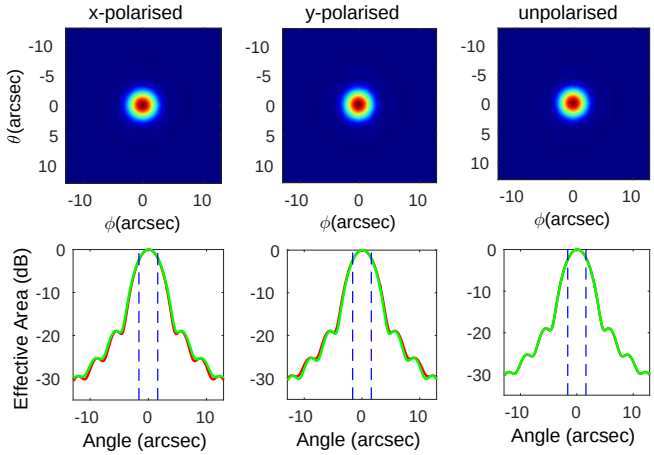

(c) 47 μm of S-Band.

Fig. 2.26 The top rows show the beam patterns of a perfect waveguide detector having a complete set of 24 waveguide modes for the central wavelength of (a)L-, (b) M-, and (c)S-Band. From left to right, θ-polarised, ϕ-polarised and unpolarised source are used. The bottom rows show cuts in the θ and ϕ directions. The green lines correspond to cuts in the θ direction, and the red lines correspond to cuts in the ϕ direction. The response are identical in the unpolarised case, and thus the green line and red line are indistinguishable. The dashed blue lines show the diffraction limits, $\pm\lambda/2D$, where D is the diameter of the primary mirror.

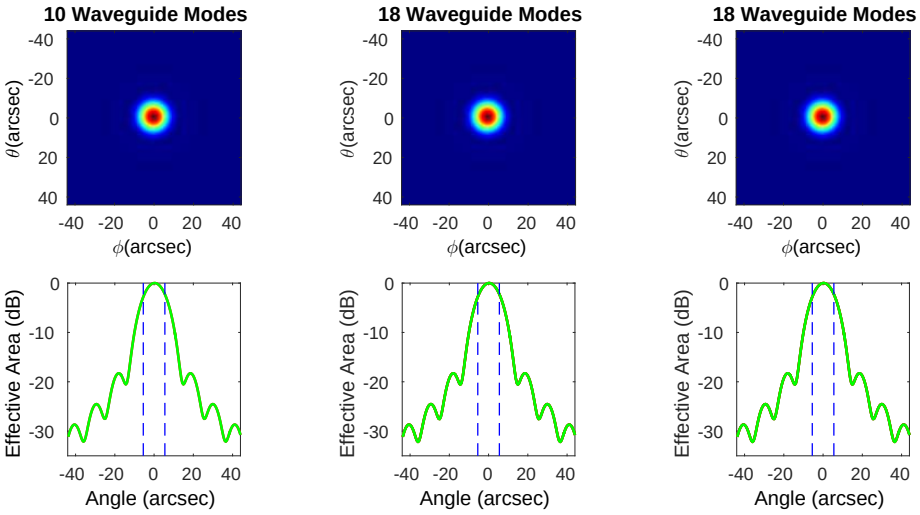

Fig. 2.27 Beam shape of using reduced set of waveguide mode for the central wavelength, 160 μm, of L-Band. The three cases shown (left to right) are for the case 10, 18 and 24 waveguide modes are used.

Table 2.6 Aperture efficiencies of the optical system for the maximal, central and minimal wavelengths of SAFARI bands.

Waveband	λ (μm)	Aperture Efficiency, η_{ap}		
		10 Modes	18 Modes	24 Modes
L-Band	210	0.135	0.148	0.148
	160	0.220	0.240	0.240
	110	0.404	0.435	0.435
M-Band	110	0.137	0.151	0.151
	85	0.218	0.238	0.238
	60	0.386	0.416	0.416
S-Band	60	0.265	0.289	0.289
	47	0.392	0.422	0.422
	34	0.596	0.629	0.629

reduced. Previously we saw that when subreflector and support legs blockage were included, the throughputs scaled with the effective telescope area with blockage, by approximately 18%. Figure 2.28 shows the effect of subreflector and support legs blockage on the beam pattern for 24 waveguide modes are used. The plots are for the central wavelengths in the SAFARI wavebands.

It can be seen that the beam pattern shapes change little as the number of waveguide modes is unchanged, but large diffraction rings can be observed around the subreflector.

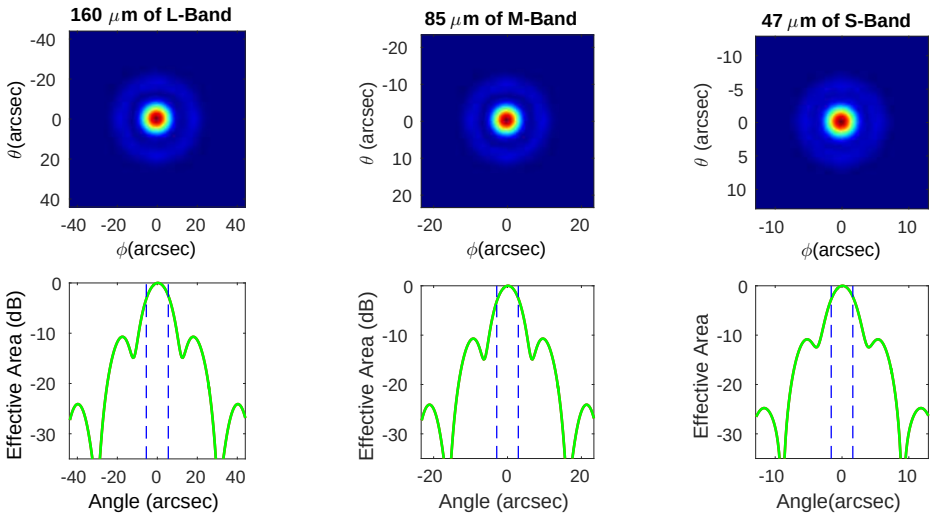

Fig. 2.28 Beam shape and the effective area with the effect of subreflector and support legs included for the central wavelengths of L-, M-, and S-Band.

However, the effective area changes significantly. For easy comparison, the effective area of the cases with and without the blockage are tabulated in Table 2.7.

Table 2.7 Reduced aperture efficiencies of the optical system for the maximal, central and minimal wavelengths of SAFARI bands.

Waveband	λ (μm)	Aperture Efficiency		
		η^{S}_{AE}	η_{AE}	$\eta^{S}_{\mathrm{AE}}/\eta_{\mathrm{AE}}$
L-Band	210	0.099	0.148	0.669
	160	0.159	0.240	0.663
	110	0.284	0.435	0.653
M-Band	110	0.101	0.151	0.669
	85	0.158	0.238	0.664
	60	0.272	0.416	0.654
S-Band	60	0.191	0.289	0.661
	47	0.276	0.422	0.654
	34	0.400	0.629	0.611

It has been found that the on-axis effective area is more sensitive, falling by 34%. This effect results from power loss into the large diffraction rings which are created by the subreflector.

The size of a single pixel is small to enable Nyquist sampled mapping, and thus the effective area of any single pixel is small. For a point source on the sky, the PSF is much larger than a single pixel. To recover some of the aperture efficiency lost through using small pixels, we can co-add the a number of pixels in order to cover the PSF more effectively [60, 45].

Figure 2.29 shows the beam pattern when a subarray of N×N pixels are added together at the central wavelengths of the 3 wavebands, and the cuts in the ϕ direction across the subarray formed by co-adding the outputs of N×N pixels.

Table 2.8 Peak aperture efficiencies for beam patterns of co-added N×N subarrays at the maximal, central and minimal wavelengths of SAFARI wavebands.

Waveband	λ (μm)	Aperture Efficiency, η_{ap}			
		1×1 Array	2×2 Array	3×3 Array	4×4 Array
L-Band	210	0.148	0.466	0.702	0.824
	160	0.240	0.634	0.801	0.824
	110	0.435	0.759	0.790	0.828
M-Band	110	0.151	0.447	0.734	0.763
	85	0.238	0.629	0.795	0.817
	60	0.416	0.715	0.825	0.829
S-Band	60	0.289	0.720	0.861	0.886
	47	0.422	0.730	0.842	0.846
	34	0.629	0.797	0.860	0.878

The summed beam patterns start to show square shapes as more subarrays were added, which shows evidence of the underlying square set of pixels. The aperture efficiencies of the subarray are high as a consequence of more of the PSF being included. Table 2.8 is a summary of the peak aperture efficiencies for different sizes of subarrays at different wavelengths when viewing a point source.

These numbers correspond to the 24 waveguide mode set. It is clear that high efficiencies can be achieved; 3×3 and 4×4 summed subarrays would give aperture efficiencies of between 70% and 80%.

2.4.6 Coupling to the Cold Baffle

In this section, the power coupled in from the cold baffle is considered. The coupling efficiencies to the baffle were calculated through the power that is not coupled to the sky, as described by Eq.(2.76) . The general arrangement has already been shown in Figure 2.5.

3 efficiency terms need to be considered to ensure that the coupling to the cold baffle is calculated correctly: the throughput of each of the optical modes, η_{opt}, the coupling between the optical modes and the waveguide modes, η_{cpl}, and the coupling between the waveguide modes and the absorber, α_{mn}. In Figure 2.30, the coupling of each of the TE (left column) types and TM (right column) types waveguide modes to the sky (red) and to the cold baffle (blue) are plotted.

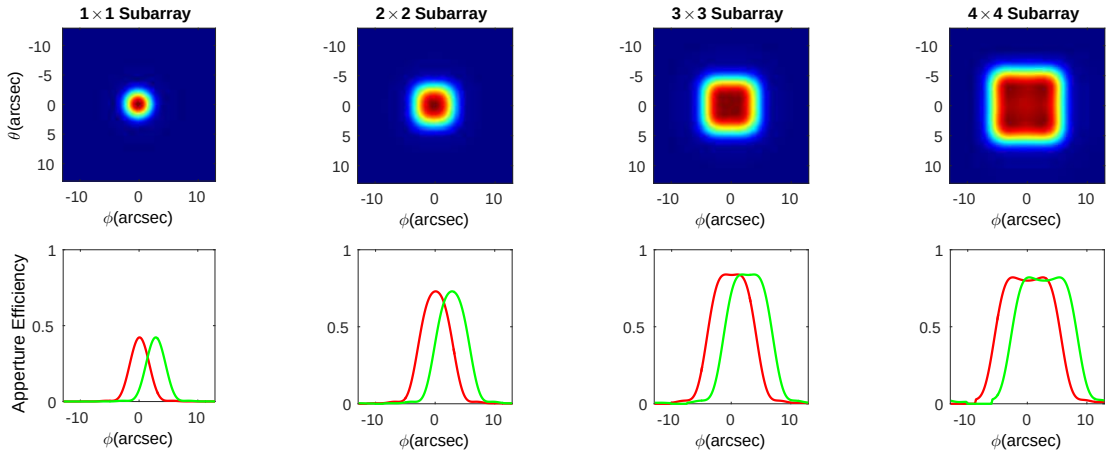

(a) 160 μm of L-Band

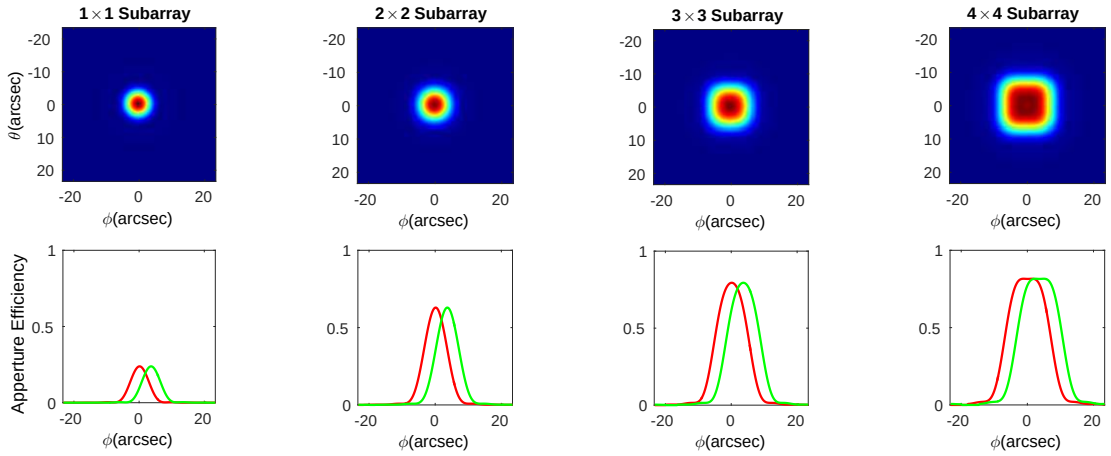

(b) 85 μm of M-Band

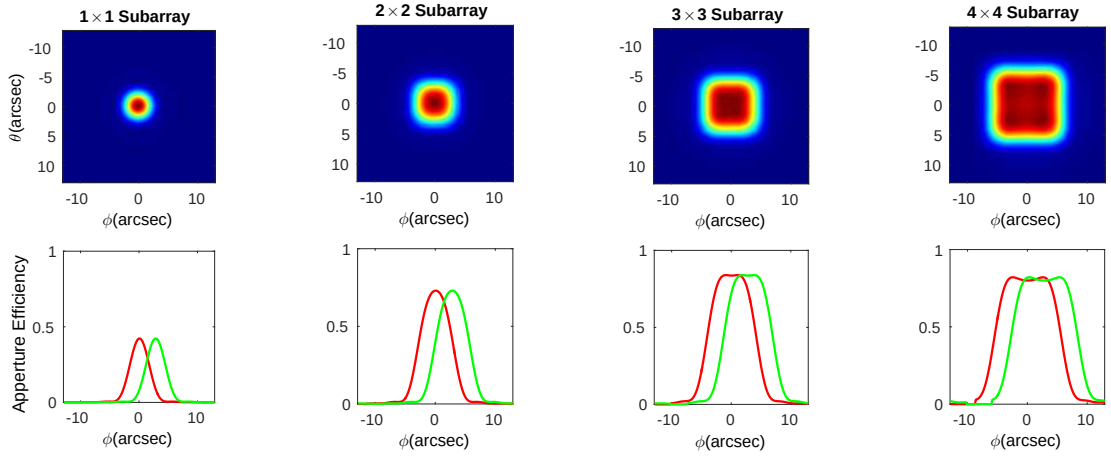

(c) 47 μm of S-Band

Fig. 2.29 Co-added beam patterns of (a) L-, (b) M- and (c) S-Band at the central wavelengths: top rows are the beam patterns of a co-added N×N subarray of the lightpipes; red plots in the bottom rows show the cuts in ϕ direction across the centre of subarrays of co-added pixels, and green plots show the output from a co-added subarray that are displaced by one pixel in ϕ direction. The individual plots shown from left to right corresponds to 1×1, 2×2, 3×3 ,and 4×4 element subarrays.

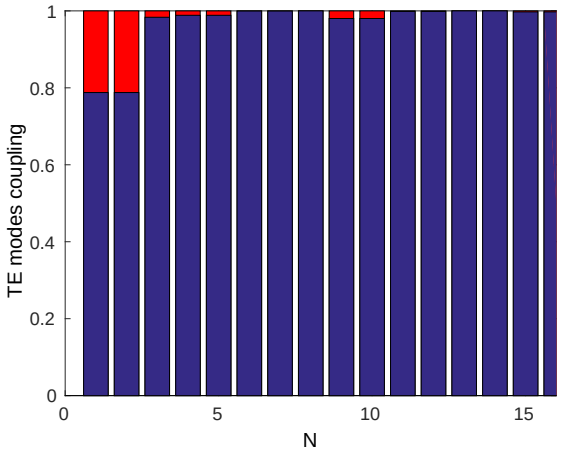

(a) TE mode coupling for L-Band at 160 μm.

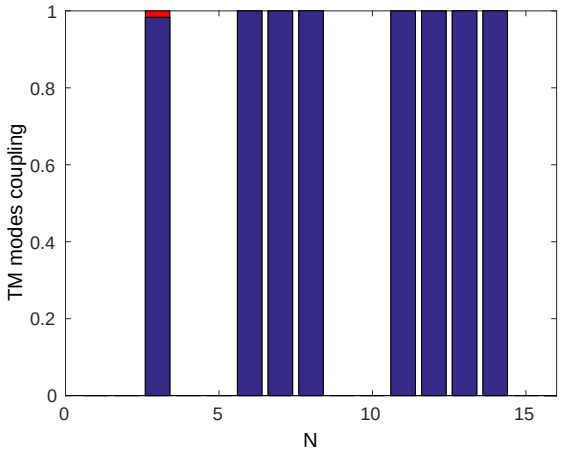

(b) TM mode coupling L-Band at 160 μm.

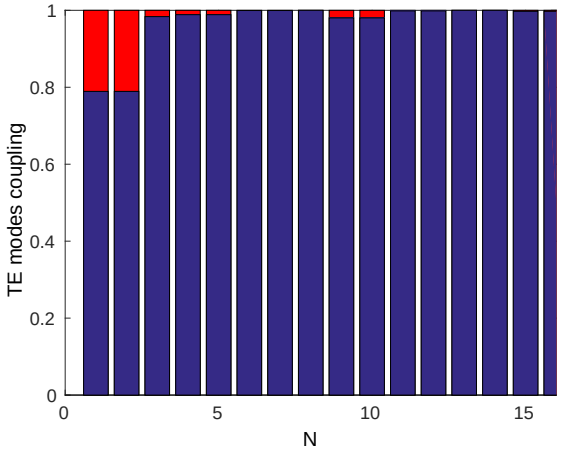

(c) TE mode coupling M-Band at 85 μm.

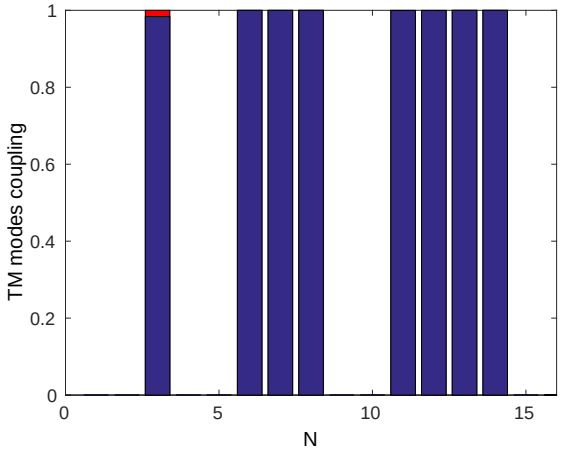

(d) TM mode coupling M-Band at 85 μm.

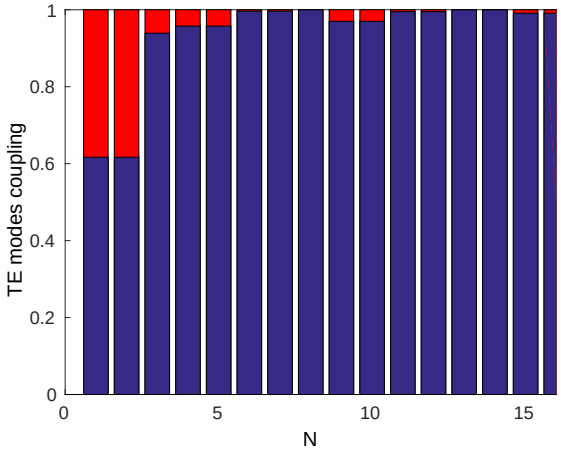

(e) TE mode coupling S-Band at 47 μm.

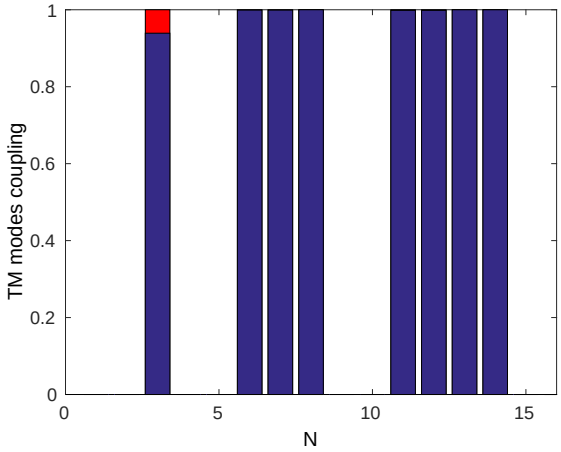

(f) TM mode coupling S-Band at 47 μm.

Fig. 2.30 Coupling of each of the TE (left column) and TM (right column) waveguide modes to the sky (red) and to the cold baffle (blue) as a function of waveguide mode number for the central wavelengths of L-, M- and S-Band.

The first row shows the results for L-Band at 160 μm, the second row is for M band at 85 μm, and the third row is for S-Band at 47 μm. It can be seen that as the number of waveguide modes increases, the signal increases, but meanwhile, more power couples to the cold baffle. The large throughput to the cold baffle is shown in all of these plots.

The cumulative throughput to the sky and to the cold baffle were also calculated. Figure 2.31 shows the cumulative throughput as a function of waveguide mode number for the central wavelengths of the 3 wavebands. The left column shows the cumulative throughput to the sky, and the right column shows the cumulative throughput to the cold baffle.

It can be seen that dramatic increases in optical efficiency occur when the number of waveguide modes are increased to 2. The optical efficiency almost reaches its maximum when 10 waveguide modes are included. Only very tiny increases can be obtained by including more waveguide modes than 10. However, the throughput to the cold baffle increases much more rapidly. It seems that limiting the number of detector modes to 18 would be sufficient. For the 24 waveguide mode set used here, almost all of the throughput of the detector is on to the cold baffle.

2.5 Conclusion

The optical performance of SAFARI system has been simulated using the optical modes of the telescope and the natural modes of the detector. In this Chapter, I have described a way of modelling the behaviour of far-infrared systems using optical modes; I then used this theory to produce a package of software, and I then illustrated the use of the software by simulating the behaviour of SAFARI. The throughput on distributed sources, the aperture efficiency as a function of source direction for point sources, and the power coupled to the cold baffle were calculated. It has been shown that the first 4 optical modes carry the majority of the power. The optical modes of different wavebands for different wavelengths have the same forms; but in each band, the optical throughput is largest at shorter wavelength. The modelling also shows that when the subreflector is included, the effective area of the telescope reduces evidently, and the optical throughput falls in accordance with the reduction in area. To answer the question that how well the focal plane fields of the optical modes are spanned by the waveguide modes of the input aperture of the lightpipe, the power coupling efficiencies between optical and waveguide modes were determined. About 80% of the power can be collected by the first 10 modes, about 89% of the power coupling to the first 18 modes, and then about 91% is gained by going to 24 modes. I have also determined the aperture efficiency, which varies significantly when different sets of waveguide modes are used, and it falls when the subreflector and support leg blockage are included. To improve the aperture

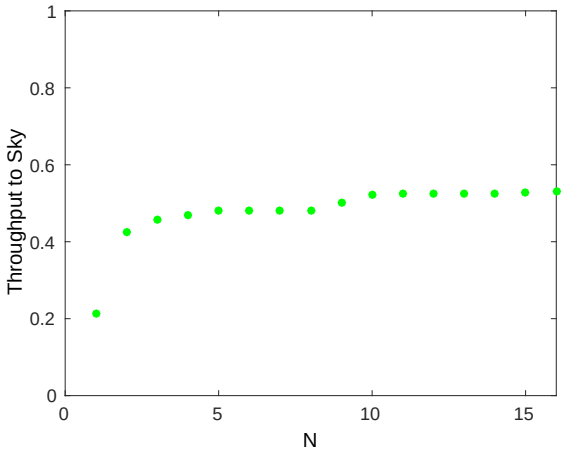

(a) L-Band at 160 μm.

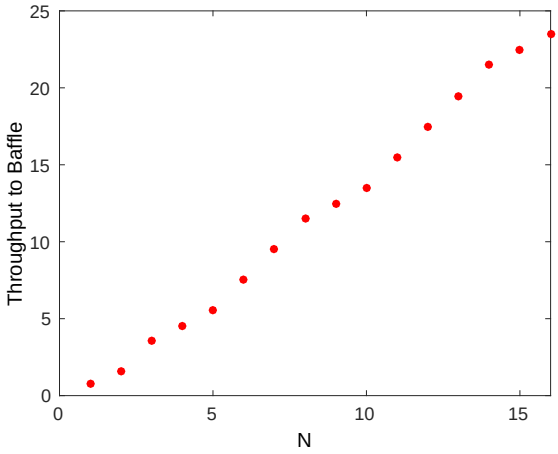

(b) L-Band at 160 μm.

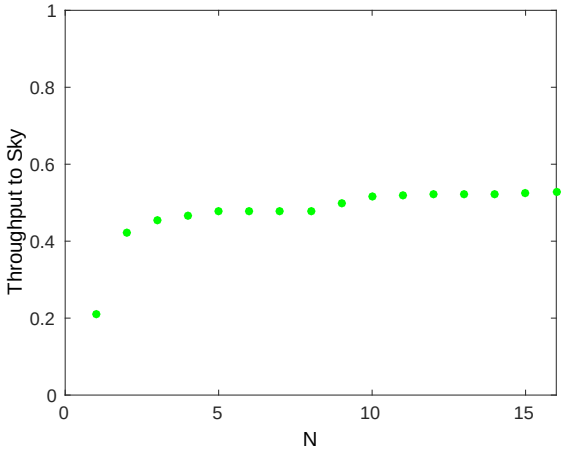

(c) M-Band at 85 μm.

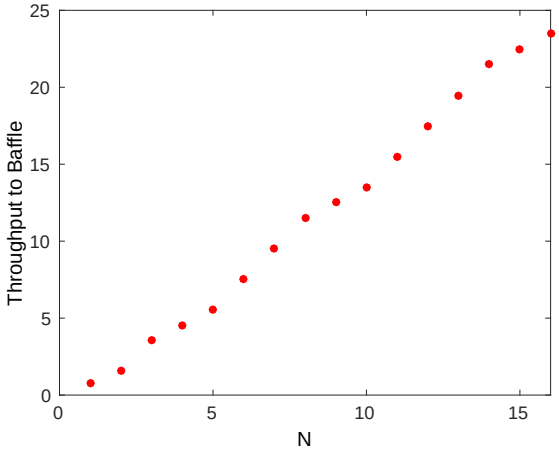

(d) M-Band at 85 μm.

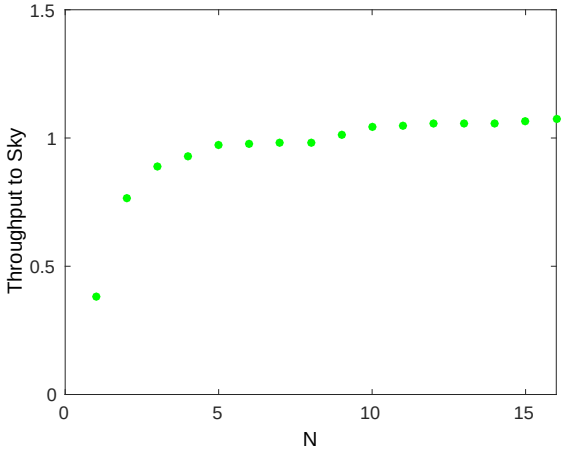

(e) S-Band at 47 μm.

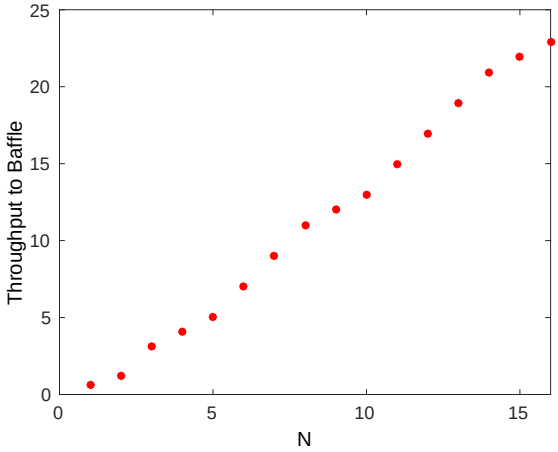

(f) S-Band at 47 μm.

Fig. 2.31 Cumulative throughput to the sky (left column) and cold baffle (right column) as a function of waveguide mode number for the central wavelengths of L-, M- and S-Band.

efficiency on point sources, a number of pixels were co-added to cover the area of the PSF. It has been shown that, when the 24 waveguide mode set is used, 3×3 and 4×4 co-added pixels would give aperture efficiencies of between 70 and 89%. However, if we consider the power coupled in from the cold baffle, then including more waveguide modes would increase the throughput to the cold baffle far more significant than the optical efficiency. The number of waveguide modes should be limited to 10, or at most 18 to optimise the optical performance of the whole system.

Chapter 3

Photon Noise and Correlations

3.1 Introduction

In this chapter I will discuss the statistical noise associated with the incident photons and the correlations between the outputs of different pixels of the imaging arrays. The main point is that the outputs of the detectors in an array will fluctuate, and it is important to know the RMS fluctuations on the values of recorded. Additionally, because in a few-moded system, the incoming radiation is partially spatially coherent, the fluctuations in the outputs of the detectors will be correlated. When using an instrument to observe an astronomical source, it is important to know the output noise, and it is also important to know the correlations between the fluctuations in the outputs in different detectors. When I was designing the test system, it was also important to calculate the fluctuations in the outputs due to the incoming thermal radiation field, because it indicates whether I would have sufficient signal-to-noise when carry out the experiment. Here I will model the effects of noise in the thermal radiation field over the SAFARI bands between 34 μm and 210 μm.

The coupled mode theory developed in [44] is powerful way of relating the variation of the output of the detectors to the partially coherent incident radiation. Using this few-mode method, we can not only calculate the noise associated with a single detector, but also determine the correlations between the fluctuations in the outputs of two different detectors. The main quantities required are the coherence tensor of the radiation and the coherence tensor of the detector.

3.2 Main Formalism for Modelling

The simulations for calculating the photon noise from the source, and the correlations between the outputs of pixels in the array are based on the following formalism. As discussed by Withington et al. in [59], the expectation value of a power related measurement, P, made on a partially coherent statistically stationary radiation field, for example a field emitted from a constant temperature blackbody, can be written as

$$\langle P \rangle = \int_B \mathrm{d}\nu \sum_{ij} \int_F \mathrm{d}^2\mathbf{r}_{t1} \int_F \mathrm{d}^2\mathbf{r}_{t2} D^{\dagger}_{ij}(\mathbf{r}_{t1}, \mathbf{r}_{t2}, \nu) E_{ij}(\mathbf{r}_{t1}, \mathbf{r}_{t2}, \nu), \tag{3.1}$$

where the spatial integrals extend over the entrance aperture of the lightpipe, which is denoted by F; B denotes the power is integrated over the frequency band; and the summations extend over any set of orthogonal polarisation vectors that are tangential to the surface of integration. $D_{ij}(\mathbf{r}_{t1}, \mathbf{r}_{t2}, \nu)$ is the detector coherence tensor, and $E_{ij}(\mathbf{r}_{t1}, \mathbf{r}_{t2}, \nu)$ is the cross spectral density of the radiation, as introduced in Chapter 2. $D_{ij}(\mathbf{r}_{t1}, \mathbf{r}_{t2}, \nu)$ and $E_{ij}(\mathbf{r}_{t1}, \mathbf{r}_{t2}, \nu)$ have the Hermiticity property [39] such that

$$D_{ij}(\mathbf{r}_{t1}, \mathbf{r}_{t2}, \nu) = D^{*}_{ji}(\mathbf{r}_{t2}, \mathbf{r}_{t1}, \nu), \tag{3.2}$$

and

$$E_{ij}(\mathbf{r}_{t1}, \mathbf{r}_{t2}, \nu) = E^{*}_{ji}(\mathbf{r}_{t2}, \mathbf{r}_{t1}, \nu). \tag{3.3}$$

Equation.(3.1) describes the way in which the optical modes of the radiation scatter power into the waveguide modes of the detector system. The spectral and detector coherence tensors can be expressed in dyadic notation as $\overline{\overline{\mathbf{E}}}(\mathbf{r}_{t1}, \mathbf{r}_{t2}, \nu)$ and $\overline{\overline{\mathbf{D}}}(\mathbf{r}_{t1}, \mathbf{r}_{t2}, \nu)$, then Eq.(3.1) becomes

$$\langle P \rangle = \int_B \mathrm{d}\nu \int_F \mathrm{d}^2\mathbf{r}_{t1} \int_F \mathrm{d}^2\mathbf{r}_{t2} \overline{\overline{\mathbf{D}}}^{\dagger}(\mathbf{r}_{t1}, \mathbf{r}_{t2}, \nu) \cdot\cdot\, \overline{\overline{\mathbf{E}}}(\mathbf{r}_{t1}, \mathbf{r}_{t2}, \nu). \tag{3.4}$$

It can be seen as the way in which the cross spectral density of the radiation projects onto the state of coherence to which the measurement system is sensitive.

It has been shown in [59] that if two power measurements P^a and P^b are recorded by pixels a and b, then the covariance between the fluctuations in the outputs, $\mathrm{C}[P^a, P^b] =$

$\langle (P^a - \langle P^a \rangle)(P^b - \langle P^b \rangle) \rangle$, is given by

$$\begin{aligned}
\mathrm{C}[P^a, P^b] = \frac{1}{\tau} \int_B \mathrm{d}\nu \int_{F_a} \mathrm{d}^2\mathbf{r}_{t1} \int_{F_a} \mathrm{d}^2\mathbf{r}_{t2} \int_{F_b} \mathrm{d}^2\mathbf{r}_{t3} \int_{F_b} \mathrm{d}^2\mathbf{r}_{t4} \\
\left[\overline{\overline{\mathbf{D}}}^{a\dagger}(\mathbf{r}_{t1}, \mathbf{r}_{t2}, \nu) \cdot \overline{\overline{\mathbf{E}}}(\mathbf{r}_{t2}, \mathbf{r}_{t3}, \nu) \right] \cdot\cdot \left[\overline{\overline{\mathbf{D}}}^{b}(\mathbf{r}_{t3}, \mathbf{r}_{t4}, \nu) \cdot \overline{\overline{\mathbf{E}}}^{\dagger}(\mathbf{r}_{t4}, \mathbf{r}_{t1}, \nu) \right] \\
+ \frac{\delta_{ab}}{\tau} \int_B h\nu \mathrm{d}\nu \int_{F_a} \mathrm{d}^2\mathbf{r}_{t1} \int_{F_a} \mathrm{d}^2\mathbf{r}_{t2} \left[\overline{\overline{\mathbf{D}}}^{a\dagger}(\mathbf{r}_{t2}, \mathbf{r}_{t1}, \nu) \cdot \overline{\overline{\mathbf{E}}}(\mathbf{r}_{t1}, \mathbf{r}_{t2}, \nu) \right] \\
= \mathrm{C}[P^a, P^b]_c + \mathrm{C}[P^a, P^b]_q, \qquad (3.5)
\end{aligned}$$

where τ is the time for which the output is integrated. The first term, $\mathrm{C}[P^a, P^b]_c$, in Eq.(3.5) can be identified with the noise associated with classical waves, and the second term, $\mathrm{C}[P^a, P^b]_q$ refers to quantum noise, which is with noise associated with photon counting [27].

From Eq.(2.60), the field coherence dyadic can be expressed in terms of the sky brightness dyadic as

$$\overline{\overline{\mathbf{E}}}(\mathbf{r}_{t1}, \mathbf{r}_{t2}) = 2Z_0 \int \mathrm{d}\boldsymbol{\Omega}_1 \int \mathrm{d}\boldsymbol{\Omega}_2 \overline{\overline{\mathbf{T}}}(\mathbf{r}_{t1}|\boldsymbol{\Omega}_1) \cdot \overline{\overline{\mathbf{B}}}(\boldsymbol{\Omega}_1, \boldsymbol{\Omega}_2) \cdot \overline{\overline{\mathbf{T}}}^{\dagger}(\boldsymbol{\Omega}_2|\mathbf{r}_{t2}), \qquad (3.6)$$

then Eq.(3.1) becomes

$$\begin{aligned}
\langle P \rangle &= 2Z_0 \int_B \mathrm{d}\nu \int_F \mathrm{d}^2\mathbf{r}_{t1} \int_F \mathrm{d}^2\mathbf{r}_{t2} \int \mathrm{d}\boldsymbol{\Omega}_1 \int \mathrm{d}\boldsymbol{\Omega}_2 \\
&\quad \overline{\overline{\mathbf{D}}}^{\dagger}(\mathbf{r}_{t1}, \mathbf{r}_{t2}, \nu) \cdot\cdot \overline{\overline{\mathbf{T}}}(\mathbf{r}_{t1}|\boldsymbol{\Omega}_1) \cdot \overline{\overline{\mathbf{B}}}(\boldsymbol{\Omega}_1, \boldsymbol{\Omega}_2) \cdot \overline{\overline{\mathbf{T}}}^{\dagger}(\boldsymbol{\Omega}_2|\mathbf{r}_{t2}) \\
&= 2Z_0 \int_B \mathrm{d}\nu \int_F \mathrm{d}^2\mathbf{r}_{t1} \int_F \mathrm{d}^2\mathbf{r}_{t2} \int \mathrm{d}\boldsymbol{\Omega}_1 \int \mathrm{d}\boldsymbol{\Omega}_2 \\
&\quad \overline{\overline{\mathbf{T}}}^{\dagger}(\boldsymbol{\Omega}_2|\mathbf{r}_{t2}) \cdot \overline{\overline{\mathbf{D}}}^{\dagger}(\mathbf{r}_{t1}, \mathbf{r}_{t2}, \nu) \cdot \overline{\overline{\mathbf{T}}}(\mathbf{r}_{t1}|\boldsymbol{\Omega}_1) \cdot\cdot \overline{\overline{\mathbf{B}}}(\boldsymbol{\Omega}_1, \boldsymbol{\Omega}_2) \\
&= \int_B \mathrm{d}\nu \int \mathrm{d}\boldsymbol{\Omega}_1 \int \mathrm{d}\boldsymbol{\Omega}_2 \overline{\overline{\mathbf{P}}}^{\dagger}(\boldsymbol{\Omega}_2|\boldsymbol{\Omega}_1) \cdot\cdot \overline{\overline{\mathbf{B}}}(\boldsymbol{\Omega}_1, \boldsymbol{\Omega}_2), \qquad (3.7)
\end{aligned}$$

where $\overline{\overline{\mathbf{P}}}^{\dagger}(\boldsymbol{\Omega}_2|\boldsymbol{\Omega}_1)$ is the power reception dyadic, which was described earlier in Eq.(2.65). For an incoherent sky, $\overline{\overline{\mathbf{B}}}(\boldsymbol{\Omega}_1, \boldsymbol{\Omega}_2) = \overline{\overline{\mathbf{B}}}_0(\boldsymbol{\Omega}_1)\delta(\boldsymbol{\Omega}_1 - \boldsymbol{\Omega}_2)$ gives

$$\langle P \rangle = \int_B \mathrm{d}\nu \int \mathrm{d}\boldsymbol{\Omega} \overline{\overline{\mathbf{P}}}^{\dagger}(\boldsymbol{\Omega}) \cdot\cdot \overline{\overline{\mathbf{B}}}_0(\boldsymbol{\Omega}). \qquad (3.8)$$

For a uniform unpolarised source, $\overline{\overline{\mathbf{B}}}_0(\boldsymbol{\Omega}) = B_0 \bar{\bar{\mathbf{I}}}$, then Eq.(3.8) becomes

$$\langle P \rangle = \int_B \mathrm{d}\nu B_0 \int \mathrm{d}\boldsymbol{\Omega} \overline{\overline{\mathbf{P}}}(\boldsymbol{\Omega}) \cdot\cdot \bar{\bar{\mathbf{I}}}, \qquad (3.9)$$

which is Eq.(2.68). Apply the same reasoning to calculate the covariance between the outputs of two pixels through Eq.(3.5). The first term, the classical noise, becomes

$$\mathrm{C}[P^a,P^b]_c = \frac{1}{\tau}\int_B \mathrm{d}\nu \int \mathrm{d}\boldsymbol{\Omega}_1 \int \mathrm{d}\boldsymbol{\Omega}_2 \int \mathrm{d}\boldsymbol{\Omega}_3 \int \mathrm{d}\boldsymbol{\Omega}_4 \\ \overline{\overline{\mathbf{P}}}^{a\dagger}(\boldsymbol{\Omega}_1|\boldsymbol{\Omega}_2)\cdot \overline{\overline{\mathbf{B}}}(\boldsymbol{\Omega}_2,\boldsymbol{\Omega}_3)\cdot\cdot \overline{\overline{\mathbf{P}}}^{b}(\boldsymbol{\Omega}_3|\boldsymbol{\Omega}_4)\cdot \overline{\overline{\mathbf{B}}}^{\dagger}(\boldsymbol{\Omega}_4,\boldsymbol{\Omega}_1). \tag{3.10}$$

Consider that the sky is fully incoherent, so that $\overline{\overline{\mathbf{B}}}(\boldsymbol{\Omega}_2,\boldsymbol{\Omega}_3) = \overline{\overline{\mathbf{B}}}_0\delta(\boldsymbol{\Omega}_2-\boldsymbol{\Omega}_3)$ and $\overline{\overline{\mathbf{B}}}(\boldsymbol{\Omega}_1,\boldsymbol{\Omega}_4) = \overline{\overline{\mathbf{B}}}_0\delta(\boldsymbol{\Omega}_1-\boldsymbol{\Omega}_4)$, then

$$\mathrm{C}[P^a,P^b]_c = \frac{1}{\tau}\int_B \mathrm{d}\nu \int \mathrm{d}\boldsymbol{\Omega}_1 \int \mathrm{d}\boldsymbol{\Omega}_2\, \overline{\overline{\mathbf{P}}}^{a\dagger}(\boldsymbol{\Omega}_1|\boldsymbol{\Omega}_2)\cdot \overline{\overline{\mathbf{B}}}_0\cdot\cdot \overline{\overline{\mathbf{P}}}^{b}(\boldsymbol{\Omega}_2|\boldsymbol{\Omega}_1)\cdot \overline{\overline{\mathbf{B}}}_0^{\dagger}. \tag{3.11}$$

If the sky is unpolarised, $\overline{\overline{\mathbf{B}}}_0 = B_0\overline{\overline{\mathbf{I}}}$, then

$$\mathrm{C}[P^a,P^b]_c = \frac{1}{\tau}\int_B \mathrm{d}\nu\, B_0^2 \int \mathrm{d}\boldsymbol{\Omega}_1 \int \mathrm{d}\boldsymbol{\Omega}_2\, \overline{\overline{\mathbf{P}}}^{a\dagger}(\boldsymbol{\Omega}_1|\boldsymbol{\Omega}_2)\cdot\cdot \overline{\overline{\mathbf{P}}}^{b}(\boldsymbol{\Omega}_2|\boldsymbol{\Omega}_1). \tag{3.12}$$

Using Eq.(2.65), Eq.(3.12) becomes

$$\begin{aligned}\mathrm{C}[P^a,P^b]_c &= \frac{1}{\tau}\int_B \mathrm{d}\nu\, B_0^2 \sum_i (1-|\Gamma_i^a|^2)\sum_{i'}(1-|\Gamma_{i'}^b|^2)\sum_{nm}\sum_{n'm'}\sigma_m\sigma_n\sigma_{m'}\sigma_{n'}S_{in}^{a*}S_{im}^{a}S_{i'n'}^{b*}S_{i'm'}^{b} \\ &\quad \int \mathrm{d}\boldsymbol{\Omega}_1 \int \mathrm{d}\boldsymbol{\Omega}_2\, \mathbf{v}_n(\boldsymbol{\Omega}_1)\mathbf{v}_m^*(\boldsymbol{\Omega}_2)\cdot\cdot\,\mathbf{v}_{n'}(\boldsymbol{\Omega}_2)\mathbf{v}_{m'}^*(\boldsymbol{\Omega}_1) \\ &= \frac{1}{\tau}\int_B \mathrm{d}\nu\, B_0^2 \sum_i (1-|\Gamma_i^a|^2)\sum_{i'}(1-|\Gamma_{i'}^b|^2)\sum_{nm}\sum_{n'm'}\sigma_m\sigma_n\sigma_{m'}\sigma_{n'}S_{in}^{a*}\sigma_{n'}S_{im}^{a}S_{i'n'}^{b*}S_{i'm'}^{b}\delta_{mn'}\delta_{nm'} \\ &= \frac{1}{\tau}\int_B \mathrm{d}\nu\, B_0^2 \sum_i (1-|\Gamma_i^a|^2)\sum_{i'}(1-|\Gamma_{i'}^b|^2)\sum_{nm}\sigma_m^2\sigma_n^2 S_{in}^{a*}S_{im}^{a}S_{i'n}^{b*}S_{i'm}^{b}. \end{aligned} \tag{3.13}$$

Considering the noise in a single detector, $a=b$, and using Eq.(2.42) to express B_0, Eq.(3.13) can be written as

$$\begin{aligned}\mathrm{C}[P^a,P^a]_c &= \frac{1}{\tau}\int_B \mathrm{d}\nu\, B_0^2 \sum_i (1-|\Gamma_i^a|^2)\sum_{i'}(1-|\Gamma_{i'}^a|^2)\sum_{nm}\sigma_m^2\sigma_n^2 S_{in}^{a*}S_{im}^{a}S_{i'm}^{a*}S_{i'n}^{a} \\ &= \frac{1}{\tau}\int_B \mathrm{d}\nu \sum_{ii'nm} S_{ni}^{a\dagger}(1-|\Gamma_i^a|^2)S_{im}^{a}\eta_m S_{mi'}^{a\dagger}\sum_{i'}(1-|\Gamma_{i'}^a|^2)S_{i'n}^{a}\eta_n \left[\frac{h\nu}{\exp\left(\frac{h\nu}{k_bT_s}\right)-1}\right]^2. \end{aligned} \tag{3.14}$$

Express Eq.(3.14) using matrix notation, then

$$\begin{aligned}\mathrm{C}[P^a,P^a]_c &= \frac{1}{\tau}\int_B \mathrm{d}\nu\,\mathrm{Tr}\left[\mathbf{S}^{a\dagger}\mathbf{R}^a\mathbf{S}^a\boldsymbol{\eta}\mathbf{S}^{a\dagger}\mathbf{R}^a\mathbf{S}^a\boldsymbol{\eta}\right]\left[\frac{h\nu}{\exp\left(\frac{h\nu}{k_bT_s}\right)-1}\right]^2 \\ &= \frac{1}{\tau}\int_B \mathrm{d}\nu\,\mathrm{Tr}\left[(\mathbf{S}^{a\dagger}\mathbf{R}^a\mathbf{S}^a\boldsymbol{\eta})^2\right]\left[\frac{h\nu}{\exp\left(\frac{h\nu}{k_bT_s}\right)-1}\right]^2. \end{aligned} \tag{3.15}$$

For a perfectly matched absorber, $\mathbf{R}=\mathbf{I}$. $\boldsymbol{\eta}$ represents the optical efficiency of the optical system, and $\mathbf{S}$ represents the coupling efficiencies between the optical modes to waveguide modes. Similarly, for $a\neq b$, Eq.(3.13) can be written as

$$\mathrm{C}[P^a,P^a]_c = \frac{1}{\tau}\int_B \mathrm{d}\nu\,\mathrm{Tr}\left[\mathbf{S}^{a\dagger}\mathbf{R}^a\mathbf{S}^a\boldsymbol{\eta}\mathbf{S}^{b\dagger}\mathbf{R}^b\mathbf{S}^b\boldsymbol{\eta}\right]\left[\frac{h\nu}{\exp\left(\frac{h\nu}{k_bT_s}\right)-1}\right]^2. \tag{3.16}$$

Likewise, the second term in Eq.(3.5), the photon counting noise, can be expressed in terms of sky brightness dyadic as

$$\begin{aligned}\mathrm{C}[P^a,P^b]_q &= \frac{\delta_{ab}}{\tau}\int_B h\nu\,\mathrm{d}\nu\int \mathrm{d}\boldsymbol{\Omega}_1\int \mathrm{d}\boldsymbol{\Omega}_2\,\overline{\overline{\mathbf{P}}}^{\dagger}(\boldsymbol{\Omega}_2|\boldsymbol{\Omega}_1)\cdot\cdot\,\overline{\overline{\mathbf{B}}}(\boldsymbol{\Omega}_1,\boldsymbol{\Omega}_2) \\ &= \frac{\delta_{ab}}{\tau}\int_B h\nu\,\mathrm{d}\nu\,B_0\int \mathrm{d}\boldsymbol{\Omega}\,\overline{\overline{\mathbf{P}}}(\boldsymbol{\Omega})\cdot\cdot\,\overline{\overline{\mathbf{I}}}, \end{aligned} \tag{3.17}$$

where a uniform unpolarised source is assumed. Using Eq.(2.65), the above equation can be written as

$$\mathrm{C}[P^a,P^b]_q = \frac{\delta_{ab}}{\tau}\int_B \mathrm{d}\nu\sum_i(1-|\Gamma_i|^2)\sum_m|S_{im}|^2\eta_m\frac{(h\nu)^2}{\exp\left(\frac{h\nu}{k_bT_s}\right)-1}. \tag{3.18}$$

Note that $\mathrm{C}[P^a,P^b]_q$ is only non-zero when $a=b$, in this case, it corresponds to the mean-square fluctuation in the output of the corresponding detector. $\mathrm{C}[P^a,P^b]_q$ is zero when $a\neq b$, because photon absorption events in different detectors are un-correlated. In the case where $a=b$,

$$\mathrm{C}[P^a,P^a]_q = \frac{1}{\tau}\int_B \mathrm{d}\nu\sum_i(1-|\Gamma_i|^2)\sum_m|S_{im}|^2\eta_m\frac{(h\nu)^2}{\exp\left(\frac{h\nu}{k_bT_s}\right)-1}. \tag{3.19}$$

Express it in matrix notation, such that Eq.(3.19) becomes

$$\mathrm{C}[P^a, P^a]_q = \frac{1}{\tau}\int_B \mathrm{d}\nu\,\mathrm{Tr}\left[\mathbf{S}^{a\dagger}\mathbf{R}^a\mathbf{S}^a\boldsymbol{\eta}\right]\frac{(h\nu)^2}{\exp\left(\frac{h\nu}{k_bT_s}\right)-1}. \tag{3.20}$$

The correlation coefficient between the fluctuations in the outputs of two detectors is then given by

$$|\gamma| = \frac{\mathrm{C}[P^a, P^b]}{\sqrt{\mathrm{C}[P^a, P^a]\mathrm{C}[P^b, P^b]}}. \tag{3.21}$$

Defining the matrix

$$\mathbf{K} = \mathbf{S}^{\dagger}\mathbf{R}\mathbf{S}\boldsymbol{\eta}, \tag{3.22}$$

gives

$$\mathrm{C}[P^a, P^b] = \frac{1}{\tau}\int_B \mathrm{d}\nu\,\mathrm{Tr}\left[\mathbf{K}^a\mathbf{K}^b\right]\left[\frac{h\nu}{\exp\left(\frac{h\nu}{k_bT_s}\right)-1}\right]^2 + \frac{\delta_{ab}}{\tau}\int_B \mathrm{d}\nu\,\mathrm{Tr}\left[\mathbf{K}^a\right]\frac{(h\nu)^2}{\exp\left(\frac{h\nu}{k_bT_s}\right)-1}. \tag{3.23}$$

The integrated total noise power for each of the SAFARI bands can be determined by taking the square-root of Eq.(3.23), in the case where $a = b$.

3.3 Simulations

As the optical throughputs of the optical modes, and the coupling between the optical modes and the detector modes have been determined, the classical and quantum noise power density across the SAFARI bands at given temperatures can be calculated from Eq.(3.16) and (3.20). Assuming an integration time of $\tau = 1$ s, and that the absorber is perfect, such that $\mathbf{R} = \mathbf{I}$. I plotted the classical and quantum noise power as a function of temperature and operating frequency, as shown in Figure 3.1. From top to bottom, the x-axes correspond to the frequency of the L-, M- and S-Band; and y-axes show the temperature the source ranging from 4 to 25 K. It can be seen that noise power increases as the source temperature increases, as would be expected. It is notable that the classical noise (left) is much smaller than quantum noise (right), particularly at S-Band.

To allow for easy comparison , I have plotted magnitude of the classical and quantum noise on the same diagrams in the left column of Figure 3.2. We can see that the quantum noise is significantly larger than classical noise. Particularly at lower temperatures, the classical noise is nearly zero over the whole waveband. The plots on the right show the sum of the classical and quantum noise contributions. We may conclude that the performance

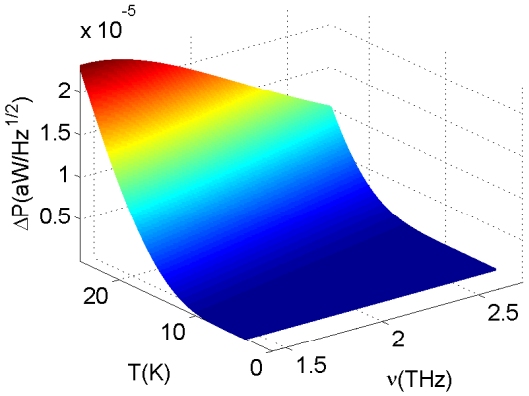

(a) L-Band classical noise spectral density

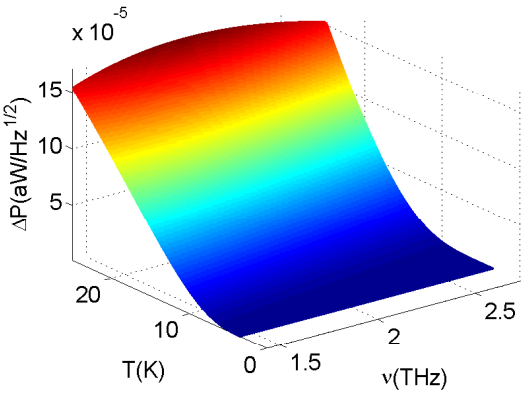

(b) L-Band quantum noise spectral density

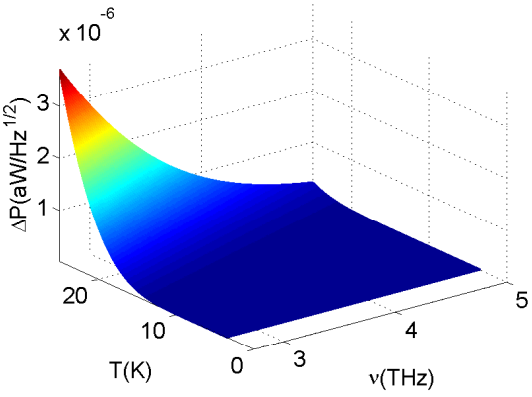

(c) M-Band classical noise spectral density

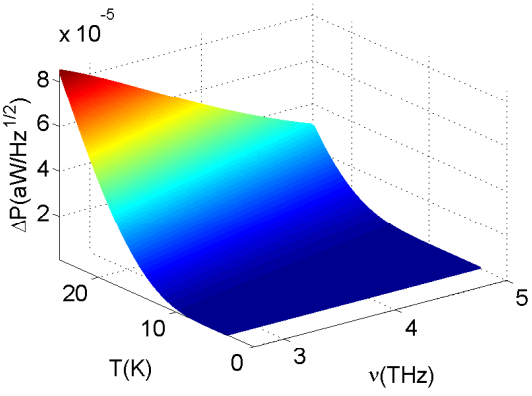

(d) M-Band quantum noise spectral density

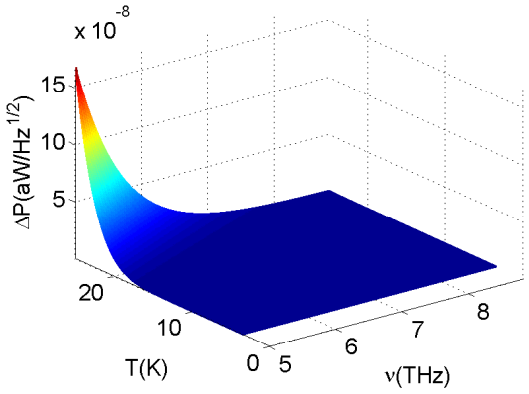

(e) S-Band classical noise spectral density

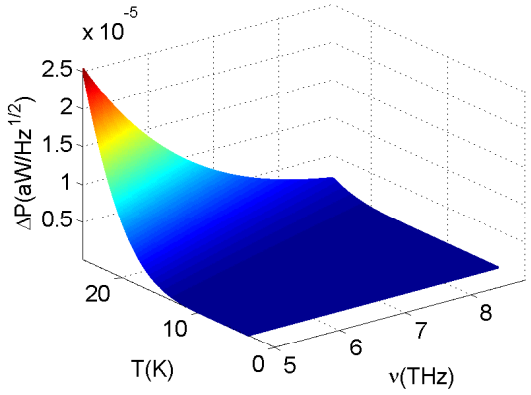

(f) S-Band quantum noise spectral density

Fig. 3.1 Classical (left column) and quantum (right column) noise of the source across L-, M-, and S-Band at temperature ranging from 4 K and 25 K.

of the system is dominated by quantum noise. The insignificance of the classical noise also indicates that the correlations between the outputs of any two pixels in the array are negligible in this case.

As we know that the SAFARI bands all fall on the tail of the blackbody spectrum at these temperatures, it would be expected that the noise power falls as a function of increasing frequency. It is notable that at the higher temperature end, the noise power for L-Band shows an increase at the low frequency end. This is because that the optical throughput of the system increases more rapidly with frequency in L-Band.

Figure 3.3 shows how the optical throughputs influence the noise power as a function of frequency. The blue dashed lines shown in Figure 3.3 show the blackbody radiation as a function of frequency in the SAFARI bands; the green dotted lines represent the optical throughputs of the optical modes of these three wavebands; and the red solid lines are the total noise power which can be seen by a perfect absorber. It can be seen that at 25 K, the optical throughputs in L-Band increase more rapidly than the blackbody noise falls, thus more noise power is cut off at the low frequency end. As going to M- and S-Band, the blackbody power drops more significantly compared with the increase in the optical throughputs, then the functional form of the noise are not altered by the increasing optical throughput. At lower temperatures, for example 4 K, the fall in blackbody noise is so dramatic that the effect on the functional forms due to the increasing optical throughputs are fairly insignificant.

The total noise power seen by a detector for each band can be calculated as a function of temperature by integrating the noise power density over the bands. The results are shown in Figure 3.4. As expected, the noise increases with temperature. Noise power for L-Band is the highest, and S-Band is the lowest.

Given that the power loading from the source and the noise are known, the signal-to-noise ratio can be estimated. Using the results shown in Figure 2.25 and 3.4, can be used to calculate the signal-to-noise ratio for each band.

Figure 3.5 shows the estimated signal-to-noise ratio for the L-, M- and S-Bands. The signal-to-noise ratios increase as increasing temperature. If the minimal signal-to-noise ratio is unity, it can be seen from Figure 3.5 that good signal-to-noise ratio can be achieved at all feasible temperatures for L-Band. Whereas for S-Band, the temperature of the source should be higher than 10 K to have a signal-to-noise ratio of unity in 1 s. Alternatively, the signal-to-noise ratio can be improved by increasing the integration time τ, according to Eq.(3.23) we can see that the covariance is inversely proportional to τ, which means the noise power decreases as integration time increases. Thus good measurements can be also achieved at lower temperatures for S-Band. Overall, the calculations suggest that we should be able to achieve high signal-to-noise ratios in each of the SAFARI bands. Noise due to

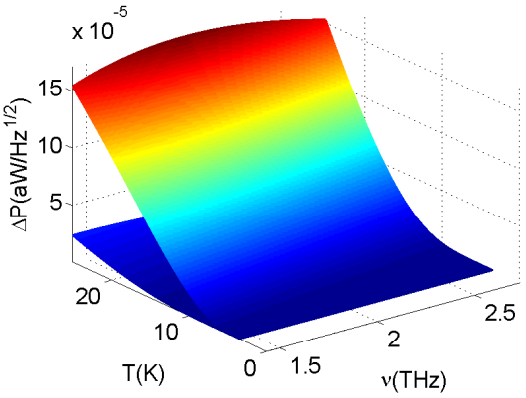

(a) L-Band noise spectral density

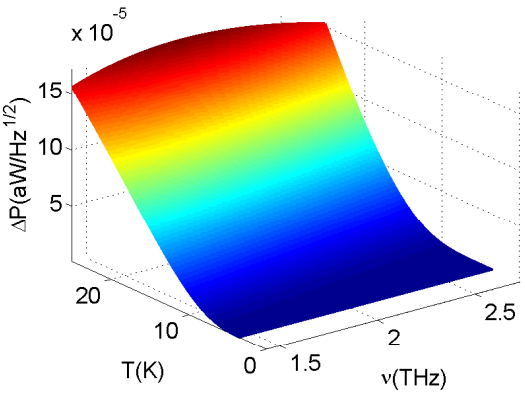

(b) L-Band summed noise spectral density

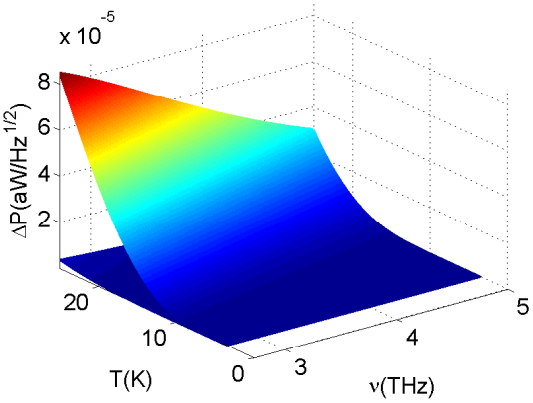

(c) M-Band noise spectral density

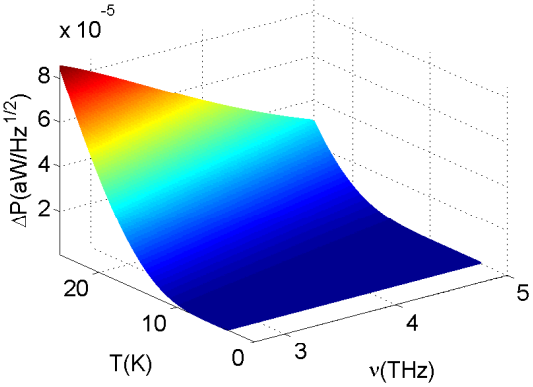

(d) M-Band summed noise spectral density

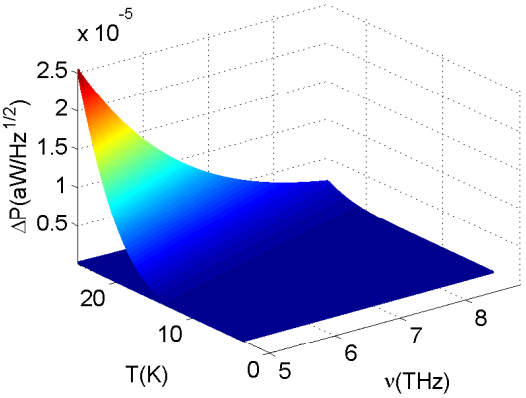

(e) S-Band noise spectral density

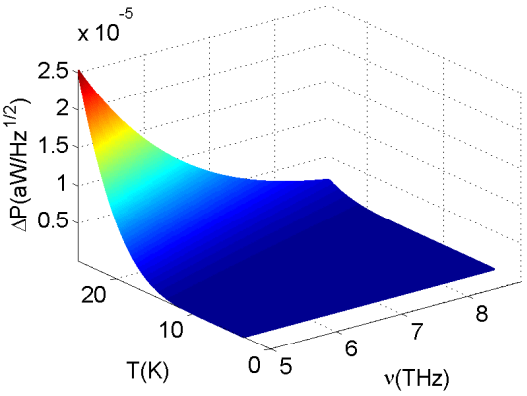

(f) S-Band summed noise spectral density

Fig. 3.2 Left: comparisons of classical and quantum noise contributions; right: the sum of the classical and quantum noise across L-, M-, and S-Band at temperature ranging from 4 K and 25 K.

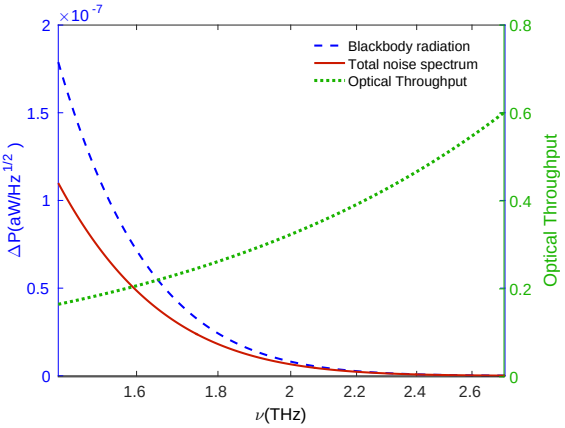

(a) L-Band at 4 K

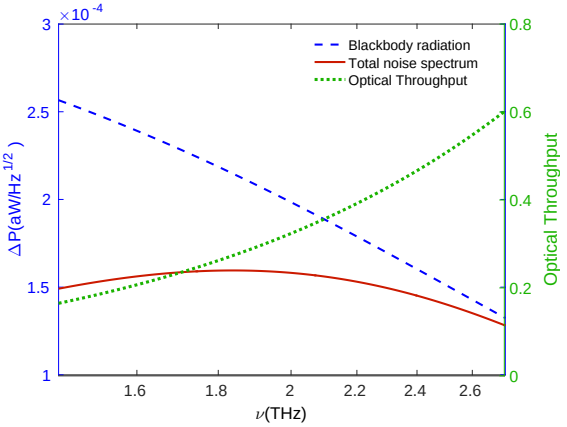

(b) L-Band at 25 K

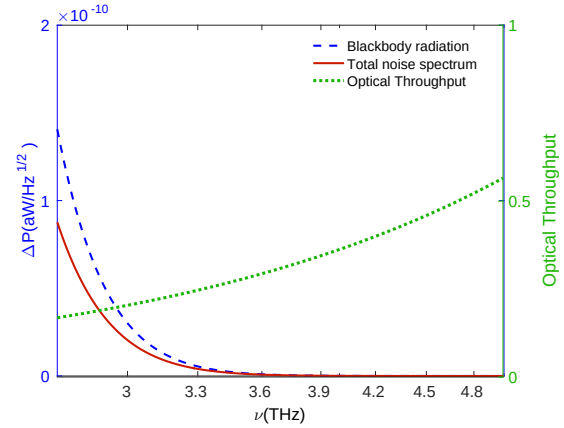

(c) M-Band at 4 K

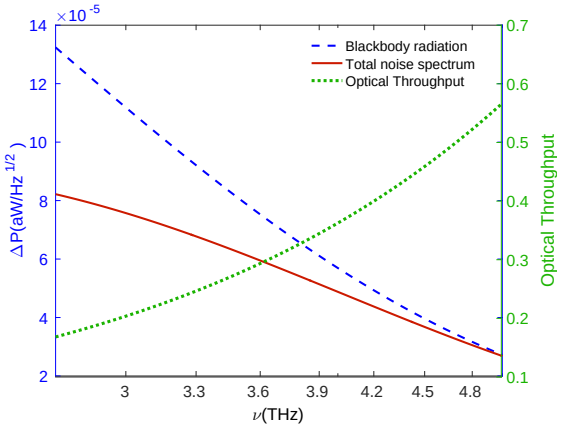

(d) M-Band at 25 K

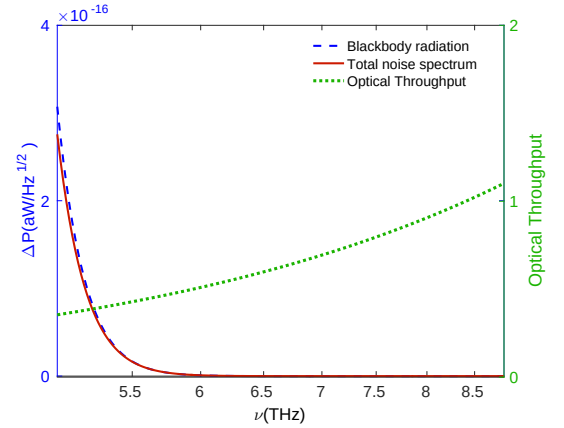

(e) S-Band at 4 K

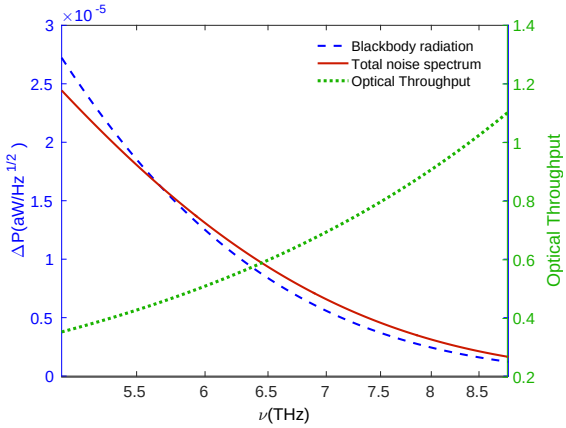

(f) S-Band at 25 K

Fig. 3.3 The total noise power spectrum, the blackbody radiation spectrum, and the optical throughputs within the L-, M-, and S-Band at 4 K and 25 K.

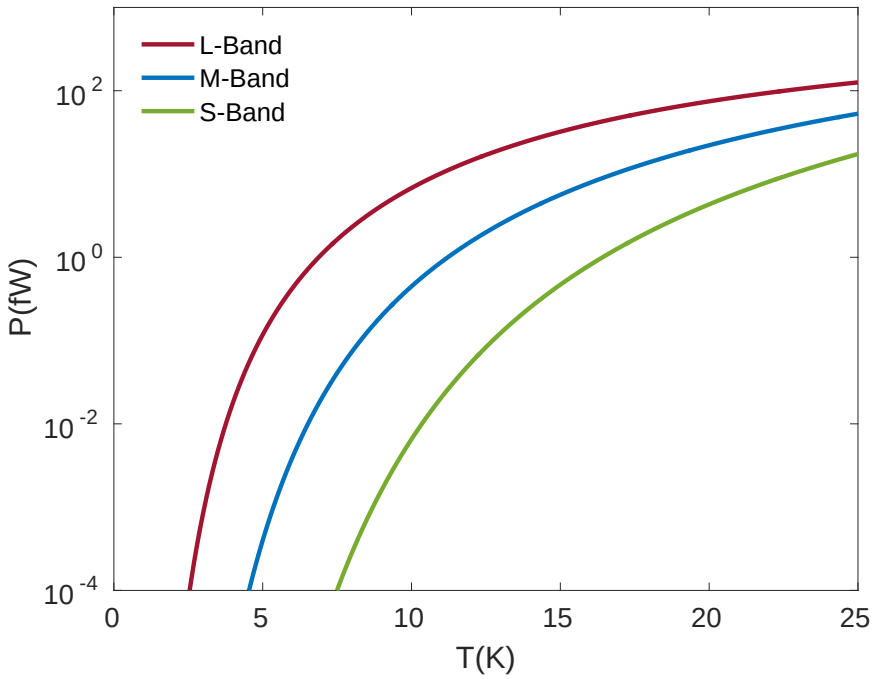

Fig. 3.4 Noise from the radiation source as a function of temperature for the L-, M-, and S-Band.

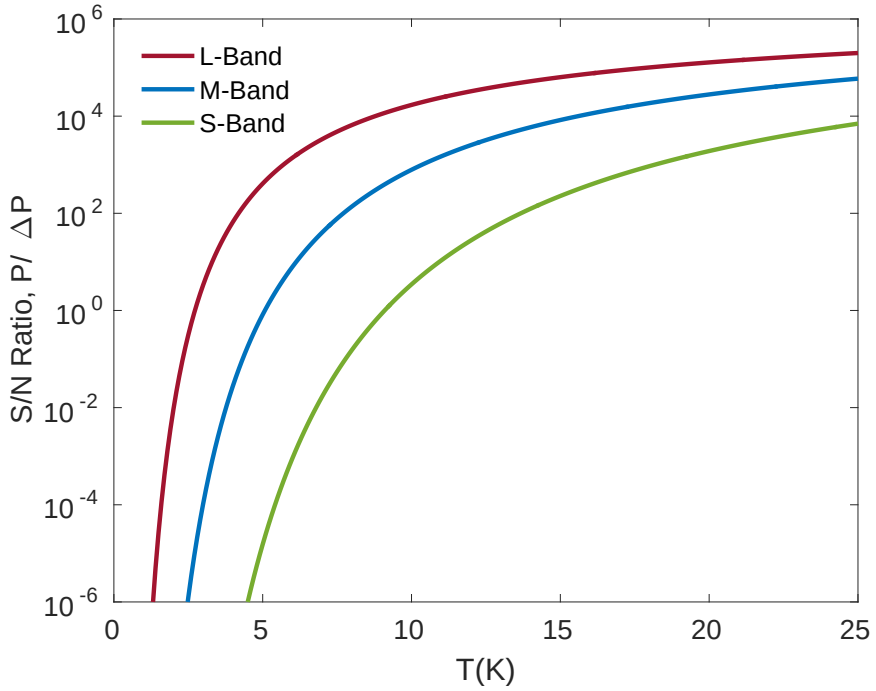

Fig. 3.5 Signal-to-noise ratio as a function of the source temperature for the L-, M-, and S-Band.

the transition edge sensors themselves have not been taken into account, because I was most interested in the intrinsic behaviour of the test system.

3.4 Conclusion

In this Chapter, I have shown how to use the few-mode model to calculate the fluctuation in the outputs of the SAFARI detectors. The formalisms are rather generic, and can be applied to other optical systems. It is found that for the SAFARI system, the classical noise is insignificant compared with the quantum noise, which means that the correlations between the outputs of pixels would be zero. For L-Band, good signal-to-noise ratio can be achieved using a hot-load operating over a temperature range 4 K to 25 K. For S-Band, higher source temperatures are needed.

Chapter 4

Optical Test System for Transition Edge Sensors

4.1 Introduction

The numerical method for modelling few-moded optical systems introduced earlier has been applied to simulate the optical behaviour of a test system for ultra-low-noise Transition Edge Sensors (TESs). More specifically, a cryogenic optical system has been designed and engineered to measure the optical efficiencies of TESs.

It was shown, in Chapter 2, that the modes of an optical system comprising an aperture, a thin lens and an entrance aperture corresponding to the footprint of the detector, are precisely the same as those of an optical system comprising two apertures of the same size that maintain the same physical opening angle, but without the thin lens. The absence of the thin lens does not alter the transformation of blackbody sources. This is because a lens can be seen as a transformation of phase, while the phases of blackbody field are essentially, at least over distances of greater than a wavelength, random. By avoiding the use of lenses, a very clean partially coherent optical beam can be established, there are no artefacts arising in the optical components between the aperture and the detector, thus the spatial form of the illuminating field is very well defined. For the optical modelling of our test system, we adopted the effective focal ratio of the original concept of the SPICA/SAFARI telescope: 16.5 for L-Band, and 20 for M-Band and S-Band. Thus the test system presents precisely the same partially coherent illumination conditions as the telescope itself. The system is operated over three different frequency ranges, each of which has its own band-defining filters: 210-110 μm for L-Band, 110-60 μm for M-Band and 60-34 μm for S-Band.

Calculations of optical throughput, total power loading of the detectors by the source, and photon noise from the source and baffle have been carried out for all wavebands in Chapter 2 and 3. It was shown that the modes and modal throughputs of the test system are almost identical with those of the telescope optics.

4.2 The Design of the Test System

In this section, I will briefly describe the design of the test system, more details will be will be discussed in Chapter 5.

Figure 4.1 shows an engineering drawing of the test assembly, and a simplified representation of the test system is shown below. The parts of the test system that relate to the following numerical simulations are highlighted in the simplified drawing. The test system was engineered to measure precisely the optical efficiencies of the detectors by illuminating the lightpipes with a blackbody source behind an aperture. By making the geometrical focal ratio of the aperture the same as the geometrical focal ratio of the telescope, it can be shown that the test system produces the same optical modes with the same efficiencies as when the telescope itself observes a uniform sky. In other words, the optical modes do not depend on whether there is a lens present in the aperture or not. Crucially, the metal mesh filters that define the spectral band are on the far side of the aperture when view from the horns. This keeps the optics in front of the lightpipes very clean.

As can be seen in Figure 4.1, a variable-temperature load, shown in purple, was used as blackbody source. It is thermally connected to a 3.3 K cold stage through a copper wire. The dimensions of the copper wire were chosen to provide optimised thermal loading and response time. The thermal load generated by the hot load is potentially high and can influence the behaviour of the cryostat, especially at elevated temperatures. Therefore the load cannot be connected to the same stage as the detectors and optics (65 mK stage). The load was suspended from the outer case by 6 Kevlar strings, and then the outer case is in turn connected to the cryostat. The low thermal conductance of the Kevlar guarantees thermal decoupling of the blackbody source from the cryostat. The outer support structure of the hot load was connected directly to a magnetic shield; a cylinder that surrounds the entire assembly, which was thermally anchored to the 3.3 K stage. In this way, the load was thermally isolated from the cold stage. A blackened labyrinth was presented to minimise stray light. The details of the hot-load will be discussed later.

The blackbody radiation generated by the hot load illuminates the detector through a cascade of filters: a thermal-blocking filter was introduced at the 4 K stage to reduce the heat load on the detectors; a series of band pass filters, one set for each band, were placed

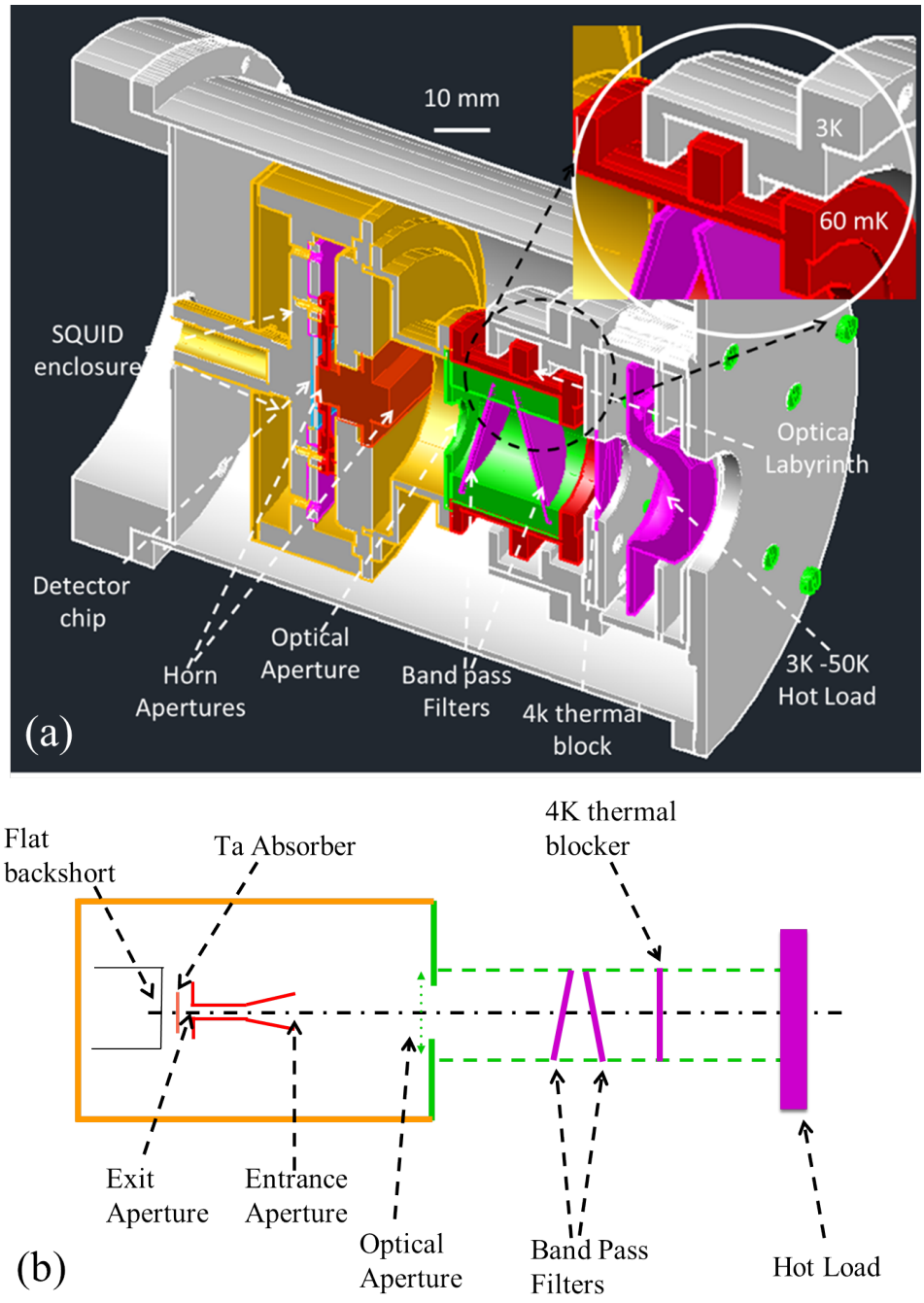

Fig. 4.1 Optical test system: (a) Mechanical drawing of the test system. The band pass filters, circular aperture, waveguides detectors are all in the 90 mK cold stage; the variable temperature load is thermally isolated by a 3 K shield. (b) Simplified illustration of the test system summarising the essential elements which are related to the optical modelling.

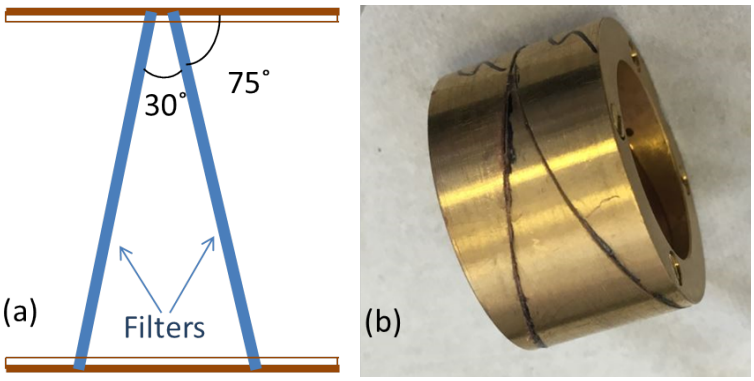

Fig. 4.2 (a)The basic layout and (b) a picture of the actual band pass filter assembly.

behind the thermal-blocking filter; and the band pass filters were angled 30° to eliminate reflections, as shown in Figure 4.2. The L- and S-Band filters and the thermal blocking filter were fabricated and optically calibrated by Professor Ade and his team in the Astronomy Instrumentation Group at Cardiff University. These filters were used for all of the optical measurements. Figure 4.2 (a) shows the layout of the band pass filters, and (b) shows the image of one of the filters assembly.

After passing through the filters, the throughput of the load is then limited by a circular aperture. The distance between the aperture plane and the detector plane, L, is 10.75 mm. Thus, having aperture sizes of 651.5 μm for L-Band, and 537.5 μm for M-Band and S-Band achieves the same focal ratios as for the 3 wavebands of the original requirements of SPICA/SAFARI.

The cryogenic test system was cooled by an Adiabatic Diamagnetic Refrigerator (ADR) with a pulse tube cooler (PTC), the PTC operated at 3.3 K. The two-stage ADR gave a base temperature of 65 mK without optical power coupling. The bath temperature was regulated at 90 mK with a variation of less than 200 μK during all tests. Figure 4.3 shows an image of the test module mounted on the ADR.

4.3 Thermal Considerations of the Variable Temperature Load

In this section, features of the variable temperature load will be introduced. The blackbody hot-load comprised a gold-plated OFHC copper cone, with blackened absorber bonded to the copper. The absorber was a mixture of black Stycast2850 and silicon carbide grit, with grain size of 1 mm. The total mass of the hot-load was 44.78 g, the mass of the copper was 37 g, and the mass of the blackened absorber was 7.78 g. Figure 4.4 shows images of the

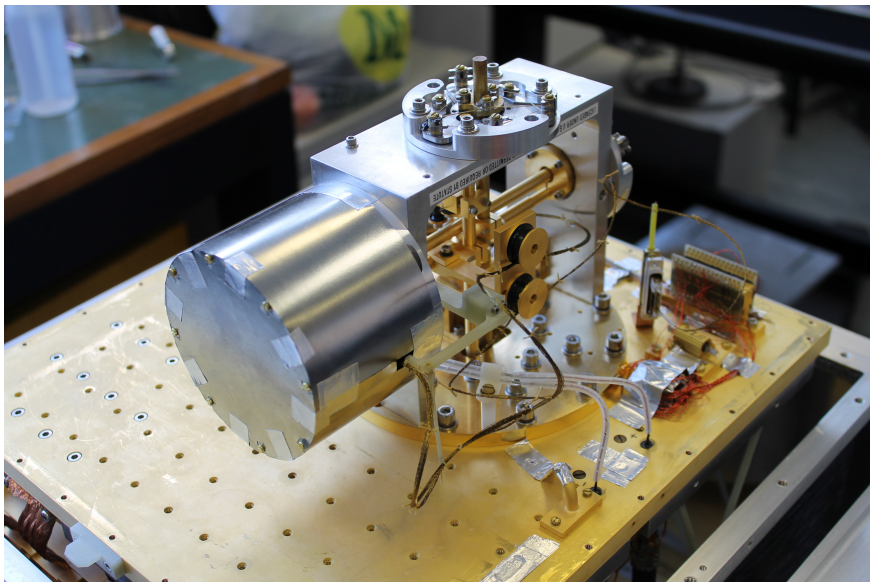

Fig. 4.3 Image of the ADR with mounted test module.

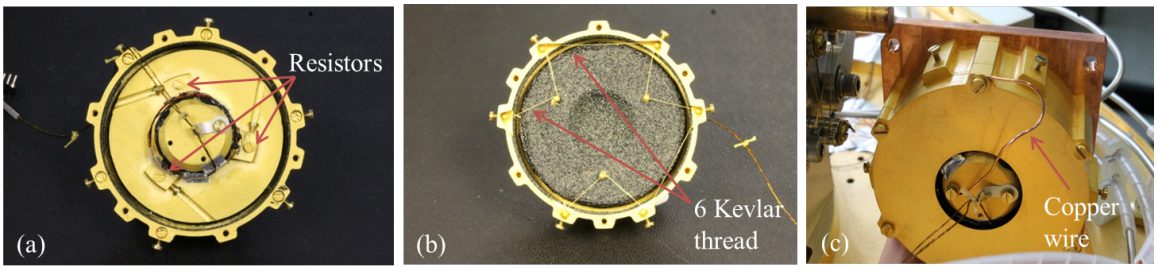

Fig. 4.4 Images of the blackened copper variable hot-load: (a) three heating resistors placed equally on the back of the load; (b)6 Kevlar strings to support the hot-load; (c)a copper wire used as a heat strap for cooling the hot-load.

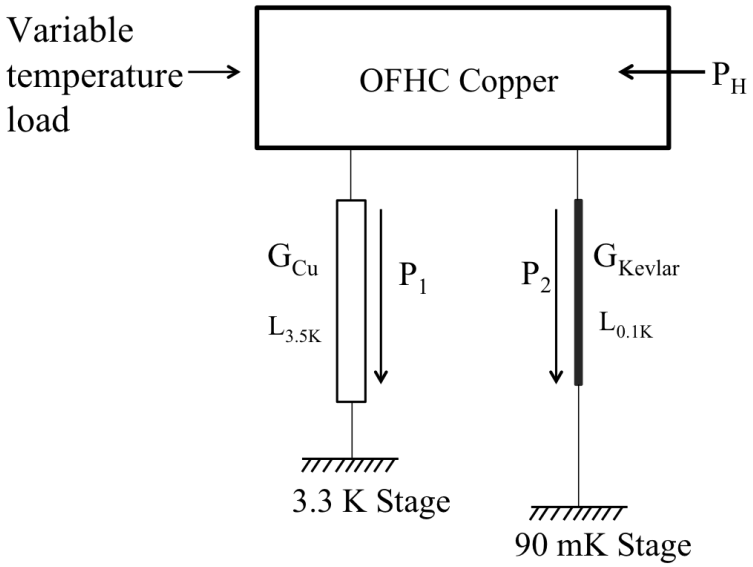

Fig. 4.5 Thermal circuit of the source when installed in a crogenic system. The variable temperature copper load is conneted to the 3.3 K stage through a copper wire, and it is conneted to the 90 mK stage through a few Kevlar strings.

hot-load. The diameter of the load was 3 cm. The hot-load was electrically heated by three resistors, which were attached to the back of the hot-load, with a total resistance of 4000 Ω. The resistors were spaced equally for uniformity at the back of the load as shown in Figure 4.4. Increasing the electrical currents raises the temperature of the load from 3 K to approximately 25 K the highest. A calibrated thermometer was mounted close to the centre.

The hot-load was mechanically anchored to the 3.3 K stage; 6 Kevlar strings were used to support the load in the centre of the housing and connect the hot-load with the outer case, which was in turn connected to the 90 mK stage. An OFHC copper wire was used as a heat strap to control the time constant of the hot-load. The time constant could be varied by changing the cross section and the length of the copper wire. I chose a time constant of around 10 s so that each set of measurements could be taken within a reasonably short period of time. The thermal circuit of the hot-load is shown in Figure 4.5.

4.3.1 Thermal Modelling

As stated earlier, the time constant is related to the dimensions of the copper wire and the mass of the hot-load. The time constant at temperature T is given by

$$\tau(T) = \frac{C(T)}{G(T)}, \tag{4.1}$$

where $C(T) = C_v(T)M$ is the total heat capacity, with $C_v(T)$ the specific heat, and M the mass of the hot-load; and $G(T) = \kappa(T)A/L$ is the thermal conductance of the heat strap, with A the cross section, and L the length of the copper wire [41]. Thus, for a copper wire having given dimensions, we can calculate the time constant as a function of source temperature.

Let $P_H(T)$ be the power applied to raise the temperature of the hot-load to T, and $P_1(T)$, $P_2(T)$ to be the heat flow down the copper wire and the Kevlar strings, respectively. The thermal behaviour is described by the relation

$$\frac{\mathrm{d}}{\mathrm{d}t}U(T) = P_H(T) - P_1(T) - P_2(T), \tag{4.2}$$

where $U(T)$ is the internal energy of the hot-load at T. At steady state, $\mathrm{d}U/\mathrm{d}t = 0$, such that

$$P_H(T) = P_1(T) + P_2(T). \tag{4.3}$$

The power travelling down the heat strap, $P_1(T)$ mainly determines how fast the temperature of the hot-load falls. As the low thermal conductivity of Kevlar ensures that the power travelling through the Kevlar strings is very small. Nevertheless, it is crucial to determine accurately how much power, $P_2(T)$ flows into the 90 mK stage through the Kevlar strings while the hot-load is cooling, to avoid having the cold stage being heated.

According to Fourier's Law, the heat flux q in the x direction can be expressed as

$$q = \frac{P}{A} = -\kappa\left(\frac{\mathrm{d}T}{\mathrm{d}x}\right), \tag{4.4}$$

where κ corresponds to the thermal conductivity; and P is power, which corresponds to the heat flow; A corresponds to the cross-section for the heat flow. This equation gives the heat flux, q, between two planes, with a distance L apart, and at temperatures T_i and T_f. By re-arranging Eq.(4.4) we get

$$q = -\frac{1}{L}\int_{T_i}^{T_f} \kappa(T)\mathrm{d}T. \tag{4.5}$$

Then we obtain the heat flow, P,

$$P(T) = -\frac{A}{L}\int_{T_i}^{T_f} \kappa(T)\mathrm{d}T. \tag{4.6}$$

Now the heat flow into the copper heat strap, $P_1(T)$ and the Kevlar strings, $P_2(T)$ can be determined from Eq.(4.6) numerically, once the thermal conductivities of the OFHC copper and Kevlar are known [6, 10].

Due to the significant difference between the thermal conductivity in the copper heat strap and Kevlar strings, the heat flow down the copper wire is responsible for the temperature change of the load. Once the dimensions of the copper wire, and heat flow through the heat strap are known, a relation can be established to express the change of temperature of the load caused by the heat flow into the heat strap [42] as

$$C(T)\frac{\mathrm{d}T}{\mathrm{d}t} = P_1(T). \tag{4.7}$$

Re-arranging this equation, we get the expression for determining the time to cool the load from temperature T_i to T_f as

$$t = -\int_{T_i}^{T_f} \frac{C(T)}{P_1(T)}\mathrm{d}T. \tag{4.8}$$

4.3.2 Simulations

Firstly, the dimensions of the heat strap must be selected. The hot-load was mainly made of OFHC copper. The specific heat capacity of OFHC copper is given by the expression

$$C_v(T) = 10^{a+b(\log T)+c(\log T)^2+d(\log T)^3+e(\log T)^4+f(\log T)^5+g(\log T)^6+h(\log T)^7+i(\log T)^8}, \tag{4.9}$$

with the coefficiencts $a = -1.9184$, $b = -0.1597$, $c = 8.6101$, $d = -18.996$, $e = 21.9661$, $f = -12.7328$, $g = 3.5432$, $h = 0.3797$ and $i = 0$. The heat strap is also made of OFHC copper, its thermal conductivity is given by expression

$$\kappa_{Cu}(T) = 10^{(a+cT^{0.5}+eT+iT^2)/(1+bT^{0.5}+dT+fT^{1.5}+hT^2)}, \tag{4.10}$$

with the coefficiencts $a = 2.2154$, $b = -0.4746$, $c = -0.8807$, $d = 0.1387$, $e = 0.2951$, $f = -0.0204$, $g = -0.0483$, $h = 0.00128$ and $i = 0.00321$ [28]. Taking the diameter of the copper wire to be 0.7 mm, we can calculate the time constant as a function of temperature for a few convenient lengths.

Figure 4.6 shows the time constant as a function of source temperature when the length of the copper wire is 2 cm, 5 cm and 10 cm. As expected, the shorter the length of the copper wire, the smaller the time constant. However, it does not necessarily mean that the length of the copper wire should be kept as short as possible. The smaller the time constant, the more power is needed to heat the load to given temperature. According to Figure 4.6, I found that having a 5 cm long copper wire gave an average time constant of about 10 s.

As now the length of the heat strap is fixed, then the heat flow through the heat strap at temperature T can be determined from Eq.(4.6). The heat flow into the 60 mK stage through

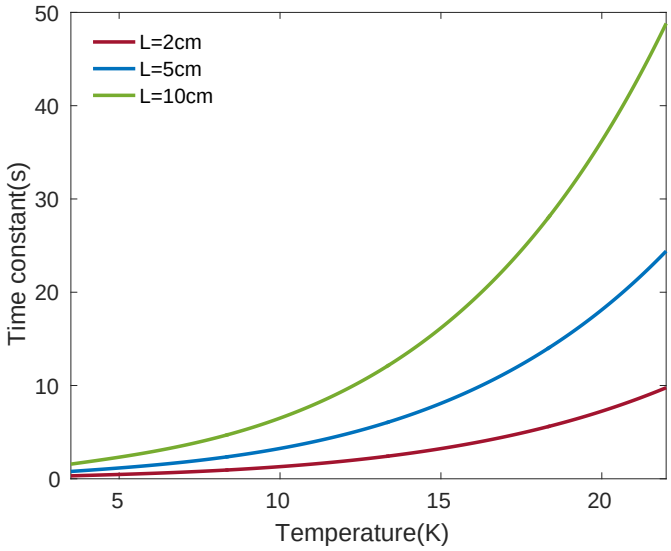

Fig. 4.6 Thermal circuit of the source when installed in a cryogenic system.

the 6 Kevlar strings can also be calculated from Eq.(4.6). The thermal conductivity of the Kevlar is [53]

$$\kappa_{\text{Kevlar}}(T) = 3.05 \times 10^{-3} T^{1.54}. \tag{4.11}$$

The heat flow onto the 3 K stage through the heat strap, $P_1(T)$, and the heat flow onto the 90 mK stage through the 6 Kevlar strings are plotted as a function of temperature in Figure 4.7. It can be seen that the power flow down the Kevlar strings is insignificant compared with the power flow down the copper strap. Thus, the cooling time can be determined by substituting Eq.(4.6) into Eq.(4.8).

4.3.3 Experimental Measurements

A set of preliminary measurements were performed to test the performance of the hot-load. A LabVIEW program was set up to record the temperature of the hot-load as a function of applied voltage. The electrical power required to raise the source temperature can be determined from the relation $P = V^2/R$, with R the resistance of the resistors. Previously, the power needed to heat the hot-load, $P_H(T)$ was estimated from Eq.(4.3). The power required to heat the hot-load, $P_H(T)$ as a function of the temperature of the hot-load are shown in Figure 4.8. In Figure 4.8, the numerical estimate of power is shown as solid line; the experimental results are also as blue points. It can be seen that the experimental results are in a good agreement with the prediction.

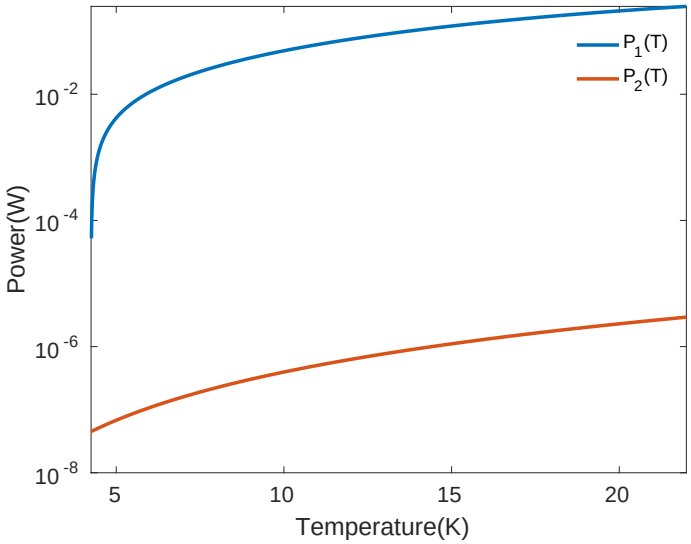

Fig. 4.7 Power flow into the heat strap, P_1, and the Kevlar strings, P_2 at temperature T.

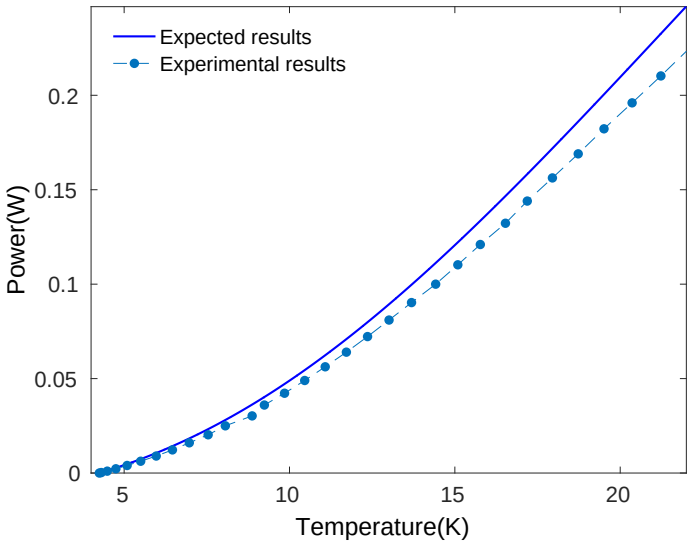

Fig. 4.8 Power input to the hot-load as a function of the temperature of the source; the blue circles are data measured from experiment, and the solid line is a numerical calculation.

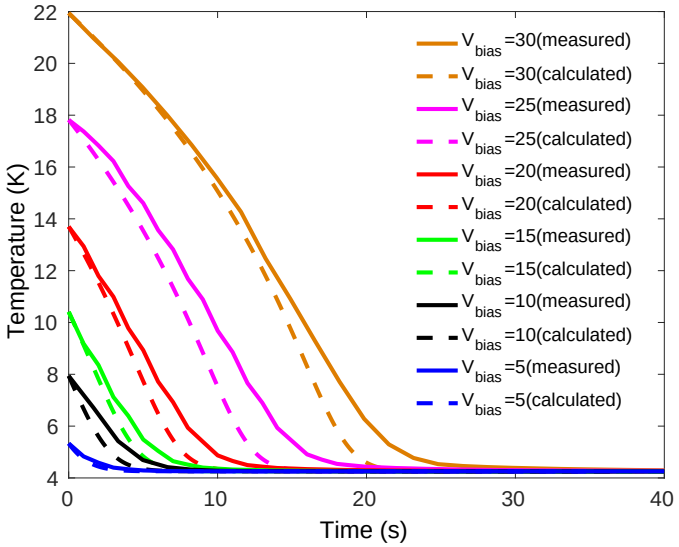

Fig. 4.9 Cooling curves of the hot load from various temperature controlled by the time constant of the heat strap when the electrical power is switched off. Expected curves are shown in dashed lines, and the experimental results are in solid lines.

Another LabView program was written to measure the length of time taken for the hot-load to cool from temperature T_h to a lower temperature T_l. Two sets of decay time results were achieved using two different methods. First, I applied constant voltage to allow the temperature of the load to reach a stable level, and turned off the voltage, and then monitored the temperature of the hot-load as a function of time to determine how long it took to cool down to the bath temperature. The highest voltage applied was 30 V, and it rose the temperature of the load to approximately 22 K. The time for the temperature of the hot-load to decay from the starting points to the bath temperature are shown in Figure 4.9. The solid lines are experimental results, and the dashed lines were calculated theoretically. The numerical results and experimental results are in good agreement. It can be seen that for lower starting temperatures, the numerical predictions are better. This might be because that the hot-load was not only made from OFHC copper, but also had the blackened absorber. Thus the specific heat used for the calculation may not be precisely correct.

In the second method of measuring cooling time, the hot-load was heated to 22 K by applying 30 V electrical power, and then the voltage was dropped in 4 V steps, such that the initial temperature was the same for all of the measurements at 22 K, and the final temperature was varied. Figure 4.10 shows the results of the measurements. It can be seen that the numerical calculations agree with the experimental results well. Both Figure 4.9 and 4.10 show that the numerical model provides a good prediction of cooling time.

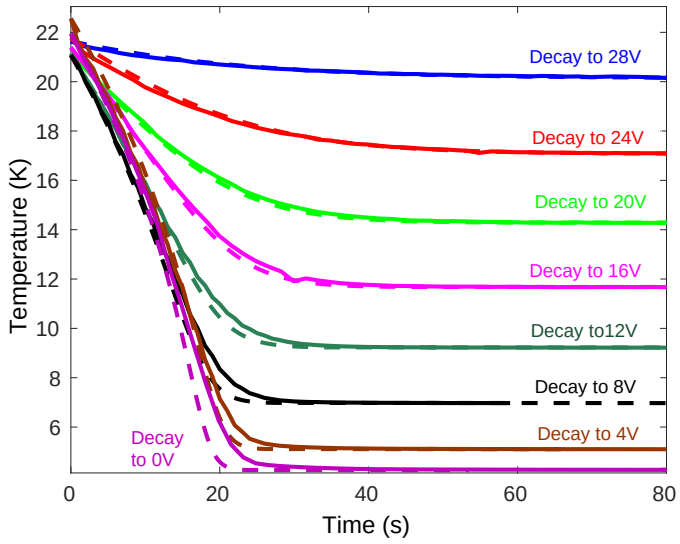

Fig. 4.10 Cooling curves of the hot load from 30V by reducing the voltage by 4V at a time; Expected curves are shown in dashed lines, and the experimental results are in solid lines.

4.4 Theory for Optical Modelling

4.4.1 Optical Modes of the Test System

I have developed a comprehensive few-mode model of the SAFARI/SPICA telescope in the few-mode limit. In this model, the optical system was characterised by a set of natural optical modes. The forms of the modes, and their individual transmission efficiencies, were determined by using classical paraxial optics, based on plane waves, to calculate the Point Spread Function (PSF) as a function of the direction of a point source on the sky. All that is necessary to find the modes is to establish a matrix where each column corresponds to the complex field at the detector plane when a point source is in a particular direction on the sky, and each column corresponds to a sampled raster of directions. This matrix is then factored through Singular Value Decomposition (SVD) to give the modes of the optical system: as distinct from the optical modes of the detector. Note that SVD is needed because the angular distribution of an incoming field on the sky is in a different Hilbert space to that of a spatial field across the image plane. The natural modes of the optical system can then be used together with the modes of the detector to calculate all aspects of behaviour.

The blackbody source can be modelled as producing the same electromagnetic field at the aperture as a blackbody in the far-field, but limited spectrally by the filter stack. The diffraction integral is needed to propagate this field to the plane of the detector.

After passing through the aperture, the diffraction integral can be used to calculate the field across the footprint of the input of the detector,

$$\mathbf{E}_f(\mathbf{r}_t'') = -\frac{i}{\lambda}\int \frac{1}{|\mathbf{r}_t'' - \mathbf{r}_t'|}\exp[ik|\mathbf{r}_t'' - \mathbf{r}_t'|]\mathbf{E}_a(\mathbf{r}_t')\mathrm{d}^2\mathbf{r}_t', \tag{4.12}$$

where $\mathbf{r}_t'$ and $\mathbf{r}_t''$ are the transverse position vectors in the plane of the aperture and the detector, respectively; k is the wavevector; $\mathbf{E}_a(\mathbf{r}_t')$ is a single coherent plane wave of a single realisation at the aperture, which is truncated by the shape of the aperture, and has the general plane-wave form

$$\mathbf{E}_a(\mathbf{r}_t') = -\frac{k^2}{2\pi}\exp(ikz')\exp(ik\boldsymbol{\Omega}\cdot\mathbf{r}_t')\hat{\boldsymbol{\varepsilon}}_i a_i(\boldsymbol{\Omega})L(\mathbf{r}_t')\mathrm{d}\boldsymbol{\Omega}, \tag{4.13}$$

where $\hat{\boldsymbol{\varepsilon}}_i$ is the associated unit polarisation vector; $\boldsymbol{\Omega}$ is the solid angle of incoming plane waves, which is given by $\boldsymbol{\Omega} \approx (\theta\hat{\mathbf{i}} + \phi\hat{\mathbf{j}})$; and $a_i(\boldsymbol{\Omega})$ represents the angular spectrum of the incoming plane waves coming from direction θ and ϕ. The off-axis distances associated with source and observation points are much smaller than, L, the distance between the aperture and the horns. Therefore,

$$|\mathbf{r}_t'' - \mathbf{r}_t'| = [L^2 + (x'' - x')^2 + (y'' - y')^2]^{1/2} \approx L + \frac{(x'' - x')^2 + (y'' - y')^2}{2L}, \tag{4.14}$$

and then the diffraction integral becomes

$$\mathbf{E}_f(\mathbf{r}_t'') = -\frac{i}{\lambda}\frac{1}{L}\exp(ikL)\int_A \mathbf{E}_a(\mathbf{r}_t')\exp[ik\frac{(x'' - x')^2 + (y'' - y')^2}{2L}]\mathrm{d}^2\mathbf{r}_t', \tag{4.15}$$

which is the Fresnel equation, allowing both near field and far field behaviour to be accommodated, A denotes the area of the aperture. Unlike for the telescope, where the detectors are in the far field of the throughput-defining aperture, the detectors in the test system are in the near field of the throughput-defining aperture. Thus no further simplifications can be made in Eq. (4.15). Substituting the incident field gives,

$$\mathbf{E}_f(\mathbf{r}_t'') = \frac{k^2}{2\pi}\frac{1}{\lambda L}\hat{\boldsymbol{\varepsilon}}_i a_i(\boldsymbol{\Omega})\exp(ikL)\mathbf{P}(x'', y''; \theta, \phi)\mathrm{d}\boldsymbol{\Omega}, \tag{4.16}$$

where $P(x'', y''; \theta, \phi)$ is the Point Spread Function in x'' and y'' for a plane wave arriving from direction θ and ϕ, which is given by

$$P(x'', y''; \theta, \phi) = \int L(x', y')\exp[ik(\theta x' + \phi y')]\exp\left[ik\frac{(x'' - x')^2 + (y'' - y')^2}{2L}\right]\mathrm{d}^2\mathbf{r}_t', \tag{4.17}$$

where $L(x',y')$ is the function of the circular aperture, it equals 1 for $\sqrt{x'^2+y'^2} \leq D/2$, where D is the diameter of the aperture, or 0 otherwise. We assume that $\hat{\boldsymbol{\varepsilon}}_i$ is always transverse, which means that the optics of the test system is studied in the paraxial approximation. We have ignored the common phase factor $-i$, as it makes no contribution to power calculations. For a coherent superposition of plane waves we then have

$$\mathbf{E}_f(\mathbf{r}_t'') = \frac{k^2}{2\pi}\frac{1}{\lambda L}\int \hat{\boldsymbol{\varepsilon}}_i a_i(\boldsymbol{\Omega}) P(x'',y'';\theta,\phi)\mathrm{d}\boldsymbol{\Omega}. \tag{4.18}$$

This can be written in the form of Dyadic as

$$\mathbf{E}_f(\mathbf{r}_t'') = \int \overline{\overline{\mathbf{G}}}(\mathbf{r}_t|\boldsymbol{\Omega})\cdot\mathbf{a}(\boldsymbol{\Omega})\mathrm{d}\boldsymbol{\Omega}, \tag{4.19}$$

where the dyadic kernel, $\overline{\overline{\mathbf{G}}}(\mathbf{r}_t|\boldsymbol{\Omega})$, is given by

$$\overline{\overline{\mathbf{G}}}(\mathbf{r}_t|\boldsymbol{\Omega}) = \frac{k^2}{2\pi}\frac{1}{\lambda L}P(x'',y'';\theta,\phi)\overline{\overline{\mathbf{I}}} \tag{4.20}$$

where $\overline{\overline{\mathbf{I}}}$ is the unit dyadic.

For simplicity, we define a dimensionless quantity, $\overline{\overline{\mathbf{T}}}(\mathbf{r}_t|\boldsymbol{\Omega})$,

$$\overline{\overline{\mathbf{T}}}(\mathbf{r}_t|\boldsymbol{\Omega}) = \frac{2\pi}{k^2}\overline{\overline{\mathbf{G}}}(\mathbf{r}_t|\boldsymbol{\Omega}), \tag{4.21}$$

which is closely related to the optical throughput. It admits a Hilbert-Schmidt decomposition,

$$\overline{\overline{\mathbf{T}}}(\mathbf{r}_t|\boldsymbol{\Omega}) = \sum_n \sigma_n \mathbf{u}_n(\mathbf{r}_t)\mathbf{v}_n^*(\boldsymbol{\Omega}), \tag{4.22}$$

where $\mathbf{u}_n(\mathbf{r}_t)$ and $\mathbf{v}_n(\boldsymbol{\Omega})$ are orthonormal sets of basis states, and σ_n is the set of real singular values of the operator. They represent a set of angular beam patterns on the aperture, $|\mathbf{v}_n(\boldsymbol{\Omega})|^2$, that map onto a set of fields over the footprint of the horn at the detector plane, $|\mathbf{u}_n(\mathbf{r}_t)|^2$, with one-to-one corresponding weighting factors, $|\sigma_n|^2$. The normalised optical throughput of an individual optical mode is given by

$$\eta_n^{\mathrm{opt}}(\nu) = \frac{\sigma_n^2(\nu)}{\lambda^2}, \tag{4.23}$$

which can be calculated easily once $\overline{\overline{\mathbf{T}}}(\mathbf{r}_t|\boldsymbol{\Omega})$ using SVD.

4.4.2 Waveguide Modes of the Detector

Once the forms of the optical modes that can propagate through the optical system have been determined, the field coupling between the individual waveguide modes in the detector plane and the individual optical modes of the test system can be determined.

The same square lightpipes as introduced in Chapter 2 are considered. Again, the rectangular waveguide modes at the aperture of the lightpipe have the spatial forms of

$$\mathbf{F}_{mn}^{TE}(\mathbf{r}_t'') = \frac{\sqrt{2}}{\sqrt{ab(n^2+m^2)}}\left[n\cos\left(\frac{m\pi x}{a}\right)\sin\left(\frac{n\pi y}{b}\right)\hat{\mathbf{i}} - m\sin\left(\frac{m\pi x}{a}\right)\cos\left(\frac{n\pi y}{b}\right)\hat{\mathbf{j}}\right], \quad (4.24)$$

for TE types, and

$$\mathbf{F}_{mn}^{TM}(\mathbf{r}_t'') = \frac{\sqrt{2}}{\sqrt{ab(n^2+m^2)}}\left[m\cos\left(\frac{m\pi x}{a}\right)\sin\left(\frac{n\pi y}{b}\right)\hat{\mathbf{i}} + n\sin\left(\frac{m\pi x}{a}\right)\cos\left(\frac{n\pi y}{b}\right)\hat{\mathbf{j}}\right], \quad (4.25)$$

for TM types [24]. a and b are the side lengths of the waveguide; m and n are used to index the waveguide modes, Eq. (4.24) and (4.25) have been normalised in the cases when $m = 0$ or $n = 0$. When m, n is not equal to 0, and an additional factor of $\sqrt{2}$ must be introduced.

The field coupling between the individual waveguide modes at the aperture of the lightpipe and the individual optical modes of the illuminating field is given by

$$S_{in} = \int \mathbf{F}_i^*(\mathbf{r}_t)\cdot\mathbf{u}_n(\mathbf{r})\mathrm{d}\mathbf{r}_t, \quad (4.26)$$

where i denotes the indices of the waveguide modes, and n denotes the indices of the optical modes. The coupling efficiency between the optical modes an the waveguide modes at frequency ν is then given by relation

$$\eta_{in}^{\mathrm{cpl}}(\nu) = |\int \mathbf{F}_i^*(\mathbf{r}_t)\cdot\mathbf{u}_n(\mathbf{r})\mathrm{d}\mathbf{r}_t|^2. \quad (4.27)$$

4.4.3 Power Loading from Source

The blackbody power loading at the detector plane, over the spatial footprint of the input aperture of the detector, can be calculated by integrating the blackbody radiation scaled by the efficiencies, η_n^{opt}, of the optical modes over the wavebands:

$$P(T) = \sum_n \int_{\nu_{\min}}^{\nu_{\max}} \eta^{\mathrm{filters}}(\nu)\eta_n^{\mathrm{opt}}(\nu)\frac{h\nu}{\exp(\frac{h\nu}{k_bT})-1}\mathrm{d}\nu, \quad (4.28)$$

where $\eta^{\text{filters}}(\nu)$ represents the transmission of the band-defining filters and the 4 K thermal filter, h is Planck's constant, k_b is Boltzmann's constant, ν is the operating frequency, and T is the temperature of the blackbody source. The power absorbed by the detector, assuming that a perfect TES absorber is used, can be determined by including the coupling efficiency, η_{in}^{cpl}, between the optical modes and waveguide modes. Thus Eq. (4.28) becomes

$$P(T) = \sum_i \sum_n \int_{\nu_{\min}}^{\nu_{\max}} \eta^{\text{filters}}(\nu)\eta_n^{\text{opt}}(\nu)\eta_n^{\text{cpl}}(\nu)\frac{2h\nu}{\exp(\frac{h\nu}{k_bT})-1}\mathrm{d}\nu, \tag{4.29}$$

where i denotes the index of the waveguide modes.

4.5 Numerical Considerations

A large number of MatLab scripts were written to numerically implement the optical model. As the original concept of SPICA/SAFARI was used as a prototype for the test system, the parameters used to model the test system were largely the same as the telescope itself. The distance between the aperture plane and the detector plane, L, was 10.75 mm. To illustrate an identical representation of the SPICA/SAFARI system, the focal ratios should be made the same. Table 4.1 summarises the main parameters used to model the test system which provides the closest representation of the telescope system.

Table 4.1 The optimum measurement geometry for the test system.

Waveband	L-Band	M-Band	S-Band
Wavelength Range (μm)	210 - 110	110 - 60	60 - 34
Focal Ratio	16.5	20	20
D (μm)	651.5	537.5	537.5

Similar to before, to calculate the optical modes of the test system, we have to represent the dyadic $\overline{\overline{\mathbf{T}}}$ shown in Eq.(4.21) in the form of a matrix. Each column of the matrix T contains the sampled PSF across the footprint of a pixel from a point source. The difference for the test system is that, the quantity $\overline{\overline{\mathbf{T}}}$ is now not simply given by a Bessel function, instead, it must be constructed numerically based on Eq.(4.17) and (4.21). To evaluate $\overline{\overline{\mathbf{T}}}$, the quantity $P(x'', y''; \theta, \phi)$ needed to be determined. To do so, a finite number of sample points for the pixel, the aperture, and the source were chosen.

Each column in the matrix represents the PSF of the point source at a sample point over the source plane, covering the whole field of view of the pixel. The MatLab in-built function SVD was used to achieve singular value decomposition described in Eq.(4.22). Optical

modelling of the test system with the parameters listed above enables us to assess the theory we have developed for the test system by checking if the optical behaviour of test system is the same as that of the telescope.

This numerical technique is rather generic, which can be used to model other optical systems. It is particularly effective for modelling few-mode systems operating at far-infrared wavelengths. Once the same modal content is achieved without using a focusing element, we know that the numerical programs for the test system are correct. Then some of the parameters, such as the size of the aperture, and size of the pixels can be changed to model different experimental realisations. For the actual optical measurements, a series of larger apertures were used so that more power was available to be detected and higher signal-to-noise ratio measurements were taken. When modelling a larger aperture, the field of view was set larger accordingly.

4.6 Simulations

The above scheme provides an elegant numerical technique for modelling the performance of the optical test system. Typical results will be presented in this section to illustrate the effectiveness of the method.

4.6.1 Optical Modes of the Test System

The optical modes and the associated optical throughputs of the test system were calculated. Figure 4.11 shows the optical modes of the test system using the detector footprint of SAFARI L-, M-, and S-Band at their central wavelengths. The intensity beam patterns, (top rows) map onto the intensity focal plane modes (bottom rows) in one-to-one correspondence. The first, second and fourth optical modes are shown left to right, and the second and third modes are degenerate with their spatial forms rotated by 90 degrees. By comparing the optical modes of the test system with those of the equivalent telescope, it has been found that the optical modes and their individual throughputs are the same. Figure 4.12 shows the associated modal throughputs. The overall throughputs of the test system calculated from the model are essentially the same as those of the telescope.

We can see that the optical modes produced by the test system have the same modal forms as those produced by the telescope, and the optical throughputs are also the same as those of the telescope, even though the test system does not have a lens in the aperture. The detailed modal throughputs of the telescope and the test system are tabulated in Table 4.2.

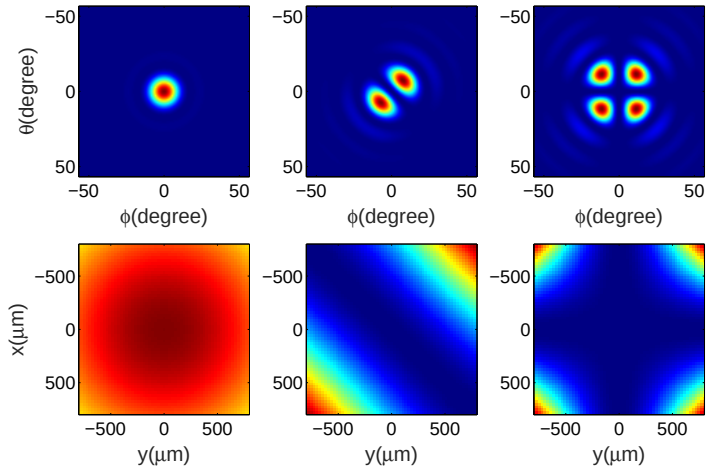

(a) L-Band at 160 μm.

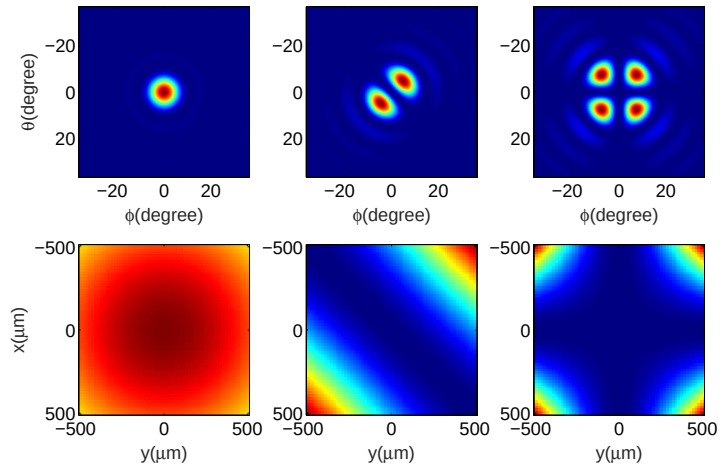

(b) M-Band at 85 μm.

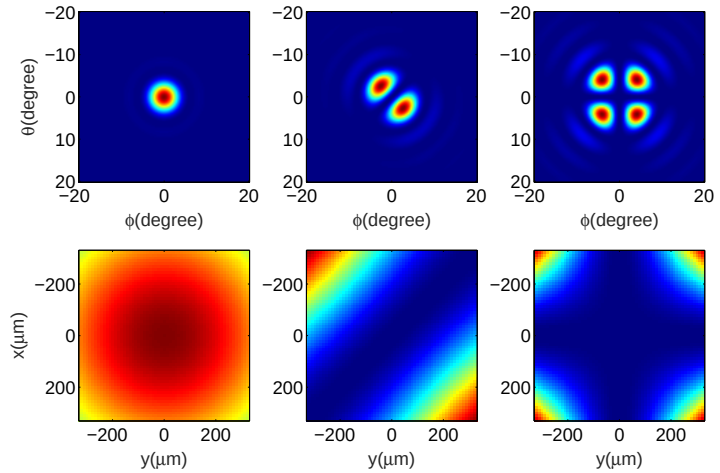

(c) S-Band at 47 μm.

Fig. 4.11 Optical modes of the test system at the central wavelength of (a)L-, (b)M- and (c)S-Band. The first, second and the fourth modes are shown left to right. The top rows show the intensity patterns at the aperture, and the bottom rows show the corresponding intensity beam patterns across the entrance aperture of the lightpipe.

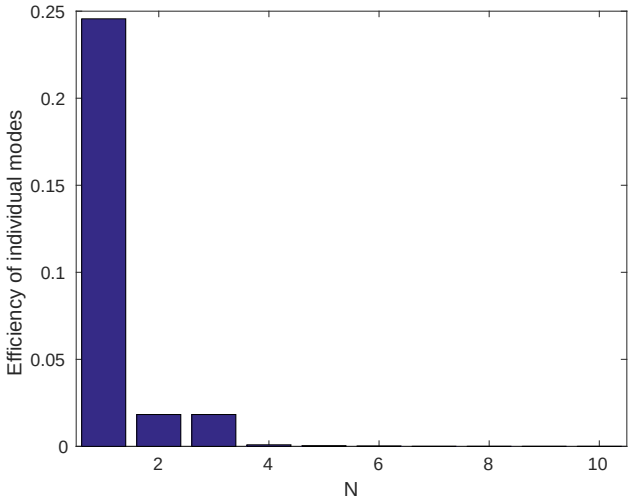

(a) L-Band at 160 μm.

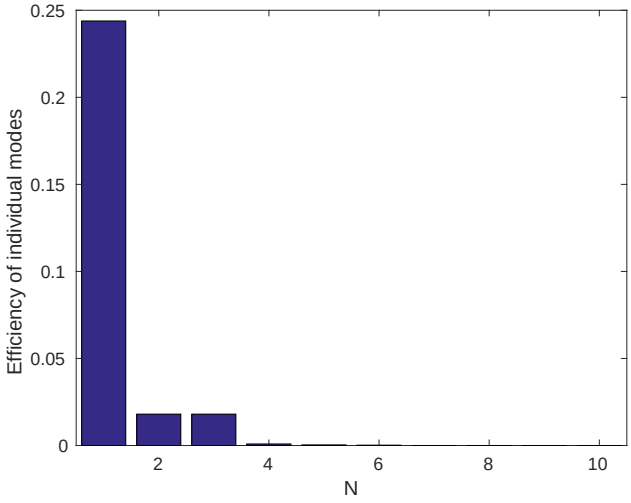

(b) M-Band at 85 μm.

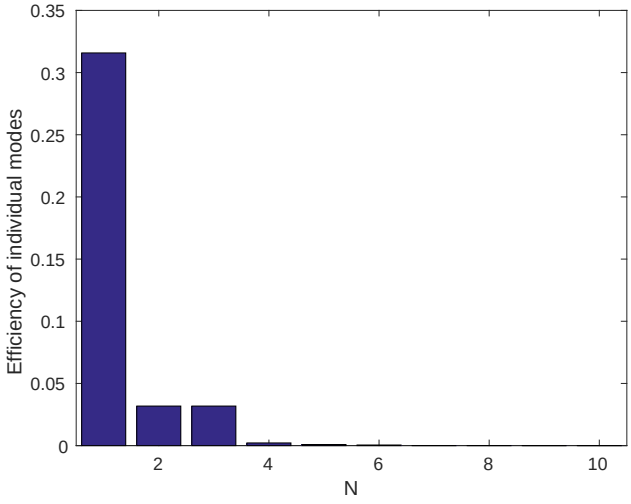

(c) S-Band at 47 μm.

Fig. 4.12 Spectral throughputs of (a)L-, (b)M- and (c)S-Band at the central wavelengths.

Table 4.2 The overall throughput of the optical modes of the telescope system, η_{tele}, and the overall throughput of the optical modes produced by the aperture of the test system, η_{aper} for the central wavelengths of the SAFARI bands.

Waveband	L-Band	M-Band	S-Band
Central Wavelength (μm)	160	85	47
η_{tele}	0.295	0.292	0.599
η_{aper}	0.289	0.287	0.587

This proves that we can obtain near identical optical behaviour for the test system by keeping the geometry the same as that of the telescope, even without using a lens.

As stated earlier, a set of different apertures were used for the optical measurements. To calculate the power detected when larger apertures were used, the optical modes and the throughputs should be determined. Figure 4.13 shows the optical throughputs for different sized aperture at the central wavelength of L-Band.

It can be seen that as the aperture becomes larger, more modes are needed to account for the throughtput to the footprint of a pixel. When the diameter of the aperture is larger than 6 mm, a large number of modes show unity throughputs. The total throughput increase significantly as the aperture size increases. Table 4.3 summarises the overall throughtput at the central wavelength of L-Band for aperture with larger sizes.

Table 4.3 The overall optical thourghputs for large apertures, with $\sum \eta_n$ the numerical results, and η the geometrical results.

D (mm)	1	2	4	6	8	10
$\sum \eta_n$	0.5434	2.2327	8.9308	20.0942	35.7231	56.1230
η	0.5582	2.2725	8.9878	20.6290	36.5898	55.8173

The $\sum \eta_n$ is the overall throughput calculated by summing optical modal efficiencies; and η corresponds to the optical throughput caluclated geometrically. The two sets of the results are essentially the same, which indicates that the numerical results are correct. These calculations have been done across the SAFARI bands for different power calculations.

4.6.2 Filter Characteristics

As stated earlier, L- and S-Band pass filters were used to spectrally limit the electromagnetic field at the aperture; in addition, a thermal blocker was used to further reduce the heat on the detectors. The transmission efficiencies of the filters are needed when calculating the detected power. The filter characteristics for L-, S-Band and the thermal blocker, which

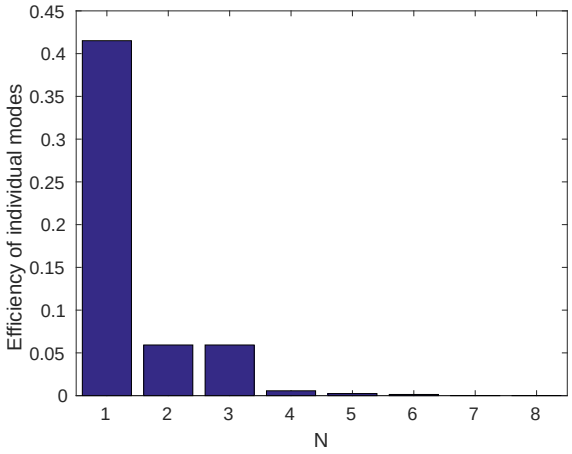

(a) D=1 mm

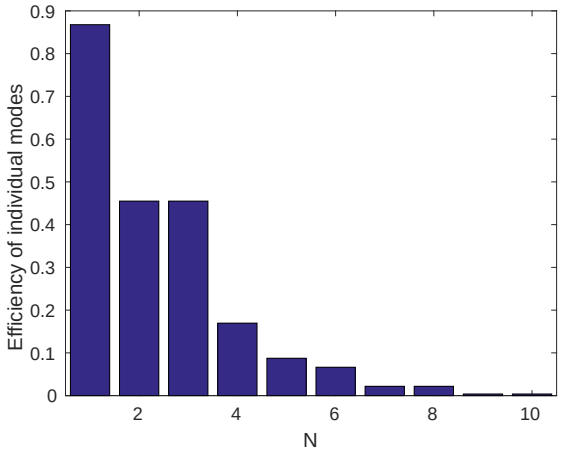

(b) D = 2mm

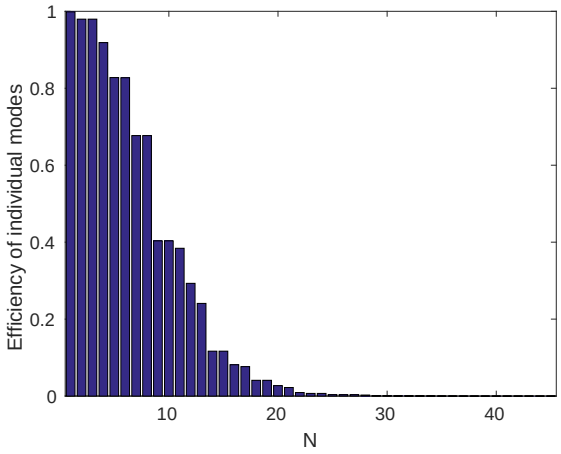

(c) D = 4 mm

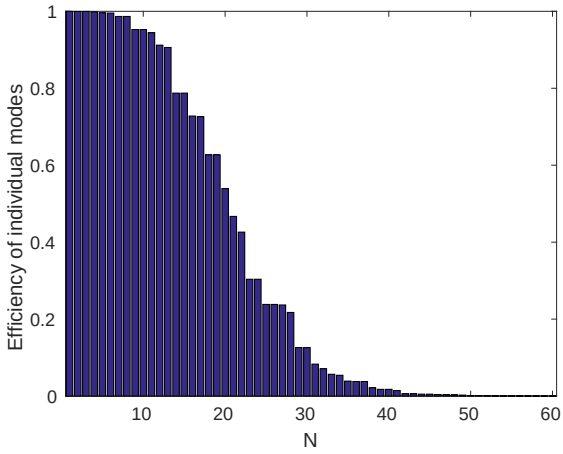

(d) D = 6 mm

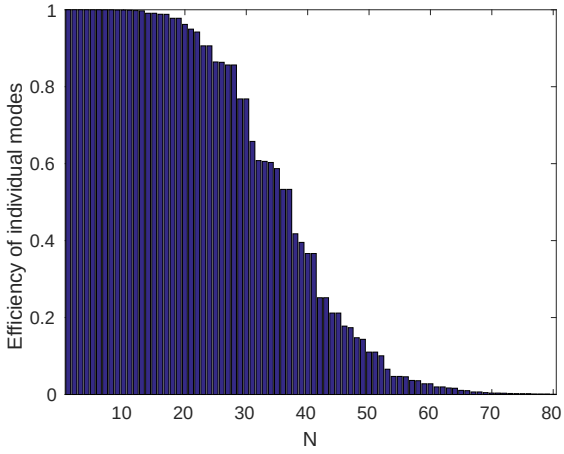

(e) D = 8 mm

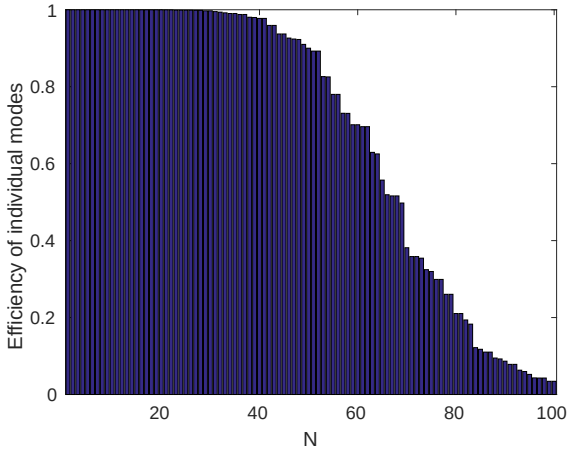

(f) D = 10 mm

Fig. 4.13 Optical throughputs at the central wavelength, 160 μm, of L-Band produced by a series of large apertures.

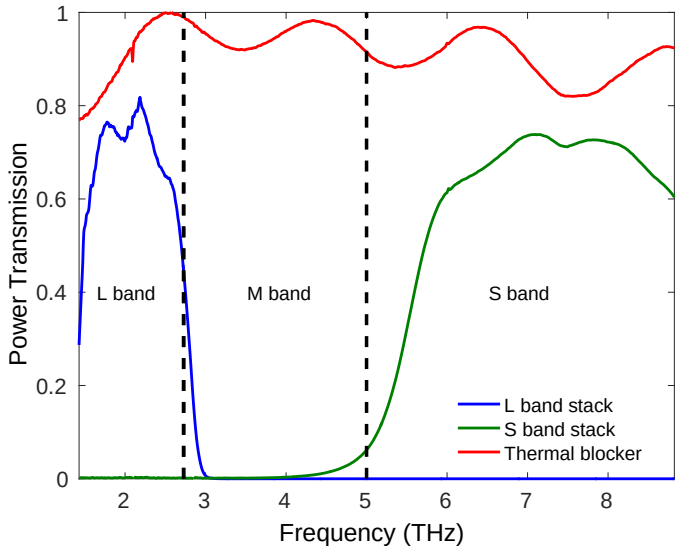

Fig. 4.14 Transmission response of the L- and S-Band filters and the 4 K thermal blocker across the SAFARI bands.

were used in the experiments, are shown in Figure 4.14. These filters were fabricated and characterised by Cardiff University.

4.6.3 Power Loading from Source

Using Eq.(4.29), and assuming use a perfect TES absorber, the power seen by a detector can be determined as a function of source temperature. Figure 4.15 shows the power loading of the source on the detector as a function of the temperature of the blackbody load for L-, M- and S-Band. The L- and S-Band, the band pass filter characteristics, and the transmission of the thermal blocker were included into the power calculations. The power increases with increasing temperature. The power levels are very different for the three SAFARI bands, which implies different source temperatures are required for the three wavebands to have reasonable signal-to-noise ratios. It is also important however to not saturate the TESs.

The maximum temperature for the source can be determined by comparing these power levels with the saturation power level of the TESs. The TESs were designed of a transition temperature of $T_c = 120$ mK. The estimated saturation powers for the L-, M- and S-Band designs are 7.0 fW, 6.6 fW and 13.2 fW, respectively. This information provides an estimate of the maximum temperatures for the source. To avoid saturating the L-, M- and S-Band TESs, the operating temperature of the source should below 7.7 K, 12.9 K and 21.2 K, respectively.

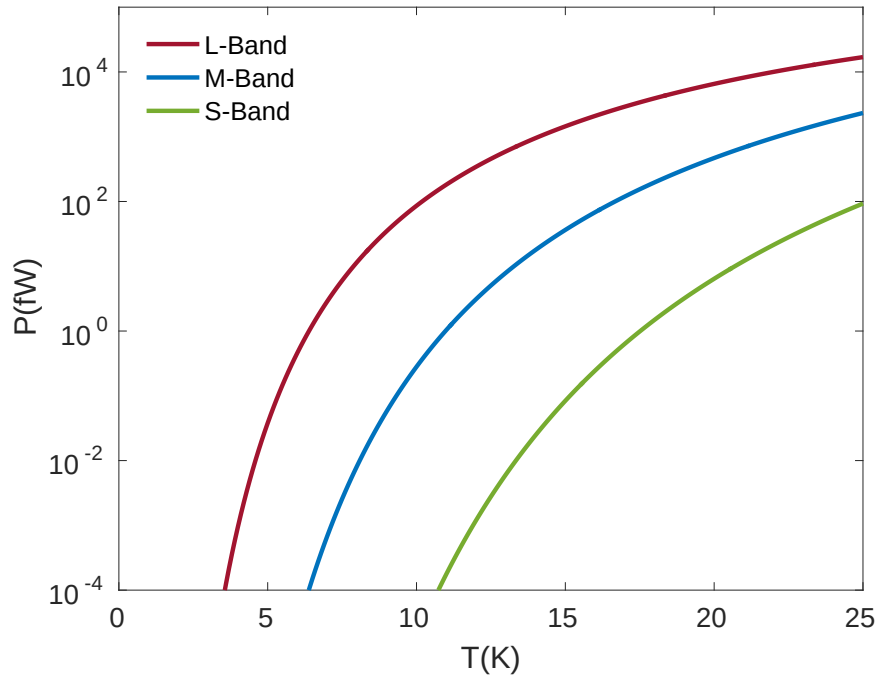

Fig. 4.15 Power collected by the detector, assuming a perfect square absorber are used, for the L-, M-, and S-Band.

4.6.4 Noise

We have described a method for analysing the noise of the telescope system. The same reasoning can be applied to the test system. Given that the optical modes and their throughputs are known, the power spectra across the SAFARI bands can be calculated.

The minimum temperature of the blackbody hot-load in the test system is 3.3 K, and the highest temperature can reach 25 K. Using Eq.(3.16), (3.20) and (3.5), the power spectral density of classical noise, quantum noise and the total of the two can be plotted. Figure 4.16 shows the noise spectra when the blackbody is at the extreme temperatures of 4 K and 25 K.

In Figure 4.16, the noise spectral determined at 4 K and 25 K are shown in the left and right columns, respectively; the results for L-, M- and S-Band are shown from top to bottom. The blue curves correspond to the classical noise, the green curves correspond to the quantum noise, and the red curves are the combined noise of the classical and quantum noise. It can be seen that, at both temperatures, the classical noise is insignificant compared with the quantum noise. Particularly at the low temperature end, the classical noise is almost zero across the SAFARI wavebands. The total noise is mostly dominated by quantum noise at shorter wavelengths. As the same as Figure 3.3, at higher temperatures the increasing optical

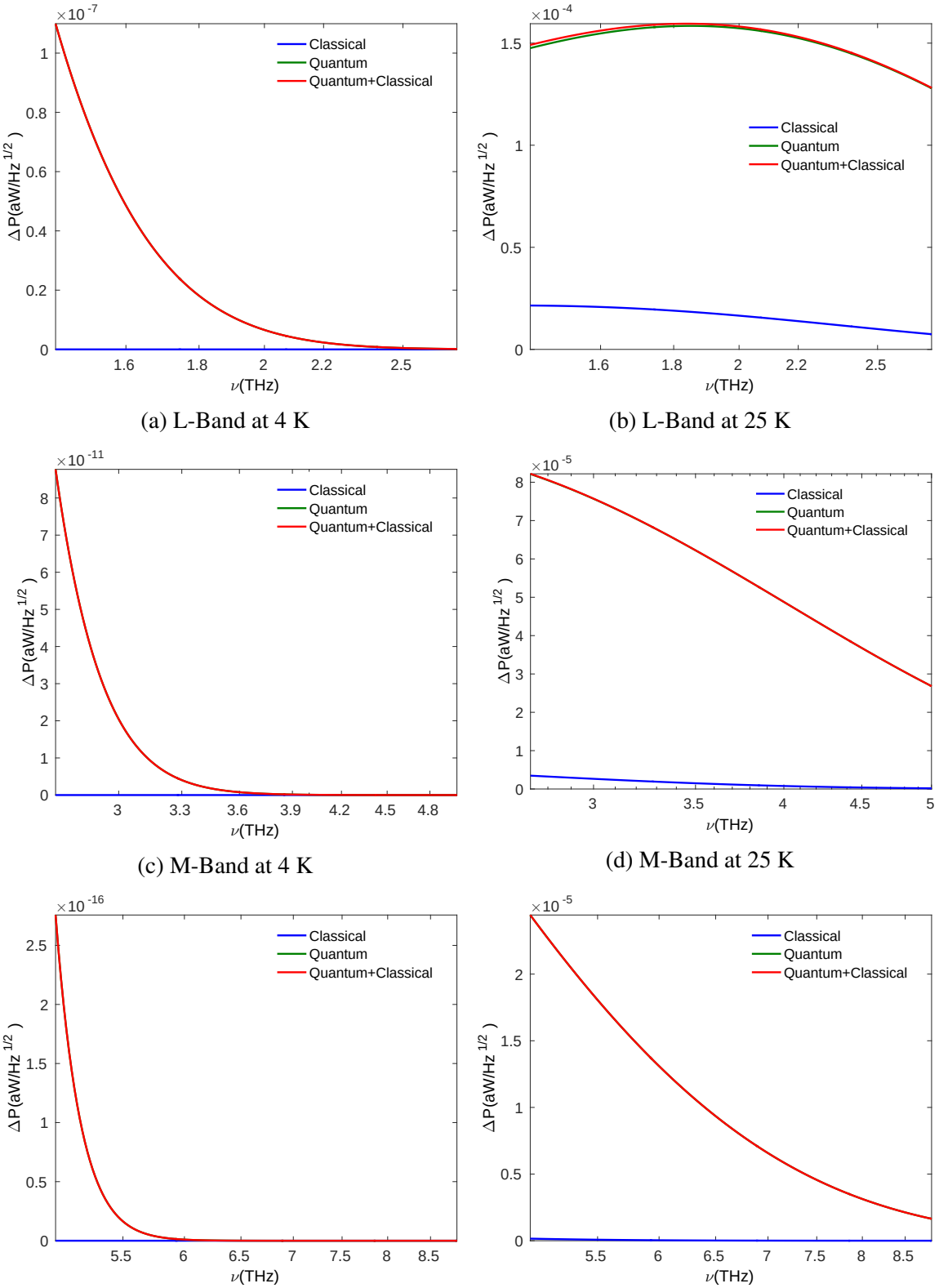

(a) L-Band at 4 K

(b) L-Band at 25 K

(c) M-Band at 4 K

(d) M-Band at 25 K

(e) S-Band at 4 K

(f) S-Band at 25 K

Fig. 4.16 Classical, quantum, and total noise power spectrum density of the source across L-, M-, and S-Band at 4K and 25K.

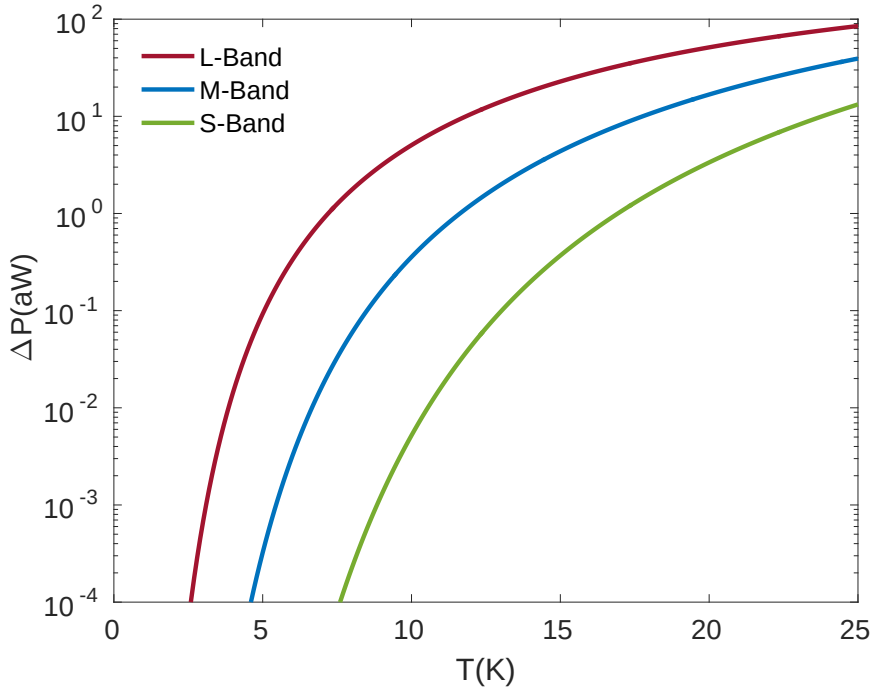

Fig. 4.17 Noise from the blackbody as a function of the source temperature for the L-, M-, and S-Band.

throughputs across the SAFARI wavebands from low to high frequency affect the functional form of the noise spectra.

The total noise power for each band is determined as a function of source temperature by integrating the noise over the bands, as given by Eq.(3.23). The results are shown in Figure 4.17. The noise increases with temperature. The noise power level drops significantly in M- and S-Band. The same calculations were also performed on the telescope system. The results from both systems are nearly identical.

4.6.5 Signal to Noise Ratio

The power and noise loading from the blackbody source to the detector have been fully determined, we can then calculate the signal to noise ratio for each of the bands. Figure 4.18 shows that the signal to noise ratios are small at low temperatures as expected. The temperature of the blackbody source varies between 3.3 K and 25 K. 1 s of integration time τ was used for the calculations, which is a plausible choice for actual test. We can see that good signal can be achieved at all feasible experimental temperatures for L band. Whereas for M- and S-Band, higher source temperatures are required. To achieve signal to noise ratios larger than unity, the minimum temperature of the source for the L- , M- and S-Bands should

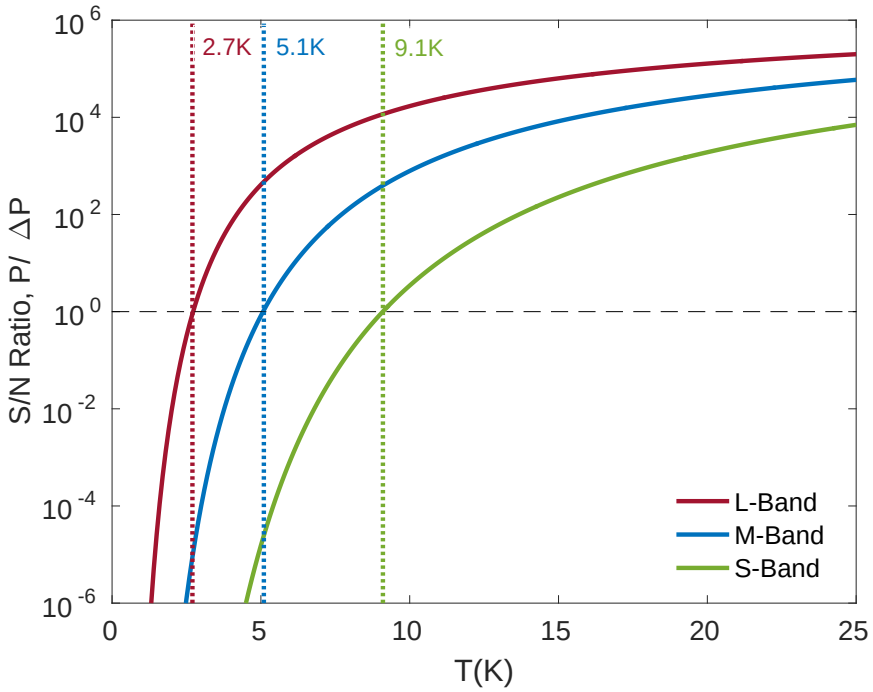

Fig. 4.18 Signal to noise ratio as a function of the source temperature for the L-, M-, and S-Band.

be around 2.7 K, 5.1 K and 9.1 K, respectively. Alternatively, higher signal to noise ratios for the shorter wavebands at lower temperatures can be achieved by increased the integration time.

4.7 Power Loading from the Cold Baffle

The design temperature of the throughput-defining aperture is 90 mK. It is crucial to understand how much power from the baffle can be seen by the detector.

4.7.1 Method

The power loading and noise from baffle to the detector can be calculated through three steps, as shown in Figure 4.19.

Firstly the detected power from a continuous sheet, P_s, can be calculated; in other words, we assume that the baffle extends to infinity and the aperture does not exist. Then we can calculate how much power can be detected from an aperture sized baffle, P_a. Then power

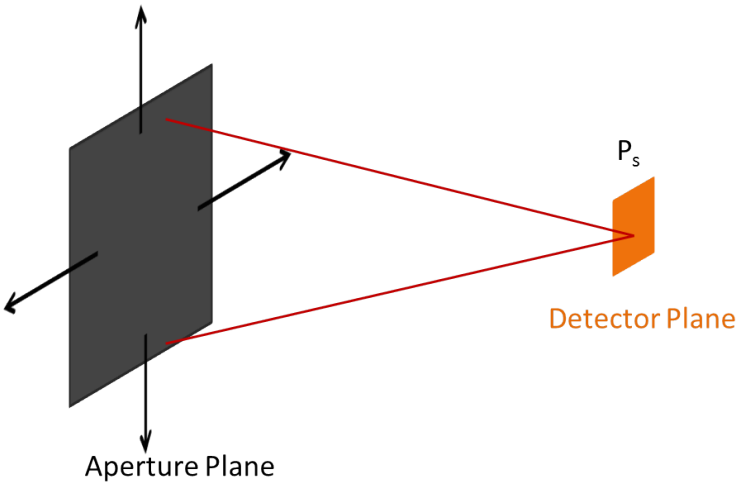

(a) A continuous baffle sheet

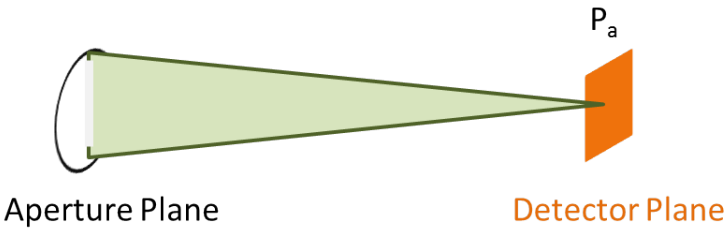

(b) Aperture

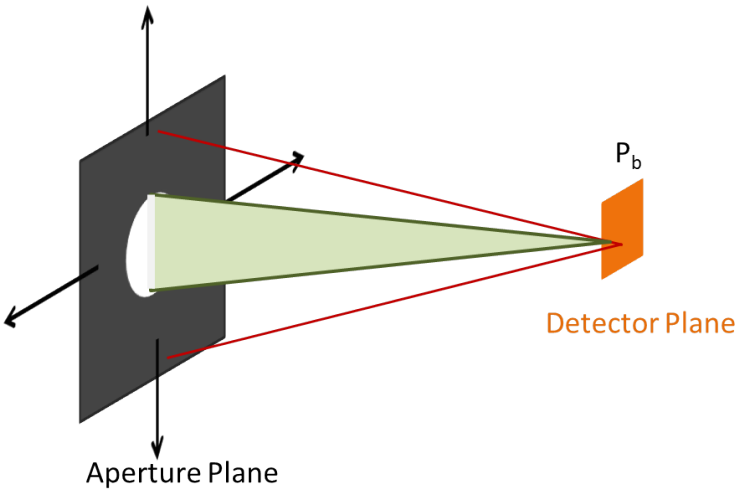

(c) Baffle with an aperture

Fig. 4.19 Scheme for calculating power and noise from the cold baffle: (a) Power and noise from a continuous sheet; (b) equivalent power and noise from the aperture area; (c) loading and noise from the baffle.

from the actual baffle, P_b, can be determined from relation

$$P_{\mathrm{b}} = P_{\mathrm{s}} - P_{\mathrm{a}}. \tag{4.30}$$

The first step can be carried out with a simplified calculation of baffle loading and noise under the following assumptions:

(a) the baffle is a continuous sheet, that the aperture hole does not exist, with uniform emissivity ε and temperature T. Then the sky brightness dyadic can be written as

$$\overline{\overline{\mathbf{B}}}\left(\mathbf{\Omega}_1, \mathbf{\Omega}_2, \nu\right) = \frac{1}{2}\varepsilon B\left(\nu, T\right)\overline{\overline{\mathbf{I}}}\delta\left(\mathbf{\Omega}_1 - \mathbf{\Omega}_2\right), \tag{4.31}$$

where $B(\nu, T)$ is the Planck blackbody brightness, which is given by

$$B\left(\nu, T\right) = \frac{2h\nu}{\lambda^2\left[\exp\left(\frac{h\nu}{kT}\right) - 1\right]}, \tag{4.32}$$

where the factor 2 denotes the two polarisations, which is consistent with Eq.(2.42), and $\overline{\overline{\mathbf{I}}}$ is the identity dyadic for the space of polarisation states;

(b) the detector is a perfect absorber with area A equal to that of the horn aperture and incoherent spatial response. The total power measured is therefore the power flow normal to the surface, which is approximated by

$$\overline{\overline{\mathbf{A}}}_E\left(\mathbf{\Omega}_1, \mathbf{\Omega}_2, \nu\right) = A\overline{\overline{\mathbf{I}}}\cos\theta\,\delta\left(\mathbf{\Omega}_1 - \mathbf{\Omega}_2\right), \tag{4.33}$$

where $\overline{\overline{\mathbf{A}}}_E(\mathbf{\Omega}_1, \mathbf{\Omega}_2, \nu)$ is the effective area dyadic describing the far-field sensitivity of detector;

(c) the detector is sensitive to frequencies ranging from the cut-off frequency of the waveguide in which the absorber is mounted and up to $\nu = \infty$. Set the side length of the square waveguide to be a, then,

$$\frac{a}{2c} \leq \nu \leq \infty, \tag{4.34}$$

where c is the speed of light in vacuum.

With these assumptions, we can calculate power and noise from the continuous sheet. The total power absorbed from the baffle, P_{s}, is

$$\begin{aligned} P_{\mathrm{s}} &= \int_{\frac{c}{2a}}^{\infty} \iint \overline{\overline{\mathbf{A}}}_E^{\dagger}(\boldsymbol{\Omega}_1, \boldsymbol{\Omega}_2, \nu) \cdot\cdot \overline{\overline{\mathbf{B}}}(\boldsymbol{\Omega}_1, \boldsymbol{\Omega}_2, \nu) \mathrm{d}\boldsymbol{\Omega}_1 \mathrm{d}\boldsymbol{\Omega}_2 \mathrm{d}\nu \\ &= \int_{\frac{c}{2a}}^{\infty} \int A \overline{\overline{\mathbf{I}}} \cos\theta \cdot\cdot \frac{1}{2} \varepsilon B(\nu, T) \overline{\overline{\mathbf{I}}} \mathrm{d}\boldsymbol{\Omega} \mathrm{d}\nu \\ &= A \int_{\frac{c}{2a}}^{\infty} \int B(\nu, T) \cos\theta \mathrm{d}\boldsymbol{\Omega} \mathrm{d}\nu \\ &= \pi A \int_{\frac{c}{2a}}^{\infty} B(\nu, T) \mathrm{d}\nu, \end{aligned} \tag{4.35}$$

it has assumed that the emissivity $\varepsilon(\nu) = 1$. The photon NEP is given by

$$\begin{aligned} \mathrm{NEP}_{\mathrm{s}}^2 = \Bigg\{ & 2 \int_{\frac{c}{2a}}^{\infty} h\nu \iint \overline{\overline{\mathbf{A}}}_E^{\dagger}(\boldsymbol{\Omega}_1, \boldsymbol{\Omega}_2, \nu) \cdot\cdot \overline{\overline{\mathbf{B}}}(\boldsymbol{\Omega}_1, \boldsymbol{\Omega}_2, \nu) \mathrm{d}\boldsymbol{\Omega}_1 \mathrm{d}\boldsymbol{\Omega}_2 \mathrm{d}\nu + \\ & 2 \int_{\frac{c}{2a}}^{\infty} \iiiint \left[\overline{\overline{\mathbf{A}}}_E^{\dagger}(\boldsymbol{\Omega}_1, \boldsymbol{\Omega}_2, \nu) \cdot \overline{\overline{\mathbf{B}}}(\boldsymbol{\Omega}_1, \boldsymbol{\Omega}_3, \nu) \right] \cdot\cdot \left[\overline{\overline{\mathbf{A}}}_E(\boldsymbol{\Omega}_3, \boldsymbol{\Omega}_4, \nu) \cdot \overline{\overline{\mathbf{B}}}^{\dagger}(\boldsymbol{\Omega}_2, \boldsymbol{\Omega}_4, \nu) \right] \Bigg\} \\ & \mathrm{d}\boldsymbol{\Omega}_1 \mathrm{d}\boldsymbol{\Omega}_2 \mathrm{d}\boldsymbol{\Omega}_3 \mathrm{d}\boldsymbol{\Omega}_4 \mathrm{d}\nu \\ = & 2\pi A \int_{\frac{c}{2a}}^{\infty} h\nu B(\nu, T) \mathrm{d}\nu + \pi^2 A^2 \int_{\frac{c}{2a}}^{\infty} [B(\nu, T)]^2 \mathrm{d}\nu, \end{aligned} \tag{4.36}$$

where the first term corresponds to photon-counting noise, whereas the second term corresponds to classical noise. The relationship between the minimum detectable signal ΔP in 1 second and NEP is given as

$$\Delta P = \frac{NEP}{\sqrt{2}}. \tag{4.37}$$

The power and noise from the aperture area has been discussed previously. In this case, the integrals in Eq. (4.29) and Eq. (3.23) should be integrated from the cut-off frequency $\frac{c}{2a}$ to ∞, thus the expression for power becomes

$$P_{\mathrm{a}} = \sum_n \int_{\frac{c}{2a}}^{\infty} \eta_n^{\mathrm{opt}}(\nu) \lambda^2(\nu) B(\nu, T) \mathrm{d}\nu, \tag{4.38}$$

and the photon NEP is

$$\mathrm{NEP}_{\mathrm{a}}^2 = \sum_n \int_{\frac{c}{2a}}^{\infty} h\nu \eta_n^{\mathrm{opt}}(\nu) \lambda^2(\nu) B(\nu, T) \mathrm{d}\nu + \sum_{nm} \int_{\frac{c}{2a}}^{\infty} \eta_n^{\mathrm{opt}} \eta_m^{\mathrm{opt}}(\nu) \lambda^4(\nu) [B(\nu, T)]^2 \mathrm{d}\nu, \tag{4.39}$$

where n and m indicate the indices of optical modes. Thus the power and photon NEP of the baffle, accounting for the aperture are determined as

$$P_{\mathrm{b}} = \pi A \int_{\frac{c}{2a}}^{\infty} B(\nu, T) \left[1 - \frac{\sum_n \eta_n^{\mathrm{opt}}(\nu) \lambda^2(\nu)}{\pi A} \right] \mathrm{d}\nu, \tag{4.40}$$

and

$$\begin{aligned} \mathrm{NEP}_{\mathrm{b}}^2 = {} & 2\pi A \int_{\frac{c}{2a}}^{\infty} h\nu B(\nu, T) \left[1 - \frac{\sum_n \eta_n^{\mathrm{opt}}(\nu) \lambda^2(\nu)}{2\pi A} \right] \mathrm{d}\nu \\ & + \pi^2 A^2 \int_{\frac{c}{2a}}^{\infty} [B(\nu, T)]^2 \left[1 - \frac{\sum_{nm} \eta_n^{\mathrm{opt}} \eta_m^{\mathrm{opt}}(\nu) \lambda^4(\nu)}{\pi^2 A^2} \right] \mathrm{d}\nu. \end{aligned} \tag{4.41}$$

Similarly as before, the first term in Eq. (4.41) is associated with photon noise, and the second term is associated with classical noise. The corresponding noise can be determined from Eq. (4.37). It is expected that the loading from baffle is insignificant if the temperature of the baffle is sufficiently low.

4.7.2 Results

Figure 4.20 shows the power from baffle, P_{b} , as a function of temperature ranging from 100 mK to 1 K. The temperature of the baffle should stay below 100 mK during test. From the calculation, we found that the L-, M-, and S-Band power loadings from baffle at 100 mK is of order of 10^{-18} fW, 10^{-27} fW and 10^{-38} fW, which are absolutely insignificant compared with the power from source. However, the baffle power does increase rather rapidly with temperature, as a consequence of the upper frequency allowing for a large number of optical modes. Thus it is crucial to keep the temperature of the baffle low, otherwise the power from the baffle would become dominant, and saturate the detectors. In practice, the temperature of the baffle has been kept under 100 mK throughout all the experiments.

4.8 Conclusion

In this chapter, the main features of a test system for ultra-low-noise TESs are introduced. The thermal considerations in designing the variable temperature load have been discussed. The test system was engineered to reproduce the optical behaviour of the SPICA/SAFARI telescope. Compared to the telescope, the test system has no focusing element. The blackbody radiation passes through an aperture and reaches the detector plane. Partially coherent optical

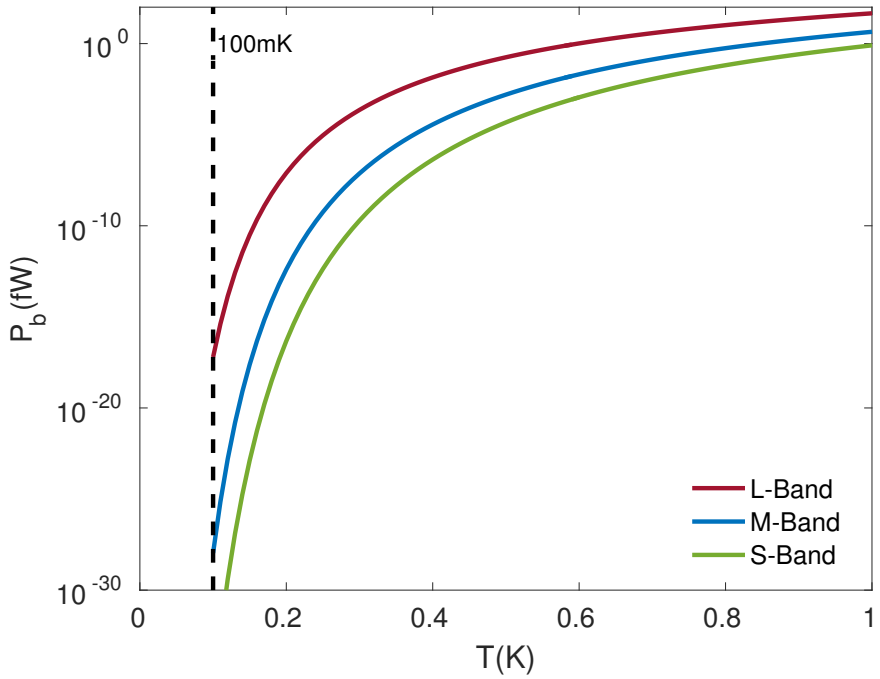

Fig. 4.20 Power loading from the cold baffle as a function of temperture for L-, M- and S-Band.

theory has been adapted for the test system. Calculations of optical throughput, total power loading of the detectors, and photon noise from the source and baffle have been carried out for all wavebands. It has been shown that, if the geometric focal ratio of the test system is the same as that of the equivalent optical system of the telescope, the modes and modal throughputs of the test system are identical with those of the telescope optics. The modal content of the illuminating condition of the test system are the same as that of the telescope. This occurs even though the telescope has an effective thin lens whereas the test system does not. Thus the partially coherent illumination conditions are identical in both cases. The loading from the surrounding baffles are also considered, it has been shown that the loading from the baffle is insignificant compared to the loading from the source. In the next chapter, it will be shown that all of these designing calculations were achieved in practice when experiments were carried out.

Chapter 5

Optical Efficiency Measurements

5.1 Introduction

In the previous chapters, I described the optical performance of ultra-low-noise TES detectors for SAFARI, and also the test system, in terms optical and waveguide modes. The underlying theory and numerical methods for modelling were discussed. In this chapter, I will present the experimental results of optical power measurements of the L-Band (210-110 μm) TES pixels performed using the cryogenic test system. I have already presented an engineering drawing of the test system in Figure 4.1. The main objective of the experimental work was to investigate the optical efficiencies of few-moded TES detectors.

5.2 Experimental Design

As introduced in Chapter 4, the main concept of the optical test system was to use a variable temperature load as blackbody source to illuminate the TES detectors through an aperture. The blackbody radiation generated by the hot-load passed through the aperture and then arrived on to the device plane. A simplified schematic diagram of the test system is shown in the centre of Figure 5.1. Images of the essential parts of the test system are also shown. Image (a) shows the gold-plated copper variable temperature load anchored on the 3 K stage. To ensure that the cryostat would not be affected by the thermal radiation generated by the hot-load, the hot-load was thermally isolated from the detectors and optics. Additionally, a thermal-blocking filter was applied to further reduce heat. A filter stack, as shown in image (b), was placed behind the thermal blocker, in order to define the bandwidth of the radiation field. The filter stack was surrounded by a blackened labyrinth, which was used to minimise stray light. Image (c) shows an example of the circular apertures, which limited the optical

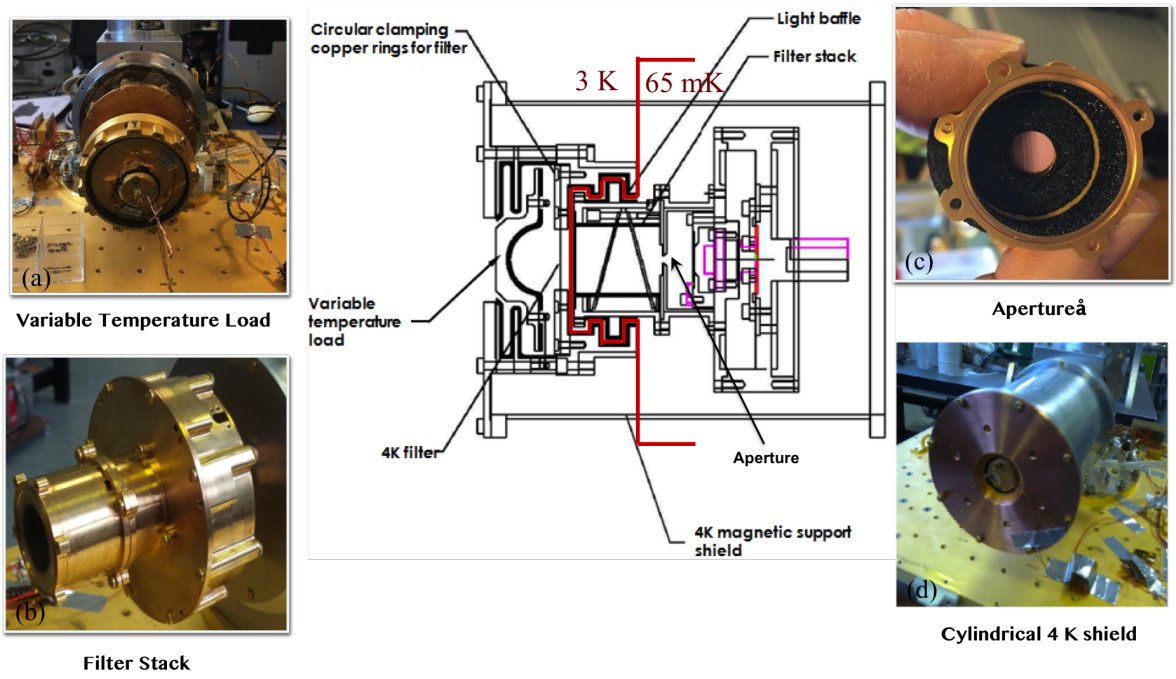

Fig. 5.1 Images and simplified schematic diagram of the cryogenic optical test system for ultra-low-noise TESs.

throughput. Both the filter stack and the circular aperture were mounted on the 65 mK cold stage. The entire test assembly was surrounded by a cylindrical outer case, as shown in image (d).

5.2.1 TES Fabrication

To describe the devices on the detector plane, I will start by introducing the characteristics of the TESs. The tested TESs and their readout electronic were designed and fabricated by the colleagues of the Quantum Sensors Group, and myself was not directly involved in the processes of manufacturing the TES or developing the readout system.

Figure 5.2 shows the mask layout used for TESs. The detector arrays described here contained 16 devices. Each of the devices was formed on a SiN_x island and consisted of a MoAu bilayer, a β-phase Ta absorber and Nb connections. The materials used to manufacture the TESs were Si, SiO_2, SiN_x, Ta, MoAu bilayer, Au and Nb.

Figure 5.3 illustrates the procedure used for fabricating the MoAu TESs. A cross-section along a single TES is shown in the diagrams. The fabrication of the TESs started from the unprocessed double-sided polished 50 mm diameter Si wafers, as illustrated in step (1): the thickness of the blank wafer was 225 μm; on both sides of these wafers there were 50 nm

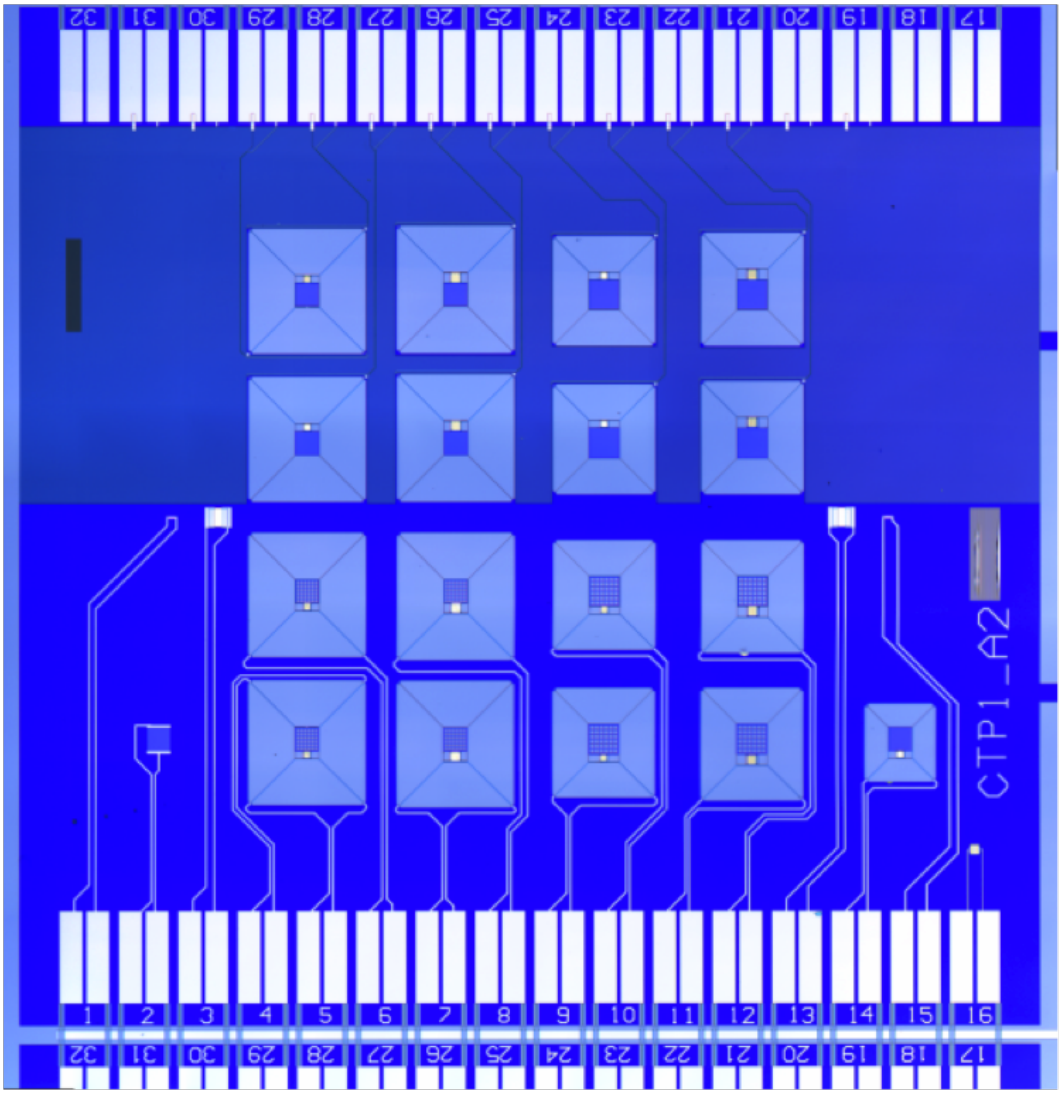

Fig. 5.2 Image of the array of 16 TESs.

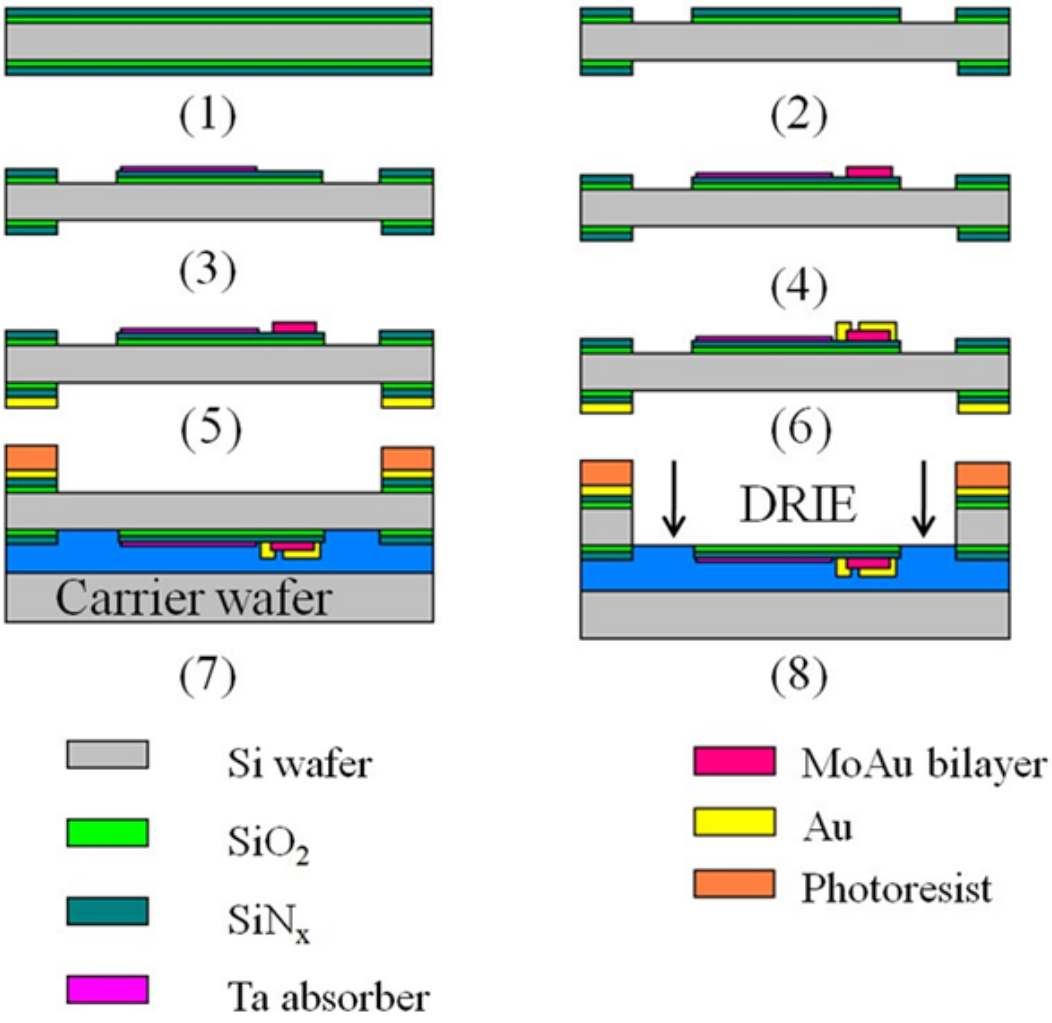

Fig. 5.3 Schematic diagram of processing steps for the fabrication of a TES.

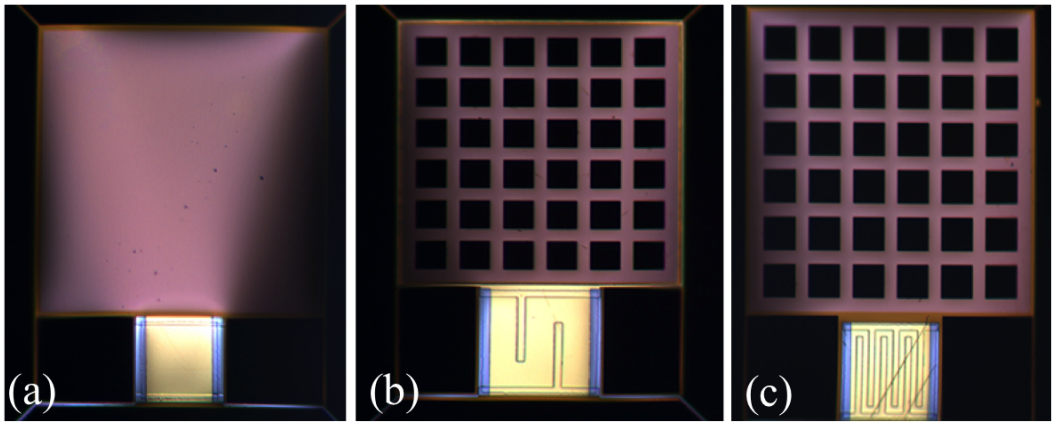

Fig. 5.4 Completed fabricated TES devices used for measurements.

films of SiO_2 and a 200 nm film of SiN_x, which was formed by low-pressure chemical vapour deposition. In step (2), the SiO_2 and SiN_x were removed by Reactive Ion Etching (RIE): the front etching gives the TES islands and SiN_x legs, the SiN_x legs thermally isolate the island from the Si wafer; and the back etching provides a window, from which the Si could be completely removed in a later step. In step (3), the β-phase Ta absorber was deposited by DC magnetron sputtering. The MoAu bilayer was then deposited using DC magnetron sputtering in high vacuum conditions in step (4). In step (5), a Au thermalising layer with a thickness of 200 nm was deposited on the back of the wafer. Step (6) shows the process of adding a Au thermalising rim around the Ta absorber, and Au bars on the top of the MoAu bilayer, which improves the thermalisation of the TES. The effect of adding Au bars on the bilayer increases the response time. In step (7), the wafer was then mounted face down onto a carrier wafer. In the final step, windows were opened up to remove the Si substrate by Deep Reactive Ion Etching (DRIE) from the back of the wafer [11].

Figure 5.4 shows the images of three manufactured TESs. A filled absorber is shown in (a); (b) and (c) have meshed absorbers. Au rims can be seen around the absorbers in images (a) and (b). The geometric structures of the three bilayer are different, to allow a good control of the $R(T,I)$ surface of the TES.

5.2.2 Readout Circuit

The TES readout is accomplished by use of superconducting Quantum Interference Devices (SQUIDs) [23]. Figure 5.5 shows a simplified diagram of the TES and readout electronics. The TES bias circuit is shown on the left side, which includes a load resistor, R_{load}, a bias resistor, R_{bias}, a stray resistance, R_{stray}, and the resistance of the TES itself, R_{TES}. V_a is the voltage used to provide the voltage bias to the TES. The current through the TES bilayer,

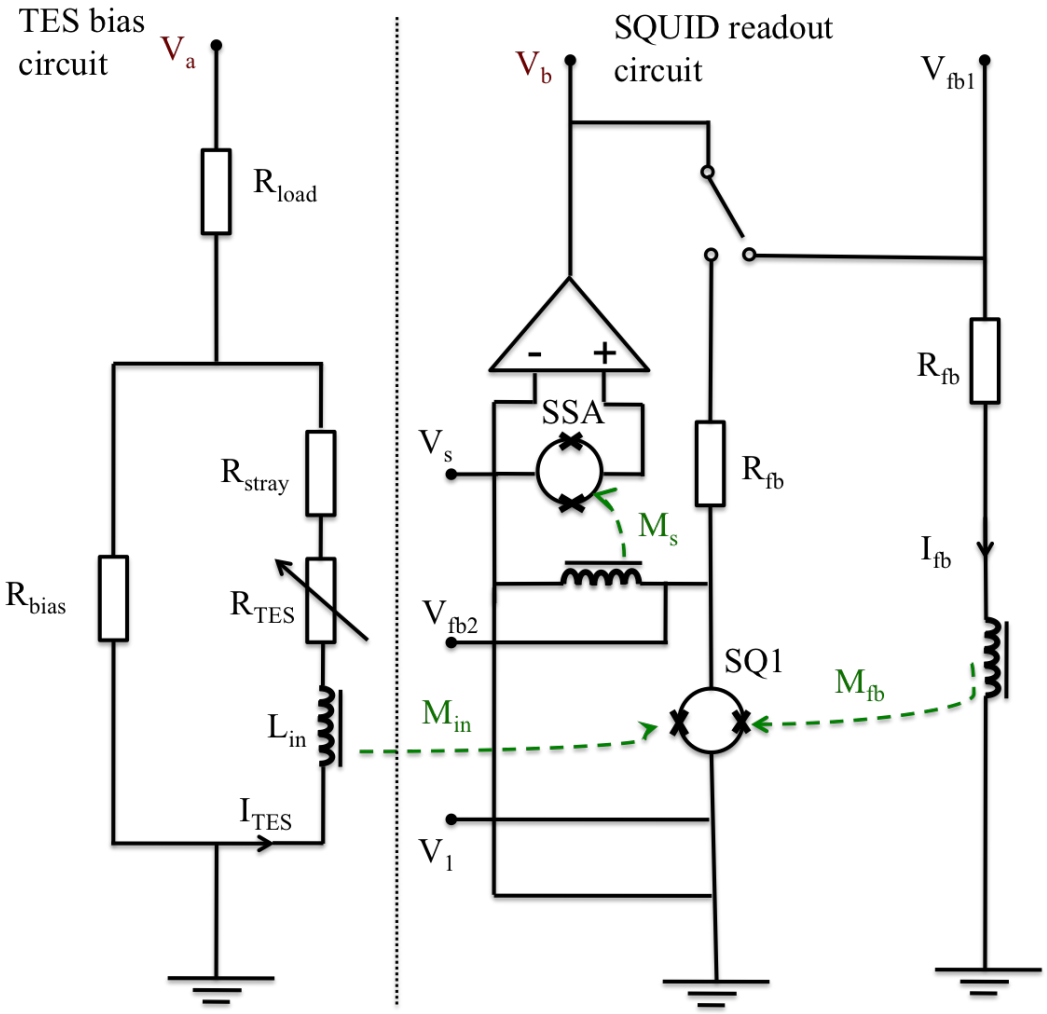

Fig. 5.5 Simplified schematic diagram of the TES circuit (left) and SQUID readout system (right).

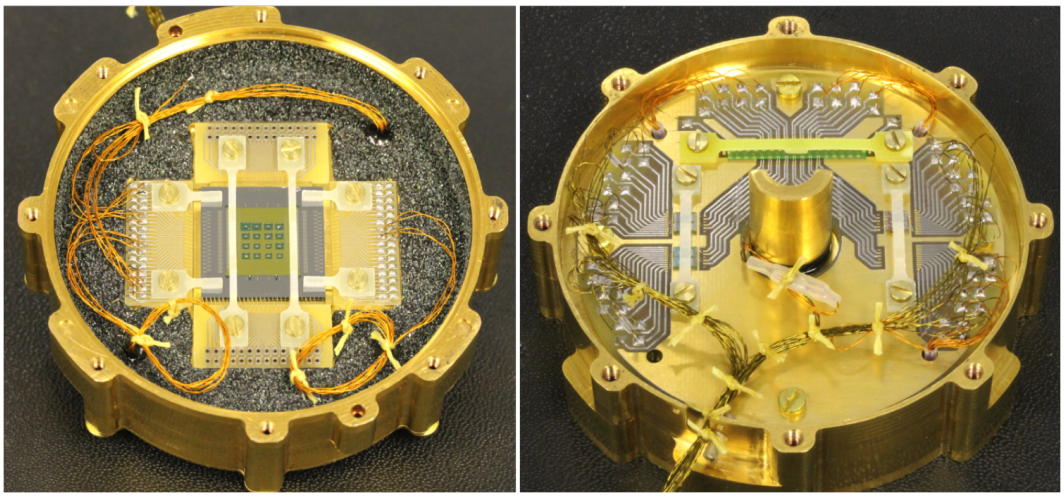

Fig. 5.6 Images of the TES (left) and the SQUID readout (right) mounted in the device housing blocks.

I_{TES}, generates a flux, in the SQUID input coil, which has inductance, L_{in}. To measure I_{TES}, the input flux associated with L_{in}, is coupled into a first stage SQUID, SQ1. Further amplification is achieved by using a SQUID Series Array (SSA), which consist of an array of SQUIDs connected in series. The overall SQUID circuit converts I_{TES} to voltage, which can be measured by V_b. The SQUID readout circuit is shown on the right side of Figure 5.5. The voltages V_a and V_b were recorded by using analogue digital converters controlled by a LabView program.

Both SQ1 and SSA need to be biased properly to ensure good sensitivity. SQ1 and SSA can be biased by adjusting the voltages labelled as V_{I} and V_{s}, respectively. There are two feedback circuits for SQ1 and SSA with their own inductance coils, as shown in Figure 5.5. Both of them share the same feedback resistance, R_{fb}. The feedback is needed needed for linearising V_b. When V_b is fed back using the coils, we say that the SQUID forms a flux-locked loop. Only one SQUID can be connected in the feedback circuit each time, but only the feedback to SQ1 is needed to measure I_{TES}.

There are three coils in total, the mutual inductances of the coils are M_{in}, M_{fb}, and M_{s}, which are for coupling SQ1 to I_{TES}, SQ1 feedback and SSA feedback, respectively. Adjusting voltages V_{fb1} and V_{fb2} can be used to adjust the flux in the two feedback coils. This is important as the feedback can become unstable and affect the signal I_{TES} if the bias fluxes are not set properly.

The TESs and SQUIDs were fabricated on separate chips, but they were held in the same device housing block. The readout was positioned in a cavity behind the detectors to avoid infrared radiation from the bias resistor heating the TESs. The TES bias circuit and SQUID

Fig. 5.7 Image of the L-Band chip, the numbering of the measured pixels are shown.

circuit were operated at the same temperature, 90 mK, to achieve low-noise measurements. Figure 5.6 shows images of the housing block used to hold the TES arrays and SQUID readout electronics. The left image shows the chip with an array of 16 TESs, with the bias wires connected to respective pads. The ultra-low-noise TESs are very sensitive to stray light. The surface of the housing block was manufactured with step-like recesses, and blackened with silicon carbide loaded epoxy to reduce light leakage. The right image shows the SQUID readout circuit; the position of the bias chip is at the top of centre, and the three 2-stage low noise SQUIDs can be seen on the left and right of centre [8].

5.2.3 L-Band TESs

The TESs were fabricated as 4×4 arrays. A composite image of the L-Band chip characterised in the optical tests is shown in Figure 5.7. The TESs were fabricated using Mo/Au bilayers with thicknesses 40/150 nm, and together with square β-phased Ta thin-film absorbers. The measured resistance of the filled absorbers was 440 Ω, which closely matches the free-space impedance, $Z_0 = 377\ \Omega$. Both meshed and filled absorbers were presented. The meshed and filled absorbers can absorb light in both polarisation directions. The meshing lowers the heat capacity of the absorber because it has less area, thus leads to a reduction of the response time. Meshed absorbers give high effective resistance, thus films with lower impedance

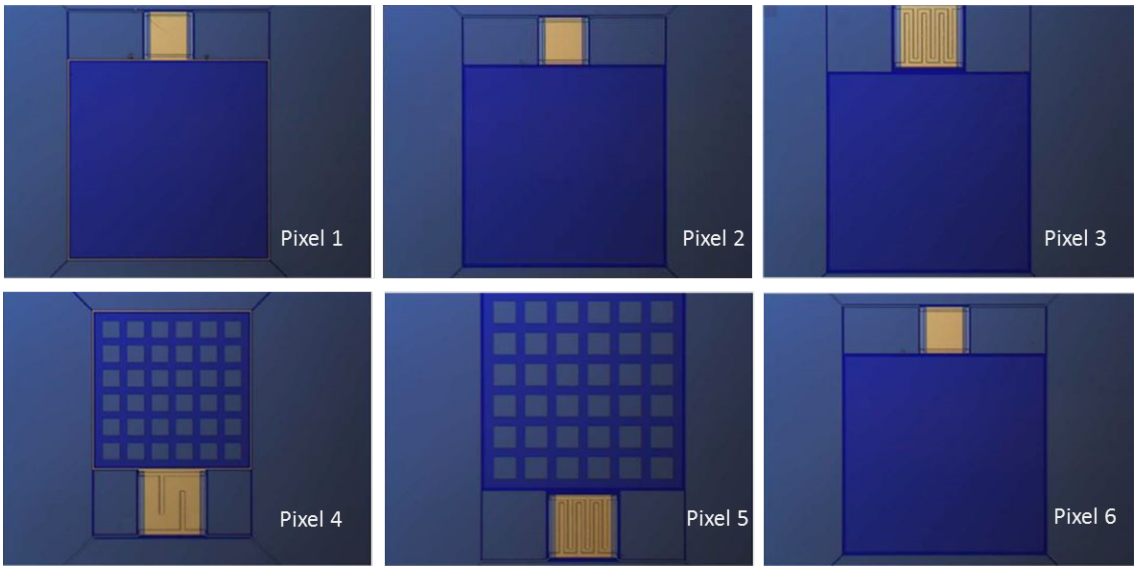

Fig. 5.8 Composite images of the 6 measured pixels.

should be used in order to have the same sheet impedance; but these TESs are fabricated at the same time, so this could not be done.

Optical power measurements were performed on 6 pixels, as labelled in Figure 5.7. The composite images of these 6 pixels are shown in Figure 5.8. The measured L-Band TESs having dimensions 100 μm or 70 μm, with $T_c \approx$110 mK; the absorbers having dimensions 320 μm or 250 μm, with $T_c \approx$870 mK. Pixels 4 and 5 have meshed absorbers, and the reduction in absorption efficiency due to the meshing can be determined from

$$\frac{\eta^{\text{mesh}}}{\eta^{\text{full}}} = \frac{(Z_0 + R_s)^2}{f(Z_0 + R_s/f)^2}, \tag{5.1}$$

where Z_0 is the wave impedance in free space, R_s is the sheet resistance, and f is the filling factor of mesh. The filling factor for pixels 4 and 5 is 0.50. From Eq. (5.1) [13], the reduction due to the meshing was calculated to be 0.822. Au bars were deposited on the bilayer of pixels 3, 4, and 5, which helps faster thermalisation, but it may slow down the thermal response time of the TESs. In doing so, the critical temperature of the bilayer is suppressed due to the proximity effect [48]. Au rims were placed around the absorbers of pixels 1 and 4, which help to thermalise the phonons in the absorber. Some of the key characteristics of the measured pixels are summarised in Table 5.1.

Table 5.1 L-Band pixels characteristics.

Pixel	Absorber dimension (μm)	Absorber type	TES dimension (μm)	Number of bars	Au rim
1	320	Filled	100	0	Yes
2	320	Filled	100	0	No
3	320	Filled	100	6	No
4	250	Meshed	70	2	Yes
5	320	Meshed	100	6	No
6	250	Filled	70	0	No

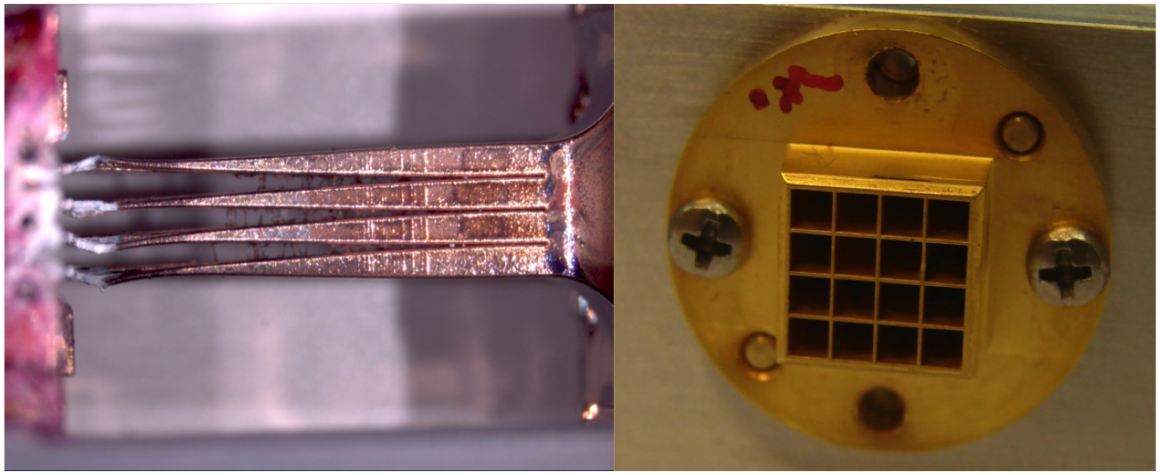

Fig. 5.9 Images of the L-Band horns: the manufacture L-Band mandrel are shown on the left; and the horn entrance apertures are shown on the right.

5.2.4 Pyramidal Horn Arrays

In the device plane, the detectors were engineered as 4×4 arrays. The prototype 4×4 horn designs were based on a pyramidal few-mode horn array that could couple the detectors to the instrument focal plane. The horns were fabricated by electro-forming Cu onto an Al mandrel. This technology was developed by Cardiff University and Thomas Keating Limited, under the direction of Professor Peter Ade. The tapered horns were designed and numerically modelled in The Department of Experimental Physics at the National University of Ireland, in Maynooth. The mandrels were firstly electro-plated with a thin layer of Au, and then electro-formed with Cu. Once the outer forms were successfully machined, the Al would be etched away [31]. Figure 5.9 shows an image of the mandrel after electro-forming Cu (left), and the final manufactured horns (right). More detailed description of the horn arrays will be introduced in Chapter 6.

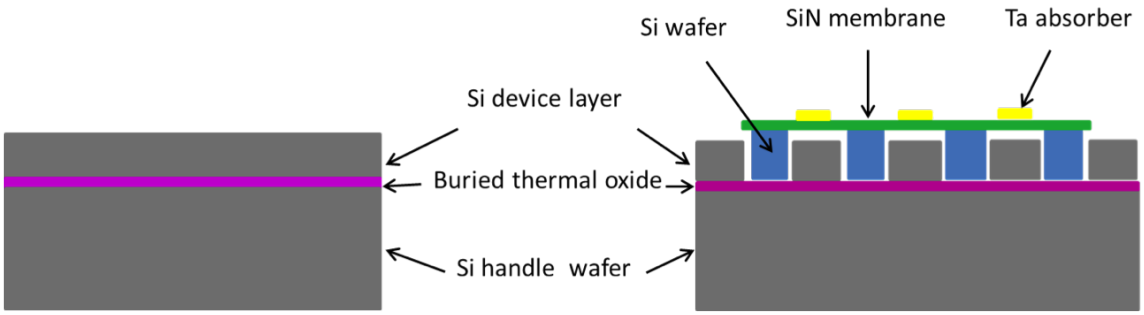

Fig. 5.10 Schematic diagram of TES array sitting on the top of backing plate.

5.2.5 Backing Plates

To increase the efficiency of the far-infrared absorbing films, a plate of conducting backshorts was designed. It improves the absorptivity by reflecting transmitted radiation back to the film. Backing plates were successfully fabricated for each of L-, M- and S-Band. Silicon-on-insulator (SoI) wafers, with different upper Si layer thickness, as shown on the left of Figure 5.10, were used for the fabrication.The wafer diameter was 100 mm, and the SoI device layer thickness used for L-Band was 190 μm, and the main wafer thickness was 500 μm. The backing plates consisted of optically-flat backshorts with high-conductivity sputtered Au. For L-Band, the distance between the Ta absorbers and backshorts was 40 μm. A layer of thermal oxide was buried underneath the silicon device layer to act as an etch stop during DRIE. The SoI device layer was etched to form the pillars and recess of the backshorts. 200 nm of Au was deposited on the pillars, and the detector array chip was precisely positioned within the recess. The diagram on the right of Figure 5.10 shows the TES array sitting in the recess of the backing plate.

Figure 5.11 shows images of an L-Band backing plate before assembly (left) and after assembly (right) with a TES array. To achieve correct positioning of the feed horn with respect to the TES absorbers in both vertical and horizontal directions, the detector array was aligned visually in the correct orientation using a microscope to ensure that the gaps between the edges of the array and the edges of the recess were the same. The absorbers were directly positioned on top of the pillars. Extensive metrology was carried out by the University of Cardiff to ensure accurate alignment.

Figure 5.12 shows the assembled camera and the camera mounted on the 65 mK stage. Image (a) shows the housing block used for holding the SQUIDs and TES arrays; (b) shows an image of the horn plate attached in front of the TESs, and mounted on the cryostat.

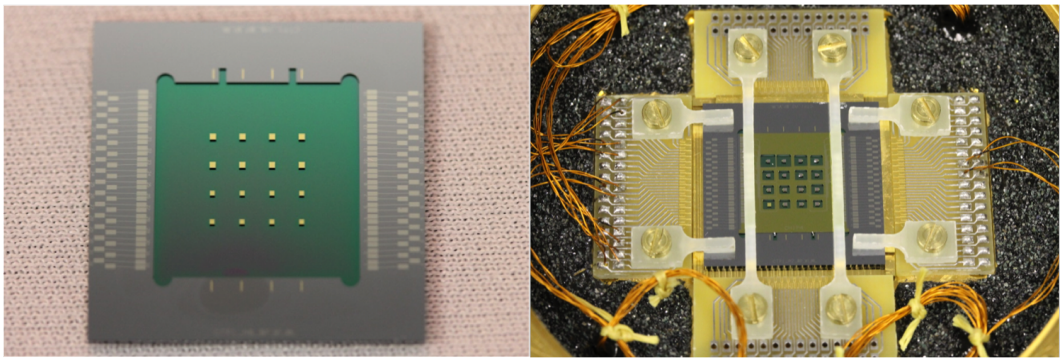

Fig. 5.11 Images of completed backing plate (left) and having the detector array mounted on in the test system.

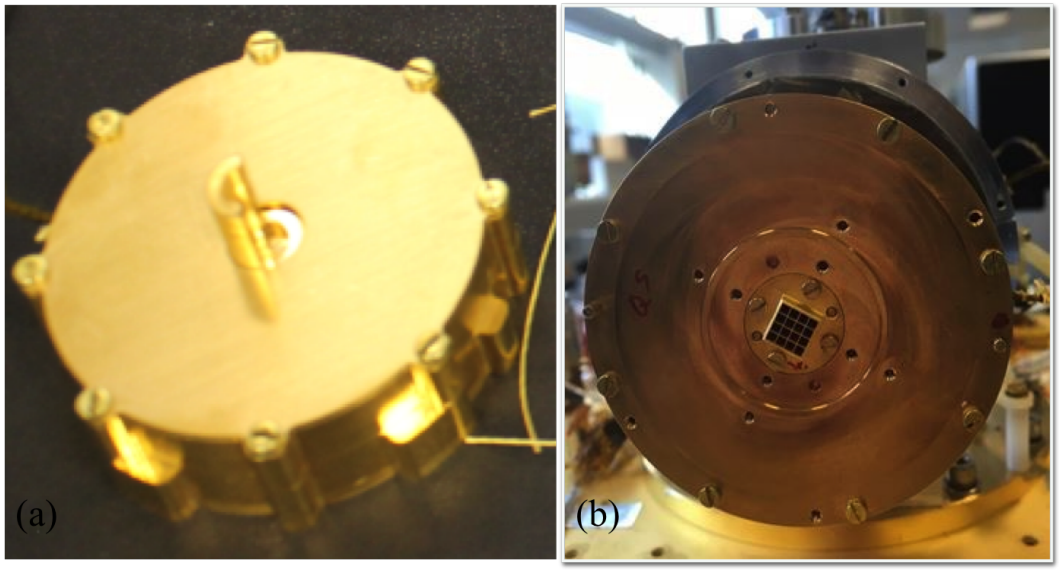

Fig. 5.12 Images of the assembled camera modules mounted on the 65 mK stage of the cryostat: (a) the device housing block contains the SQUIDs and TES arrays; (b) the L-Band horns placed in front of the TES detectors.

5.3 Experimental Methods

The principle of measuring the detected power, P_{meas}, as a function of the temperature of the hot load, T, was to measure the reduction in Joule bias power as a function of blackbody temperature from the TES I-V curves. The I-V curves plot the current through the TES, I_{TES}, against the voltage across the TES, V_{TES}. From the I-V curves, we can derive the Joule power as a function of voltage, P_{Joule}-V_{TES} curves, from relation $P_{\text{Joule}} = I_{\text{TES}}V_{\text{TES}}$. Thus precise measurements of the absorbed power could be achieved using the I-V curves.

A series of optical measurements were performed on the L-Band pixels, with different sized apertures. The TESs were cooled in the ADR giving a base temperature of 65 mK. Two-stage low-noise SQUIDS supplied by PTB were used for readout [9]. A LabVIEW PID program was used for temperature control, which read the temperature of the detector housing and controlled it by the application of current in the ADR magnet. The temperature was regulated at 90 mK, and the temperature stabilisation software provided a stability of 0.2 mK.

To interpret the I-V measurements, we need to know the normal state resistance, R_n, stray resistance, R_{stray}, bias voltage, V_{TES}, and bias current, I_{TES}. The normal state resistance, R_n, and the stray resistance, R_{stray}, varied from one TES to another. The bias voltage, V_{TES}, and current across the TES bilayer, I_{TES} can be calculated from V_a and V_b using

$$V_{\text{TES}} = \frac{R_{\text{bias}}V_a - I_{\text{TES}}(R_{\text{load}}(R_{\text{bias}} + R_{\text{stray}}) + R_{\text{stray}}R_{\text{bias}})}{R_{\text{bias}} + R_{\text{load}}}, \tag{5.2}$$

and

$$I_{\text{TES}} = \frac{V_b}{M_{\text{ratio}}R_{\text{fb}}}. \tag{5.3}$$

The load resistance, R_{load}, and bias resistance, R_{bias}, were 4800 Ω and 1.45 mΩ. The values of the stray resistance, R_{stray}, were measured to be between 1.9 mΩ and 2.3 mΩ. The values of M_{ratio} and R_{fb} in Eq.(5.3) were 7.65 and 24106 Ω.

To achieve I-V measurements at temperature T, the first step was to increase V_a to apply a high voltage, e.g. 10 V, for a very short time, to the TES. In doing so, the TES would be driven into its normal state. Then decrease the voltage to approximately 250 mV. The TES would change from the normal state to the superconducting transition phase as the bias voltage kept decreasing. A LabView program was set to sweep V_a from 250 mV to 0mV, different numbers of steps were used in different parts of the I-V curve: the step of the first 30 data points was -5 mV, which were essentially taken in the normal region; 70 measurements were taken in the transition region, with a voltage step of -2 mV. The I-V and P_{Joule}-V_{TES} curves were designed to update in real time. Meanwhile, the temperature of the TES was

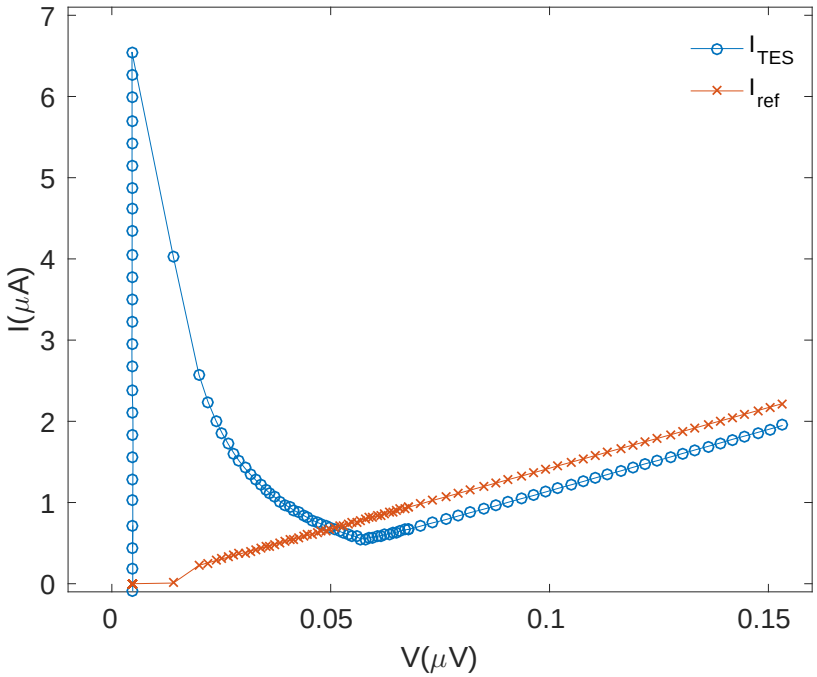

Fig. 5.13 Un-calibrated I-V for pixel 2 measured at the base temperature of the blackbody source, 3.37 K.

recorded for each data point simultaneously. A set of measurements for V_a, V_b and T_{TES} were recorded as raw data. Using Eq.(5.2) and (5.3), the initial I-V and P_{Joule}-V_{TES} curves could be obtained.

An example of a typical uncalibrated I-V curve is shown in Figure 5.13. The blue circles show the measured data. The circles in red form a straight line, which shows the reference current, I_{ref}, as a function of bias voltage, V_{TES}, which was used to calibrate the normal current regions of the I-V curves. The reference current can be calculated from $I_{\mathrm{ref}} = V_{\mathrm{TES}}/R_n$. The gradient of the straight line corresponds to the normal resistance, R_n, which is also the gradient of the normal state region of the I-V curve of the TES. After that, the transition region of the TES I-V curve is traced. As the bias voltage is decreased further, the TES becomes superconducting, where all of the current in the bias circuit goes through the TES branch.

The corresponding P_{Joule}-V_{TES} curve is shown in Figure 5.14. The blue squares show the measured Joule power, the yellow stars represent the saturation power, and the red circles shows the normal state dissipation. An Excel spreadsheet was used to produce the I-V and P_{Joule}-V_{TES} curves based on Eq.(5.2) and (5.3). Four parameters needed to be adjusted: (i) the normal resistance, R_n; (ii) the offset in V_a; (iii) the offset in V_b; and (iv) the stray resistance,

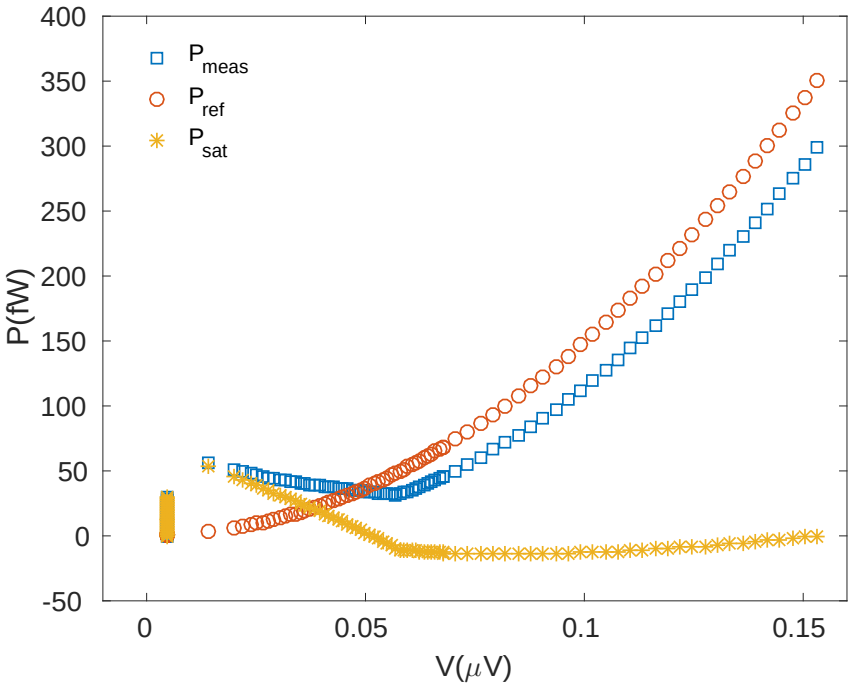

Fig. 5.14 Un-calibrated P-V for pixel 2 measured at the base temperature of the blackbody source, 3.37 K.

R_{stray}. The normal resistance, R_n, for pixel 2 was 78 mΩ, which defined the gradient of the normal region of the TES I-V curve. Changing the offsets of V_a and V_b could move the I-V curve along x-axis and y-axis respectively. In this case, the y-axis offset ΔV_a and x-axis offset ΔV_b were -0.405 V and -0.0148V. The superconducting region was adjusted to be parallel to the y-axis by setting the stray resistance R_{stray} to correct value. In the case of Figure 5.13, R_{stray}=1.95 mΩ.

The calibrated I-V and P_{Joule}-V_{TES} curves are shown in Figure 5.15 and 5.16. From Figure 5.15, it can be seen that the reference current perfectly fits the normal section of the I-V curve, and the bias current drops vertically when the bias voltage hits zero. The measured Joule dissipation power is shown as blue squares in Figure 5.16. It is pleasing that the power plateau is very flat, because it indicates the calibration has been performed correctly. By measuring the average dissipated power over the transition region, this power can be plotted as a function of the blackbody source temperature.

The saturation power was measured at the base temperature of the blackbody load, T_B=3.3 K, which is the maximum power that could be dissipated by the TES without driving it normal. As the temperature of the blackbody source changes, the power absorbed by the

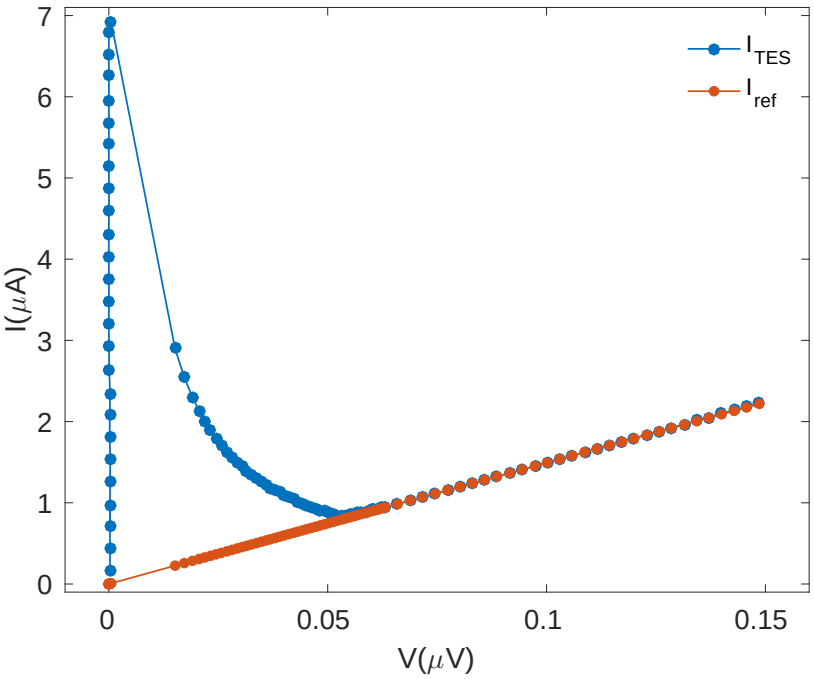

Fig. 5.15 Calibrated I-V for pixel 2 measured at the base temperature of the blackbody source, 3.37 K.

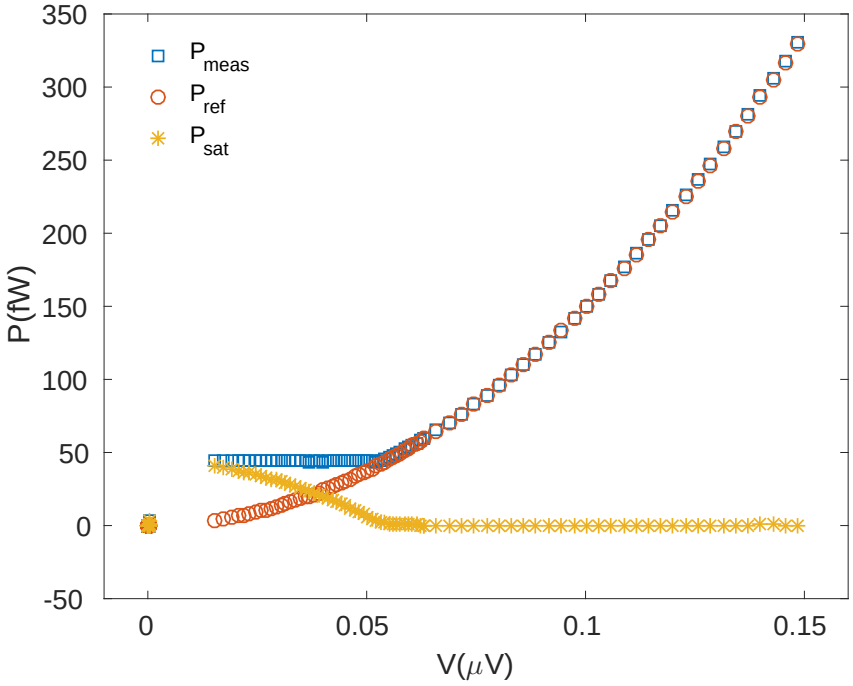

Fig. 5.16 Calibrated P-V for pixel 2 measured at the base temperature of the blackbody source, 3.37 K.

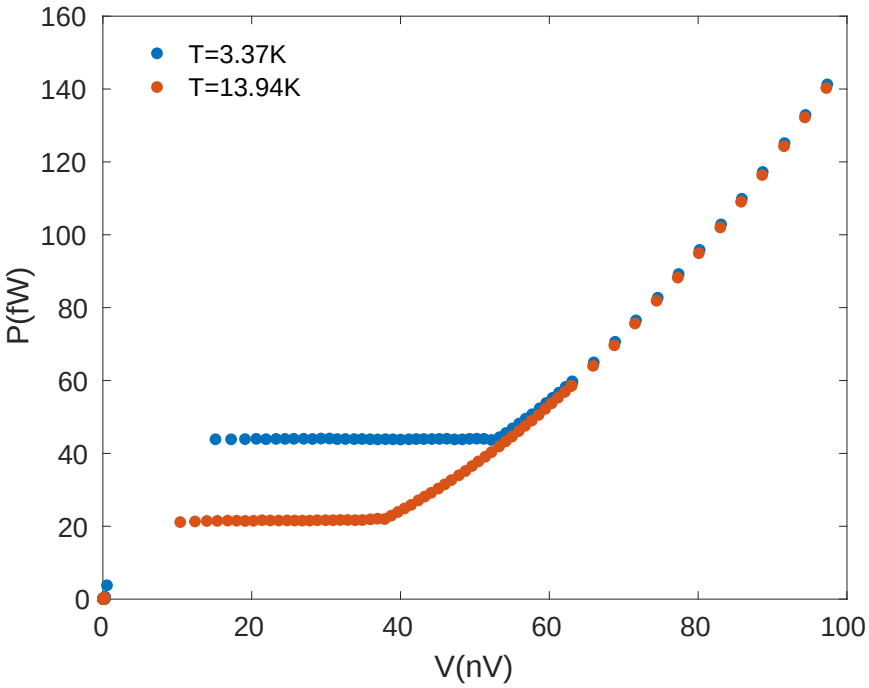

Fig. 5.17 P-V curves at different source temperature, calculated from the I-V curves.

TES, $P_{\mathrm{meas}}(T)$, could be determined from relation

$$P_{\mathrm{meas}}(T) = P_{\mathrm{Joule}}(T_{\mathrm{B}}) - P_{\mathrm{Joule}}(T), \tag{5.4}$$

where $P_{\mathrm{Joule}}(T_{\mathrm{B}})$ is the Joule power dissipated in the plateau region of the TES I-V.

Figure 5.17 shows an example of the Joule power plotted against the TES voltage at two different illuminating temperatures. The plot shows the data of pixel 2 measured with a 10 mm aperture at 3.37 K (base temperature) and 13.94 K. Two extremely flat plateaus can be seen. The Joule power dissipated in the detector was determined by calculating the average value of the power cross the plateau region. The blue circles correspond to measurements taken at the base temperature of the blackbody source. The reduction in Joule power dissipated in the TES at 13.94 K corresponds to the extra absorbed power.

5.4 Experimental Results and Analysis

5.4.1 Power Measurements on Horn-coupled Pixels

My numerical simulations suggest that having an aperture size of 651.5 μm would provide near identical optical performance as that of the telescope itself. For the purpose of making high signal-to-noise ratio measurements, a number of larger sized apertures were chosen. A series of apertures with diameters of 1, 2, 4, and 10 mm were engineered and used for testing.

Figures 5.18 to 5.21 show the detected optical power measured as a function of the blackbody temperature, with four different sized apertures for the L-Band pixels. The experimental results can be compared to the power predicted by the few-mode optical model. The plots on the left of these figures are the power measurements for pixel 2, which is the central pixel with filled absorber, and side length of 320 μm: the red data points shown in the plots are the experimental results, which are the absorbed power calculated from the I-V curves measured at different temperatures of the blackbody hot-load; the blue dashed lines show the expected power determined from the few-mode optical model; the green solid lines are the modelled power scaled by a factor that fits the experimental efficiency. The full few-mode model for the optical test system was explicitly introduced in Chapter 3, which takes into account the actual effective throughput of the optics and detector.

It can be seen that as the aperture size increases, the power measurements saturate at lower temperatures, since more power passes through the detector. The base temperature of the blackbody was 3.3 K, and the saturation temperatures for the measurements of pixel 2 taken with 1 mm, 2 mm and 4 mm apertures were 10.47 K, 9.52 K and 8.49 K, respectively. In the case of using a 10 mm aperture, a neutral-density filter with transmission efficiency of 0.425% was added, so that the measurements could be studied over a wider temperature range: thus the power measurements for the 10 mm aperture was taken from 3.3 K to 16.5 K. The band forming filters and neutral-density filter were developed and kindly made available by Professor Ade at the University of Cardiff.

Measurements were also performed on pixels 1, 3, 4 and 5. The results are shown on the right of Figures 5.18 to 5.21. Each of the plots on the right shows the power measurements taken with the same sized aperture of the five measured pixels. Pixels 2 and 4 were both located at the centre of the array, but their absorber types were different. By comparing the results made on these two pixels, we can see that the experimental efficiencies for pixel 4 are smaller than that of pixel 2 by approximately 20%, which is precisely consistent with the estimated reduction in efficiency due to meshing.

Table 5.2 summarises the scaling factor, found through fitting, that needed to be applied to the measurements in order to make the results consistent with the theoretical few-mode

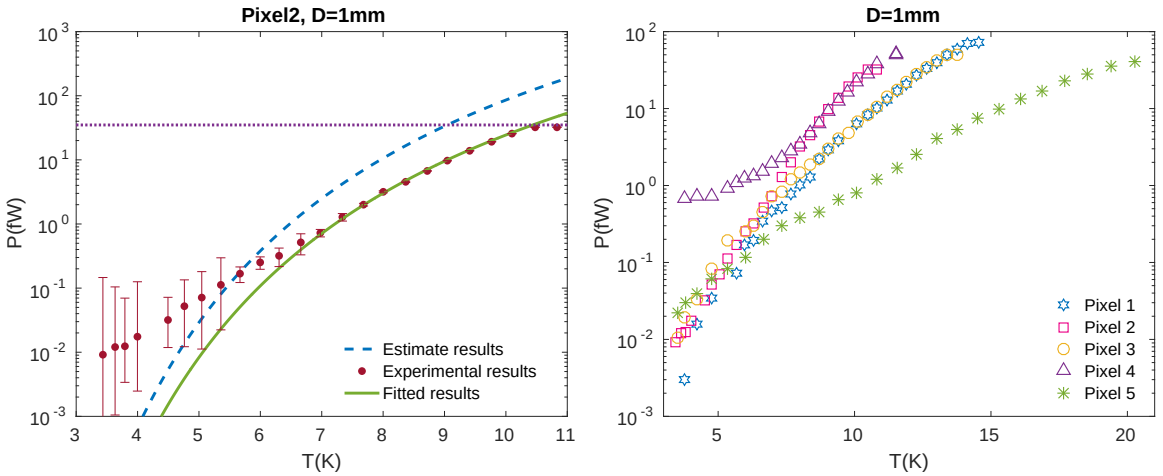

Fig. 5.18 Power loading to the detector as a function of the temperature of the blackbody source with a 1 mm aperture: (a) the red circles are the detected optical power for pixel 2, the purple dotted line indicates the saturation level of the detector, the blue dashed line is the expected power determined from the numerical model, and the green solid line is the numerical simulation scaled by a factor of 0.285; (b) optical measurements for L-Band pixel 1 to 5.

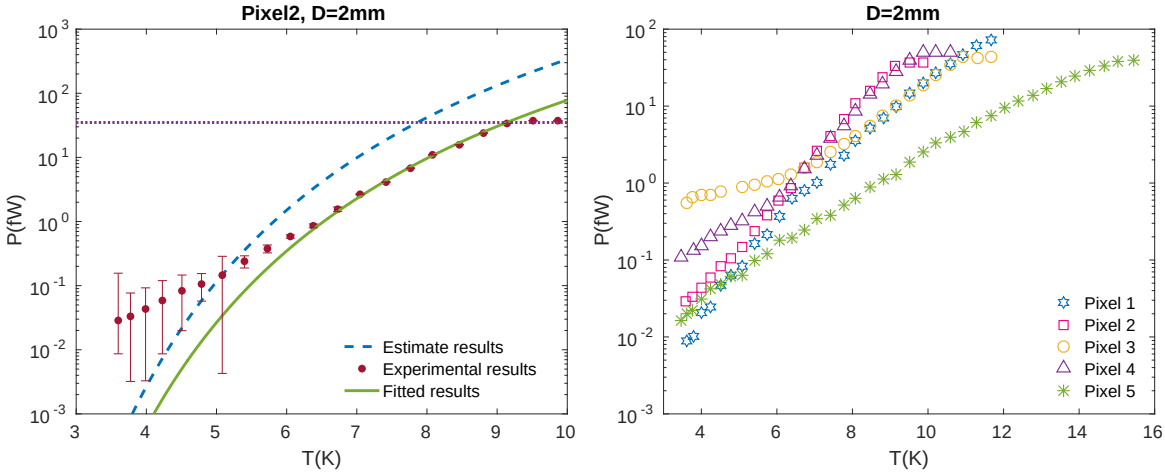

Fig. 5.19 Power loading to the detector as a function of the temperature of the blackbody source with a 2 mm aperture. Left: red circles are the detected optical power for pixel 2; the purple dotted line indicates the saturation level of the detector; the blue dashed line is the expected power determined from the numerical model; and the green solid line is the numerical simulation scaled by a factor of 0.231. Right: optical measurements for L-Band pixel 1 to 5.

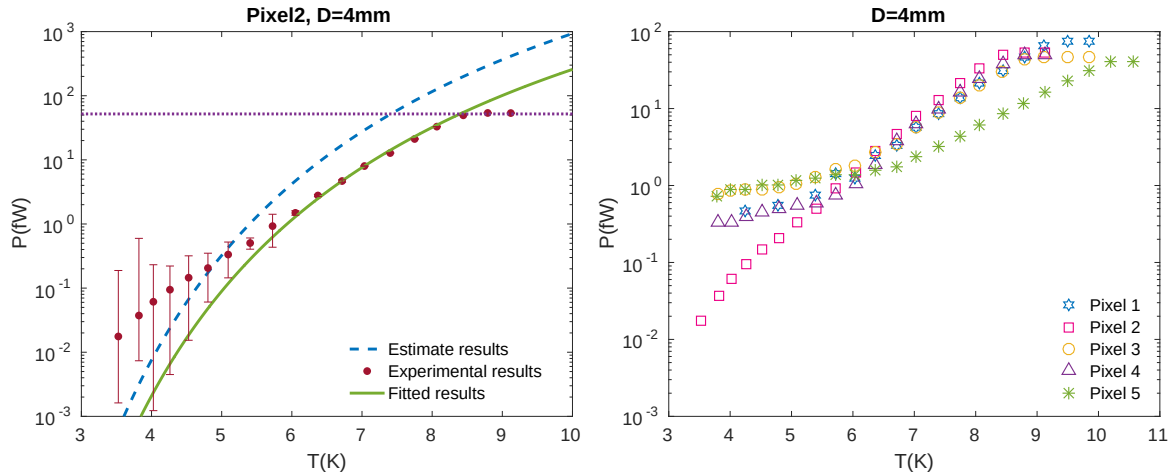

Fig. 5.20 Power loading to the detector as a function of the temperature of the blackbody source with a 4 mm aperture. Left: red circles are the detected optical power for pixel 2; the purple dotted line indicates the saturation level of the detector; the blue dashed line is the expected power determined from the numerical model; and the green solid line is the numerical simulation scaled by a factor of 0.276. Right: optical measurements for L-Band pixel 1 to 5.

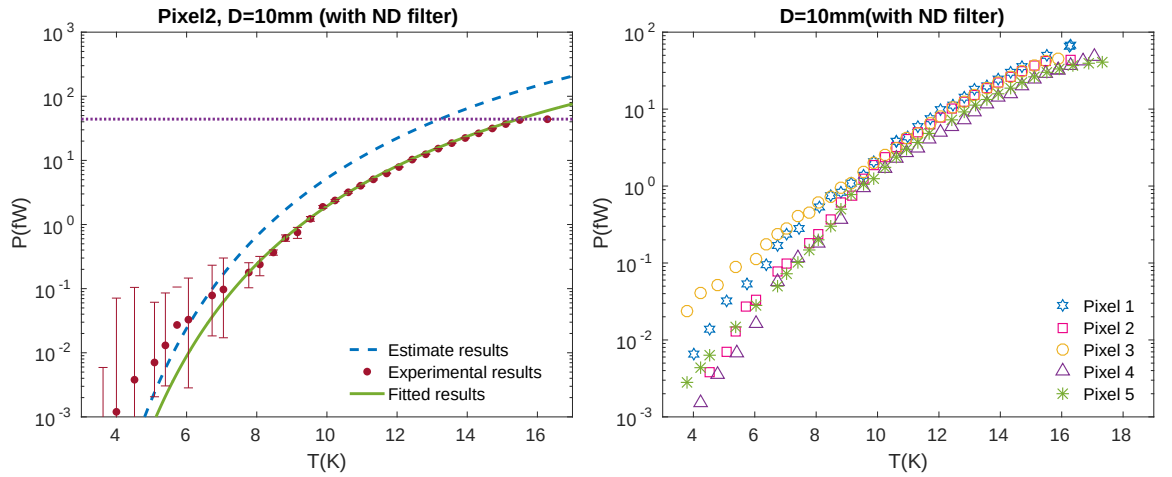

Fig. 5.21 Power loading to the detector as a function of the temperature of the blackbody source with a 10 mm aperture and an ND filter applied. Left: the red circles are the detected optical power for pixel 2; the purple dotted line indicates the saturation level of the detector; the blue dashed line is the expected power determined from the numerical model; and the green solid line is the numerical simulation scaled by a factor of 0.375. Right: optical measurements for L-Band pixel 1 to 5.

Table 5.2 Few-mode power scaling factors for all measured L-Band pixels taken with different sized apertures.

Aperture size, D (mm)	Pixel 1	Pixel 2	Pixel 3	Pixel 4 (meshed)	Pixel 5 (meshed)
1	0.067	0.285	0.067	0.241	0.267
2	0.069	0.231	0.066	0.195	0.007
4	0.169	0.276	0.436	0.224	0.112
10	0.425	0.375	0.367	0.324	0.267

model. The pixels which are closer to the centre could detect more power. The meshing of absorber has a pronounced effect on the performance, which reduces the efficiency by approximately 20%.

Figure 5.22 shows the power measurements made on each of the pixels. The data measured with different sized apertures are shown in different colours. The effect of using different apertures can be seen clearly in these plots. As the area of the aperture increases, the detected power levels increase accordingly. The triangular data points shown in purple are the measurements made with a 10 mm aperture, and used a ND filter with transmission of 0.425%.

For pixels 1 to 4, the detected power levels of the 10 mm aperture with ND filter were lower than that of the 1 mm aperture, which is consistent with the numerical models; whereas for pixel 5, which was the pixel located furthest from the centre, the detected power measured with the 10 mm aperture was higher than that of the 1 mm aperture. This indicates that the positions of the pixels could affect the power measurements, particularly when the aperture size was small. I take this to indicate that the aperture is moving down the side of the collimated beam.

5.4.2 Effective Number of Modes

The measured results can be interpreted straightforwardly in terms of effective number of detected modes. To determine the effective number of modes, we need to calculate the optical power for a single mode of a single polarisation:

$$\mathrm{P_{SM}}(T) = \int_{\nu_{\min}}^{\nu_{\max}} \eta^{\mathrm{filters}}(\nu) \frac{h\nu}{\exp(\frac{h\nu}{k_b T}) - 1} \mathrm{d}\nu, \tag{5.5}$$

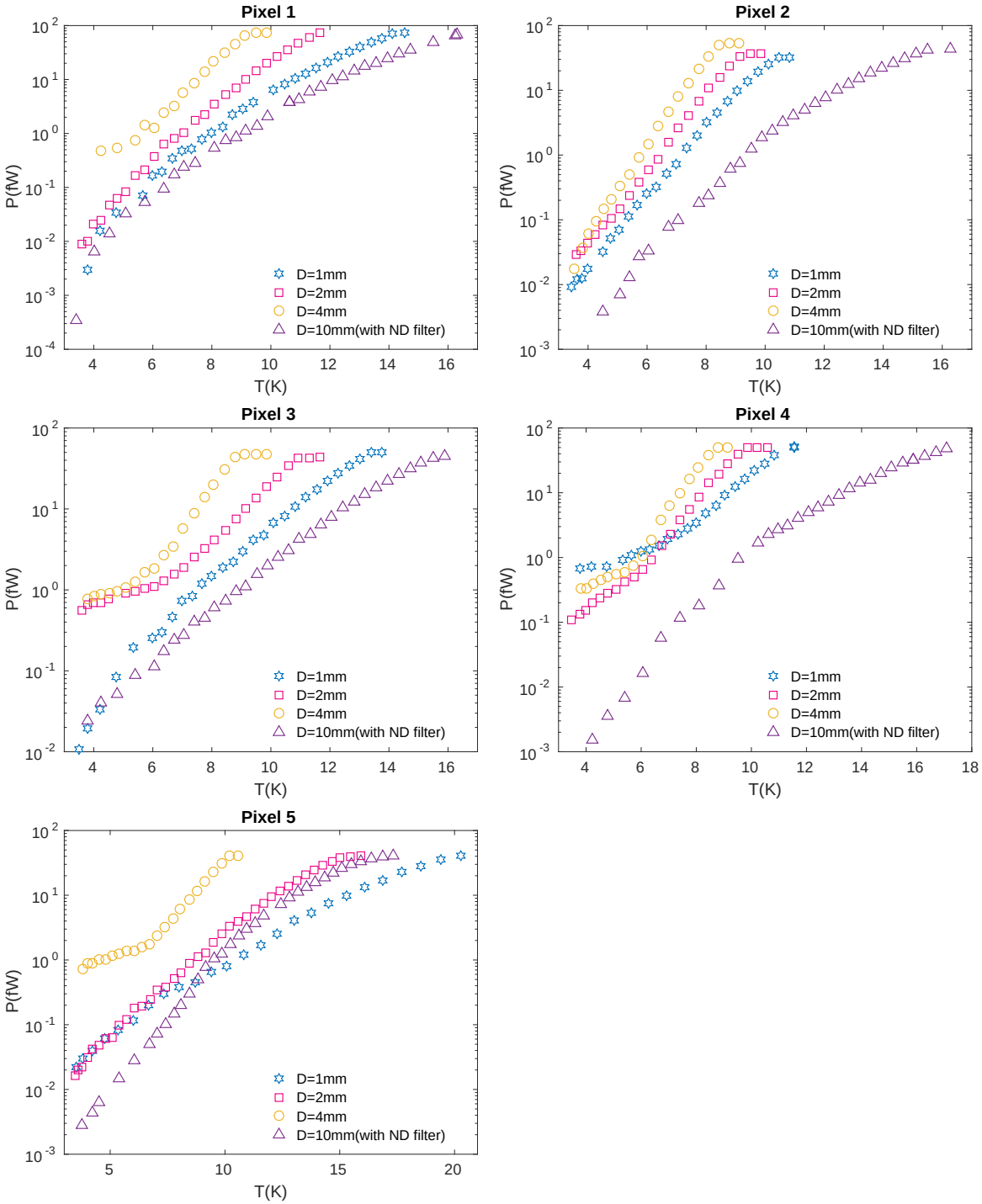

Fig. 5.22 Detected power measured with different sized apertures on the L-Band pixels.

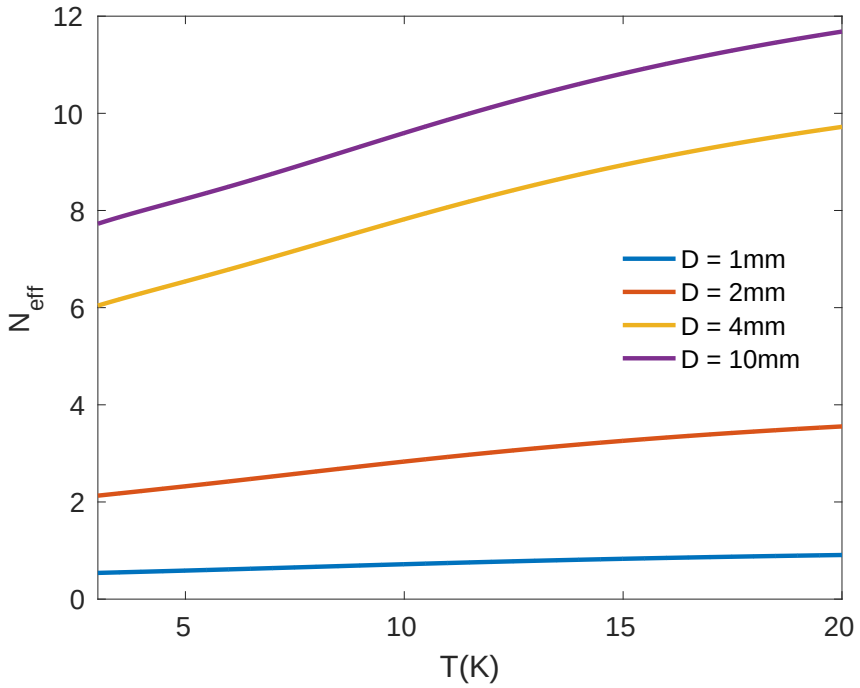

Fig. 5.23 Expected effective number of modes of pixel 2 for different sized apertures as a function of the blackbody temperature.

where $\eta^{\text{filters}}(\nu)$ represents the filter responses. Then the effective number of modes can be expressed as a function of the source temperature as

$$\mathrm{N}_{\text{eff}}(T) = \frac{\mathrm{P}_{\text{FM}}(T)}{\mathrm{P}_{\text{SM}}(T)}, \tag{5.6}$$

where P_{FM} corresponds to the power calculated from the few-mode model.

Figure. 5.23 shows the modelled effective number of modes of pixel 2 for different sized apertures as a function of the temperature of the blackbody hot-load. The model shows that a larger number of effective number of modes is detected. The effective number of modes also increases as increasing source temperature. This increase is more notable when the aperture is large: for the 10 mm aperture, in the temperature range of 3.3 K to 20 K, the number of modes varies between 7.9 to 11.8.

In Figures 5.24-5.27, the modelled and measured results of the detected power are plotted as a function of the power in a single mode in a single polarisation. The results are presented both in logarithmically (left) and linearly (right). The dashed blue lines correspond to the power levels calculated from the full few-mode model; the red dashed lines correspond to

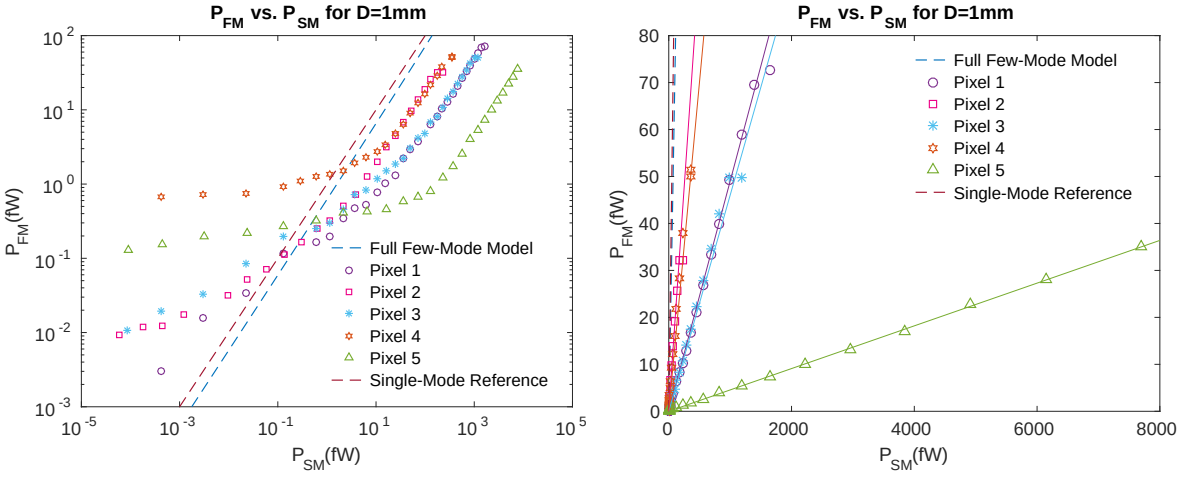

Fig. 5.24 Calculations of effective number of modes for L-Band measurements taken with a 1 mm aperture in logarithmic (left) and linear (right) scale. Blue and red dashed lines are the numerical calculation determined from the few-mode optical model and the perfect single-mode detector model, respectively. Different sets of data points show the power measured for the different pixels against the single mode power, the straight lines are the least square linear fitting to the data sets. Gradients of the straight lines correspond to the effective number of modes.

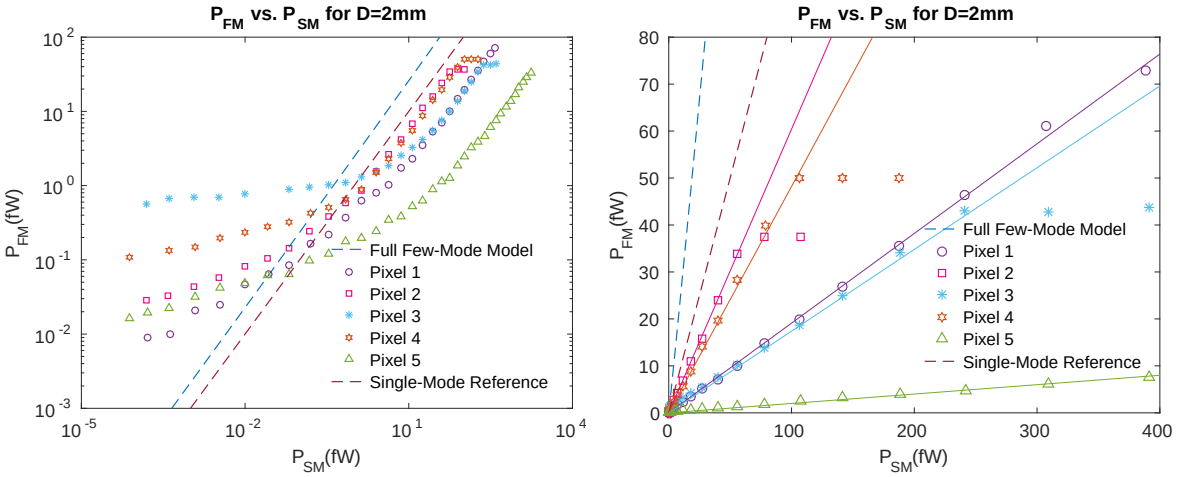

Fig. 5.25 Calculations of effective number of modes for L-Band measurements taken with a 2 mm aperture in logarithmic (left) and linear (right) scale. Blue and red dashed lines are the numerical calculation determined from the few-mode optical model and the perfect single-mode detector model, respectively. Different sets of data points show the power measured for the different pixels against the single mode power, the straight lines are the least square linear fitting to the data sets. Gradients of the straight lines correspond to the effective number of modes.

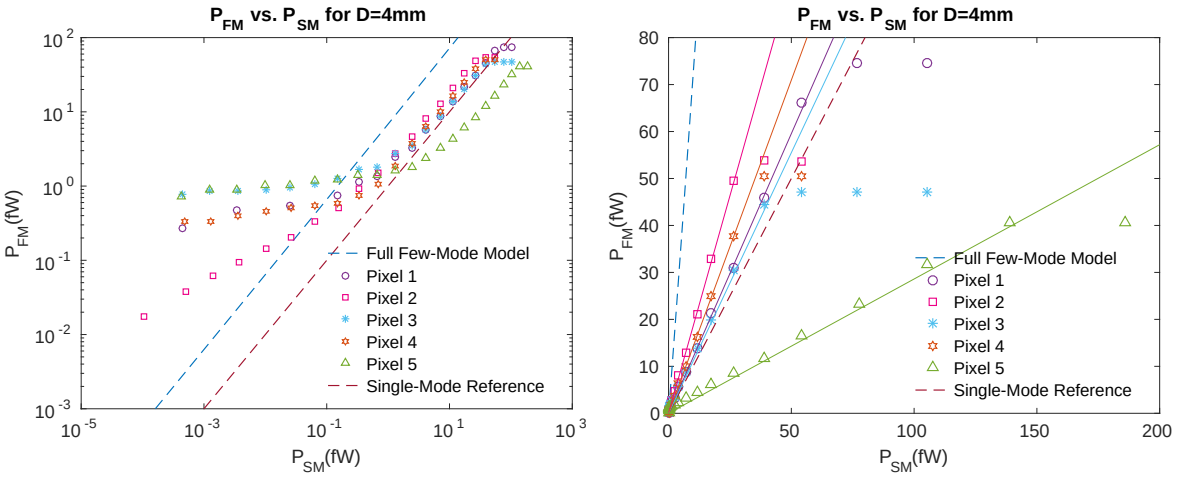

Fig. 5.26 Calculations of effective number of modes for L-Band measurements taken with a 4 mm aperture in logarithmic (left) and linear (right) scale. Blue and red dashed lines are the numerical calculation determined from the few-mode optical model and the perfect single-mode detector model, respectively. Different sets of data points show the power measured for the different pixels against the single mode power, the straight lines are the least square linear fitting to the data sets. Gradients of the straight lines correspond to the effective number of modes.

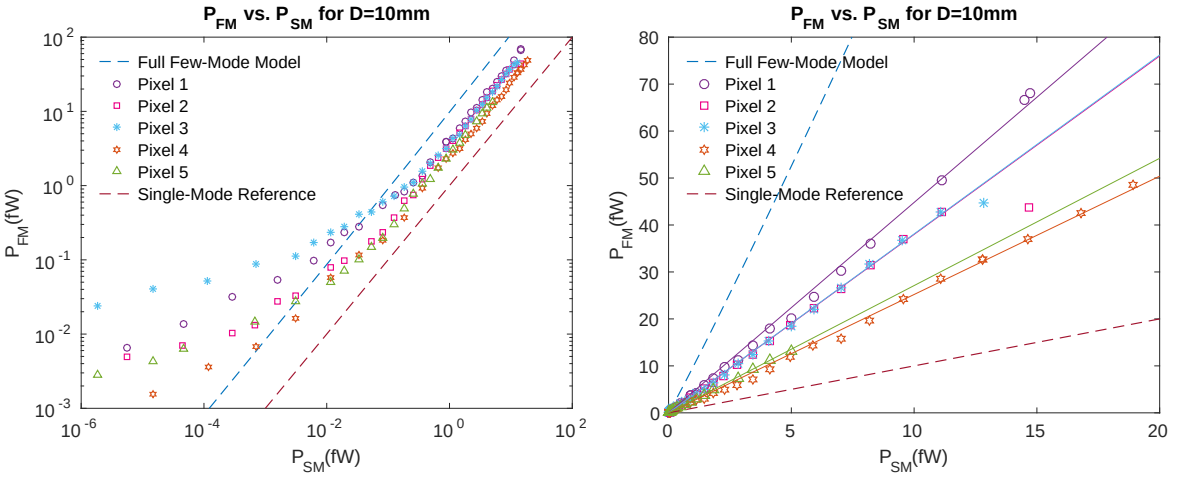

Fig. 5.27 Calculations of effective number of modes for L-Band measurements taken with a 10 mm aperture in logarithmic (left) and linear (right) scale. Blue and red dashed lines are the numerical calculation determined from the few-mode optical model and the perfect single-mode detector model, respectively. Different sets of data points show the power measured for the different pixels against the single mode power, the straight lines are the least square linear fitting to the data sets. Gradients of the straight lines correspond to the effective number of modes.

optical behaviour of a perfect single mode detector; the different sets of data points shown in the figures are the powers measured from the 5 pixels.

To calculate the effective number of modes, I found the gradients of the lines using least square fits to the measured results. Only high power data points were used to avoid the regions where the effects of straylight are seen. The fits to the data are shown in the linear scale plots.

The gradients for each set of data correspond to the average effective number of modes of those measurements. The gradient of the red dashed lines is 1, which corresponds to having a single mode detector, and the gradients of the blue dashed lines are listed in the last column of Table 5.3, which are the expected effective number of modes determined from the few-mode model. The measured effective number of modes are summarised in the table.

Table 5.3 Effective number of detected modes of the measurements and the numerical predictions.

N_{eff}	Pixel 1	Pixel 2	Pixel 3	Pixel 4	Pixel 5	Model
N_{eff} (D=1 mm)	0.049	0.190	0.046	0.140	0.0045	0.798
N_{eff} (D=2 mm)	0.191	0.604	0.174	0.482	0.020	2.887
N_{eff} (D=4 mm)	1.191	1.853	1.110	1.039	0.286	7.726
N_{eff} (D=10 mm)	4.62	3.44	3.71	2.58	2.71	11.05

It can be seen in Table 5.3, that the detectors behave in a few-mode optical manner when the size of the aperture becomes larger than 4 mm. For the measurements taken on different pixels but with the same aperture, the effective number of modes detected for the meshed pixels 4 and 5 are smaller than the others pixels, as expected. As stated earlier, all of the pixels were off-axis, whereas the optical model simulates the case of having the pixels on-axis. It is known that the overall optical throughput is approximately given by $A\Omega/\lambda^2$, with A the area of the pixel, and Ω the solid angle. A simple modification can be made by correcting the solid angle for the off-axis pixels. It is known that the solid angle approximates to $\pi\theta^2 \approx \pi(r/L)^2$, with r the radius of the aperture, and L the distance between the aperture to the entrance aperture of the pixels. In this case, L varies for different positioned pixels, and it can be determined geometrically for each pixel. Thus, the change in solid angle can be calculated once the change in distance L is known. Then the overall optical throughputs can re-calculated. The ratios between the modified solid angle, Ω^*, and the initial values of the solid angle, Ω, are listed in Table 5.4.

Multiplying the scaling parameters listed in Table 5.4 to the results in Table 5.3, the modified effective number of modes can be determined. The updated results are tabulated in Table 5.5.

Table 5.4 Scaling factors to correct the solid angles for the off-axis pixels.

	Pixel 1	Pixel 2	Pixel 3	Pixel 4	Pixel 5
Ω^*/Ω	1.055	1.011	1.055	1.011	1.100

Table 5.5 Modified effective number of detected modes by correcting the position offsets of the pixels.

N^*_{eff}	Pixel 1	Pixel 2	Pixel 3	Pixel 4	Pixel 5	Model
N^*_{eff} (D=1 mm)	0.052	0.192	0.049	0.142	0.005	0.798
N^*_{eff} (D=2 mm)	0.202	0.611	0.184	0.487	0.022	2.887
N^*_{eff} (D=4 mm)	1.257	1.875	1.172	1.501	0.315	7.726
N^*_{eff} (D=10mm)	4.876	3.478	3.912	2.812	2.980	11.05

From the data summarised in Table 5.5 we can see that, the efficiencies are not as high as the model estimated, the loss could have occurred due to various reasons. In the next sections, I will consider whether the few-mode horns were the cause of this problem.

5.4.3 Power Measurements with Blanked off Horns

It is notable that the power detected at low temperatures were all higher than predicted. One possibility was that the detectors were being illuminated by straylight from another unknown source. To investigate this problem, a set of dark measurements were performed by entirely blanking off the pixels. If the blackbody hot-load was the only source illuminating the detectors, then no power should be detected.

Physically, this was achieved by replacing the apertures with a blank plate. All other aspects of the experiment were kept the same. The same experimental methods were used, that the power measurements were taken by increasing the temperature of the blackbody source from the base temperature, 3.3 K. Identical measurements were performed on the 5 pixels, and the results are shown in Figure 5.28.

In Figure 5.28 it can be seen the detected power did vary as the temperature of the blackbody source was varied. The power levels measured by pixels 2 to 5 are relatively flat as a function of temperature. A more obvious increase can be seen from measurements taken on pixel 1, the maximum power was 1.37 fW, measured at 10.2 K.

We conclude that it is a source of straylight that is illuminating the detectors. For example, the hot-load could be heating the aperture plate, which then re-radiates. Instead, there is another possibility is the power is leaking from the body of the camera through a route, but does not involve the main optical path. Nevertheless, the power levels taken in the dark environment were significantly smaller than the previous measurements. The straylight

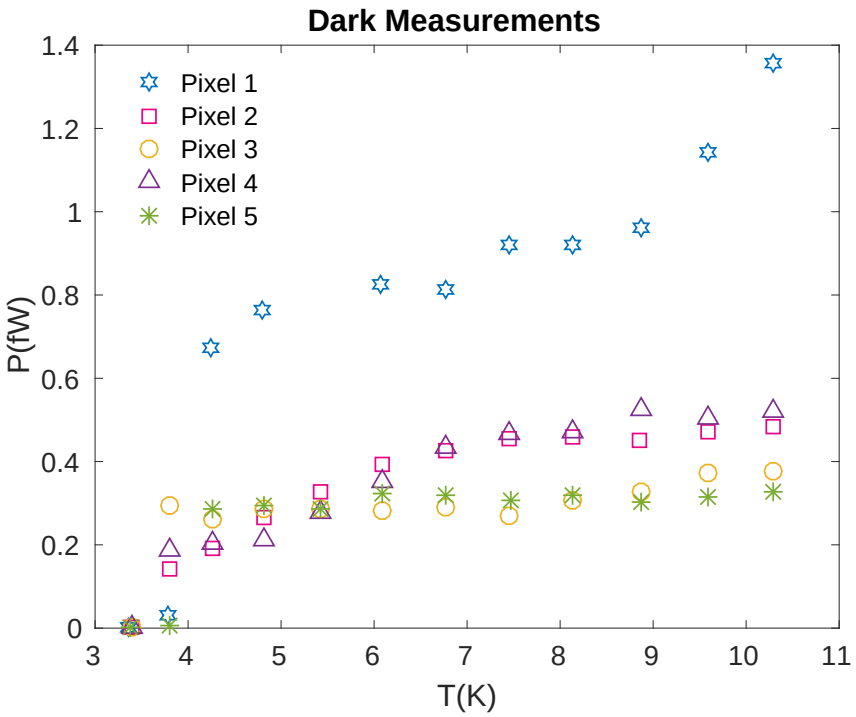

Fig. 5.28 Power measurements taken with the pixels blanked off.

powers were then subtracted from the data with open apertures, and attempted to explain the excess power at low temperatures. The measured results became comparable to the numerical predictions.

5.4.4 Power Measurements on Open Pixels

To investigate how the horns and waveguides affect the optical performance, I also made a set of measurements without the horns, with only the bare pixels placed in the detection plane. The measurements were performed on 6 pixels, as marked in Figure 5.29. The 10 mm aperture was used for these tests.

With the absence of the horns, the radiation emitted from the blackbody source arrived directly at the plane of absorbers after passing through the 10 mm circular aperture. Previously, the distance between the aperture to the entrance aperture of the horns was 10.75 mm, and the length of the L-Band horns is 12.527 mm, which gives the distance between the aperture and the open pixels to be 23.725 mm. The optical modes and the associated throughput, η_n^{opt}, could be determined for the new geometrical arrangement. The modelled results are shown in Figure 5.30.

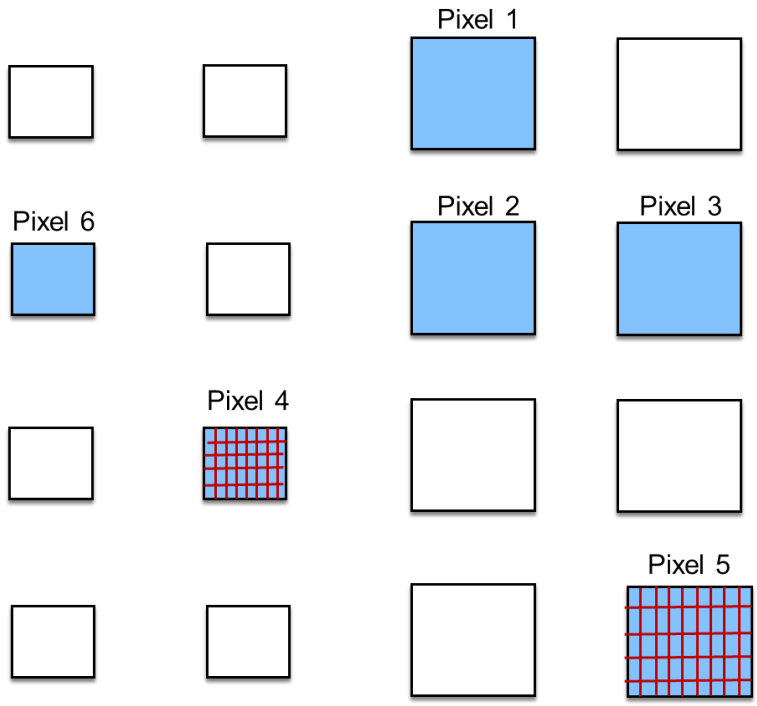

Fig. 5.29 6 measured L-Band bare pixels in the plane of detection used for measurements coloured in blue.

The absorber sizes for the L-Band pixels are 320 μm and 250 μm. The difference in absorber size of the measured pixels should be taken into account when calculating the optical throughputs. The overall optical throughputs determined from the few-mode model were also compared with the geometrical results calculated using $A\Omega/\lambda^2$.

Table 5.6 Total throughput, η_{cal}, and geometrical throughput, η_{geo}, for the maximal, central and minimal wavelengths of the SAFARI L-Band determined for the open pixel geometrical arrangement.

Absorber Size	λ (μm)	η_{cal}	η_{geo}	$\eta_{\text{cal}}/\eta_{\text{geo}}$
320 μm	210	0.331	0.324	1.022
	160	0.570	0.558	1.022
	110	1.206	1.181	1.138
250 μm	210	0.202	0.198	1.020
	160	0.348	0.341	1.021
	110	0.736	0.721	1.021

The comparisons are listed in Table 5.6. The simulated values and the geometrical values of the optical throughputs are essentially the same. The optical throughputs of optical system with the arrangement of the horns absent were calculated over the L-Band. Then the optical

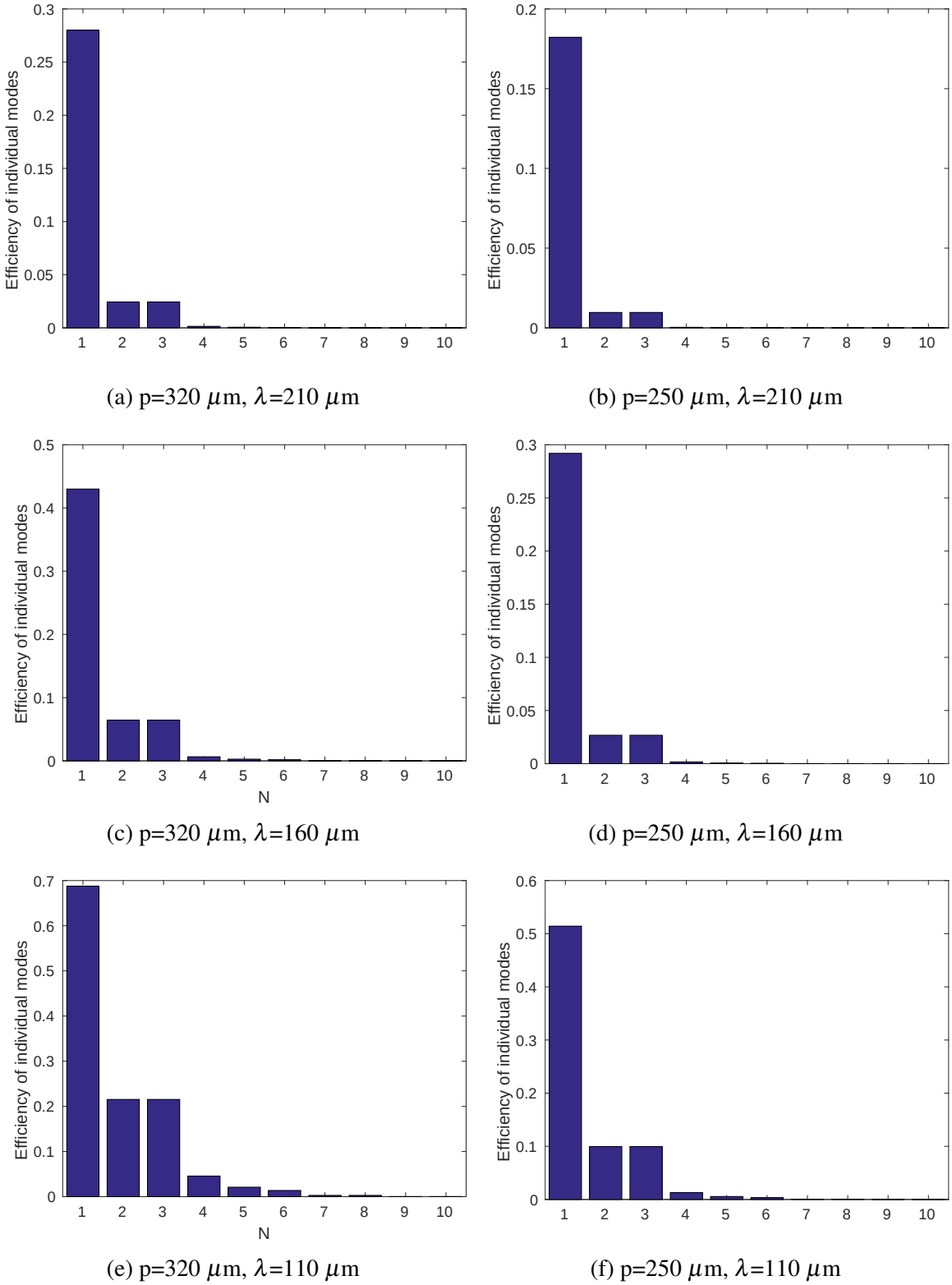

(a) p=320 μm, λ=210 μm

(b) p=250 μm, λ=210 μm

(c) p=320 μm, λ=160 μm

(d) p=250 μm, λ=160 μm

(e) p=320 μm, λ=110 μm

(f) p=250 μm, λ=110 μm

Fig. 5.30 Optical throughputs for the open pixels arrangements at the maximal, central and minimal wavelength of L-Band: p denotes the absorber size, and λ denotes the wavelength.

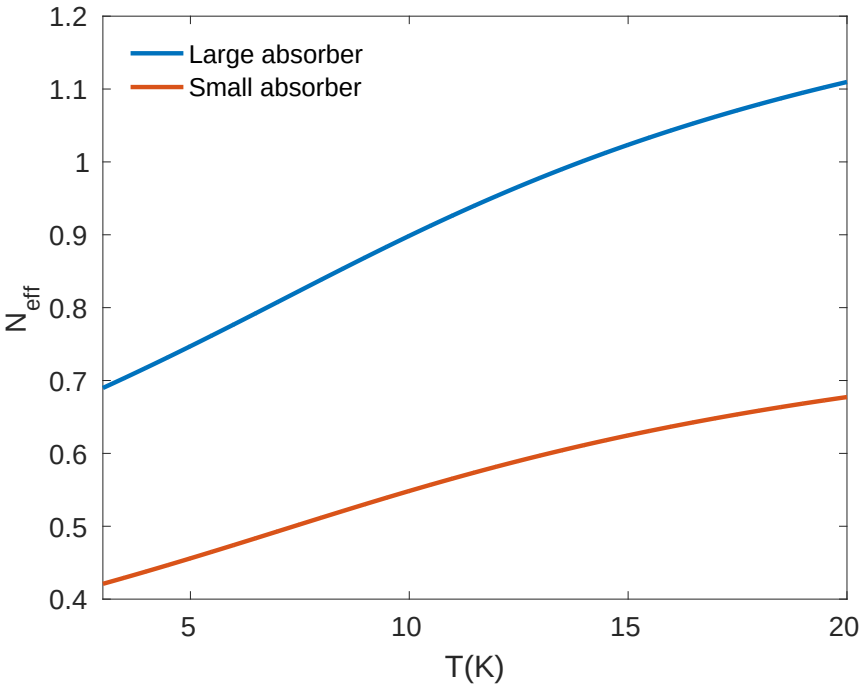

Fig. 5.31 Expected effective number of modes of an 10 mm aperture, without having the horns.

power arrived at the pixels can be determined from Eq.(4.28). Thus the expected effective number of modes can be obtained from Eq.(5.6).

Figure 5.31 shows the calculated effective number of modes for the open pixel arrangement. The plot shows that the effective number of modes should be less than unity for measurements performed using the small absorber, and near unity for measurements performed using the large absorber.

Figure 5.32 shows the optical power measured with a 10 mm aperture for the L-Band open pixels. The plot on the left shows the results measured on pixel 2. Comparing the measured power of pixel 2 with the optical model, I found that a factor of 1.1 was indeed needed. The same procedures of measurement and analysis were also used on the other 5 pixels, and the scaling factors for each set of measurements are listed in the second rows of Table 5.7.

The measured effective number of modes were also determined using the same technique, by plotting the measured power against single mode power, and fitting the data with straight lines. Figure 5.33 shows the modelled and measured results of detected power plotted as a function of the power in a single mode of a single polarisation. The same data are presented using a logarithmic scale on the left, and in linear scale as shown on the right of each figure.

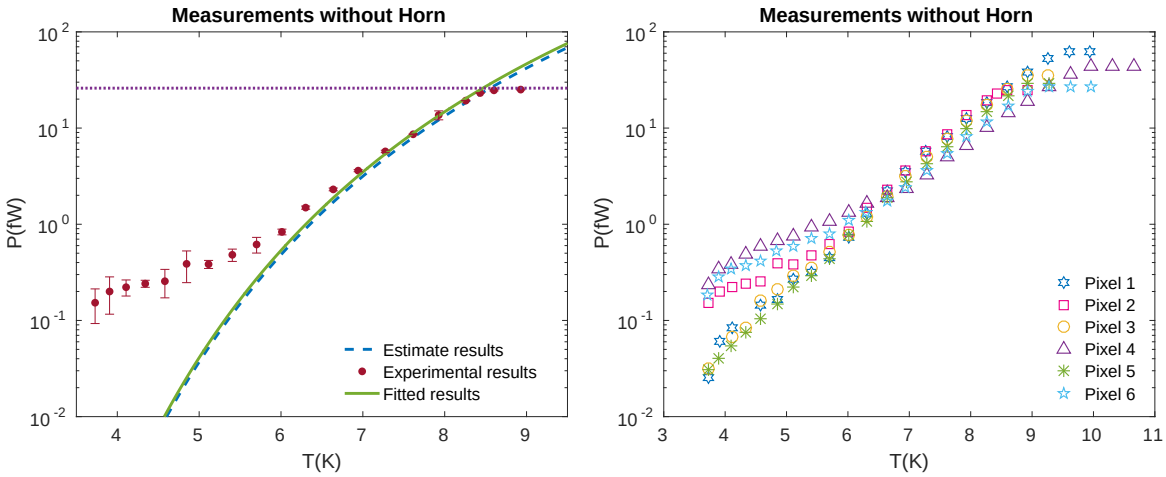

Fig. 5.32 Power measurements of open pixels taken with a 10 mm aperture. Left: the red circles are the detected optical power for pixel 2; the purple dotted line indicates the saturation level of the detector; the blue dashed line is the expected power determined from the numerical model; and the green solid line is the numerical simulation scaled by a factor of 1.1. Right: optical measurements for L-Band pixel 1 to 6.

The effective number of modes were found from the gradients of the linear plots through least-square fits. The results are listed in Table 5.7.

The fact that the calculated powers and the measured powers are in precise agreement when a bare pixel was used, shows that the TESs were absorbing power with essentially 100% efficiency. This in turn shows that the optical backshorts were operating well, despite the fact that the backshorts were optimised at a single frequency. The loss of efficiency when the horns were used can therefore be attributed entirely to the horns. I will discuss this point in a later chapter.

Table 5.7 Few-mode scaling factors and effective number of detected modes of the open pixels measurements and the numerical predictions:

(a) Large absorber pixels;

Large absorber	Pixel 1	Pixel 2	Pixel 3	Pixel 5 (meshed)	Model
Scaling factor	0.98	1.1	0.97	0.82	1
N_{eff}	0.7933	0.8461	0.7927	0.6628	0.8878

(b) Small absorber pixels.

Small absorber	Pixel 4 (meshed)	Pixel 6	Model
Scaling factor	0.8	1.02	1
N_{eff}	0.435	0.5187	0.5419

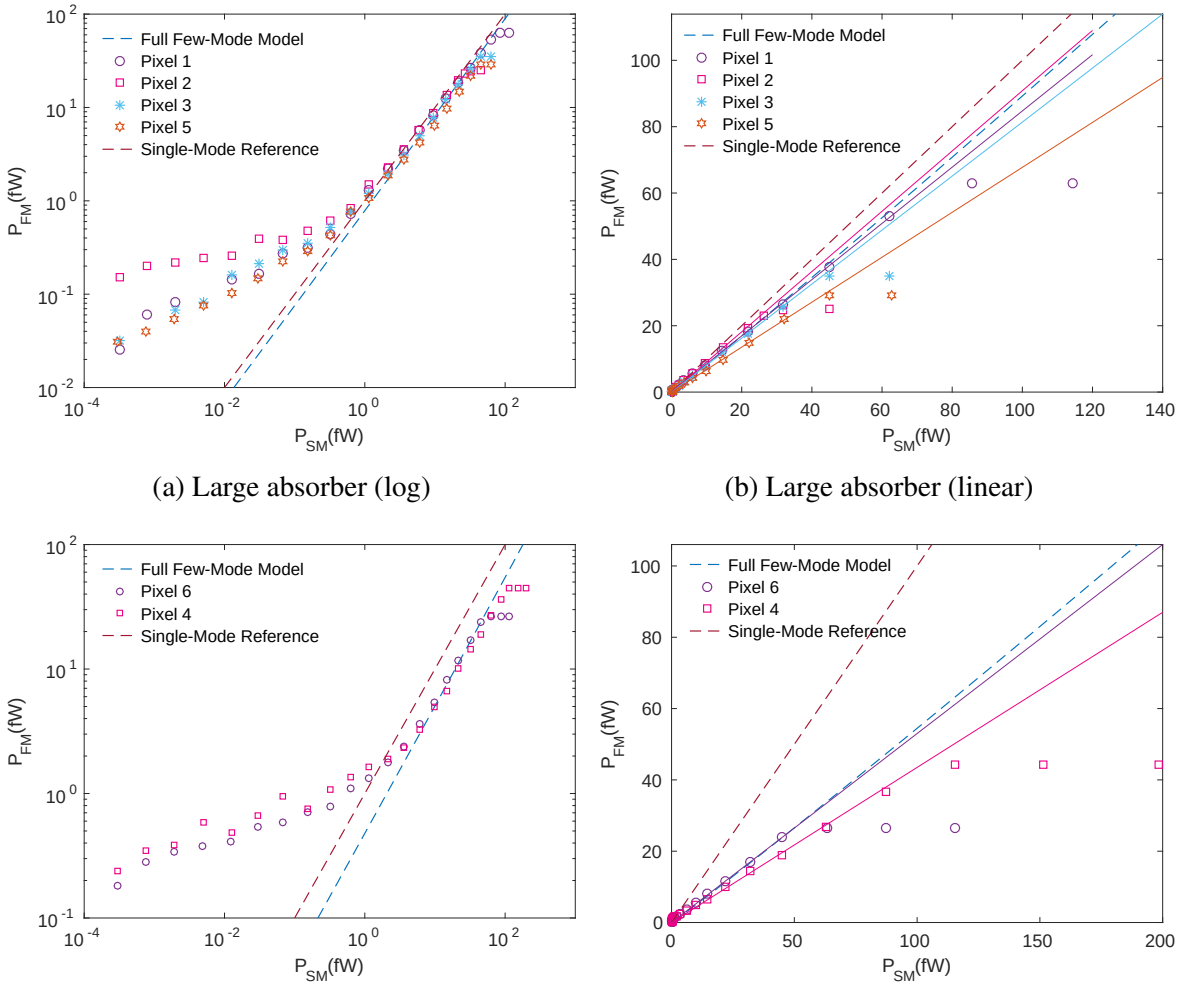

(a) Large absorber (log)

(b) Large absorber (linear)

(c) Small absorber (log)

(d) Small absorber (linear)

Fig. 5.33 Effective number of modes for open pixels measurements: a 10 mm aperture was used, blue and red dashed lines represent the expected results determined from the few-mode optical model and the perfect single-mode detector model, respectively. Different sets of data points show the power measured for the different pixels against the single mode power, the straight lines are the least square linear fitting to the data sets. Gradients of the straight lines correspond to the effective number of modes.

According to Table 5.7, we can see that the measured data agree with the predictions well. We should also consider the offsets in position of the pixels. The scaling factor to correct the solid angle are tabulated in Table 5.8.

Table 5.8 Scaling factors to correct the solid angles for the off-axis pixels.

	Pixel 1	Pixel 2	Pixel 3	Pixel 4	Pixel 5	Pixel 6
N^*_{eff}/N_{eff}	1.011	1.002	1.011	1.002	1.020	1.011

The modified results of effective number of detected modes for the open pixel measurements are listed in Table 5.9. It can be seen that, the effective numbers of modes of the filled

Table 5.9 Modified effective number of detected modes of the open pixels measurements and the numerical predictions:

(a) Large absorber pixels;

Large absorber	Pixel 1	Pixel 2	Pixel 3	Pixel 5 (meshed)	Model
Scaling factor	0.991	1.102	0.981	0.836	1
N_{eff}	0.8020	0.8478	0.8016	0.6761	0.8878

(b) Small absorber pixels.

Small absorber	Pixel 4 (meshed)	Pixel 6	Model
Scaling factor	0.802	1.031	1
N_{eff}	0.436	0.5244	0.5419

absorber pixels are nearly identical to the estimates of the optical model. For the meshed absorbers, the efficiency is lower by about 20%, which is exactly the effect of meshing that we have calculated.

5.5 Conclusion

A series of optical measurements have been performed on 6 L-Band pixels to assess the optical efficiency of the ultra-low-noise TESs using a cryogenic test system. The measurements were taken with different sized apertures, at different temperatures of the blackbody source. The measured results were compared to the full few-mode optical model. The optical performance was described in terms of the effective number of detected modes.

The experimental optical efficiencies for filled absorbers are higher than that of meshed absorbers. The meshing of the absorber reduces the efficiency by approximately 20%, which is consistent with a simple model of the effect of meshing on the sheet resistance.

It has been shown that the full few-mode model provides a good description of the optical behaviour of the test system and detectors. The functional form of the optical power as a function of the blackbody load temperature is well predicted by the model. The detectors behaved in a few-moded manner. It was also seen that the TESs saturated at the optical power they were designed for.

In the case of bare pixels almost perfect behaviour were seen, with 100% few-mode optical efficiency. For the horn-coupled power measurements, the measured effective number of modes were smaller than the numerical estimates. A possible reason for this loss might be due to the conductor losses in the waveguide walls, which will be explicitly discussed in the next chapter.

Chapter 6

Modelling the Multimoded Horns and Waveguides

6.1 Introduction

The results of the L-Band optical measurements indicate that there may be losses in the few-mode horns and waveguides. In this Chapter, I will investigate different potential losses in the few-mode horns and waveguides.

As introduced earlier in Chapter 5, the arrays of pyramidal horns were produced by electro-forming Cu and Au onto an Al sacrificial mandrel. The Al was then etched out to form the horn array. For the purpose of testing the ultra-low-noise TESs, a number of 4×4 horn arrays were manufactured by the Astronomy Instrument Group at Cardiff University [31].

The horns were profiled with a sine-squared form along their length; the side length, a, of each horn is given as a function of, z, as

$$a(z) = a_1 + (a_2 - a_1)\sin^2(\pi z/2L), \tag{6.1}$$

where a_1, a_2 refer to the width of the entrance and exit apertures; and L is the axial length of the horn. L- and S-Band horns were manufactured and used for optical measurements. The wall between the neighbouring pixels was 150 μm. An additional 1 mm section of waveguide was present on both ends of the profile, as can be seen in Figure 6.1. The design drawings of the L- and S-Band mandrels are shown in Figure 6.1. The geometric parameters for the L- and S-Band horn arrays are listed in Table 6.1.

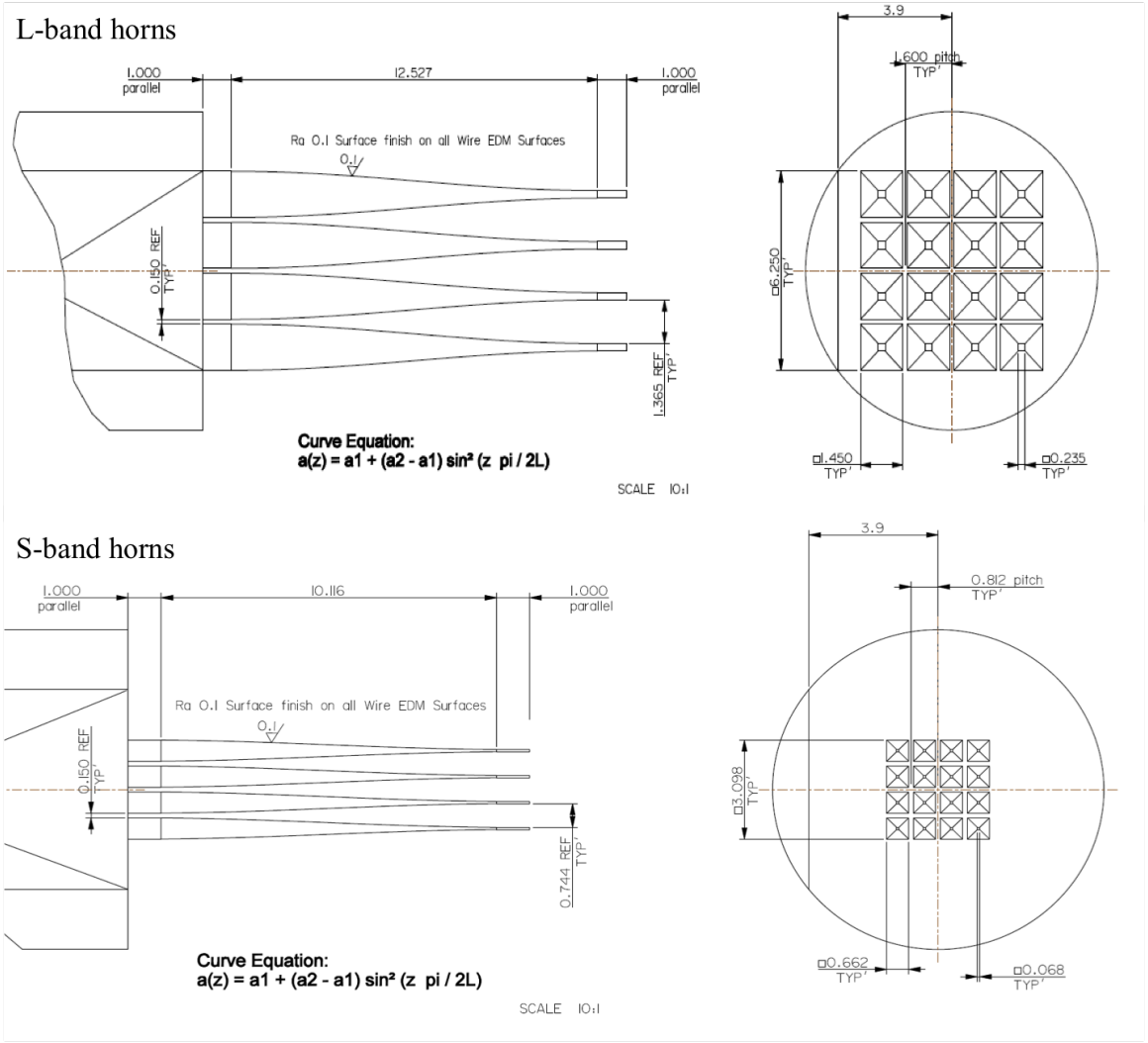

Fig. 6.1 Schematic drawings show the geometry of the L- and S-Band mandrel: the mandrel profiles along z-axis are shown on the left, and the entrance apertures are shown on the right.

Table 6.1 Geometric parameters for L- and S-Band horn arrays.

	L-Band	**S-Band**
a_1 (μm)	1450	662
a_2 (μm)	235	68
L_{pf} (mm)	12.527	10.116
L_{wg} (mm)	1	1

In this chapter, I will investigate the loss in efficiency in the L- and S-Band horns in two respects: (i) the reflection at the exit aperture of the horns due to waveguide impedance mis-match; (ii) the conductor loss in the waveguide wall itself.

6.2 Propagating Modes in the Waveguides

A set of 24 waveguide modes were used in the study, which are the same set as described in Chapter 2. The indices of those waveguide modes are listed in Table 2.4. From the sizes of the square waveguides, we can identify which of the TE and TM modes can propagate by calculating the cut-off frequencies of the modes. Only waves with frequencies above cut-off will propagate. In a square waveguide, the cut-off frequency is given by

$$\nu_c = \frac{c}{2a}(m^2+n^2)^{1/2}, \tag{6.2}$$

where a denotes the side length of the waveguide, c is the speed of light, and m, n are the indices of the waveguide modes [19].

The propagation of these modes in the waveguides can be determined: we know that L-Band covers the frequency range from 1.43 to 2.73 THz, and S-Band covers 5 to 8.82 THz. The waveguide size of L- and S-Band horns are 235 μm and 68 μm. A colour map can be produced to illustrate whether a mode is propagating or evanescent at given frequency.

The colour map shown in Figure 6.2 has the 24 waveguide modes on the y-axis, and the wave frequencies on the x-axes. At frequency ν, each mode is coloured in either blue or yellow depending on whether the frequency is below or above the cut-off frequency, ν_c. The top plot shows the results for L-Band, and the bottom plot shows S-Band. It can be seen that TE_{01}, TE_{10}, TE_{11}, TE_{20}, TE_{02}, TE_{21}, TE_{12}, TM_{11}, TM_{21}, and TM_{12} exist at all available frequencies in both the L- and S-Band horns. As the order of waveguide mode increases, the cut-on frequencies of the modes shift to higher values. TE_{04} and TE_{40} are just cut on at the highest frequency in S-Band, which corresponds to the lowest wavelength in S-Band, 34 μm, which is indeed half of the waveguide size.

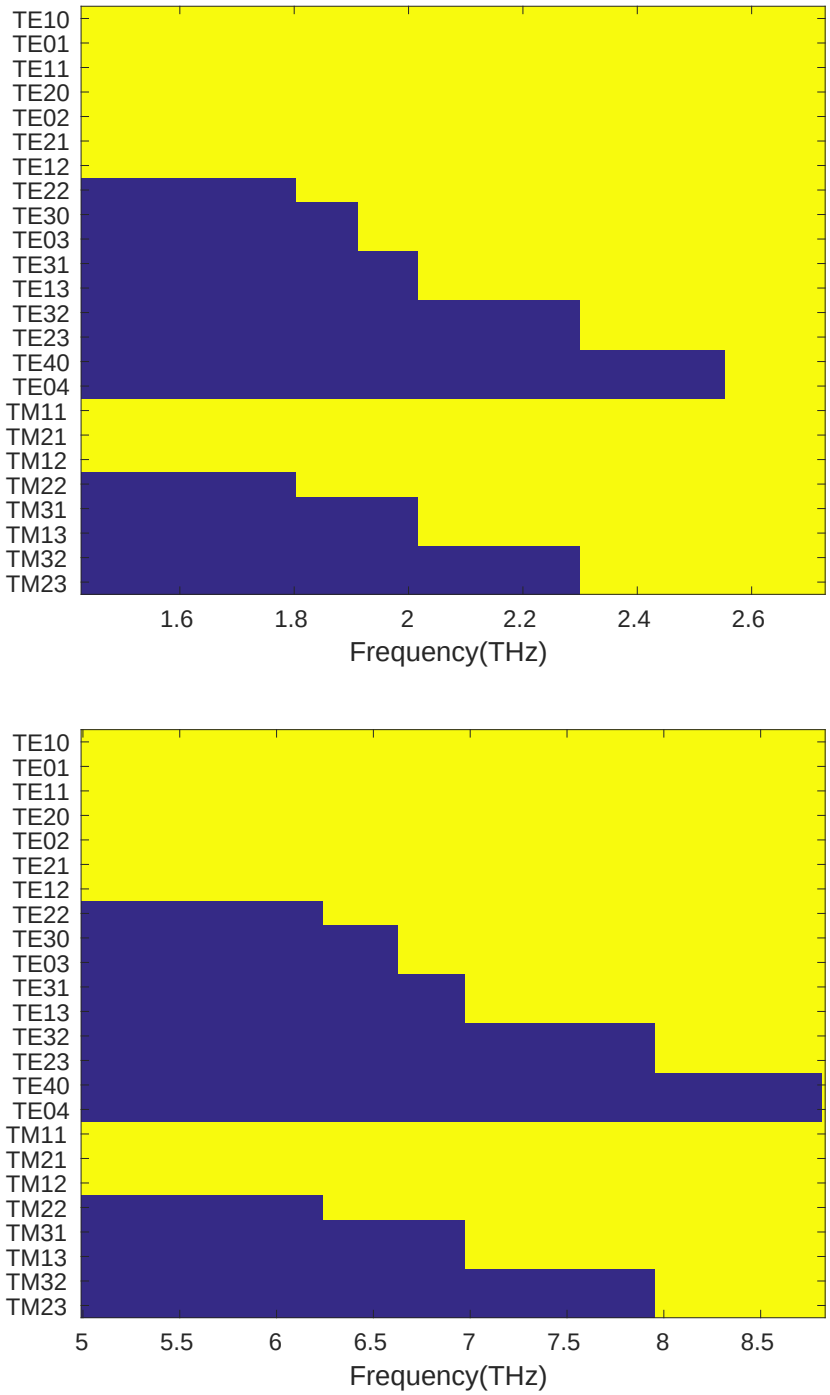

Fig. 6.2 The propagation of the TE and TM modes versus the L- (top) and S-Band (bottom) frequencies: if $\nu < \nu_c$ (evanescent), modes coloured in blue; if $\nu > \nu_c$ (propagating), modes coloured in yellow.

Assume that the transmission efficiencies of the propagating modes are unity, and the non-propagating modes are zero, and then take the sum of the propagating modes; in this way it is possible to determine the number of propagating modes as a function of frequency. The steps shown in Figure 6.3 illustrate the increasing number of excited modes in the waveguides as increasing frequency. It shows that if the cut-on of the modes are perfect, the number of propagating modes will range from 10 to 24.

6.3 Waveguide Impedance Mis-matching

Previously, the absorbers of the TES were assumed to fill the whole waveguides in the optical model. However, they were placed behind the exit apertures of the horns, and followed with flat backshorts, as shown in Figure 6.4. The sizes of the absorbing films were slightly larger than the sizes of the exit aperture. To further improve on the analysis and have a more accurate simulation of the system, an enhanced model is needed.

A mode travels within the waveguide with modal impedance Z_{mn}; at the exit aperture, reflection occurs due to impedance mis-match as the modes are radiated into free space. A transmission factor, $\eta^{Z}_{mn}(\nu)$, can be then determined from relation

$$\eta^{Z}_{mn}(\nu) = 1 - \left| \frac{Z_{mn}(\nu) - Z_0}{Z_{mn}(\nu) + Z_0} \right|^2, \tag{6.3}$$

where Z_0 is the wave impedance of free space, and $Z_{mn}(\nu)$ is the waveguide impedance with $Z^{\mathrm{TE}}_{mn}(\nu) = Z_0[1-(\nu_c/\nu)^2]^{-1/2}$ and $Z^{\mathrm{TM}}_{mn}(\nu) = Z_0[1-(\nu_c/\nu)^2]^{1/2}$ [24].

Figures 6.5 and 6.6 show the impedance of the TE and TM modes across L- and S-Band. For both L- and S-Band, the impedances of TE_{01} and TE_{11} are the well matched to the free space wave impedance, 377 Ω. The higher the order of a mode, the more mis-matched its impedance. For the TM modes, apart from TM_{11}, the impedance is smaller than Z_0. We can expect that the reflection of high order modes will be more significant.

Figures 6.7 and 6.8 show the transmission efficiencies of the waveguide modes as a function of frequency across L- and S-Band, due to the impedance mis-match. As we would expect, the TE_{10} and TE_{01} show almost unit efficiency across the bands. The transmission efficiencies of TE_{11} and TM_{11} are also high, but slightly lower than those of the two lowest order modes. The reflection of higher order modes are more significant. We can also see that the higher order modes slowly cut-on with increasing frequency. TE_{04} and TE_{40} do not propagate in S-Band.

The cumulative efficiencies are plotted in Figure 6.9 by summing the transmission efficiencies together, which corresponds to the effective number of propagating modes even

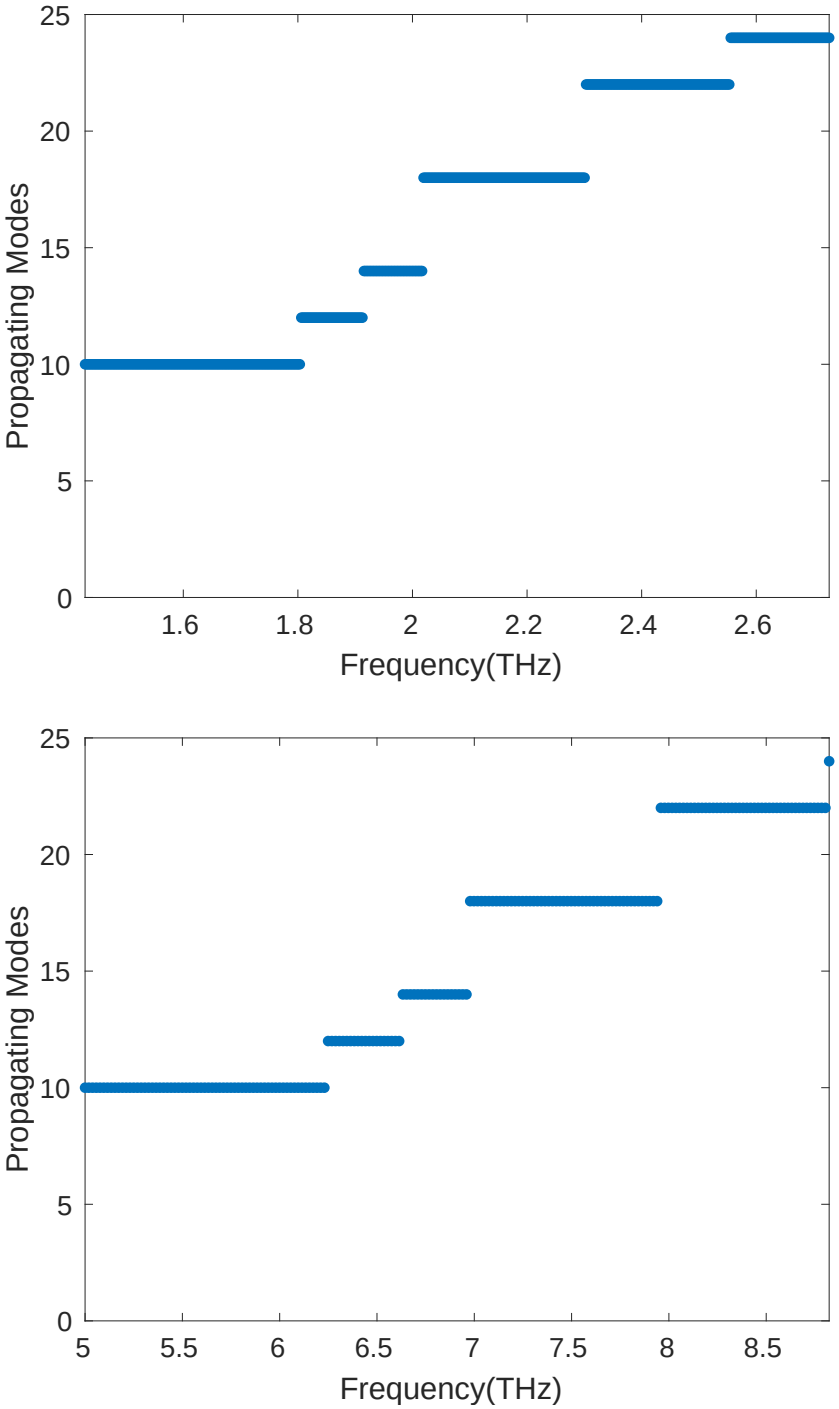

Fig. 6.3 Number of propagating modes in the L- (top) and S-Band (bottom) waveguides, with assumption that all modes have sharp cut-on.

Fig. 6.4 Enhanced model of the absorber.

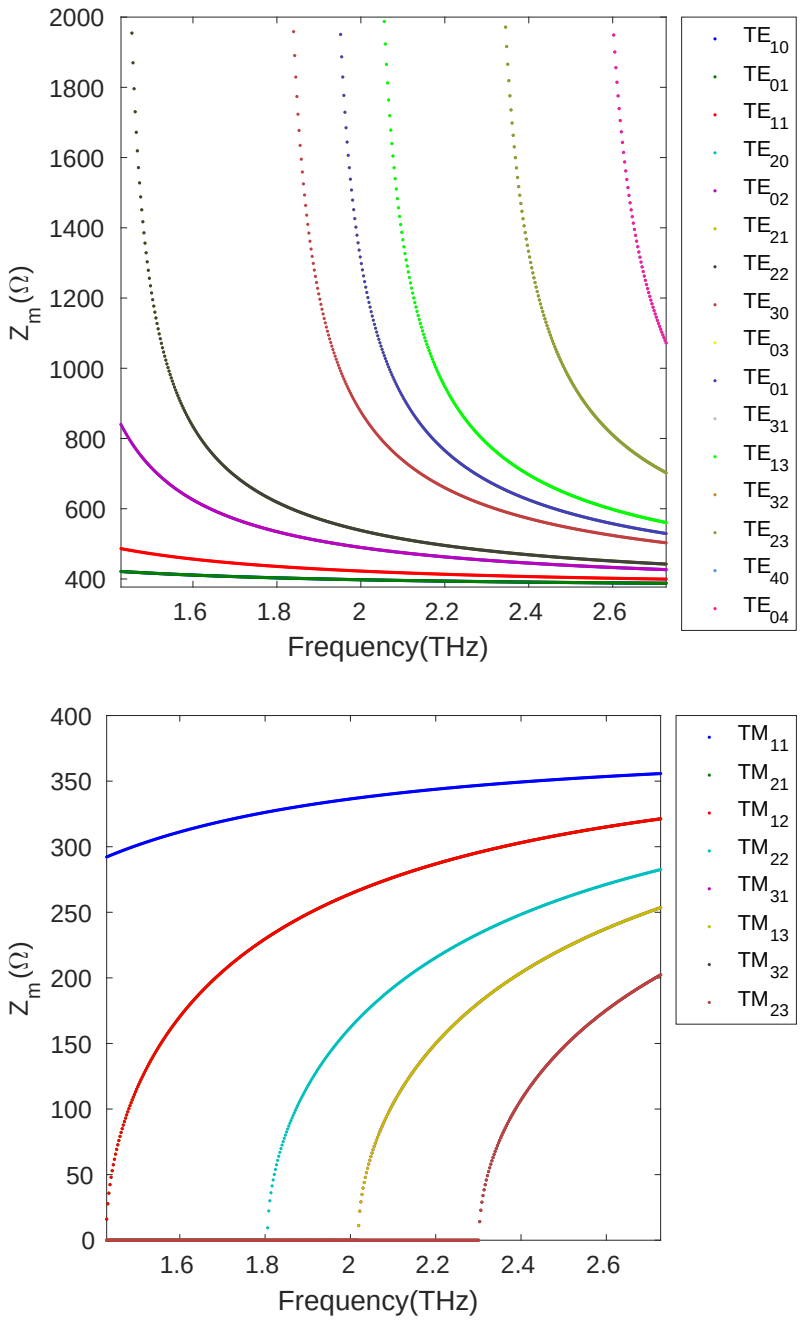

Fig. 6.5 Impedance of the waveguide modes across L-Band.

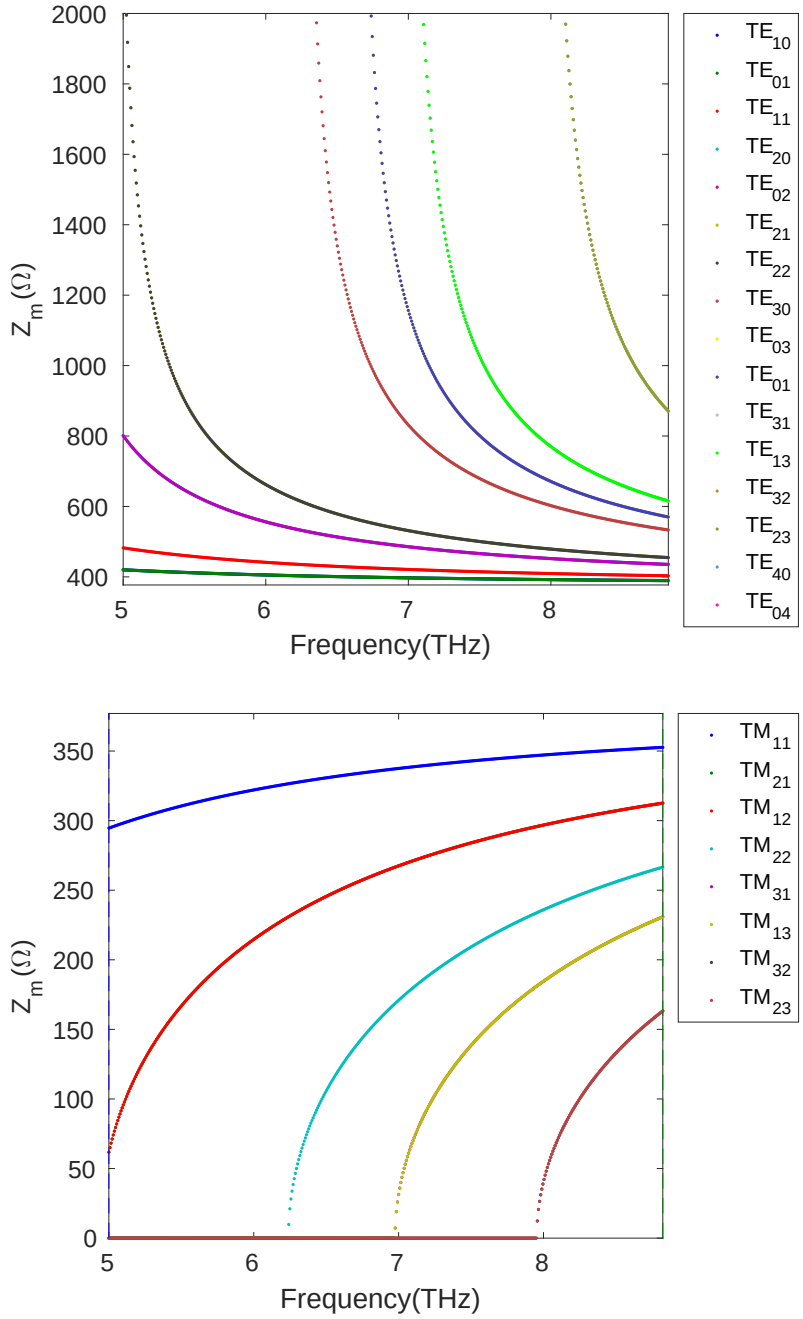

Fig. 6.6 Impedance of the waveguide modes across S-Band.

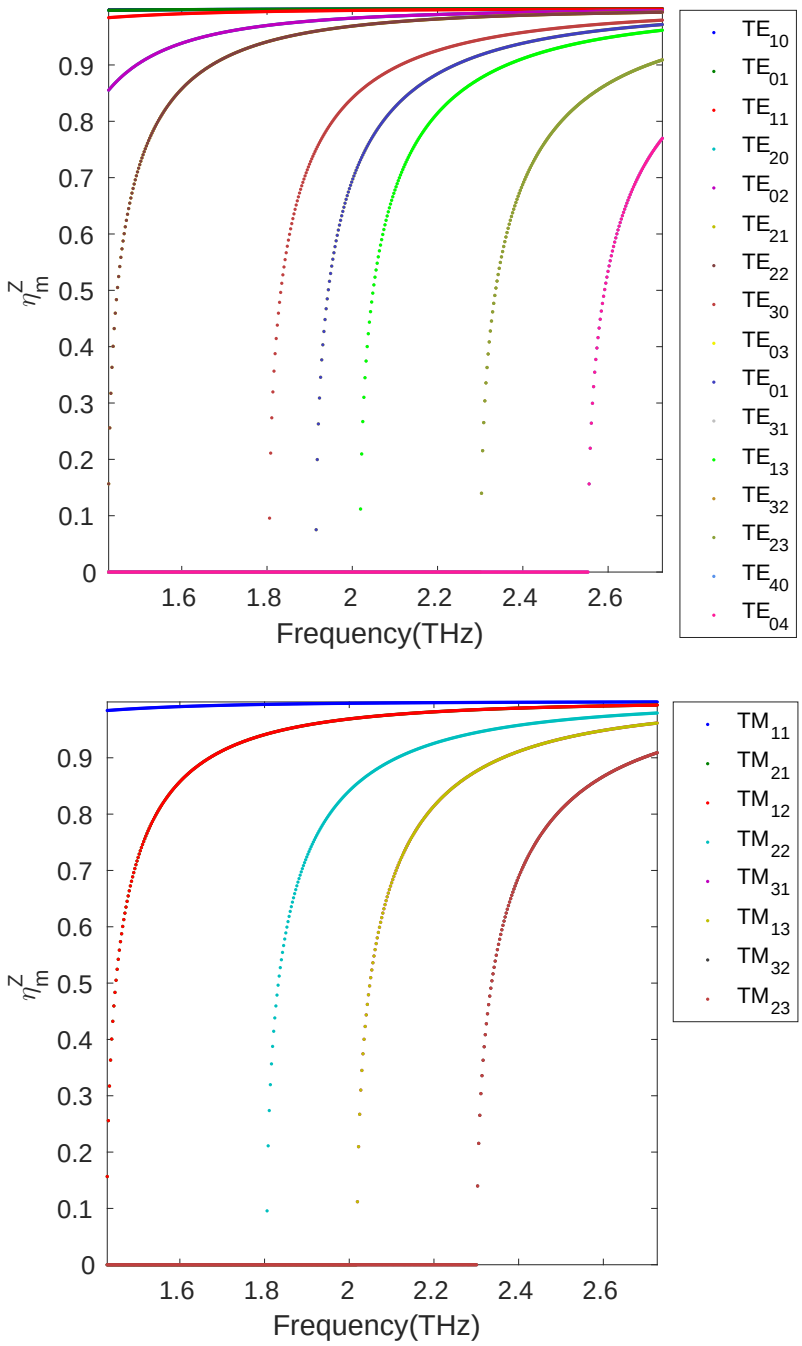

Fig. 6.7 Transmission efficiencies of the TE and TM modes in the L-Band horns due the impedance mis-matching.

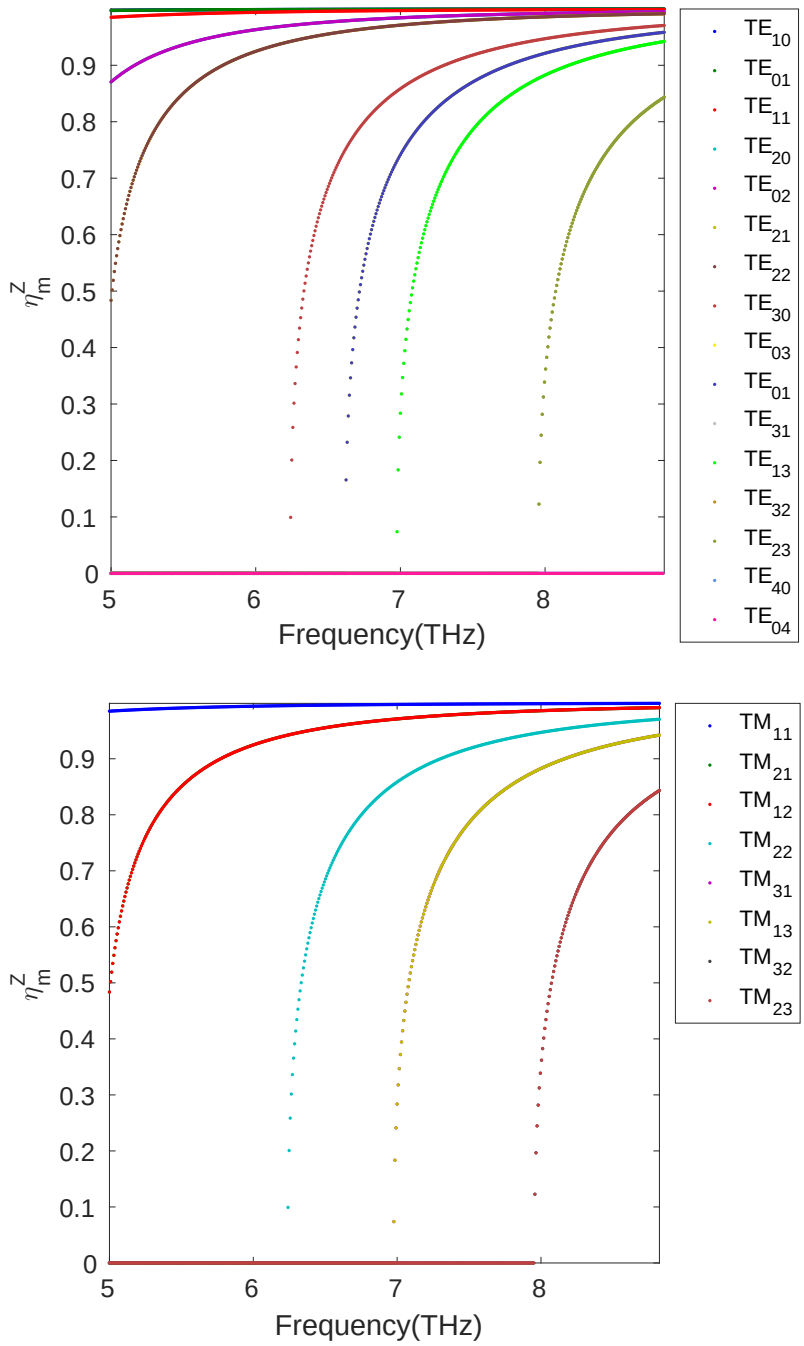

Fig. 6.8 Transmission efficiencies of the TE and TM modes in the S-Band horns due the impedance mis-matching.

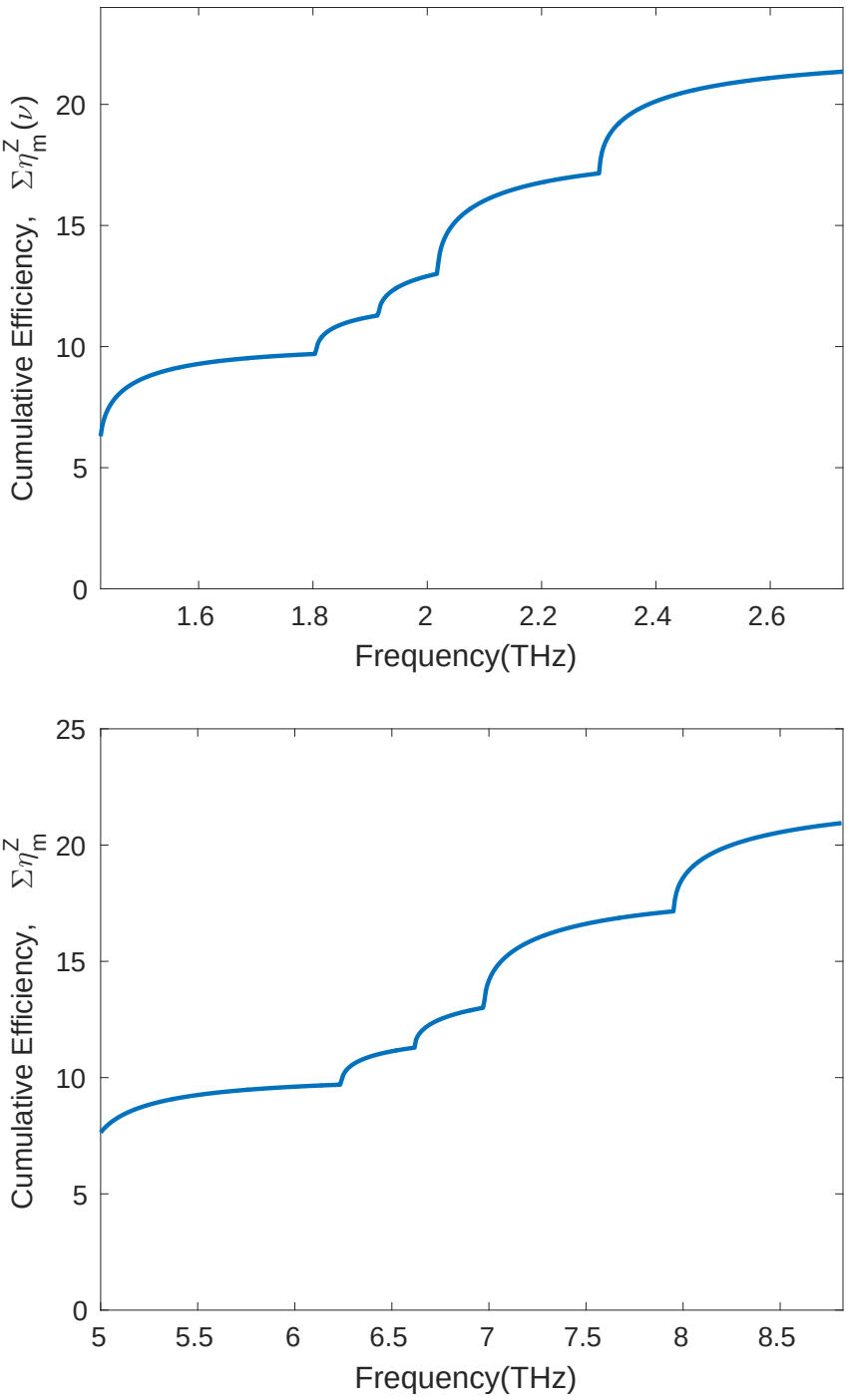

Fig. 6.9 Cumulative transmission efficiency due to impedance mis-matching across L- (top) and S-Band (bottom).

when impedance mis-match is present. Comparing these results with the sharp cut-on case, shown in Figure 6.3, we can see that the slow cut-on of the waveguide modes due to the impedance mismatch has reduced the number of propagating modes across the bands: about 6.3 modes exist at the low frequency end of L-Band, and about 23 modes can propagate at the highest frequency. For S-Band, the effective number of propagating modes is about 8 at the lowest frequency, which is slightly higher than that of L-Band, and the number at the shortest wavelength is about 21.

6.4 Ohmic Losses in the Waveguide Walls

The inner surfaces of the horns were plated with a thin layer of Au, and then electro-formed with Cu. Non-ideal surfaces can result in losses. The losses due to the waveguide wall itself can be calculated from the equations for Ohmic loss. For a square waveguide, the attenuation constant from conductor losses can be written as a function of frequency as

$$\alpha_{mn}^{\mathrm{TE}}(\nu) = \frac{2R_S}{aZ_0\sqrt{1-\left(\frac{\nu_c}{\nu}\right)^2}}\left[1+\left(\frac{\nu_c}{\nu}\right)^2\right], \tag{6.4}$$

for $\mathrm{TE}_{mn}(n \neq 0)$ modes,

$$\alpha_{m0}^{\mathrm{TE}}(\nu) = \frac{R_S}{aZ_0\sqrt{1-\left(\frac{\nu_c}{\nu}\right)^2}}\left[1+2\left(\frac{\nu_c}{\nu}\right)^2\right], \tag{6.5}$$

for TE_{m0} modes, and

$$\alpha_{mn}^{\mathrm{TM}}(\nu) = \frac{2R_S}{aZ_0\sqrt{1-\left(\frac{\nu_c}{\nu}\right)^2}} \tag{6.6}$$

for TM_{mn} modes. m and n are the indices used to identify the waveguide modes, a is the side length of the waveguide, and R_S is the equivalent surface resistance of the waveguide, which can be determined from $R_S = \sqrt{\frac{\pi\nu\mu}{\sigma}}$, with μ the magnetic permeability, and σ the bulk conductivity [36].

The value of the conductivity of Au used for my calculations is $\sigma = 7.3 \times 10^7\ \Omega^{-1}\mathrm{m}^{-1}$, which was measured at 20 K for high purity gold with a thickness of 100 nm. The unit of the attenuation constant given by the above equations are in decibels per meter (dB/m), from which, we can calculate the fraction of power transferred, $\eta^l(\nu)$, through the additional 1 mm waveguide section on the exit aperture side of the horns, because the current density is highest in the section we would expect this part of the horn to cause the greatest loss.

Figures 6.10 and 6.11 show the transmission efficiencies of TE and TM modes due to Au attenuation in the square waveguides. The width of the L- and S-Band waveguides used for the calculations was 235 μm and 68 μm, respectively.

From Figures 6.10 and 6.11, we can see that the attenuation due to Ohmic loss is more notable for S-Band: for L-Band, the modes TE_{10}, TE_{01} TE_{11}, and TM_{11} have near unit transmission efficiency, whereas for S-Band, the transmission efficiencies of the low order modes drop to approximately 90%. The higher order modes TE_{20}, TE_{02}, TE_{21}, TE_{12}, TM_{21}, and TM_{12} propagate in both L- and S-Band, but with larger attenuation compared to the low order modes. It can be seen that the higher order modes cut-on slowly at higher frequencies.

Figure 6.12 shows the cumulative transmission efficiencies as a function of frequency by taking the waveguide loss into account, which gives the effective number of modes that can propagate in the L- (top) and S- (bottom) Band horns across the wavebands. At the lower frequency ends for L- and S-Band, the number of propagating modes are at their minima, which are 8.2 and 6.3 respectively. At the highest frequency of the wavebands, the effective number of modes increases to 23.2 and 17.1 for L- and S-Band respectively.

6.5 Overall Effect

By bringing these two effects together, we can examine the overall behaviour. Figure 6.13 shows the effective number of propagating modes in the L- (top) and S- (bottom) Band horns. The sharp cut-on, shown as blue dotted lines, correspond to the perfect cut-on without either the imperfections of the waveguide, or the impedance mis-match. In this case, we can see the number of modes increases in sharp steps as the frequency is increased. The red dotted lines show the effective number of propagating modes in the case of having taken waveguide attenuation into account, which can be seen in Figure 6.12. The brown dash-dotted lines represent the cumulative efficiency when considering the reflection at the exit aperture due to impedance mis-match. The solid green lines are multiplications of the red dashed and the brown dash-dotted lines, which show the overall response. The overall number of propagating modes ranges from 6 to 22, and 5.8 to 16.5 for L- and S-Band respectively.

From Figure 6.13, we can see that neither of these two factors reduces the effective number of propagating modes dramatically, although the reduction due to Ohmic loss is relatively significant for S-Band.

There is a possibility that the conductivity we have assumed for the inner waveguide walls is too high. To assess how the conductivity of waveguide walls affects the optical performance of the L- and S-Band horns, we calculated the effective number of propagating modes with a reduced conductivity of Au: the value of σ used for calculation was decreased

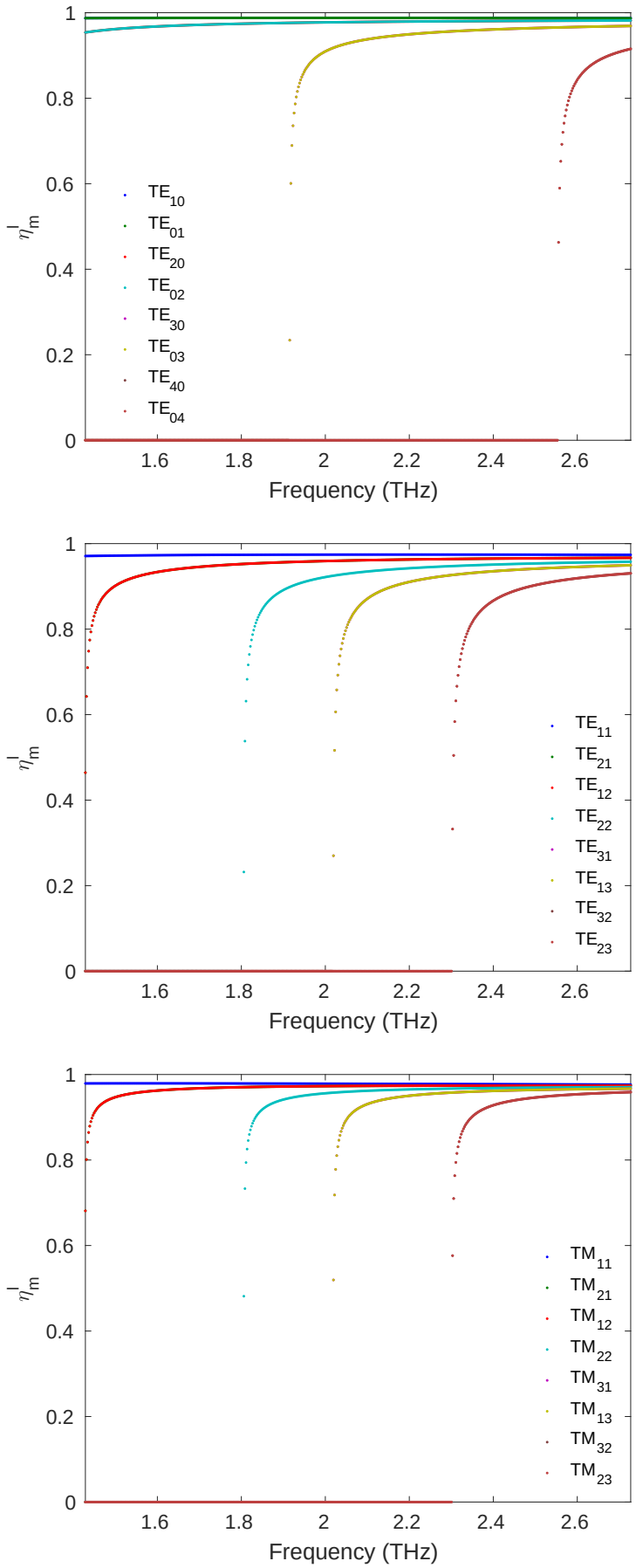

Fig. 6.10 Transmission efficiencies of TE and TM modes due to Ohmic loss in the L-Band horns.

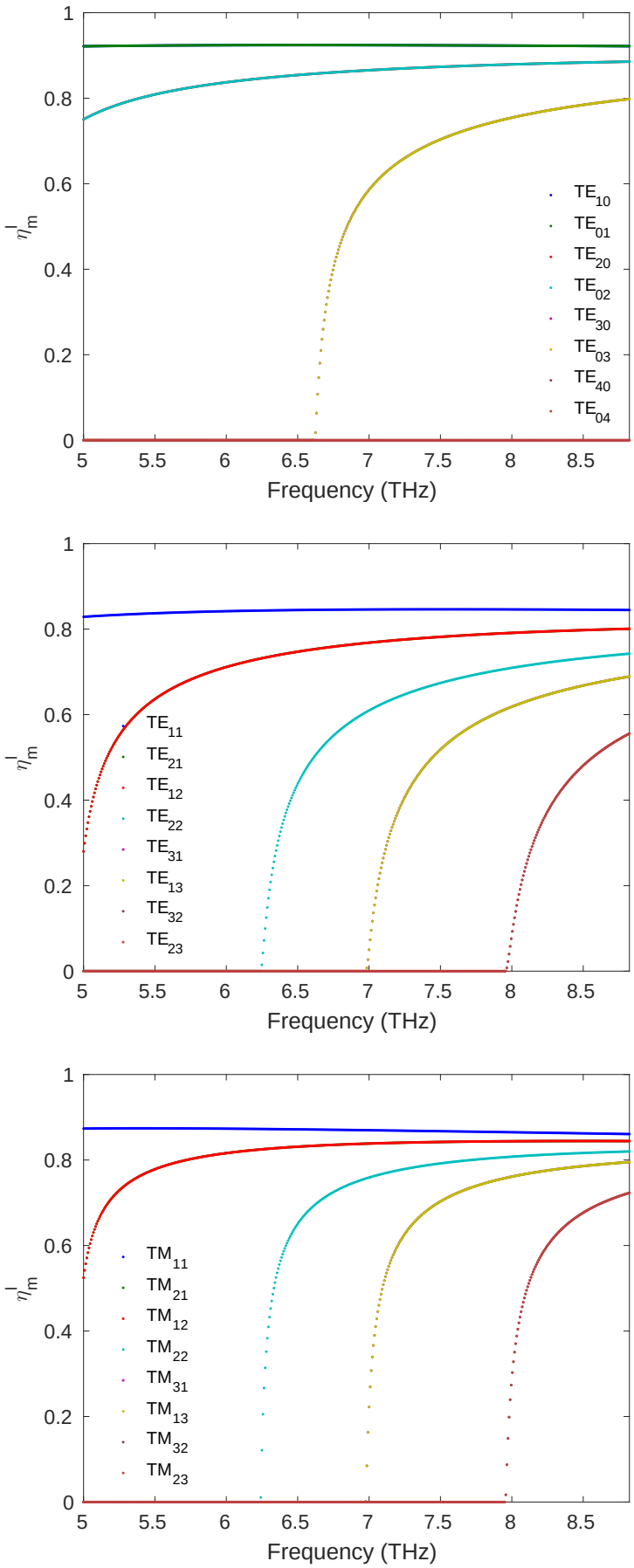

Fig. 6.11 Transmission efficiencies of TE and TM modes due to Ohmic loss in the S-Band horns.

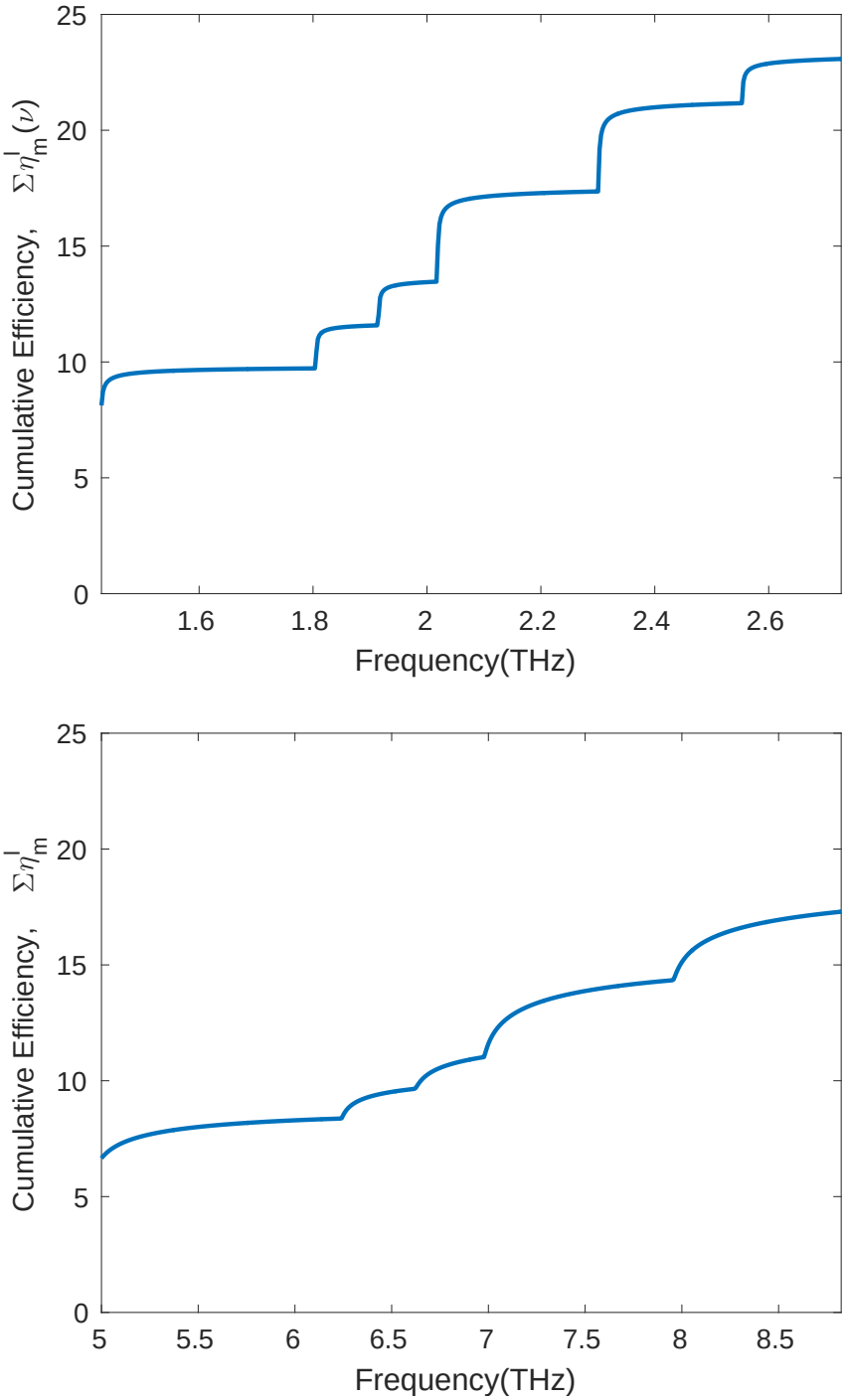

Fig. 6.12 Cumulative transmission efficiency due to waveguide loss across L- (top) and S-Band (bottom).

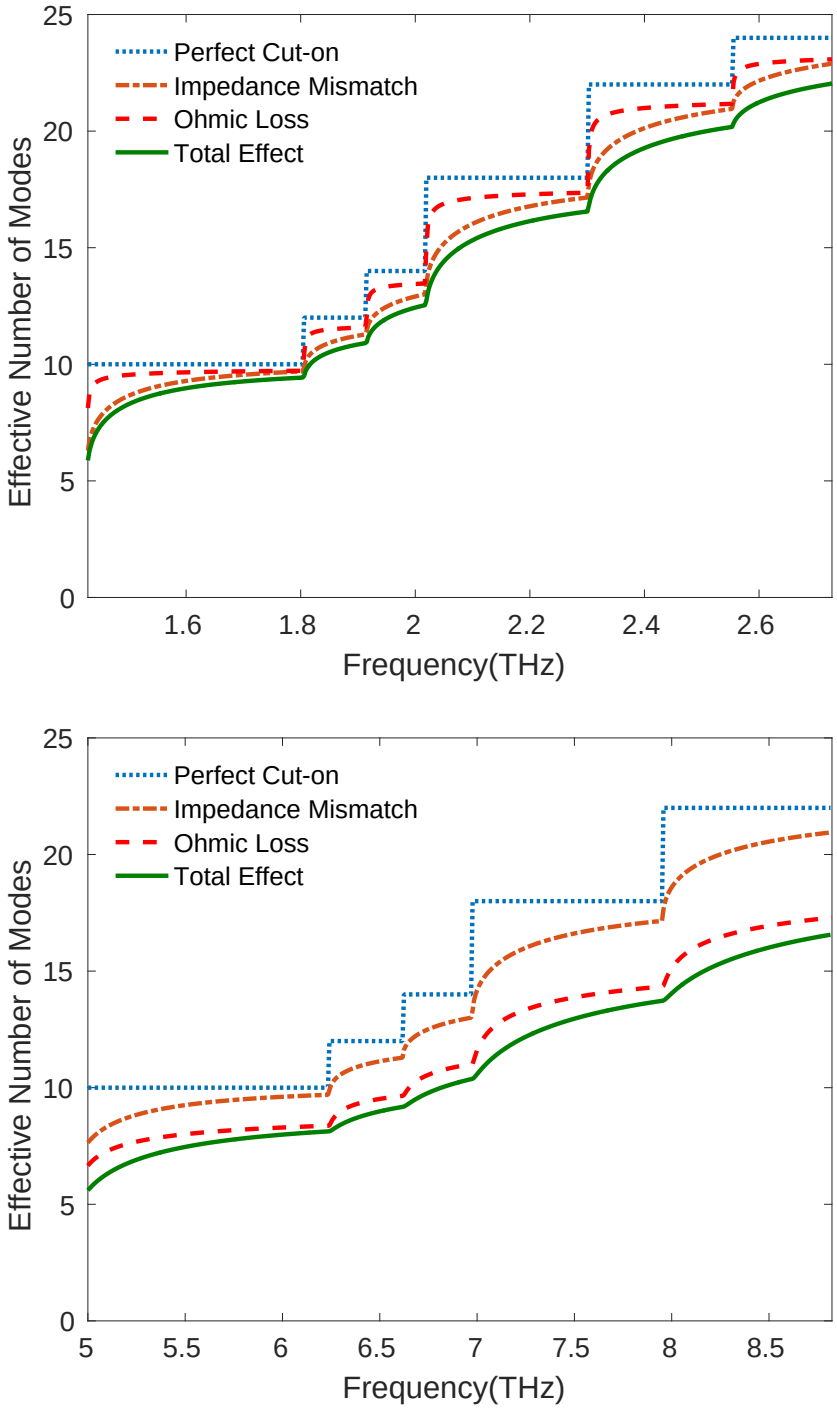

Fig. 6.13 Effective number of modes in L- (top) and S-Band (bottom) with considering the overall effect of waveguide attenuation and impedance mis-matching.

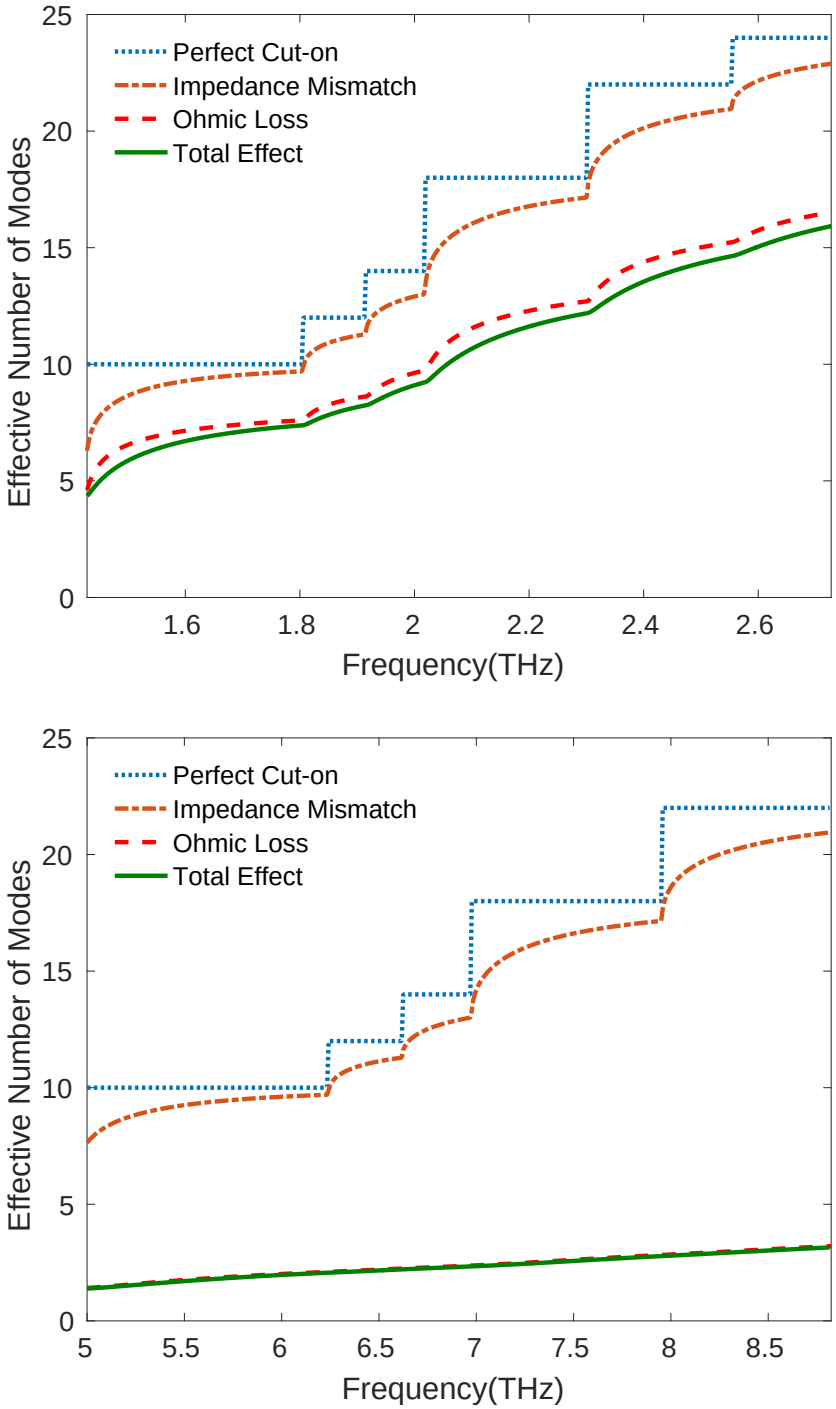

Fig. 6.14 Overall effective number of modes calculated with the conductivity of gold, $\sigma = 7.3 \times 10^6\ \Omega^{-1}\mathrm{m}^{-1}$, for L- (top) and S-Band (bottom).

to $1/10$ of the initial value. The results are shown in Figure 6.14. For L-Band, about 4.8 modes can be detected at the lowest frequency, and about 16 modes at the highest frequency. For S-Band, the reduction in effective number of modes is more significant, about 1.7 modes are detected at the low frequency end, and 3.4 at the high frequency end. It suggests that the manufacture of the S-Band horns is more challenging, as it is crucial to have very high quality waveguide walls to ensure good optical performance.

The full expression for calculating the detected power can now be expressed as

$$P_{\mathrm{FM}}(T) = \sum_i \sum_n \int_{\nu_{\min}}^{\nu_{\max}} \eta^{\mathrm{filters}}(\nu)\eta_n^{\mathrm{opt}}(\nu)\eta_n^{\mathrm{cpl}}(\nu)\eta_i^{Z}(\nu)\eta_i^{L}(\nu)\frac{h\nu}{\exp(\frac{h\nu}{kT})-1}\mathrm{d}\nu, \qquad (6.7)$$

and it can be used to assess the experimental power measurements made at L-Band. To account for the differences between the L-Band measured results and the numerical results, the conductivity of gold used for calculation should be about $1/50$ of the initial value. In that case, the effective number of modes across L-Band would range 2 to 5.2, as shown in Figure 6.15.

Subsequent to carry out this work, colleagues in the Astronomy Instrumentation Group at the Cardiff University re-etched the horns, re-measured their behaviour, and their performance was found to improved significantly. We now believe that a thin layer of the Al mandrel, or oxide which may have formed on the mandrel, was left on the inside of the horns. The work I have carried out helped identify this problem, and the performance of the detectors was significantly improved.

6.6 Conclusions

The optical modelling of the detectors was improved by investigating the losses in the few-moded horns. Modal analyses were carried out at L- and S-Band, from two aspects:

- the effects of reflection due to impedance mis-match at the exit aperture of the waveguide;
- the attenuation of the waveguide walls due to Ohmic loss.

It has been shown that the loss of efficiency due to waveguide impedance mismatch is relatively insignificant, compared to the attenuation due to Ohmic loss. The conductivity of the waveguide walls is crucial here as the attenuation is strongly affected by the conductivity. This effect is particularly pronounced in shorter wavelength band. It is believed that a thin layer of the Al mandrel, or oxide which may have formed on the mandrel, was left on the inside of the horns, and thus increased the conductor loss in the waveguide walls.

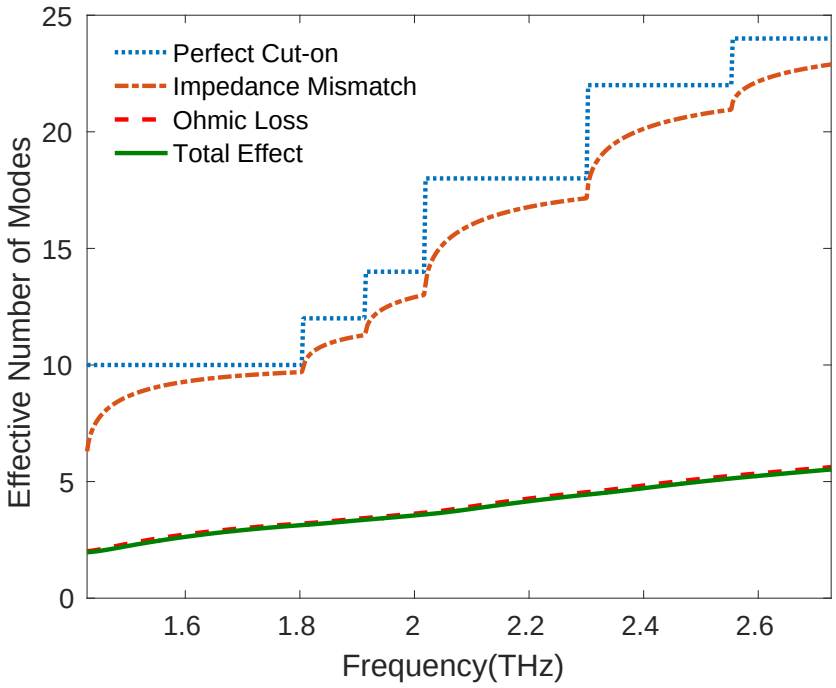

Fig. 6.15 L-Band overall effective number of modes calculated with conductivity of gold, $\sigma = 1.6 \times 10^6\ \Omega^{-1}\mathrm{m}^{-1}$.

Chapter 7

Electromagnetic Modelling of Far-Infrared Waveguide-Mounted Thin Films

7.1 Introduction

The optical model discussed in the previous chapters has provided a description of the partially coherent optical behaviour of ultra-low-noise multi-mode detectors. I have explicitly introduced theories and numerical methods to study the partially coherent optical behaviour of horn-coupled TESs in the far-infrared. However I have assumed that the waveguide-mounted absorbing thin film of the detector has perfect absorption, and extends over the whole cross-section of the waveguide, with a flat backshort behind it, as shown in the left diagram in Figure 7.1. In practice, it is more usual to place finite sized absorbers behind the exit aperture of the waveguide, followed with backshorts, as shown on the right of Figure 7.1. The effect of the backshort has been studied in earlier modelling, and the step in the waveguide dimensions at the exit aperture is a well understood problem, which I will not discuss in this chapter [4, 61]. The part that remains unknown is the scattering description of the finite sized thin film. Properties such as the size, geometry and position of the thin film have an influence on the number and form of the natural modes to which the detector is sensitive.

For far-infrared horn-coupled TESs, metallic thin films are commonly used as absorbers [62]. Understanding the electromagnetic behaviour of metallic absorbing films is important for designing devices. The choice of numerical methods used for analysis

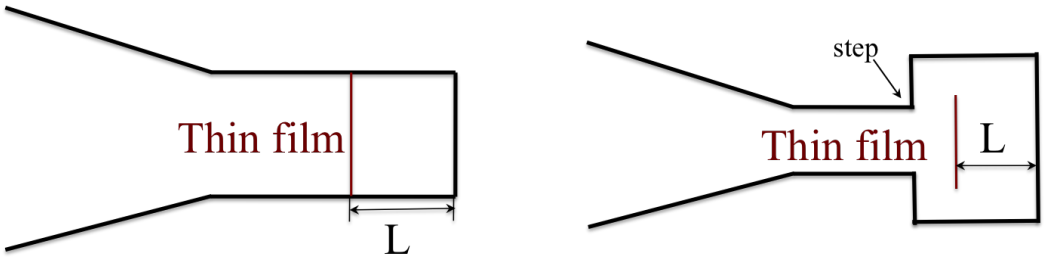

Fig. 7.1 A simplified model that a waveguide-mounted thin film fills over the whole cross-sectional area of a multimode lightpipe (left); and a finite sized metallic absorber placed behind the exit of the waveguide.

and design of electromagnetic field problems is crucial. An method called the Method of Moments (MoM) is a computationally efficient approach in this case [18].

Previously, a Method of Moments (MoM) approach had been introduced by Thomas and Withington in [50] to simulate the partially coherent optical behaviour of the resistive film of free-space coupled TESs. The method was based on a boundary condition on the film, which took into account the film's surface impedance and allowed the authors to express the applied field in terms of the induced current on the film. In [50], instead of using a set of testing functions as in a traditional MoM approach as describe in [34], a set of basis functions was used to expand the incident field and induced sheet current; in addition, the model was extended to consider moving the thin film from free-space to waveguide; calculations such as the power absorbed by the thin film could be also obtained from the model.

The optical behaviour of the absorbing thin films of horn-coupled detectors has not been studied in detail yet. The choice of numerical methods is crucial for analysis and design to achieve efficient and accurate simulations. In this chapter, I will develop a mode-matching scheme to investigate the optical behaviour of patterned resistive films contained entirely in the transverse plane of a metallic waveguide. The formalism for calculating the induced sheet current will be presented in this chapter. Knowing the relationship between the incident electromagnetic field and the induced surface current is important for understanding the optical behaviour of the detectors. We start by choosing a set of basis functions to expand the sheet current density over the film. The film was described by a sheet admittance function $Y_S(\mathbf{r})$ over the plane, while the waveguide walls were assumed to be perfectly conducting. We have developed a method to analytically calculate the inner products between the basis functions of a waveguide-mounted thin film. The method applies to films having different geometrical forms, such as fully filled, strip and meshed. I will also show how to calculate the matrix of scattering parameters of the film in the basis of the waveguide modes.

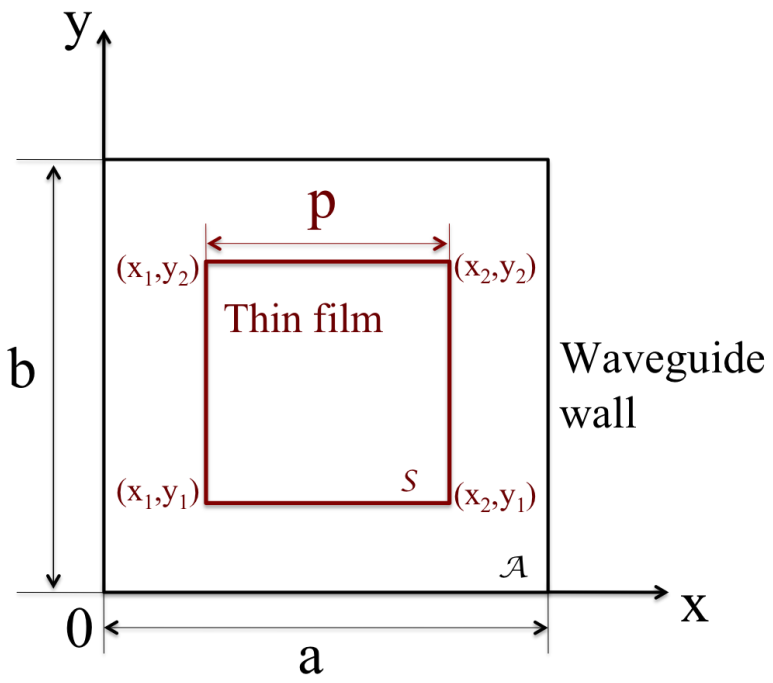

Fig. 7.2 Metallic film with area S mounted within a waveguide with cross-sectional area A.

7.2 Induced Sheet Current

Consider a square film with side length p mounted in a waveguide, as shown in Figure 7.2. An incident field $\mathbf{E}_I(\mathbf{r})$ will induce a sheet current on the film. The induced current then itself radiates, producing a scattered field, $\mathbf{E}_S(\mathbf{r})$. To calculate the scattering parameters, we need to work out the relationship between the form of the incident field, $\mathbf{E}_I$ and the induced sheet current density $\mathbf{J}$. As the film is mounted in a waveguide, a set of waveguide modes can be chosen as the basis functions to expand the sheet current induced by incident electric field. The main reason for choosing waveguide modes is that we know that the induced sheet current $\mathbf{J}$ is proportional to the incident field $\mathbf{E}_I$, since $\mathbf{E}_I$ is limited to waveguide modes, and thus $\mathbf{J}$ is also limited to waveguide modes. Moreover, it is expected that the distribution of $\mathbf{J}$ is reasonably close to the waveguide modes that are incident, which makes the waveguide modes a physically sensible basis in this case. Following [46], the total electric field, $\mathbf{E}_T$ and the induced surface current density are related by the constitutive relation

$$\begin{aligned}\mathbf{J}(\mathbf{r}) &= Y_S(\mathbf{r})\mathbf{E}_T(\mathbf{r}) \\ &= Y_S(\mathbf{r})[\mathbf{E}_I(\mathbf{r}) + \mathbf{E}_S(\mathbf{r})],\end{aligned} \tag{7.1}$$

where $\mathbf{J}(\mathbf{r})$ is the induced sheet current density on the film which is tangential to the film surface and has units Am^{-1}. $Y_S(\mathbf{r})$ is the effective sheet admittance as a function of position on the film. We define that the admittance has constant value everywhere on the film, and it is zero off the film. $\mathbf{E}_T(\mathbf{r})$ is the total transverse electric field at the surface of the absorber, which is the sum of the known incident field, $\mathbf{E}_I(\mathbf{r})$, and the scattered filed, $\mathbf{E}_S(\mathbf{r})$, radiated by the induced sheet current. Assume that the electric field generated by the transverse current density can be written in terms of a Green's dyadic of the form

$$\mathbf{E}_S(\mathbf{r}) = \int_A \overline{\overline{G}}(\mathbf{r},\mathbf{r}') \cdot \mathbf{J}(\mathbf{r}')\mathrm{d}^2\mathbf{r}', \tag{7.2}$$

where A denotes the cross-sectional area of the waveguide, and $\overline{\overline{G}}(\mathbf{r},\mathbf{r}')$ is the Green's dyadic, which can be expressed in terms of waveguide modes as [62]

$$\overline{\overline{G}}(\mathbf{r},\mathbf{r}') = -\frac{1}{2}\sum_{m=1}^{\infty} Z_m(\nu)\mathbf{U}_m(\mathbf{r})\mathbf{U}_m(\mathbf{r}'), \tag{7.3}$$

where $Z_m(\nu)$ is the impedance of the corresponding mode at the frequency of interest, the factor of $-\frac{1}{2}$ comes from the fact that the propagation of the wave goes in two directions, and $\{\mathbf{U}_m(\mathbf{r})\}$ are the transverse electric field components of the combined set of TE and TM modes, which is the same as the symbol $\mathbf{F}_n(\mathbf{r})$ introduced in Chapter 2 for waveguide modes. Using Eq. (7.1) and (7.2), the relationship between $\mathbf{E}_I(\mathbf{r})$ and $\mathbf{E}_T(\mathbf{r})$ can be written

$$\mathbf{E}_I(\mathbf{r}) = \mathbf{E}_T(\mathbf{r}) - Y_S(\mathbf{r}')\int_A \overline{\overline{G}}(\mathbf{r},\mathbf{r}') \cdot \mathbf{E}_T(\mathbf{r}')\mathrm{d}^2\mathbf{r}'. \tag{7.4}$$

The induced sheet current can be determined by inverting the above equation.

To do this, we firstly need to expand the sheet current density over the film $\mathbf{J}(\mathbf{r})$ and the incident electric field $\mathbf{E}_I(\mathbf{r})$ using a finite set of the waveguide modes as

$$\mathbf{J}(\mathbf{r}) = \sum_{m=1}^{N} j_m h(\mathbf{r})\mathbf{U}_m(\mathbf{r}), \tag{7.5}$$

and

$$\mathbf{E}_I(\mathbf{r}) = \sum_{m=1}^{E} e_m^{(I)}\mathbf{U}_m(\mathbf{r}), \tag{7.6}$$

where N in Eq. (7.5) is the set of modes used to expand the current, with

$$h(\mathbf{r}) = \begin{cases} 1, & \mathbf{r} \in S \\ 0, & \text{otherwise}, \end{cases} \tag{7.7}$$

which guarantees $\mathbf{J}(\mathbf{r}) = \mathbf{0}$ over the empty regions; and E in Eq. (7.6) is the size of the waveguide mode set needed for the expansion of $\mathbf{E}_I(\mathbf{r})$. The induced sheet current density can be approximated by the expansion in terms of the waveguide modes, because the current distributions induced on the film are closely related to the spatial forms of the waveguide modes. In practice, the summation in the Green's function, $\overline{\overline{G}}(\mathbf{r},\mathbf{r}')$, can be truncated to a finite mode set G. Substituting the approximations as described in Eq. (7.5), (7.2) and (7.6) into Eq. (7.1) gives

$$\sum_{m=1}^{N} j_m h(\mathbf{r})\mathbf{U}_m(\mathbf{r}) = Y_S \left[\sum_{m=1}^{E} e_m^{(I)} \mathbf{U}_m(\mathbf{r}) - \frac{1}{2} \sum_{m=1}^{G} \sum_{n=1}^{N} Z_m(\nu) C_{mn} j_n \mathbf{U}_m(\mathbf{r}) \right], \tag{7.8}$$

where $\{C_{mn}\}$ is a matrix of inner products between the basis functions over the area of the film:

$$C_{mn} = \int_S \mathbf{U}_m^*(\mathbf{r}) \cdot \mathbf{U}_n(\mathbf{r}) \mathrm{d}^2\mathbf{r}. \tag{7.9}$$

Rearranging Eq.(7.8) and taking the inner product with each of the $\mathbf{U}_m^*(\mathbf{r})$, we have

$$Y_S \mathrm{C} \cdot \mathbf{e}_I = [\mathrm{C} + \frac{1}{2} Y_S \mathrm{C} \cdot \mathrm{Z} \cdot \mathrm{C}^\dagger] \cdot \mathbf{j}, \tag{7.10}$$

where

$$\{\mathrm{Z}\}_{mn} = Z_p \delta_{mn}, \tag{7.11}$$

where Z_p is the waveguide impedance of the p-th mode. Then $\mathbf{j}$ can be solved from Eq.(7.10) as

$$\mathbf{j} = Y_S [\mathrm{C} + \frac{1}{2} Y_S \mathrm{C} \cdot \mathrm{Z} \cdot \mathrm{C}^\dagger]^{-1} \cdot \mathrm{C} \cdot \mathbf{e}_I. \tag{7.12}$$

However, I encountered two numerical issues while simulating the current distributions induced on the film: (i) there is redundancy in the basis, and therefore the C-matrix has a null-space; (ii) the impedance of some of the TE modes tend to infinity, such that singularities occur in the inversion routine, as the matrix Z contains very large elements. In the following sections, I will firstly describe the analytical method of calculating the C_{mn}, and then I will address solutions to the numerical issues mentioned above.

Another advantage of using waveguide modes is from the perspective of fast numerical simulations: the conventional method of determining the overlap integrals over a finite area (C-matrix) for a large set of modes can be numerically difficult and extremely time-consuming. Using rectangular waveguide modes as the basis functions allows us to analytically evaluate the overlap integral of the inner product of the basis functions, which provides a fast and efficient computational approach to determine the C-matrix.

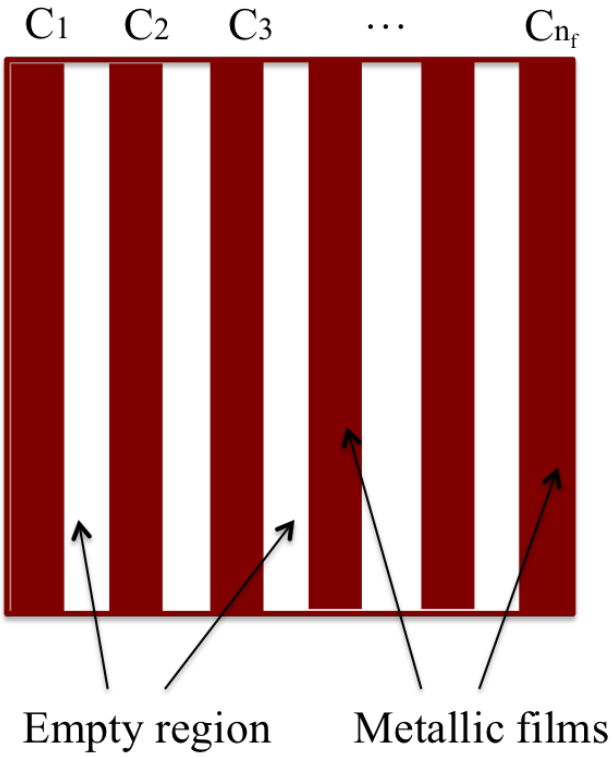

Fig. 7.3 *C*-matrix calculations for stripped films.

7.2.1 *C*-matrix Calculations

The *C*-matrix can be determined for an absorber having any size and being placed at any position. Some absorbers of ultra-low-noise detectors are designed to be striped or meshed to achieve higher impedance. This numerical technique can handle the modelling of absorbers having patterned structures, which is useful in designing frequency selecting surfaces. In the case of having a strip absorber, as shown in Figure 7.3, the total effective *C*-matrix can be determined by summing over all of the individual strips, as the area of the integrals can be split as $S = \sum S_i$. Thus the corresponding *C*-matrix of the stripped film can be determined by summing the individual *C*-matrices of each segment of the film, as

$$\mathrm{C}_{\mathrm{stripped}} = \sum_{n_f} \mathrm{C}_i, \tag{7.13}$$

where the absorber is considered to consist of n_f rectangular small films. For a film having a grid structure, as shown on the right of Figure 7.4, similar reasoning can be applied:

1. firstly we calculate the *C*-matrix with the assumption that there is no meshing on the film, $\mathrm{C}_{\mathrm{filled}}$, as shown in the left diagram of the figure;

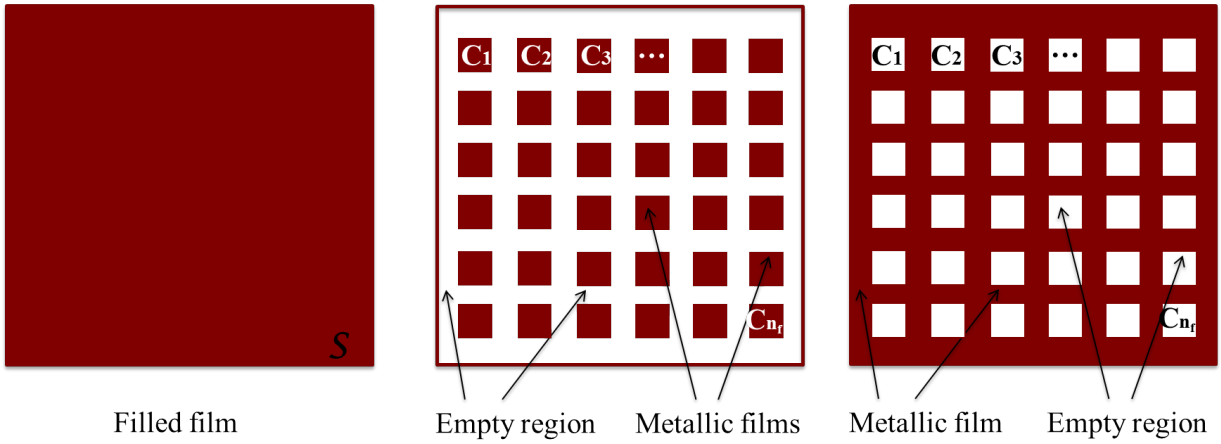

Fig. 7.4 C-matrix calculations for grid films.

2. then we treat the film as consisting of n_f small films, as shown in the centre, and the C-matrices of each of the films C_i can be calculated from Eq. (7.13)

3. the C-matrix of the meshed film can then be obtained as

$$\mathrm{C}_{\mathrm{grid}} = \mathrm{C}_{\mathrm{filled}} - \sum_{n_f} \mathrm{C}_i. \tag{7.14}$$

7.2.2 Analytical Evaluation of the C-matrix

Figure 7.2 shows the cross-section of a rectangular waveguide, with side length a and b, containing a conductive thin film. The waveguide modes in a rectangular waveguide $\{\mathbf{U}_m(\mathbf{r})\}$ have the normalised spatial forms of

$$\begin{aligned}\mathbf{U}_{mn}^{\mathrm{TE}} = \left(\frac{\varepsilon_{0n}\varepsilon_{0m}}{ab}\right)^{1/2} \frac{1}{k_{c,mn}} [k_{y,m}\cos(k_{x,n}x)\sin(k_{y,m}y)\hat{\mathbf{x}} \\ - k_{x,n}\sin(k_{x,n}x)\cos(k_{y,m}y)\hat{\mathbf{y}}]\end{aligned} \tag{7.15}$$

for TE modes, and

$$\begin{aligned}\mathbf{U}_{mn}^{\mathrm{TM}} = \left(\frac{\varepsilon_{0n}\varepsilon_{0m}}{ab}\right)^{1/2} \frac{1}{k_{c,mn}} [k_{x,n}\cos(k_{x,n}x)\sin(k_{y,m}y)\hat{\mathbf{x}} \\ + k_{y,m}\sin(k_{x,n}x)\cos(k_{y,m}y)\hat{\mathbf{y}}]\end{aligned} \tag{7.16}$$

for TM modes. m and n are the two indices used to identify each waveguide mode. In the case of $n = 0$, $\varepsilon_{0n} = 1$; in the case of $n > 0$, $\varepsilon_{0n} = 2$. $k_{x,n} = n\pi/a$ and $k_{y,m} = m\pi/b$ are the

transverse wave vectors, and $k_{c,mn} = \sqrt{k_{x,n}^2 + k_{y,m}^2}$ is the cutoff wave vector of the mn-th mode. The $\{\mathbf{U}_m(\mathbf{r})\}$ are the normalised forms of the transverse electric field, which satisfy the orthonomality relation

$$\int_A \mathbf{U}_m^*(\mathbf{r}) \cdot \mathbf{U}_n(\mathbf{r}) \mathrm{d}^2\mathbf{r} = \delta_{mn}, \tag{7.17}$$

with the integral taken over the whole cross-sectional area of the waveguide.

To calculate the C_{mn}, four integrands in Eq.(7.9) must be considered: $C_{mn}^{\mathrm{TE\cdot TE}}$, $C_{mn}^{\mathrm{TE\cdot TM}}$, $C_{mn}^{\mathrm{TM\cdot TE}}$ and $C_{mn}^{\mathrm{TM\cdot TM}}$, which are given by expressions

$$\begin{aligned} C_{mnm'n'}^{\mathrm{TE\cdot TE}} =& \frac{(\varepsilon_{0n}\varepsilon_{0m}\varepsilon_{0n'}\varepsilon_{0m'})^{1/2}}{abk_{c,mn}k_{c,m'n'}} \int_S\int_S \big[k_{y,m}k_{y,m'}\cos(k_{x,n}x)\sin(k_{y,m}y)\cos(k_{x,n'}x)\sin(k_{y,m'}y) \\ &+k_{x,n}k_{x,n'}\sin(k_{x,n}x)\cos(k_{y,m}y)\sin(k_{x,n'}x)\cos(k_{y,m'}y)\big]\,\mathrm{d}^4\mathbf{r}, \end{aligned} \tag{7.18}$$

$$\begin{aligned} C_{mnm'n'}^{\mathrm{TE\cdot TM}} =& \frac{(\varepsilon_{0n}\varepsilon_{0m}\varepsilon_{0n'}\varepsilon_{0m'})^{1/2}}{abk_{c,mn}k_{c,m'n'}} \int_S\int_S \big[k_{y,m}k_{x,n'}\cos(k_{x,n}x)\sin(k_{y,m}y)\cos(k_{x,n'}x)\sin(k_{y,m'}y) \\ &-k_{x,n}k_{y,m'}\sin(k_{x,n}x)\cos(k_{y,m}y)\sin(k_{x,n'}x)\cos(k_{y,m'}y)\big]\,\mathrm{d}^4\mathbf{r}, \end{aligned} \tag{7.19}$$

$$\begin{aligned} C_{mnm'n'}^{\mathrm{TM\cdot TE}} =& \frac{(\varepsilon_{0n}\varepsilon_{0m}\varepsilon_{0n'}\varepsilon_{0m'})^{1/2}}{abk_{c,mn}k_{c,m'n'}} \int_S\int_S \big[k_{x,n}k_{y,m'}\cos(k_{x,n}x)\sin(k_{y,m}y)\cos(k_{x,n'}x)\sin(k_{y,m'}y) \\ &-k_{y,m}k_{x,n'}\sin(k_{x,n}x)\cos(k_{y,m}y)\sin(k_{x,n'}x)\cos(k_{y,m'}y)\big]\,\mathrm{d}^4\mathbf{r}, \end{aligned} \tag{7.20}$$

and

$$\begin{aligned} C_{mnm'n'}^{\mathrm{TM\cdot TM}} =& \frac{(\varepsilon_{0n}\varepsilon_{0m}\varepsilon_{0n'}\varepsilon_{0m'})^{1/2}}{abk_{c,mn}k_{c,m'n'}} \int_S\int_S \big[k_{x,n}k_{x,n'}\cos(k_{x,n}x)\sin(k_{y,m}y)\cos(k_{x,n'}x)\sin(k_{y,m'}y) \\ &+k_{y,m}k_{y,m'}\sin(k_{x,n}x)\cos(k_{y,m}y)\sin(k_{x,n'}x)\cos(k_{y,m'}y)\big]\,\mathrm{d}^4\mathbf{r}. \end{aligned} \tag{7.21}$$

From Eq. (7.18) to (7.21), we can see that only four combinations of integrals need to be evaluated:

$$\begin{aligned} f_1(x) &= \int_{x_1}^{x_2} \cos(k_{x,n}x)\cos(k_{x,n'}x)\mathrm{d}x \\ f_2(x) &= \int_{x_1}^{x_2} \sin(k_{x,n}x)\sin(k_{x,n'}x)\mathrm{d}x \\ f_3(y) &= \int_{y_1}^{y_2} \cos(k_{y,m}y)\cos(k_{y,m'}y)\mathrm{d}y \\ f_4(y) &= \int_{y_1}^{y_2} \sin(k_{y,m}y)\sin(k_{y,m'}y)\mathrm{d}y, \end{aligned} \tag{7.22}$$

where x_1, x_2, y_1, and y_2 define the film size and its position with respect to the waveguide in z-plane. The wavevectors $k_{x,n}$ and $k_{y,m}$ can be written as $n\pi/a$ and $m\pi/b$. It can be seen that the above integrals can be further reduced to evaluating two integrals: for $f_1(x)$ and $f_3(y)$, we can write $I_1^{pq}(u) = \int_{u_1}^{u_1} \cos(p\pi u/l)\cos(q\pi u/l)\mathrm{d}u$; and for $f_2(x)$ and $f_4(y)$, there is $I_2^{pq}(u) = \int_{u_1}^{u_2} \sin(p\pi u/l)\sin(q\pi u/l)\mathrm{d}u$, with l is a or b, u is x or y depends on it is integrated along x- or y-direction. I_1^{pq} and I_2^{pq} can be numerically set as functions of three parameters u_1, u_2 and l for rectangular waveguides and films having any size:

$$\begin{aligned} I_1^{pq}(u_1,u_2,l) &= \int_{u_1}^{u_1} \cos\left(\frac{p\pi u}{l}\right)\cos\left(\frac{q\pi u}{l}\right)\mathrm{d}u \\ &= \frac{1}{2}\left\{u_2\mathrm{sinc}\left[\frac{\pi}{l}(p+q)u_2\right] + u_2\mathrm{sinc}\left[\frac{\pi}{l}(p-q)u_2\right]\right. \\ &\quad \left. -u_1\mathrm{sinc}\left[\frac{\pi}{l}(p+q)u_1\right] - u_1\mathrm{sinc}\left[\frac{\pi}{l}(p-q)u_1\right]\right\}, \end{aligned} \tag{7.23}$$

and

$$\begin{aligned} I_2^{pq}(u_1,u_2,l) &= \int_{u_1}^{u_2} \sin\left(\frac{p\pi u}{l}\right)\sin\left(\frac{q\pi u}{l}\right)\mathrm{d}u \\ &= \frac{1}{2}\left\{u_2\mathrm{sinc}\left[\frac{\pi}{l}(p+q)u_2\right] - u_2\mathrm{sinc}\left[\frac{\pi}{l}(p-q)u_2\right]\right. \\ &\quad \left. -u_1\mathrm{sinc}\left[\frac{\pi}{l}(p+q)u_1\right] + u_1\mathrm{sinc}\left[\frac{\pi}{l}(p-q)u_1\right]\right\}. \end{aligned} \tag{7.24}$$

Thus, Eq.(7.18) to (7.21) can be written as functions of

$$\begin{aligned} C_{mnm'n'}^{\mathrm{TE\cdot TE}} = &\frac{(\varepsilon_{0n}\varepsilon_{0m}\varepsilon_{0n'}\varepsilon_{0m'})^{1/2}}{abk_{c,mn}k_{c,m'n'}}\left[k_{y,m}k_{y,m'}I_1^{nn'}(x_1,x_2,a)I_2^{mm'}(y_1,y_2,b)\right. \\ &\left. +k_{x,n}k_{x,n'}I_2^{nn'}(x_1,x_2,a)I_1^{mm'}(y_1,y_2,b)\right], \end{aligned} \tag{7.25}$$

$$C^{\mathrm{TE\cdot TM}}_{mnm'n'} = \frac{(\varepsilon_{0n}\varepsilon_{0m}\varepsilon_{0n'}\varepsilon_{0m'})^{1/2}}{abk_{c,mn}k_{c,m'n'}} \Big[k_{y,m}k_{x,n'} I_1^{nn'}(x_1,x_2,a) I_2^{mm'}(y_1,y_2,b) - k_{x,n}k_{y,m'} I_2^{nn'}(x_1,x_2,a) I_1^{mm'}(y_1,y_2,b) \Big], \tag{7.26}$$

$$C^{\mathrm{TM\cdot TE}}_{mnm'n'} = \frac{(\varepsilon_{0n}\varepsilon_{0m}\varepsilon_{0n'}\varepsilon_{0m'})^{1/2}}{abk_{c,mn}k_{c,m'n'}} \Big[k_{x,n}k_{y,m'} I_1^{nn'}(x_1,x_2,a) I_2^{mm'}(y_1,y_2,b) - k_{y,m}k_{x,n'} I_2^{nn'}(x_1,x_2,a) I_1^{mm'}(y_1,y_2,b) \Big], \tag{7.27}$$

and

$$C^{\mathrm{TM\cdot TM}}_{mnm'n'} = \frac{(\varepsilon_{0n}\varepsilon_{0m}\varepsilon_{0n'}\varepsilon_{0m'})^{1/2}}{abk_{c,mn}k_{c,m'n'}} \Big[k_{x,n}k_{x,n'} I_1^{nn'}(x_1,x_2,a) I_2^{mm'}(y_1,y_2,b) + k_{y,m}k_{y,m'} I_2^{nn'}(x_1,x_2,a) I_1^{mm'}(y_1,y_2,b) \Big]. \tag{7.28}$$

and the C-matrix is grouped as

$$\mathrm{C_{pq}} = \begin{pmatrix} \mathrm{C^{TE\cdot TE}} & \mathrm{C^{TE\cdot TM}} \\ \mathrm{C^{TM\cdot TE}} & \mathrm{C^{TM\cdot TM}} \end{pmatrix}. \tag{7.29}$$

As stated earlier, this is an efficient method to set up the C-matrix of a thin film placed in a waveguide at any position, and the method is valid for absorbers having various patterned structures.

7.2.3 Null-Space in the C-Matrix

C_{mn} can be populated as a $N \times N$ matrix with N the number of waveguide modes used to expand the current. If the film fills the whole waveguide, then C_{mn} satisfy the orthonormality relation

$$\int_S \mathbf{U}_m^*(\mathbf{r}) \cdot \mathbf{U}_n(\mathbf{r}) \mathrm{d}^2\mathbf{r} = \int_W \mathbf{U}_m^*(\mathbf{r}) \cdot \mathbf{U}_n(\mathbf{r}) \mathrm{d}^2\mathbf{r} = \delta_{mn}, \tag{7.30}$$

showing that the waveguide modes are orthogonal with respect to the inner product. There is a possibility that combination of the mode exist $\mathbf{J}(\mathbf{r}) = \sum_{m=1}^{N} j_m \mathbf{U}_m(\mathbf{r})$ that are zero everywhere over the film, which indicates that there is redundancy in the assumed basis functions over the conducting area of the film. The redundancy can be examined by calculating the rank of

the C-matrix: given a function $\mathbf{J}(\mathbf{r})$ in the space spanned by $\{\mathbf{U}_n(\mathbf{r})\}$, there is

$$\int_S \mathbf{U}^*(\mathbf{r}) \cdot \mathbf{J}(\mathbf{r}) \mathrm{d}^2\mathbf{r} = \mathbf{C}_{NN} \cdot \mathbf{j}, \tag{7.31}$$

where $\mathbf{j}$ are vectors of the decomposition coefficients of $\mathbf{J}(\mathbf{r})$ in $\{\mathbf{U}_n(\mathbf{r})\}$. If the rank of the C-matrix, R, is determined to be smaller than N, then it is indicating that the basis has needless components, that are zero everywhere on the film. Assume $\mathbf{j}$ is in this null space, then $\mathbf{j}$ satisfies

$$\mathbf{C}_{NN} \cdot \mathbf{j} = 0, \tag{7.32}$$

and there is

$$\int_S |\mathbf{J}(\mathbf{r})|^2 \mathrm{d}^2\mathbf{r} = 0 \Longleftrightarrow \mathbf{J}(\mathbf{r}) = \mathbf{0} \; \forall \; \mathbf{r} \in S. \tag{7.33}$$

From simulations we have found that, for a large number of modes, the rank R of the C-matrix is much smaller than N, which means some of the eigenvalues must be zero. Figure 7.5 shows the rank of C-matrix, R, as a function of number of field modes E. The operating wavelength was chosen to be λ=1000 μm, and the size of the waveguide is 10λ. The plot shows the results of having different sized films, vary from λ, 2λ, 4λ, 6λ, 8λ and 10λ. The number of current modes N was set to be 840. The number of field modes E varies from 840 to 1860. It can be seen that, for the smaller films, the ranks of C are much less than 840, which means a large number of the basis functions are 0 everywhere. As the film size increases, the number of fields in null space are reduced. In order to recover all of the modes in the case of small films, the number of field modes, E, should be increased.

Although this is not physically important, the existence of these modes can cause problems in numerical evaluations. To overcome this problem, the null-space in the C-matrix should be removed and a smaller set of basis functions without the null-space needs to be derived from the original set. To identify those $\mathbf{j}$ that meet this condition, we consider the eigenvector expansion of C_{NN}, as given by

$$\{C_{NN}\}_{mn} = \sum_{p=1}^{N} \lambda_p V_{mp} V_{np}^*, \tag{7.34}$$

where $\{\lambda_p\}$ are the set of real and non-zero eigenvalues, and V_{mp} is a $N \times N$ matrix of the decomposition coefficients of the eigenvectors of the C-matrix in the basis, which follows

$$\sum_{p=1}^{N} V_{mp} V_{np}^* = \sum_{p=1}^{N} V_{mp}^* V_{np} = \delta_{mn}. \tag{7.35}$$

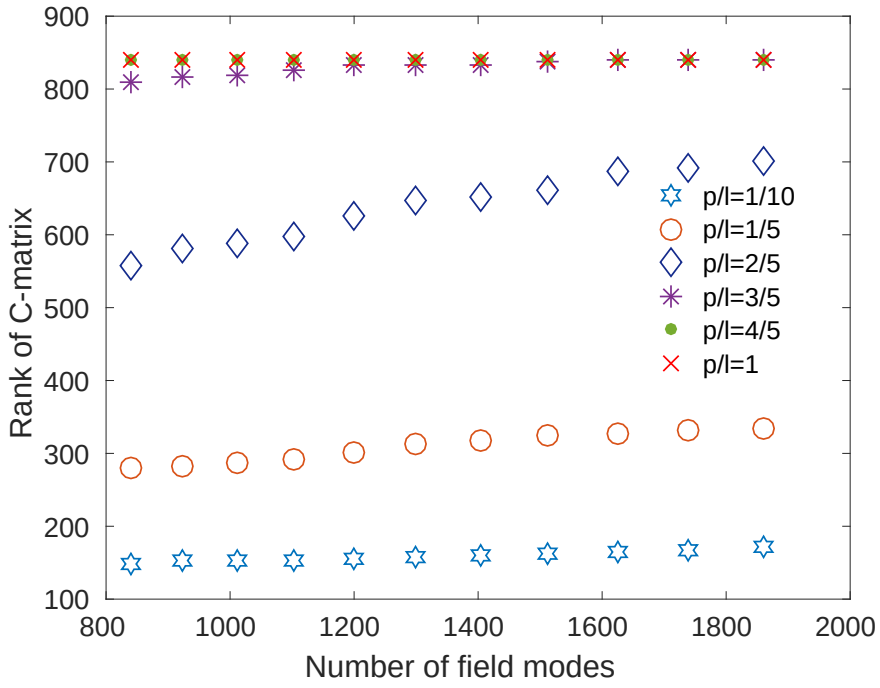

Fig. 7.5 Rank(C_{NN}) as a function of the field mode set, E for various sized films.

In numerical simulations, the eigenvalues $\{\lambda_p\}$ can be sorted in descending order with p. It is the eigenvectors with zero eigenvalues that correspond to solutions that satisfy Eq.(7.32). Express Eq. (7.34) in the form of matrices as

$$\mathbf{C} = \mathbf{V} \cdot \mathbf{S} \cdot \mathbf{V}^{\dagger}. \tag{7.36}$$

Manipulating the above algebraic expression we have

$$\mathbf{S}^{-1/2} \cdot \mathbf{V}^{\dagger} \cdot \mathbf{C} \cdot \mathbf{V} \cdot \mathbf{S}^{-1/2} = \mathbf{I}. \tag{7.37}$$

Thus the null-space can be then stripped out. Thus a new basis without this null-space can be defined as

$$\{\mathbf{K}_p(\mathbf{r}) = \sum_{n=1}^{N} \lambda_p^{-1/2} V_{np} h(\mathbf{r}) \mathbf{U}_n(\mathbf{r}), p = 1,2,3,...R\}, \tag{7.38}$$

which will be the minimum sized basis function that spans the non-zero field distributions over S, and $\mathbf{K}_m(\mathbf{r}) = 0$ in the empty region by definition. It follows from Eq. (7.38) and (7.35) that $\{\mathbf{K}_m(\mathbf{r})\}$ satisfy orthonomality relation

$$\int_A \mathbf{K}_m^*(\mathbf{r}) \cdot \mathbf{K}_n(\mathbf{r}) \mathrm{d}^2\mathbf{r} = \int_S \mathbf{K}_m^*(\mathbf{r}) \cdot \mathbf{K}_n(\mathbf{r}) \mathrm{d}^2\mathbf{r} = \delta_{mn}. \tag{7.39}$$

The field distributions given by the new basis function can be calculated from $|\mathbf{K}_n(\mathbf{r})|^2$. Select a film with side length $l = 2\lambda$, mounted in a waveguide with side length $p = 10\lambda$, with the operating wavelength λ=1000 μm. The $\mathbf{C}_{NN}$ matrix was produced by using a total of 840 of current modes, with 440 TE modes and 400 TM modes. If there is redundancy in the basis $\{\mathbf{U}_n(\mathbf{r})\}$, the rank of C_{NN} should be less than 840. From the numerical calculations, it was found that the rank of the C-matrix, R, was 280, which is telling us that there are 560 modes having zero eigenvalues.

Figures 7.6 to 7.9 show the field intensities of waveguide modes normalised to their maxima. The basis functions $\{\mathbf{U}_n(\mathbf{r})\}$ and $\{\mathbf{K}_n(\mathbf{r})\}$ were used to produced the intensity distributions on the left and right column respectively. The $\hat{x}$-, $\hat{y}$- and unpolarised field distributions are shown from the first row to the bottom. The red square shown on each plot represents the position and the size of the film within the waveguide. A MatLab program was written to sort the mode set in descending order of eigenvalues. Figures 7.6 to 7.9 show the 1st, 15th, 30th and 300th mode of the sorted mode set: the 1st, 15th and 30th modes have non-zero eigenvalues, and 300th mode has zero eigenvalue. Figure 7.6 shows the intensity patterns of mode TE_{10}. It can be seen that for the modes with non-zero eigenvalues, the fields given by $\{\mathbf{K}_n(\mathbf{r})\}$ are well constrained within the film, as shown in Figures 7.6, 7.7 and 7.8. Figure 7.9 shows an example of a null space, it can be seen that the field is zero everywhere in the waveguide.

7.2.4 Infinity Modal Impedance in Z-Matrix

As stated earlier, the $\{\mathrm{Z}\}_{mn}$ in Eq.(7.12) can cause numerical problems, as the mode impedances of the TE modes tends to infinity when frequency is close to the cut-off. Thus the Z-matrix can contain very large terms, and create a dynamic range problem for the inversion routine. To solve this problem, we can rewrite $\{\mathrm{Z}\}_{mn}$ as the product of two diagonal matrices

$$\mathbf{Z} = \mathrm{P}^{-1} \cdot \mathrm{Q}, \tag{7.40}$$

where

$$\{\mathrm{P}\}_{mn} = \begin{cases} Z_p^{-1}, & m = n \text{ and } p \text{ is a TE mode} \\ 1, & m = n \text{ and } p \text{ is a TM mode} \\ 0, & m \neq n, \end{cases} \tag{7.41}$$

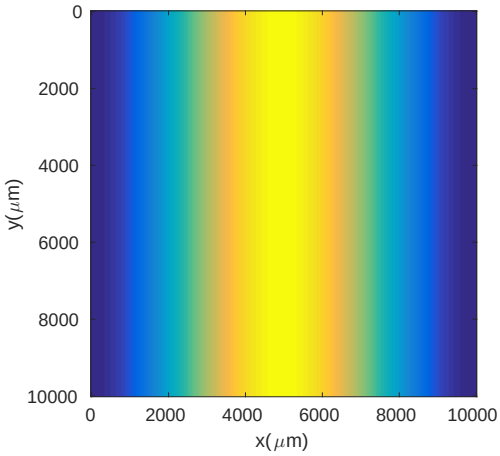

(a) $|\mathbf{U}_x(\mathbf{r})|^2$

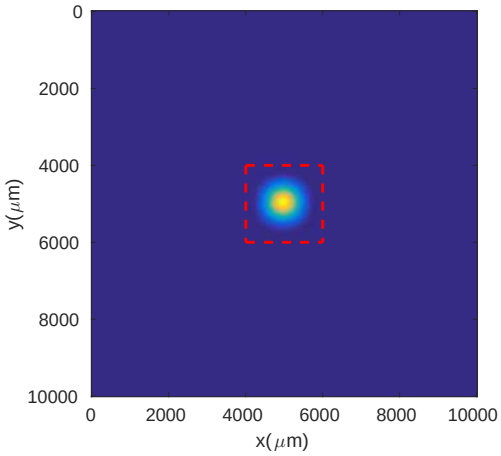

(b) $|\mathbf{K}_x(\mathbf{r})|^2$

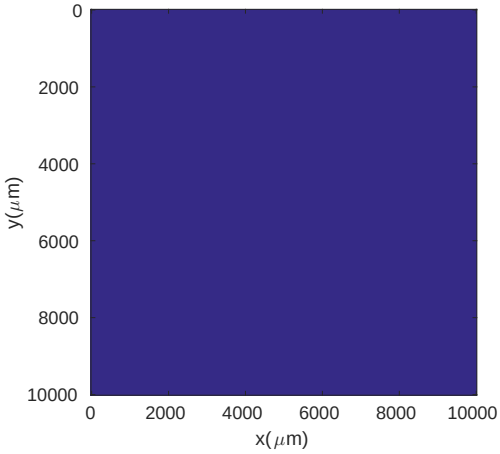

(c) $|\mathbf{U}_y(\mathbf{r})|^2$

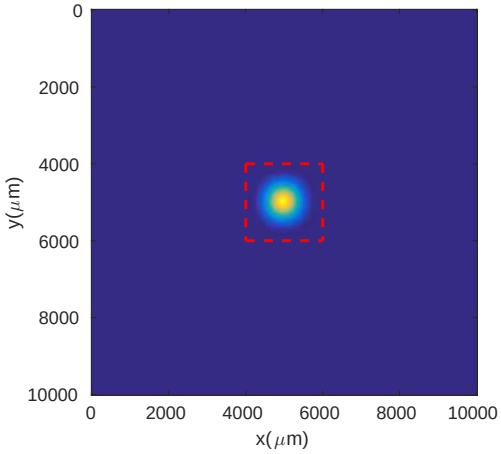

(d) $|\mathbf{K}_y(\mathbf{r})|^2$

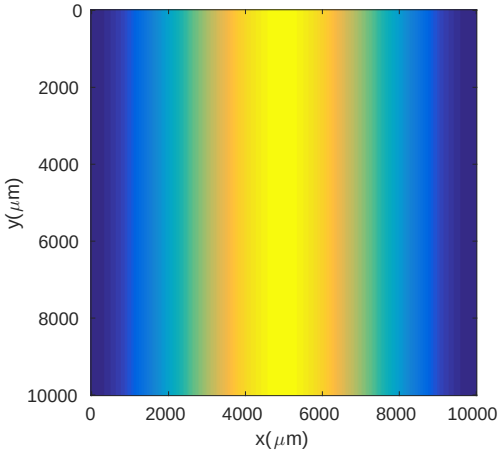

(e) $|\mathbf{U}_x(\mathbf{r})|^2+|\mathbf{U}_y(\mathbf{r})|^2$

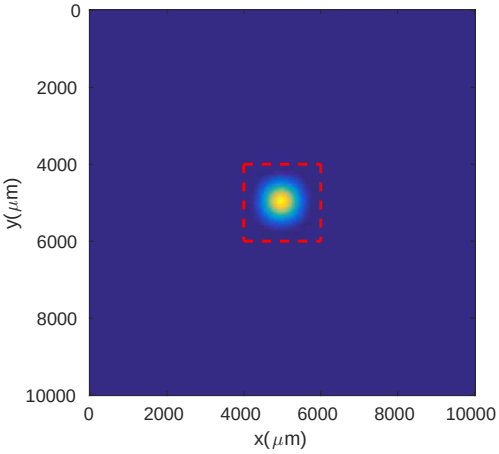

(f) $|\mathbf{K}_x(\mathbf{r})|^2+|\mathbf{K}_y(\mathbf{r})|^2$

Fig. 7.6 The intensity distributions of the 1st mode in the simulations that has non-zero eigenvalue across the cross-section of waveguide at wavelength λ=1000 μm, with the side length of the waveguide l=10λ and that of film p=2λ. Red dashed square represents the position and size of the film with respect to the waveguide. Plots on the left and right columns are produced with basis functions $\mathbf{U}(\mathbf{r})$ and $\mathbf{K}(\mathbf{r})$ respectively; each row plots the different polarisations of the field, the x-, y- and unpolarised field are shown from top to bottom.

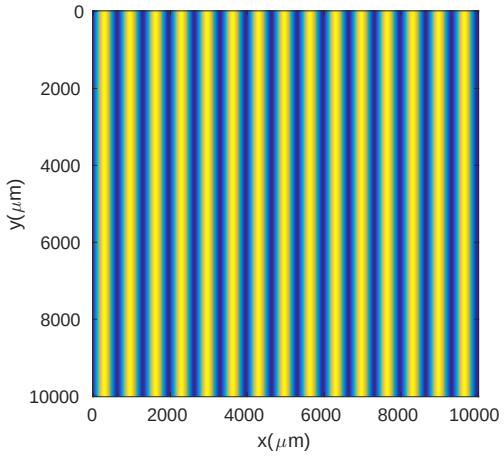

(a) $|\mathbf{U}_x(\mathbf{r})|^2$

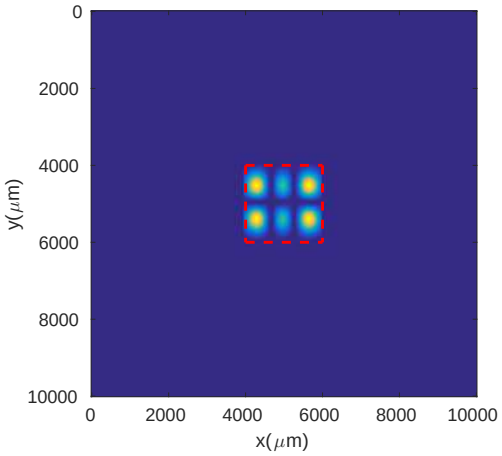

(b) $|\mathbf{K}_x(\mathbf{r})|^2$

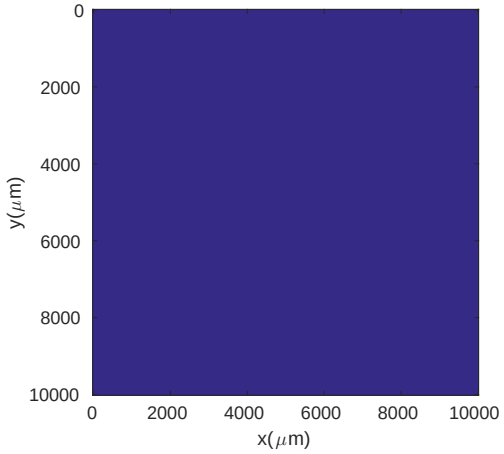

(c) $|\mathbf{U}_y(\mathbf{r})|^2$

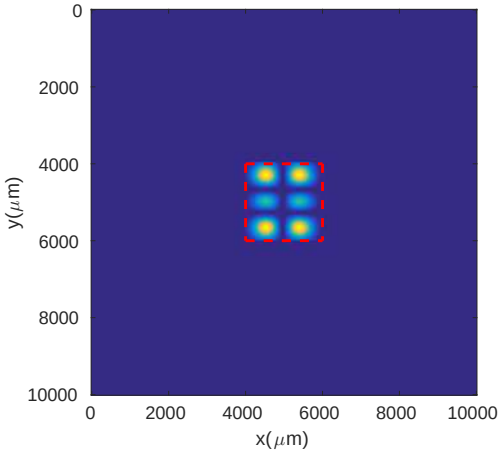

(d) $|\mathbf{K}_y(\mathbf{r})|^2$

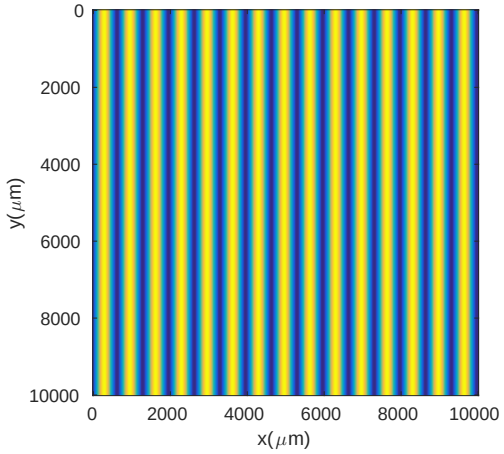

(e) $|\mathbf{U}_x(\mathbf{r})|^2+|\mathbf{U}_y(\mathbf{r})|^2$

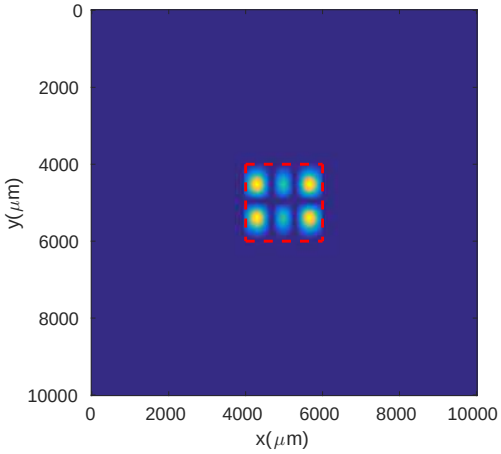

(f) $|\mathbf{K}_x(\mathbf{r})|^2+|\mathbf{K}_y(\mathbf{r})|^2$

Fig. 7.7 The intensity distributions of the 15th mode in the simulations that has non-zero eigenvalue across the cross-section of waveguide at wavelength λ=1000 μm, with the side length of the waveguide l=10λ and that of film p=2λ. Red dashed square represents the position and size of the film with respect to the waveguide. Plots on the left and right columns are produced with basis functions $\mathbf{U}(\mathbf{r})$ and $\mathbf{K}(\mathbf{r})$ respectively; each row plots the different polarisations of the field, the x-, y- and unpolarised field are shown from top to bottom.

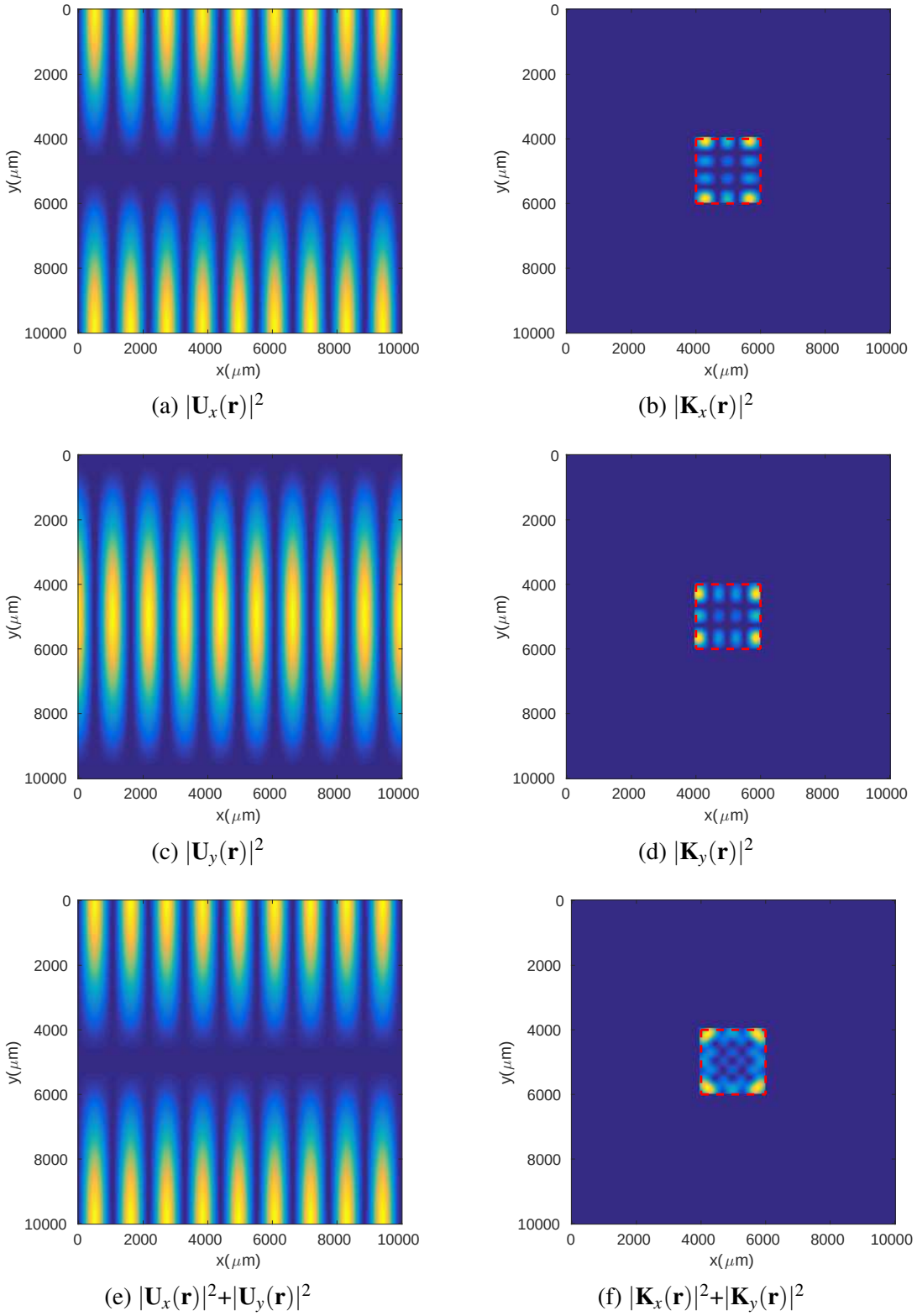

(a) $|\mathbf{U}_x(\mathbf{r})|^2$ (b) $|\mathbf{K}_x(\mathbf{r})|^2$

(c) $|\mathbf{U}_y(\mathbf{r})|^2$ (d) $|\mathbf{K}_y(\mathbf{r})|^2$

(e) $|\mathbf{U}_x(\mathbf{r})|^2+|\mathbf{U}_y(\mathbf{r})|^2$ (f) $|\mathbf{K}_x(\mathbf{r})|^2+|\mathbf{K}_y(\mathbf{r})|^2$

Fig. 7.8 The intensity distributions of the 30th mode in the simulations that has non-zero eigenvalue across the cross-section of waveguide at wavelength λ=1000 μm, with the side length of the waveguide l=10λ and that of film p=2λ. Red dashed square represents the position and size of the film with respect to the waveguide. Plots on the left and right columns are produced with basis functions $\mathbf{U}(\mathbf{r})$ and $\mathbf{K}(\mathbf{r})$ respectively; each row plots the different polarisations of the field, the x-, y- and unpolarised field are shown from top to bottom.

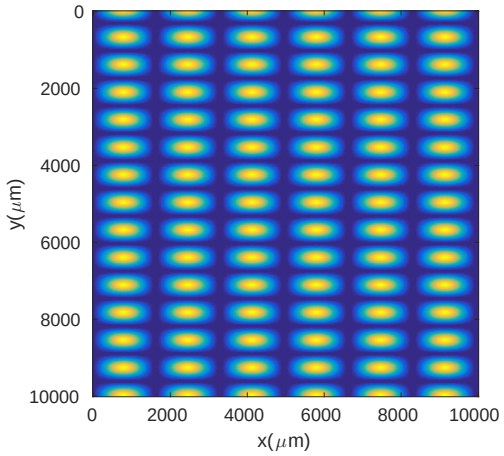

(a) $|\mathbf{U}_x(\mathbf{r})|^2$

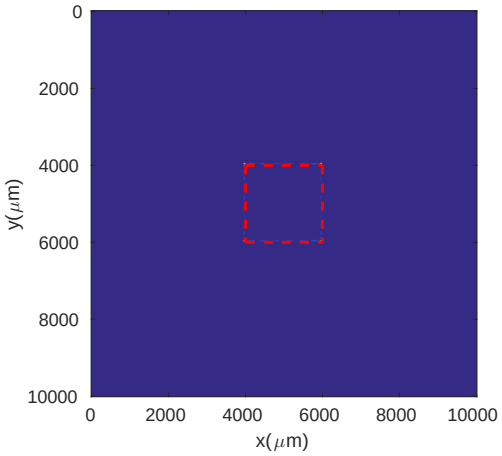

(b) $|\mathbf{K}_x(\mathbf{r})|^2$

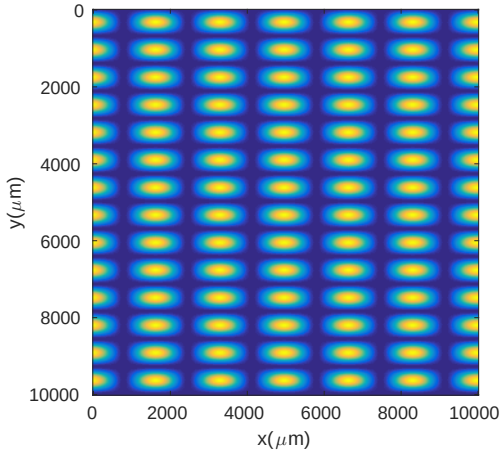

(c) $|\mathbf{U}_y(\mathbf{r})|^2$

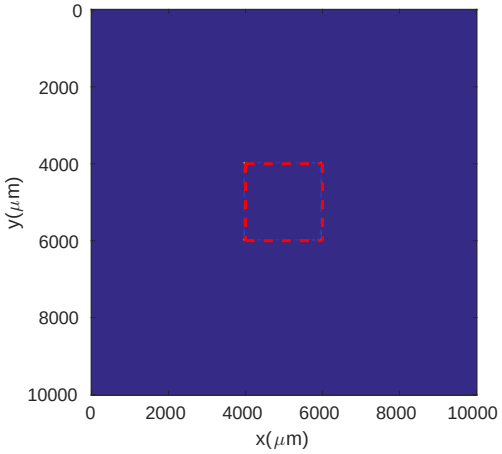

(d) $|\mathbf{K}_y(\mathbf{r})|^2$

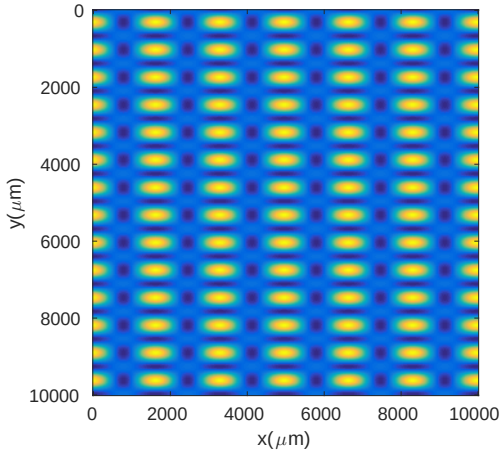

(e) $|\mathbf{U}_x(\mathbf{r})|^2+|\mathbf{U}_y(\mathbf{r})|^2$

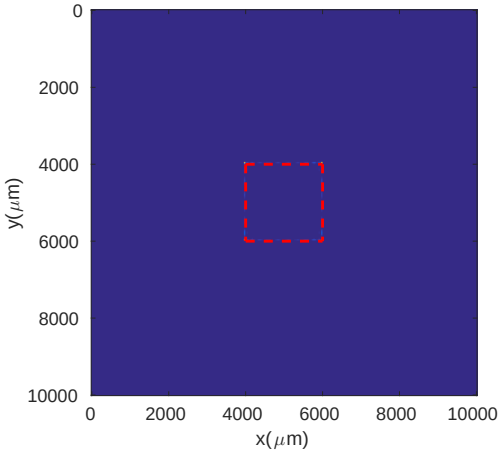

(f) $|\mathbf{K}_x(\mathbf{r})|^2+|\mathbf{K}_y(\mathbf{r})|^2$

Fig. 7.9 The intensity distributions of the 300th mode in the simulations that has non-zero eigenvalue across the cross-section of waveguide at wavelength λ=1000 μm, with the side length of the waveguide l=10λ and that of film p=2λ. Red dashed square represents the position and size of the film with respect to the waveguide. Plots on the left and right columns are produced with basis functions $\mathbf{U}(\mathbf{r})$ and $\mathbf{K}(\mathbf{r})$ respectively; each row plots the different polarisations of the field, the x-, y- and unpolarised field are shown from top to bottom.

and

$$\{\mathrm{Q}\}_{mn} = \begin{cases} Z_p, & m = n \text{ and } p \text{ is a TM mode} \\ 1, & m = n \text{ and } p \text{ is a TM mode} \\ 0, & m \neq n. \end{cases} \tag{7.42}$$

Both P and Q have well-defined inverses.

7.3 Solving the Current Equation

7.3.1 Formalisms

Expand the induced sheet current density $\mathbf{J}(\mathbf{r})$ in terms of the new basis functions, $\mathbf{K}_m(\mathbf{r})$, as

$$\mathbf{J}(\mathbf{r}) = \sum_{m=1}^{R} j'_m \mathbf{K}_m(\mathbf{r}). \tag{7.43}$$

Comparing to Eq.(7.5), $\mathbf{J}(\mathbf{r}) = \mathbf{0}$ when $\mathbf{j}' = \mathbf{0}$ in Eq.(7.43), which provides a better numerical conditioning. Inserting Eq.(7.38) into (7.43),

$$\mathbf{J}(\mathbf{r}) = \sum_{n=1}^{N} \sum_{m=1}^{R} \lambda_m^{-1/2} V_{nm} j'_m h(\mathbf{r}) \mathbf{U}_n(\mathbf{r}), \tag{7.44}$$

where R is the set of current modes. The current can be reconstructed from $\mathbf{j}'$, which can be obtained from

$$\begin{aligned} j'_m &= \int_S \mathbf{K}_m^*(\mathbf{r}) \cdot \mathbf{J}_S(\mathbf{r}) \mathrm{d}^2\mathbf{r} \\ &= \int_S \mathbf{K}_m^*(\mathbf{r}) \cdot Y_S[\mathbf{E}_I(\mathbf{r}) + \mathbf{E}_S(\mathbf{r})] \mathrm{d}^2\mathbf{r} \\ &= Y_S \int_S \mathbf{K}_m^*(\mathbf{r}) \cdot \mathbf{U}_n(\mathbf{r}) \mathrm{d}^2\mathbf{r} \\ &- \frac{1}{2} Y_S \sum_m Z_m \int_S \mathbf{K}_m^*(\mathbf{r}) \cdot \mathbf{U}_n(\mathbf{r}) \mathrm{d}^2\mathbf{r} \int_S \mathbf{U}_n^*(\mathbf{r}) \cdot \sum_m j'_m \mathbf{K}_m(\mathbf{r}) \mathrm{d}^2\mathbf{r}, \end{aligned} \tag{7.45}$$

which can be expressed with a matrix equation as

$$\mathbf{j}' = Y_S \mathbf{A}_{RE} \cdot \mathbf{e}_I - \frac{1}{2} Y_S \mathbf{A}_{RG} \cdot \mathbf{Z}_{GG} \cdot \mathbf{A}_{GR}^{\dagger} \cdot \mathbf{j}', \tag{7.46}$$

where

$$A_{mn} = \int_S \mathbf{K}_m^*(\mathbf{r}) \cdot \mathbf{U}_n(\mathbf{r}) \mathrm{d}^2\mathbf{r} = \sum_{p=1}^{N} \lambda_n^{-1/2} V_{pm}^* C_{pn}. \tag{7.47}$$

The subscripts of matrix A indicate the matrix sizes, A_{RE} and A_{RG} are $R \times E$ and $R \times G$ matrices: R is the set of current modes, E is the size of modes needed to expand $\mathbf{E}_I(\mathbf{r})$, and G is the number of modes used in the Green's function expansion. Vectors $\{\mathbf{e}_I\}$ can be determined from relation

$$\{\mathbf{e}_I\}_m = \int_S \mathbf{U}_m^*(\mathbf{r}) \cdot \mathbf{E}_I(\mathbf{r}) \mathrm{d}^2\mathbf{r}. \tag{7.48}$$

$\mathbf{j}'$ can be solved from Eq. (7.46) as

$$\mathbf{j}' = Y_S \left[\mathrm{I}_R + \frac{1}{2} Y_S \mathrm{A}_{RG} \cdot \mathrm{Z}_{GG} \cdot \mathrm{A}_{GR}^{\dagger} \right]^{-1} \cdot \mathrm{A}_{RE} \cdot \mathbf{e}_I. \tag{7.49}$$

The inversion in the above equation can be expanded using Woodbury Matrix Identity [21, 65],

$$(A + BCD)^{-1} = A^{-1} - A^{-1}U(C^{-1} + DA^{-1}B)^{-1}DA^{-1}, \tag{7.50}$$

to give

$$\mathbf{j}' = Y_S \left[\mathrm{I}_R - \frac{1}{2} Y_S \mathrm{A}_{RG} \cdot \left(\mathrm{I}_G + \frac{1}{2} Y_S \cdot \mathrm{Z}_{GG} \cdot \mathrm{A}_{GR}^{\dagger} \cdot \mathrm{A}_{RG} \right)^{-1} \cdot \mathrm{Z}_{GG} \cdot \mathrm{A}_{GR}^{\dagger} \right] \cdot \mathrm{A}_{RE} \cdot \mathbf{e}_I. \tag{7.51}$$

To avoid having singularities in the inversion routine in Eq.(7.51), Z_{GG} can be re-written using Eq.(7.41) and (7.42). Then Eq.(7.51) can be expressed as

$$\mathbf{j}' = Y_S \left[\mathrm{I}_R - \mathrm{A}_{RG} \cdot \left(Y_S^{-1} \cdot 2\mathrm{P}_{GG} + \mathrm{Q}_{GG} \cdot \mathrm{A}_{GR}^{\dagger} \cdot \mathrm{A}_{RG} \right)^{-1} \cdot \mathrm{Q}_{GG} \cdot \mathrm{A}_{GR}^{\dagger} \right] \cdot \mathrm{A}_{RE} \cdot \mathbf{e}_I, \tag{7.52}$$

with the infinite terms removed. In numerical simulation, G should be chosen large enough so that $\mathbf{j}'$ converges. From $\mathbf{j}'$, the induced sheet currents can be determined for any given incident field.

7.3.2 Numerical Method

To numerically obtain the current distributions from Eq.(7.52), a finite set, N, of basis functions are firstly required to expand the current, then the redundancy in the basis should be checked by determining the rank, R, of the $N \times N$ C-matrix. If $\mathrm{rank}(C) < N$, which indicates that there is null space in the C-matrix. The redundancy should be then removed by defining a modified basis, such that the eigenvalues of the C-matrix are all real and non-zero, and the

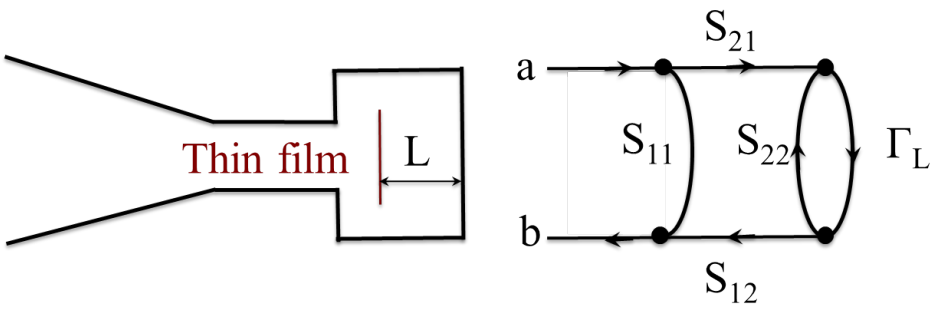

Fig. 7.10 Metallic thin film mounted in a shorted multimode waveguide (left); the relative signal flow graph (right).

C-matrix can be written as an eigenvector decomposition as described in Eq.(7.34) summing from 1 to *R*. The new basis set will be the minimum sized basis that spans the non-zero field distributions over the area considered. By doing these steps, the current density can be written as a single decomposition of the new basis, summing over from 1 to *R*.

The Green's dyadic is given by a infinite sum, thus the numerical evaluation of $\overline{\overline{G}}(\mathbf{r},\mathbf{r}')$ requires we truncate the infinite sum to the first *G* modes. The coefficients of the induced current density j'_m are solved as described in Eq.(7.52). Once the current basis functions have been fixed, the first term in Eq.(7.52) is fixed; whereas the second term in the equation depends on the choice of *G*, as we have artificially truncated the Green's dyadic to a subset of all the waveguide modes. Therefore, *G* must be set sufficiently large such that the second term converges. During the numerical test, *G* was usually chosen to be the same as *N* initially, and the number was increased gradually until the functional form of the generated current plots remained unchanged.

7.4 Scattering Parameters

Consider a rectangular thin film is mounted in a multimoded waveguide, and a reflective backshort placed behind the film, as shown in Figure 7.10. Assume a travelling wave **a** is incident on the thin film, and another wave **b** is reflected from the film. The absorbed power is simply given by

$$P = |\mathbf{a}|^2 - |\mathbf{b}|^2. \tag{7.53}$$

The trace of the incoming waves through the system can be described by the scattering parameters.

To find the natural modes which are responsible for absorbing energy, we can set up a response matrix Π,

$$\Pi = \mathrm{I} - \Gamma^{\dagger}\Gamma, \tag{7.54}$$

where Γ corresponds to the total input reflection, which is given by

$$\Gamma = \mathrm{S}_{11} + S_{12}[I - \Gamma_L \mathrm{S}_{22}]^{-1}\Gamma_L \mathrm{S}_{21}. \tag{7.55}$$

$\{\Gamma_L\}_{mn}$ is the reflection from the backshort for the mn-th mode, which can be populated as a reflection matrix from

$$(\Gamma_L)_{mn} = -\exp[+i\beta_{mn}2L]\delta_{nm}, \tag{7.56}$$

where L is the distance between the film and the backshort, β_{mn} are the modal propagation constant, which was introduced earlier in Eq.(2.55) from Chapter 2. The response matrix Π can be diagonalised as

$$\Pi = \mathrm{W}\Lambda\mathrm{W}^{\dagger}, \tag{7.57}$$

where W is the matrix containing the eigenvectors of Π, and Λ is a diagonal matrix containing the associated eigenvalues. The eigenvectors and eigenvalues correspond to the natural modes that the system is sensitive to and the relative sensitivities. The full derivations are presented by Withington and Thomas in [63].

To determine the eigenvectors and eigenvalues in Eq.(7.57), the scattering parameters must be calculated. The field scattered by the currents, $\mathbf{E}_S(\mathrm{r})$, can be expanded as in terms of a set of waveguide modes as

$$\mathbf{E}_S(\mathrm{r}) = \sum_{m=1}^{E} e_m^{(S)} \mathbf{U}_m(\mathrm{r}). \tag{7.58}$$

Similarly, vectors $\{\mathbf{e}_S\}$ can be calculated from relation

$$\{\mathbf{e}_S\}_m = \int_S \mathbf{U}_m^*(\mathbf{r}) \cdot \mathbf{E}_S(\mathbf{r}) \mathrm{d}^2\mathbf{r}. \tag{7.59}$$

Substituting Eq. (7.2) and (7.3) into (7.59), $\{\mathbf{e}_S\}$ can be solved as

$$\begin{aligned}\mathbf{e}_S &= -\frac{1}{2}\mathrm{Z}_{EE} \cdot \mathrm{A}_{RE}^{\dagger} \cdot \mathbf{j}' \\ &= -\frac{1}{2} Y_S \mathrm{Z}_{EE} \cdot \mathrm{A}_{RE}^{\dagger} \cdot \left[\mathrm{I}_R - \mathrm{A}_{RG} \cdot \left(Y_S^{-1} \cdot 2\mathrm{P}_{GG} + \mathrm{Q}_{GG} \cdot \mathrm{A}_{GR}^{\dagger} \cdot \mathrm{A}_{RG}\right)^{-1} \cdot \mathrm{Q}_{GG} \cdot \mathrm{A}_{GR}^{\dagger}\right] \cdot \mathrm{A}_{RE} \cdot \mathbf{e}_I.\end{aligned} \tag{7.60}$$

Thus the scattering parameters are given by

$$\mathrm{S}_{11} = -\frac{1}{2} Y_S \mathrm{Z}_{EE} \cdot \mathrm{A}_{RE}^{\dagger} \cdot \left[\mathrm{I} - A_{RG} \cdot \left(Y_S^{-1} \cdot 2\mathrm{P}_{GG} + \mathrm{Q}_{GG} \cdot \mathrm{A}_{GR}^{\dagger} \cdot \mathrm{A}_{RG} \right)^{-1} \cdot \mathrm{Q}_{GG} \cdot \mathrm{A}_{GR}^{\dagger} \right] \cdot \mathrm{A}_{RE}, \tag{7.61}$$

and

$$\begin{aligned} \mathrm{S}_{12} &= \mathrm{I} + \mathrm{S}_{11} \\ &= \mathrm{I} - \frac{1}{2} Y_S \mathrm{Z}_{EE} \cdot \mathrm{A}_{RE}^{\dagger} \cdot \left[\mathrm{I}_R - A_{RG} \cdot \left(Y_S^{-1} \cdot 2\mathrm{P}_{GG} + \mathrm{Q}_{GG} \cdot \mathrm{A}_{GR}^{\dagger} \cdot \mathrm{A}_{RG} \right)^{-1} \cdot \mathrm{Q}_{GG} \cdot \mathrm{A}_{GR}^{\dagger} \right] \cdot \mathrm{A}_{RE}. \end{aligned} \tag{7.62}$$

From the symmetry of the problem we know that $\mathrm{S}_{11} = \mathrm{S}_{22}$ and $\mathrm{S}_{12} = \mathrm{S}_{21}$. Once the scattering parameters are calculated, matrix Π in Eq.(7.57) can be then constructed. It then can be diagonalised to determine the modes which are responsible for energy absorption and their associated sensitivities.

7.5 Simulations

7.5.1 Eigenvalue spectra of the films

The model was used to analyse the optical behaviour of a thin film in a square waveguide. This system was using a different approach from Withington and Thomas [63]. The parameters for the simulations presented here are the same as those used in the cited paper. Consider the film is positioned in a square waveguide with side length 10λ, and the film extends all the way across the waveguide. The operating wavelength was chose to be 1000 μm. Assume the sheet impedance of the film Z_S=377 Ω.

Figure 7.11 shows the eigenvalues spectra of a $10\lambda \times 10\lambda$ thin film in a $10\lambda \times 10\lambda$ waveguide as the position of the backshort is varied. The eigenvalues correspond to the efficiencies of the waveguide modes which are responsible for absorbing energy. The different plots represent different distances from the film to the backshorts. In my simulation, a total of 967 waveguide modes were used, with 483 TE modes, and 484 TM modes. Only 628 of them are propagating modes, which are able to transfer energy. All of the 628 modes were used to produce the response matrix. The step-like structure shown in the plot indicates the degeneracies. It can be seen that some of the eigenvalues are much less than 1, even the film was across the whole waveguide cross-section. This is because the impedance mismatch is more significant for the modes having higher impedance. In addition, the position of the backshort also affect the sensitivities. The overall performance peaks when

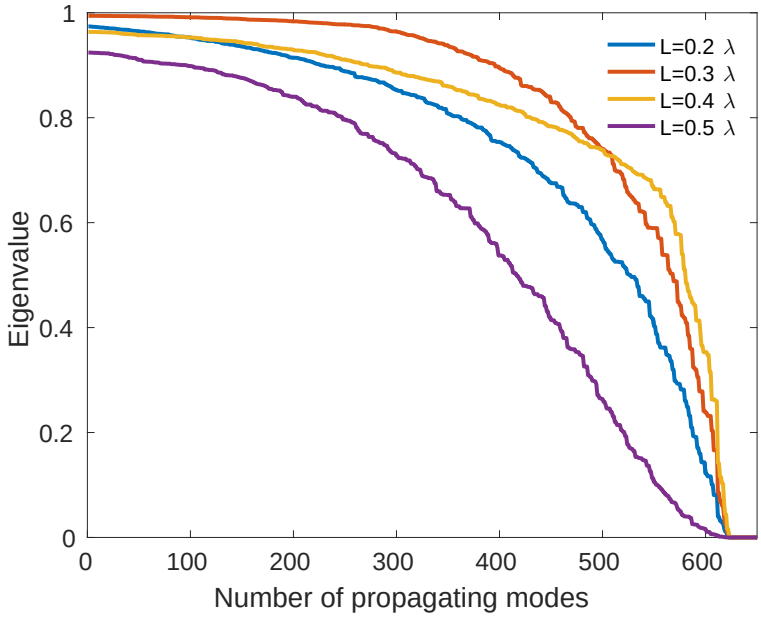

Fig. 7.11 Eigenvalues spectra of a thin film mounted within a shorted multimode waveguide having dimensions $10\lambda \times 10\lambda$, and assuming the film fills over the whole waveguide. The different plots correspond to have a backshort placed 0.2λ, 0.3λ, 0.4λ and 0.5λ behind the thin film, and λ=1000 μm. The impedance of the film used for calculation was 377 Ω.

$L = 0.3\lambda$. Figure 7.11 are identical compared to what was presented earlier in the cited paper, which indicates that the new procedure for modelling the optical behaviour of thin films in waveguide is correct.

Figure 7.12 shows how the mode coefficients change as p/λ is varied. The eigenvalue spectra of the thin films having dimensions of $4\lambda \times 4\lambda$, $2\lambda \times 2\lambda$, $1\lambda \times 1\lambda$, $0.5\lambda \times 0.5\lambda$, and $0.25\lambda \times 0.25\lambda$ in a $10\lambda \times 10\lambda$ waveguide are shown in the plot. The films were all centred on the axis of the waveguide. The position of the backshort was fixed at 0.3λ, as from Figure 7.11, it seems that the overall performance reached the optimum at this position. The other parameters, such as the impedance of the film, number of waveguide modes considered, were all set the same as in the previous simulations. It can be seen that as the size of the film decreases, the number of modes decreases accordingly, as would be expected. When $p/\lambda < 1$, only a small number of modes are present, and some of these are degenerate. These results are nearly identical with simulations presented in [63].

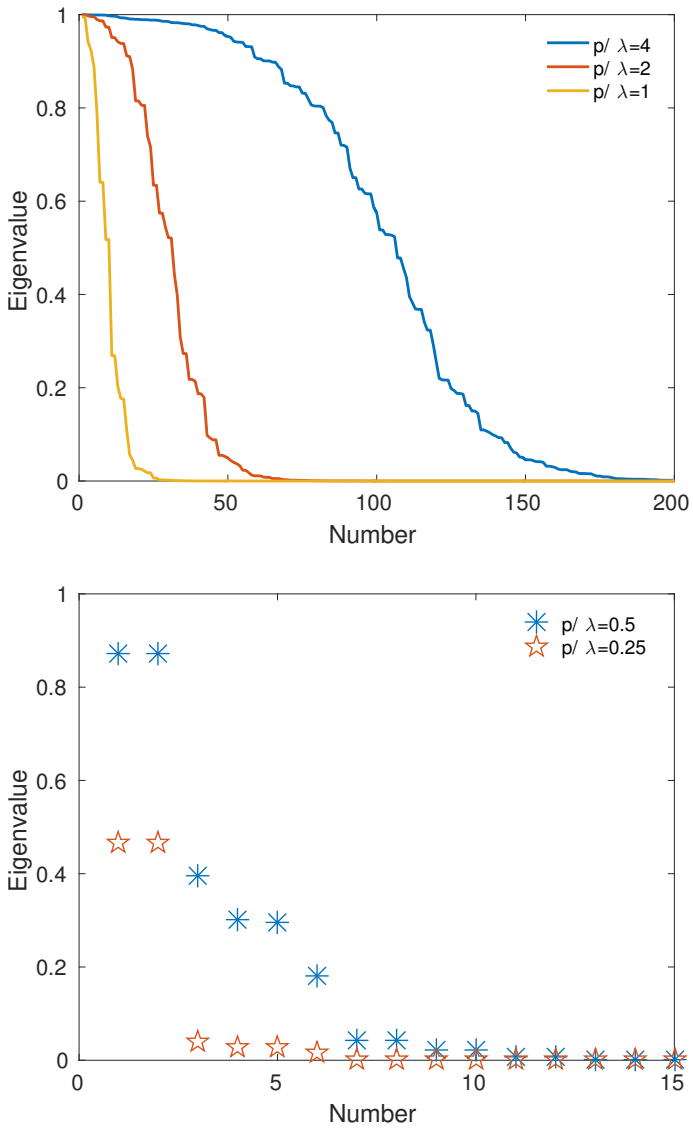

Fig. 7.12 Eigenvalue spectra of square absorbers having dimensions $4\lambda \times 4\lambda$, $2\lambda \times 2\lambda$, $1\lambda \times 1\lambda$, $0.5\lambda \times 0.5\lambda$, and $0.25\lambda \times 0.25\lambda$ in a square waveguide with side length of 10λ, a backshort placed 0.3λ behind the thin film is considered.

7.5.2 Induced Sheet Currents

Using Eq.(7.52), the induced sheet currents on the film can be calculated. For all the simulations, it was assumed that filled absorbers were mounted in a waveguide whose side length was 10λ. Figure 7.13 shows the current distribution induced at the centre of films having various sizes and impedances. The side length of the film, p/λ, increases from left to right across the figure, and the impedance of film, Z_S, increases from top down to the bottom of the figure. The y-axis of each plot shows the x-component of the sheet currents, $|J_x|$, which has been normalised to the magnetic field intensity of the wave $|H_y|$ to remove the dependence on field strength. The blue line in each plot shows the current along the cut $(x, b/2, 0)$, and the red line shows the current along $(a/2, y, 0)$. The dashed black line corresponds to the approximated current distribution expected along the two cuts, which is uniform across the centre of the film and given by relation [50],

$$\frac{|J_x|}{|H_y|} \approx \frac{Z_0}{Z_S + \frac{1}{2}Z_0}, \tag{7.63}$$

which is the value for an infinite sheet. The values of $|J_x|/|H|$ determined from Eq. (7.63) for different Z_S are listed in Table 7.1.

Table 7.1 Effective number of detected modes of the measurements and the numerical predictions.

Z_S/Z_0	0.0	0.5	1.0	2.0	10.0
$\|J_x\|/\|H_y\|$	2.00	1.00	0.67	0.40	0.10

From Figure 7.13, it can be seen that the sheet current at the centre of each film is symmetric. The red lines, y-cuts, correspond to the current directions tangential to the film boundary, and the blue lines, x-cuts, correspond to the current directions normal to the edges.

For fixed impedance Z_S/Z_0, the mean value of current roughly stays at the same level for various sized absorbers. For fixed absorber size, p/λ, the mean value of current decreases as Z_S increases, and the current distributions are flatter for larger impedance.

For films having non-zero impedance, the sheet current at the centre of 2λ and 4λ films are almost the same as the simple model predicts (black dashed lines). But the simple model cannot provide an estimation for the current at the edges, and this is noticeable in almost all of the plots in Figure 7.13. This is an issue with the behaviour at the edges.

In the case of having zero impedance, the current tends to infinity at the edges. Except for the smallest absorber, the current distributions found for the zero-impedance case are comparable with those in the literature [7]. When the film impedance Z_S is Z_0 or $Z_0/2$, the

currents at the centre of smaller films are greater than in the case of having larger films. As the impedance increased to $Z_S = 10Z_0$, the currents are almost constant across the centre of the films, which are essentially equal to what the simple model calculation.

In [50], Thomas et. al. presented the sheet induced currents induced on free-space coupled square films calculated using a rigorous impedance sheet model, and it is pleasing to see that the results of my model in the regime that detector technology is required are in good agreement. My model however struggles to recover the sheet current for the extreme cases where the absorber size $p/\lambda < 1$ and the sheet impedance of the absorber, Z_S is 0. Noticeable edge-effects are seen in the current plots on small absorbers, as would be expected [30, 20]. Nevertheless, the method presented here provides an efficient numerical approach for studies on astronomical detectors.

The electric field can be recovered by determining the eigenmodes of the films using Eq.(7.57), as W is the matrix containing the eigenvectors of the response matrix, and each column of the matrix corresponds to the coefficients of that eigenmode. Figure 7.14 and 7.15 show the magnitude of x- and y-oriented electric field associated with the first eigenmode that have the highest mode coefficients for those films having dimensions $p/\lambda > 1$ and non-zero impedance absorbers. The films were considered as placed within the centre of a $10\lambda \times 10\lambda$ waveguide, as illustrated by the dashed red squares in the plots. It can be seen that the field is not merely constrained on the thin film. The non-zero field presents at about one wavelength away from the edges. As the absorber size increases, more standing waves add up and forms more complex functional forms.

7.6 Conclusions

A mode-matching method for modelling waveguide-mounted thin films in infrared detectors has been developed. The method is numerically efficient, and can handle calculations with a large number of modes for various types of absorbing films. The waveguide modes were chosen to be the basis functions to expand the incident field and sheet current. An analytical procedure of calculating the overlap integral of the basis functions over a finite area was presented, which made the numerical modelling of the thin films more efficient, which also opens a possibility to efficiently simulate the electromagnetic behaviours of other components such as band-pass filters.

The scattering parameters of a finite sized film were determined, and used to calculate the response of a thin film mounted in a waveguide. The eigenvalue spectra of the thin film having various dimensions were determined, which are identical to the results in the cited paper, where a different approach was applied.

I have calculated the induced sheet current on the film for various film sizes and impedances. There were two numerical issues in the current simulations, which was the existence of null-space in the C-matrix, and the infinity elements exist in the Z-matrix. I have described a method to form a new basis functions of the field without null-space, which is crucial for calculating of the induced sheet currents on the films, as fields in null-space cannot be constrained numerically; and a method to avoid having the modes with very large impedance appear in the Z-matrix. The method provides a good estimation of the behaviour of films having dimensions $p/\lambda > 1$ and with non-zero impedance, which is suitable for application to designing astronomical detectors.

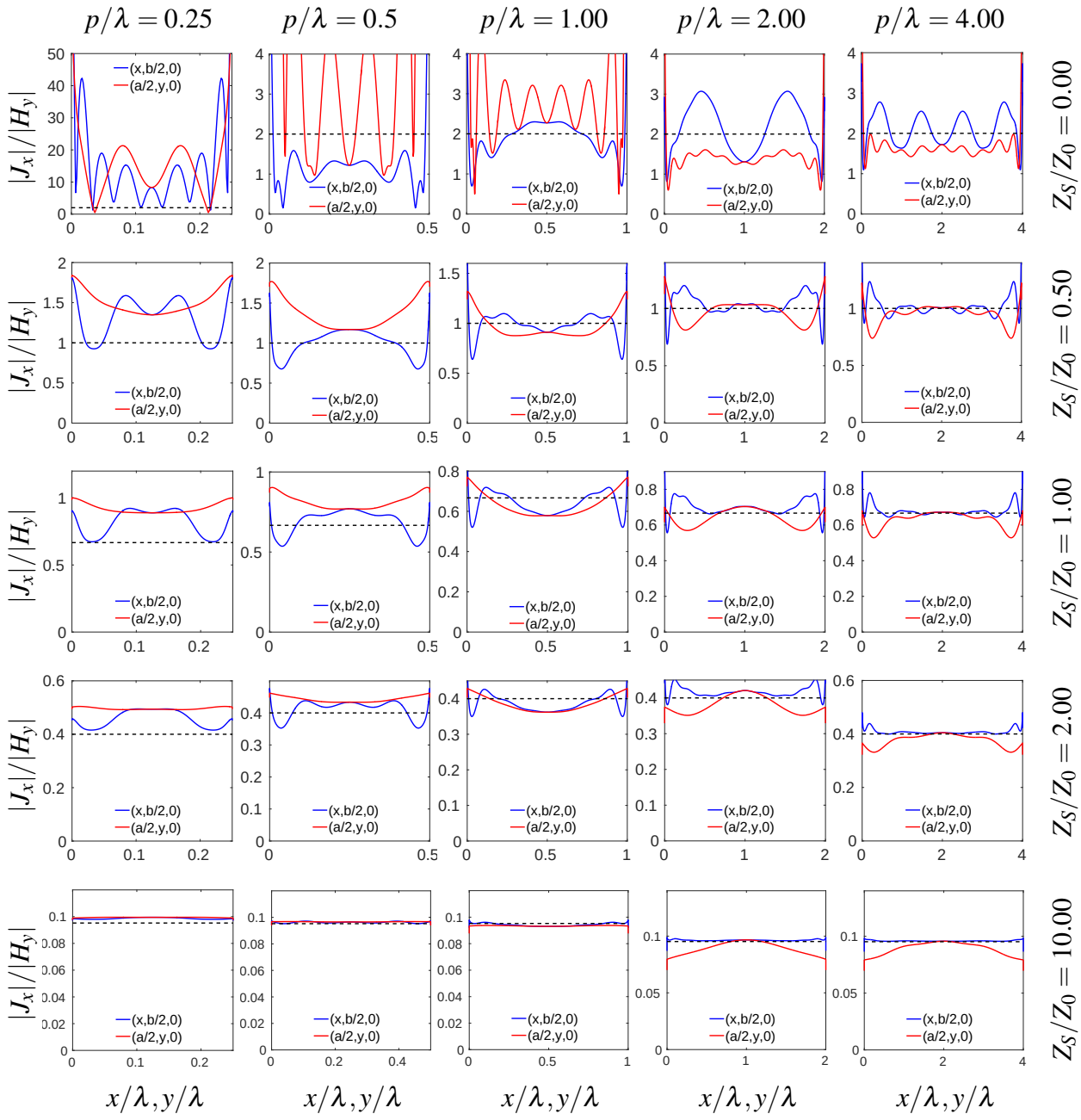

Fig. 7.13 Sheet currents induced on square films of various side length p and sheet impedance Z_S by incident radiatons of wavelength λ=1000 μm. The side length of the film varies each column,and the impedance of the film varies each row. The currents are induced by x-directed electric field, and have been normalised to the magnetic field intensity of the wave $|H_x|$. The blue and red lines in each plot correspond to the x-component of the sheet current of the centre of the film along x- and y-direction.

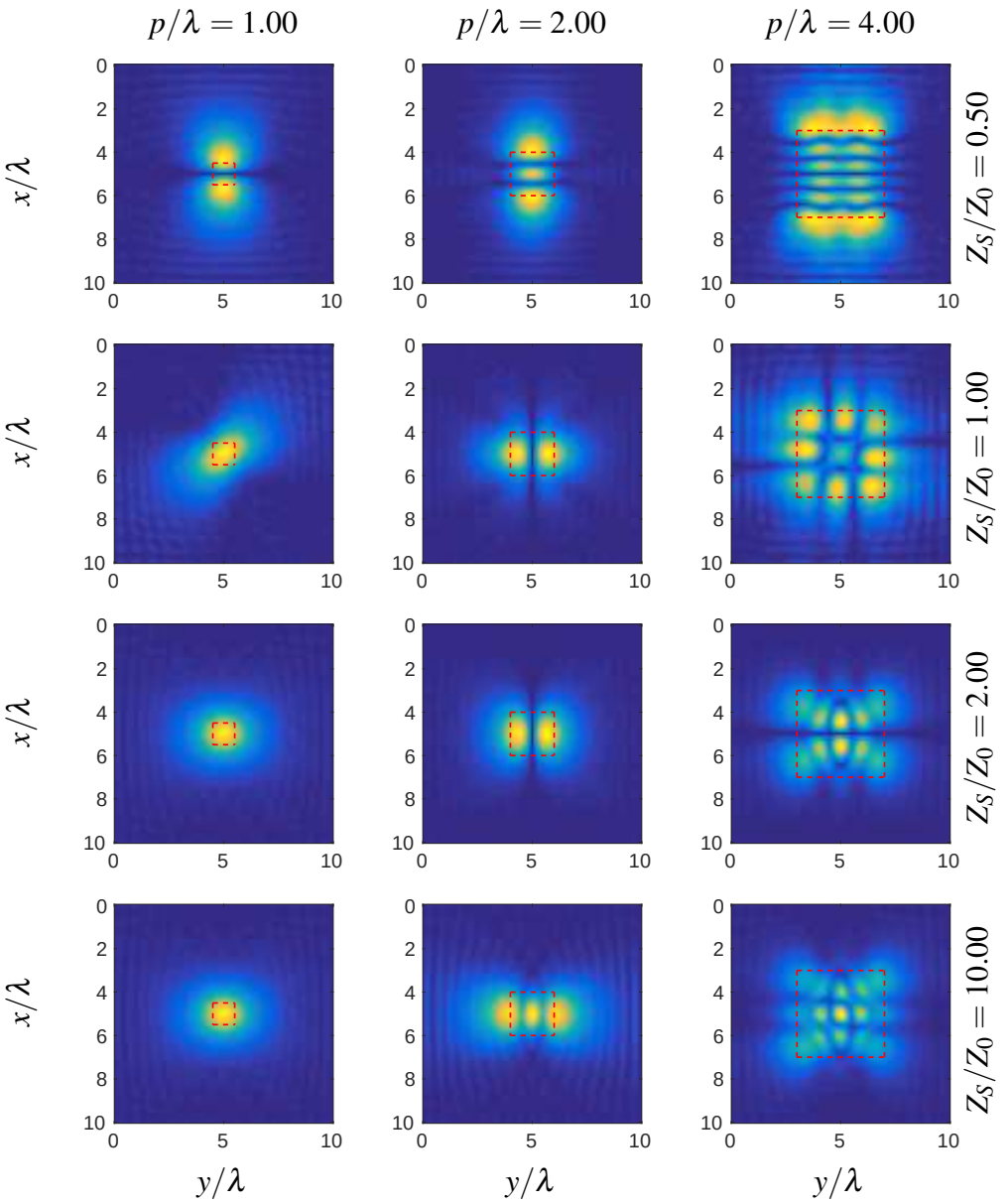

Fig. 7.14 The x-oriented electric field associated with the first mode for films having non-zero impedance and $p/\lambda > 1$ absorbers in a $10\lambda \times 10\lambda$ waveguide.

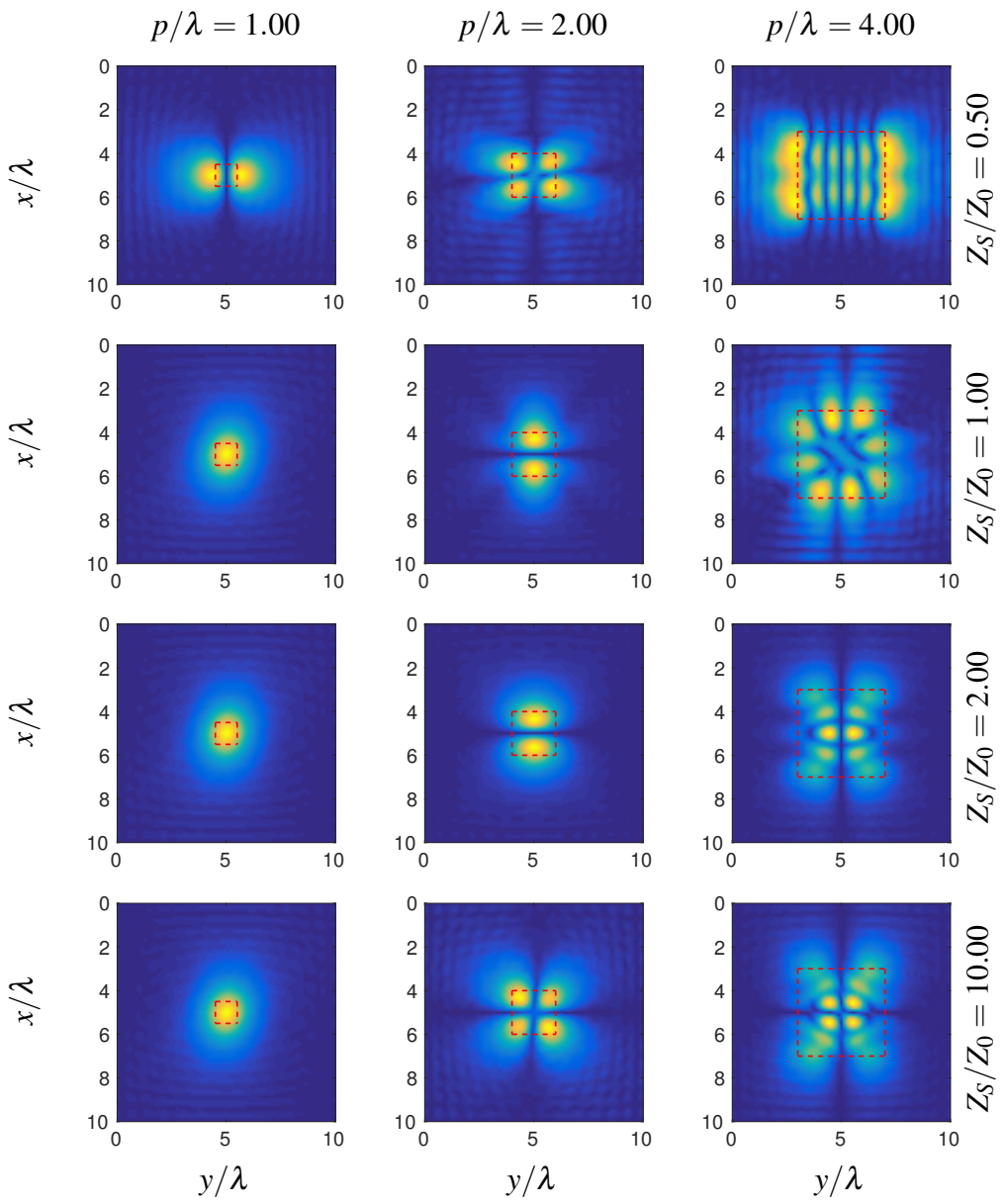

Fig. 7.15 The y-oriented electric field associated with the first mode for films having non-zero impedance and $p/\lambda > 1$ absorbers in a $10\lambda \times 10\lambda$ waveguide.

Chapter 8

Conclusions

In this thesis, I have developed a range of new theoretical and experimental techniques for modelling and measuring the optical behaviour of ultra-low-noise TESs for far-infrared (210 - 110 μm) space science. I have concentrated on demonstrating and optimising the scientific performance of the SPICA-SAFARI detector system, but the techniques developed are applicable to a wide range of instruments and wavelengths. A major achievement has been the realisation and optical testing of detectors having NEPs approaching 10^{-19} W/$\sqrt{\text{Hz}}$. These measurements and the demonstration of this technology has been highly influential in leading ESA towards considering SAFARI as a viable M5 mission. In order to carry out the measurements, a new cryogenic (100 mK) optical test system had been devised and built. Using this system, I was able to achieve high dynamic range on ultra-low-noise detectors, which are necessarily extremely sensitive to straylight. The demonstration of an optical test system was also a significant achievement. The experimental work was supported by a strong program of few-mode optical modelling. A large amount of software was written and used to calculate the optical behaviour of a full generic instrument, and also the optical behaviour of the few-mode test system. Many aspects of this modelling are unique and cannot be found in the scientific literature. For example, I was able to illuminate each detector with the same optical modes in the same proportions, as a full instrument using just a single aperture.

In addition, the optical study was further developed for a test system which mimics the partially illuminating conditions of the SPICA-SAFARI telescope. This system was designed to assess the multimode optical performance. I carried out measurements of ultra-low-noise TESs using the newly developed test system. In practice, making this kind of far-infrared measurements has been challenging as the signal are weak at cryogenic temperatures, and thermal noise could easily disturb the performance of the extremely high sensitive detectors. I successfully minimised thermal loading from the surroundings, and achieved experimental results that were well matched with the results from the theoretical modelling work.

A crucial part of my work has been to develop new electro-magnetic techniques for calculating the modal behaviour of each of the SAFARI detectors. Each detector consists of a film across a far-infrared lightpipe, backed by a high reflective gold, silicon-micro machined reflector. If the film extends across the whole way of the waveguide, the modes of the detector are the same as the modes of the waveguide; if however, the film does not extend the whole way of the waveguide, the modes are different. Join the course of my work, I developed a way of modelling the partially coherent optical behaviour that results. Again I emphasise that I used the SAFARI instrument as the template of my work, the techniques and results are applicable to a wide range of instruments and wavelengths.

A number of specific observations and conclusions are as follows.

I have developed and demonstrated a technique for modelling the partially coherent behaviour of long wavelength optical system, the technique consists of calculating the optical modes of the instrument, and the optical modes of the detector, and then calculating the overall behaviour by coupling the two sets. I would like to emphasise that the modes of the optical system are not the same as the modes to which the detector is receptive. In fact, this thesis describes for the first time, to my knowledge, what even in principle is meant by the modes of the optical system. The problem is that the mathematical vector space on the sky that describes the beam is not the same as the mathematical space across the focal plane. Therefore, it is mathematically meaningless to attempt to diagonalise an operator which maps a field from the sky onto the focal plane. This work shows that a Hilbert-Schmidt transformation is the needed form. I have explore the principle by calculating the optical modes of the SPICA space telescope, and the modes of the detectors that we are developing for the telescope. Pleasingly, this model has enable me to determine all the performance in the context of a single theoretical framework. Going forward, the SPICA team and other instrument teams can use this method to assess the behaviour of their designs.

During my work, I investigated comprehensively the optical behaviour of a generic imaging instrument comprising a telescope and an array of multi-mode horn-coupled detectors. This work shows that the modal method can be used as an effective tool for not only calculating the behaviour of a single detector, but also the behaviour of complete imaging systems, where several pixels are needed to cover the point spread function of the illuminating optical system. Indeed, the modal content and throughput of the natural modes were used to determine informations such as the effective throughput on distributed sources; the aperture efficiency as a function of source direction in the case of point sources; how well the optical modes are spanned by the waveguide modes on the focal plane; the loading from spillover of the cold baffle; and the power loading to the detectors as a function of the temperature of the illuminating field. During the course of my work, it became apparent that it is very difficult

to describe the performance of a multi-mode system by referring into efficiency, because there are always difficulties defining the behaviour of the ideal system to which the efficiency is being referenced. It is much more meaningful to refer to the effective number of modes. This clarification has been valuable to the SAFARI project team.

The SAFARI/SPICA detectors were designed to be sensitive to 10 to 16 modes, as the wavelength varies across each band. This was done to achieve a delicate compromise between achieving high optical throughput but avoiding straylight into modes that are not well coupled to the astronomical source. In my simulations, I found the first 4 optical modes carry the majority of the power, and the higher order modes adding the majority the straylight, 89% of power is coupled to the first 18 waveguide modes, and 91% of power can be recovered in the first 24 modes. Using the number of waveguide modes larger than 24 would only increase the coupling to the baffle dramatically, but without gaining much signal power. Therefore seems that for point sources, the number of detector modes selected by the SAFARI team was about right. Ultimately, this balance depends on the temperature of the surface onto which the poorly coupled modes are terminated. I also found the precise modal forms are similar for each of the SAFARI bands. The optical throughput is greater at shorter wavelengths. I also showed the aperture efficiency of the instrument can be significantly improved by co-adding a number of pixels. The aperture efficiency can be increased to 89% for a 4×4 sub-array. Because both the optical system and the individual detectors are behaving in the few-moded way, it is not obvious that the aperture efficiency can be improved in this way.

To demonstrate the power of the modal technique, I also included the subreflector and its support legs of the telescope into the model. The aim was not to design the optical SAFARI system, but to show that the optical modes can be calculated for even complex system. I developed formalisms and numerical software for including effects such as blockage. An indicator that the results are correct is the throughput decreased in approximate accordance with the blocked area, 20%. It was also found that the aperture efficiency was reduced by 34% due to power lost into the large diffraction rings created by the sub-reflector. The main achievement of this power to the work was to show that even complicated optical systems can be described efficiently in terms of modes, and that these modes can then be used to calculate the coupling of the optical modes of the few-mode detector.

Another achievement was to show how the modes of the detector and the modes of the optical system can be used to calculate the fluctuations in the in the outputs of single detectors, and the correlations between the fluctuations in the outputs of different detectors in an imaging array. A single and very elegant expression was presented for calculating these fluctuations using knowledge of the modal structure of the various components. This expression accounted for both classical noise and photon-counting noise, but extended it to

the few-mode case. We are not aware of this expression appearing anywhere in publishing literature. In the context of my SAFARI modelling, I have shown that the classical noise is tiny compared to the quantum noise over each of the SAFARI bands. This results shows that there should be no correlations between the outputs of different pixels and this has implications for the way in which the outputs of different pixels are combined in imaging software.

A key part of my work was to innovate design and engineer a cryogenic optical system capable of measuring the optical efficiency of ultra-low-noise TESs. For demonstration purposes, the SAFARI/SPICA telescope was used as the prototype. This system had a number of important features. Firstly, the test system illuminates the detectors with the same spatial modes in the same ratios of a complete instrument on a telescope. Given that the test system has no focusing element on the aperture plane, it is not obvious that the modes should be identical. When testing a detector, it is not sufficient to simply say that incoming beam has a certain size; it is necessary to define the forms and proportions of the individual modes. We were desperately keen to avoid using the lenses in the test system, because they lead to reflection on standing waves which can destroy the spatial modal content of the incoming field. Another feature of the test system is that there is no optical elements between the far-field beam-forming aperture and the input plane of the detectors. In fact, all of the band-defining filtering takes place in a blackened lightpipe that precedes the beam defining aperture. Finally, there is a blackened labyrinth that prevents straylights from the 4 K environment of the refrigerator leaking in to the detectors. This worked extraordinary well and allowed high dynamic range measurements. Overall, the test performed extremely well and the design can be used as a starting point for others wishing to test ultra-low-noise detectors.

My optical modelling software was modified to calculate the modal behaviour of the test system itself, and thereby predict the level of power that would be measured when the temperature of the blackbody load was increased. My calculations were in exceptionally good agreement with the powers ultimately measured. I would like to emphasise again that the illuminating conditions of the test system were the same as those of the telescope. I have shown that as long as the geometric focal ratios of the test system is the same as that of the telescope, the optical modes and throughputs are almost identical to that of the telescope, even without using a lens. I also calculated the photon noise from the source and baffle for all of the SAFARI bands. The results indicated that the performance of an ideal telescope is the same as that of a test system. A key conclusion is that by designing the modes of a clean optical system, the performance of an ultra-low-noise detector can be measured precisely

against the well-define incoming optical field. But this degree of clarity is important for high performance space instrument.

As part of my work, several arrays of ultra-low-noise TESs were fabricated for the SAFARI bands. In addition, techniques were developed for mounting these arrays and their optical backing wafers into the camera housings. These units house the detectors at the front and the readout SQUIDs at the back to avoid straylight from the readout electronics being seen by the detectors. There is a need to ensure the whole electrical path from the TESs themselves to the SQUIDs consist of superconducting wiring. Another key problem was to ensure the absorbers on the TESs are placed and aligned to within a few microns to the exit apertures of the lightpipes. This has to be done despite the inevitable differential thermal contraction between the TES wafers and the camera housing. I am grateful to colleagues at University of Cardiff for developing the metrology and machining necessary to make this work. At no point did we ever lose wafers or TESs due to mechanical damage on cooling. My dark measurements show that the camera housings behaved exceedingly well approaching the SAFARI specification for the noise equivalent power. As part of my optical testing work, a series of illuminating apertures, with diameters of 1, 2, 4, 8 and 10 mm, were manufactured, so that different illumination conditions could be tested.

A series of optical measurements were performed on a set of L-Band SAFARI pixels to investigate the optical efficiencies of the TESs using the optical test system. Initially, I tested bare pixels without lightpipes, the performance measured was essentially identical to that calculated for a suspended planar absorber. This work showed that many aspects of the TES must have been working perfectly. For example, it showed the reflective gold film, which was placed a quarter of wavelength behind the optical absorber was working correctly. In the early days of our design, there were discussion as to whether this configuration would work. My tests show that this arrangement works exceptionally well. These early tests also show that the impedance and absorptivity of the thin film β-phase Ta absorber works well. Although we tested the DC resistance of these films, and monitored it for some time to check for long term oxidation, it is not obvious it necessarily means that these films absorb well in infrared wavelength. The fact these free-space pixels behaved essentially ideally was a key achievement, and it forms a calibrations against which performance of lightpipes could be measured. The power measurements were taken on 6 pixels as a function of the temperature the variable blackbody load. In accordance with my optical modelling results, the results were interpreted in terms of the effective number of detected modes. By comparing the experimental results with the numerical models, I demonstrated that the simulations provided a good description of the optical behaviour of the test system and detectors. Few-mode optical

behaviour was clearly observed. My demonstration of the fact that detectors configured for good optical performance can also achieve extremely low NEPs was a key achievement.

For the horn-coupled devices, however, the experimental measurements resulted in efficiency that were smaller than the numerical predictions. With the horns removed, such the absorbers act as free-space pixels, the experimental measurements matched almost perfectly with the model. I carried out simulations in an attempt to understand why the lightpipes were not operating according to expectations. My measurements, together with beam pattern measurements carried out at Cardiff University, led us to the conclusion that high optical modes would be lost. It was not simply the case that all optical modes are being attenuated equally. We now believe that the losses occurred due to imperfections in the walls of the multi-mode waveguides. In particular, we think that a low conductivity oxide was left on the internal walls of the lightpipes from the processing method. Work to understand and solve this problem continues.

I also carried out measurements on meshed absorbers, meshed absorbers were seen as a way of lowering the heat capacity of the TESs, and thereby increasing the speed of the long wavelength detectors. Because the meshing was on a scale smaller than a wavelength, the optical performance should not be degraded. Because, however, the meshed and filled absorbers were fabricated during the same deposition step, we did not adjust the surface impedance of the meshed absorbers to the correct amount. The efficiencies measured on meshed absorbers were lower than that of the filled absorbers by approximately 20%, which is consistent with the theoretical estimates. If the correct filming impedance has been used, the meshed absorbers would have the same optical performance as the filled absorbers, and in fact, the Quantum Sensors Group has demonstrated this effect subsequent to my work. Crucially, during my work, I showed that meshed absorbers can be used increasing speed, while not degrade the optical performance. This is an important observation for the SAFARI team.

It was observed that the power measurements made with low blackbody source temperatures (about 3.3 K to 6 K) tended to be higher than the calculated values. To examine if there was a low level source of straylight, a set of measurements were performed with the horns were blanked off. For these dark measurements, power was detected as the source temperature increased, which indicated that there was a source of straylight which was illuminating the detectors. By subtracting the straylight power from the data with open apertures, the measured results became comparable to the numerical simulations. Again, subsequent of my work, the Quantum Sensors Group has found this leak firstly identified in my measurements.

A simplified model was developed to investigate the efficiency loss in the L- and S-Band horns and waveguides. The horns were manufactured from electro-forming Cu on a Au plated Al mandrel, and then etching the Al away once the horn profiles were formed. The model analysed the losses from two aspects: the effects of reflection due to impedance mis-match at the exit aperture of the waveguide; and the Ohmic loss to the metallic waveguide walls. I have shown that the reflections at the discontinuity is insignificant. It is believed that a thin layer of the Al mandrel, or oxide, was left on the inside of the horns, which affected the effective conductivity of the waveguide walls, and thus increased the conductor loss.

I have developed a mode-matching method to model the optical behaviour of waveguide-mounted thin films in the infrared. An analytical method of calculating the C-matrix (the inner products between the basis functions) was developed. It has been shown that the method is numerically efficient to handle calculations with large number of modes. In addition, the simplicity of establishing the C-matrix of the film may be beneficial for simulations of band-pass filters in the future. I have addressed two numerical difficulties in the current simulations using this method, which was that a null-space existed in the C-matrix, and some numerically large elements are found in the Z-matrix. I have developed formalisms to form a new set of basis functions of the field without the null-space. A method to avoid having the modes with very large waveguide impedances in the Z-matrix was presented. The scattering parameters were determined, and used to calculate the response of the waveguide mounted thin films. The eigenvalue spectra of different sized thin films were determined, which are identical to the results in the cited paper, where a different approach was applied. I have calculated the induced sheet current on the film for various film sizes and impedances. The results for the films having dimensions $p/\lambda > 1$ and with non-zero impedance were in good agreement with the induced sheet currents on free-space films [49], which the regime that detector technology is interested. This work on modelling the electromagnetic behaviour of patterned thin films in waveguide will lead to more sophisticated analysis and designs.

During my work on this project, I have developed a range of new techniques for modelling the behaviour of long wavelength ultra-low-noise few-mode optical systems and detectors. I developed a cryogenic optical test system working at 70 mK and calculated its behaviour in terms of optical modes. I demonstrated a number of ultra-low-noise TESs of the kind that would be suitable for the SAFARI instrument on the SPICA space telescope. The demonstration of this technology in Europe has been a key part of convincing the European Space Agency of the viability of this technology for a new generation far-infrared cooled aperture space telescopes. Prior to my work, there was only one of the groups internationally who would make optical measurements on ultra-low-noise detectors, and all of them measurements were carried out at shorter S-Band wavelength. My measurements are still to date

the only demonstrate worldwide of high performance optical efficiency measurements on L-Band arrays. I believe that this work will form the foundation of a whole new generation of technology based on Transition Edge Sensors.

References

[1] Audley, M. D., de Lange, G., Gao, J.-R. . R., Khosropanah, P., Hijmering, R., Ridder, M., Mauskopf, P. D., Morozov, D., Trappe, N. A., and Doherty, S. (2016). Optical performance of an ultra-sensitive horn-coupled transition-edge-sensor bolometer with hemispherical backshort in the far infrared. *Review of Scientific Instruments*, 87(4):043103.

[2] Benford, D. J. (2008). Transition edge sensor bolometers for cmb polarimetry. *CMBPol technology whitepaper*.

[3] Cabrera, B., Krauss, L. M., and Wilczek, F. (1985). Bolometric detection of neutrinos. *Physical Review Letters*, 55(1):25.

[4] Chuss, D. T., Wollack, E. J., Moseley, S. H., Withington, S., and Saklatvala, G. (2008). Diffraction considerations for planar detectors in the few-mode limit. *Publications of the Astronomical Society of the Pacific*, 120(866):430.

[5] Crill, B. P., Ade, P. A. R., Battistelli, E. S., Benton, S., Bihary, R., Bock, J. J., Bond, J. R., Brevik, J., Bryan, S., and Contaldi, C. R. (2008). Spider: a balloon-borne large-scale cmb polarimeter. In *SPIE Astronomical Telescopes+ Instrumentation*, pages 70102P–70102P. International Society for Optics and Photonics.

[6] Cryotronics, L. (2012). Cryogenic reference tables. *online in: http://www. lakeshore. com/Documents/LSTC_appendixI_l. pdf*.

[7] Dardenne, X. (2007). *Method of moments simulation of infinite and finite periodic structures and application to high-gain metamaterial antennas*. PhD thesis, Ph. D. dissertation, Inst. Inf. Commun. Technol., Electron. Appl. Math., Univ. Catholique Louvain, Louvain-la-Neuve, Belgium.

[8] Drung, D. (2003). High-tc and low-tc dc squid electronics. *Superconductor Science and Technology*, 16(12):1320.

[9] Drung, D., Abmann, C., Beyer, J., Kirste, A., Peters, M., Ruede, F., and Schurig, T. (2007). Highly sensitive and easy-to-use squid sensors. *IEEE Transactions on Applied Superconductivity*, 17(2):699–704.

[10] Flynn, T. (2004). *Cryogenic engineering, revised and expanded*. CRC Press.

[11] Glowacka, D. M., Crane, M., Goldie, D. J., and Withington, S. (2012). A fabrication route for arrays of ultra-low-noise moau transition edge sensors on thin silicon nitride for space applications. *Journal of Low Temperature Physics*, 167(3-4):516–521.

[12] Goicoechea, J. R. and Nakagawa, T. (2011). Spica: the next generation infrared space telescope. *EAS Publications Series*, 52:253–258.

[13] Goldie, D. J., Glowacka, D. M., Withington, S., Chen, J., Ade, P. A. R., Morozov, D., Sudiwala, R., Trappe, N. A., and Quaranta, O. (2016). Performance of horn-coupled transition edge sensors for l-and s-band optical detection on the safari instrument. In *SPIE Astronomical Telescopes+ Instrumentation*, pages 99140A–99140A. International Society for Optics and Photonics.

[14] Goldie, D. J., Velichko, A. V., Glowacka, D. M., and Withington, S. (2012). Towards ultra-low-noise moau transition edge sensors. *Journal of Low Temperature Physics*, 167(3-4):248–253.

[15] Goodman, J. W. (2005). *Introduction to Fourier optics*. Roberts and Company Publishers.

[16] Gori, F., Santarsiero, M., Simon, R., Piquero, G., Borghi, R., and Guattari, G. (2003). Coherent-mode decomposition of partially polarized, partially coherent sources. *JOSA A*, 20(1):78–84.

[17] Hadfield, R. H. and Johansson, G. (2016). Superconducting devices in quantum optics. *Quantum*.

[18] Harrington, R. F. and Harrington, J. L. (1996). *Field computation by moment methods*. Oxford University Press.

[19] Haskal, H. (1964). Matrix description of waveguide discontinuities in the presence of evanescent modes. *IEEE Transactions on Microwave Theory and Techniques*, 12(2):184–188.

[20] Heins, A. E. and Silver, S. (1955). The edge conditions and field representation theorems in the theory of electromagnetic diffraction. In *Mathematical Proceedings of the Cambridge Philosophical Society*, volume 51, pages 149–161. Cambridge Univ Press.

[21] Horn, R. A. and Johnson, C. R. (2012). *Matrix analysis*. Cambridge university press.

[22] Irwin, K. D. and Hilton, G. C. (2005). Transition-edge sensors. In *Cryogenic particle detection*, pages 63–150. Springer.

[23] Jackson, B. D., De Korte, P. A. J., Van der Kuur, J., Mauskopf, P. D., Beyer, J., Bruijn, M. P., Cros, A., Gao, J.-R. . R., Griffin, D., and Den Hartog, R. (2012). The spica-safari detector system: Tes detector arrays with frequency-division multiplexed squid readout. *IEEE Transactions on Terahertz Science and Technology*, 2(1):12–21.

[24] Jackson, J. D. and Fox, R. F. (1999). Classical electrodynamics. *American Journal of Physics*, 67(9):841–842.

[25] Kessler, M. F. (2002). The infrared space observatory (iso) mission. *Advances in Space Research*, 30(9):1957–1965.

[26] Khosropanah, P., Dirks, B., Parra-Borderias, M., Ridder, M., Hijmering, R., Van der Kuur, J., Gottardi, L., Bruijn, M., Popescu, M., and Gao, J. R. (2010). Low-noise transition edge sensor (tes) for safari instrument on spica. In *SPIE Astronomical Telescopes+ Instrumentation*, pages 77410L–77410L. International Society for Optics and Photonics.

[27] Mandel, L. and Wolf, E. (1995). *Optical coherence and quantum optics*. Cambridge university press.

[28] Marquardt, E. D., Le, J. P., and Radebaugh, R. (2002). Cryogenic material properties database. In *Cryocoolers 11*, pages 681–687. Springer.

[29] Mauskopf, P. D., Ade, P. A., Beyer, J., Bruijn, M., Gao, J. R., Glowaca, D., Goldie, D., Griffin, D., Griffin, M., and Hoevers, F. (2010). A tes focal plane for spica-safari. In *Proceedings of the 21st International Symposium on Space Terahertz Technology*, pages 246–255.

[30] Meixner, J. (1972). The behavior of electromagnetic fields at edges. *IEEE Transactions on Antennas and Propagation*, 20(4):442–446.

[31] Morozov, D., Sudiwala, R., Ade, P. A. R., Goldie, D. J., Glowacka, D. M., Withington, S., and Trappe, N. A. (2016). Optical characterisation of a camera module developed for ultra-low nep tes detector arrays at fir wavelengths. In *SPIE Astronomical Telescopes+ Instrumentation*, pages 991409–991409. International Society for Optics and Photonics.

[32] Murakami, H., Baba, H., Barthel, P., Clements, D. L., Cohen, M., Doi, Y., Enya, K., Figueredo, E., Fujishiro, N., and Fujiwara, H. (2007). The infrared astronomical mission akari. *Publications of the Astronomical Society of Japan*, 59(sp2):S369–S376.

[33] Neugebauer, G., Habing, H. J., Van Duinen, R., Aumann, H. H., Baud, B., Beichman, C. A., Beintema, D. A., Boggess, N., Clegg, P. E., and De Jong, T. (1984). The infrared astronomical satellite (iras) mission. *The Astrophysical Journal*, 278:L1–L6.

[34] Ney, M. M. (1985). Method of moments as applied to electromagnetic problems. *IEEE transactions on microwave theory and techniques*, 33(10):972–980.

[35] Olshausen, B. A. (2000). Aliasing. *PSC 129–Sensory Processes*, pages 3–4.

[36] Ramo, S., Whinnery, J. R., and Van Duzer, T. (2008). *Fields and waves in communication electronics*. John Wiley & Sons.

[37] Remazeilles, M., Dickinson, C., Eriksen, H. K. K., and Wehus, I. K. (2016). Sensitivity and foreground modelling for large-scale cosmic microwave background b-mode polarization satellite missions. *Monthly Notices of the Royal Astronomical Society*, 458(2):2032–2050.

[38] Richard, P. (1994). Bolometers for infrared and millimetre waves. *J. Appl. Phys*, 76:1–24.

[39] Riley, K. F., Hobson, M. P., and Bence, S. J. (1999). Mathematical methods for physics and engineering.

[40] Roellig, T. L. (1995). The infrared telescope in space (irts) mission. In *From Gas to Stars to Dust*, volume 73.

[41] Rostem, K., Chuss, D. T., Lourie, N. P., Voellmer, G. M., and Wollack, E. J. (2013). A waveguide-coupled thermally isolated radiometric source. *Review of Scientific Instruments*, 84(4):044701.

[42] Russell, D., Cleary, K., and Reeves, R. (2012). Cryogenic probe station for on-wafer characterization of electrical devices. *Review of Scientific Instruments*, 83(4):044703.

[43] Saklatvala, G. (2009). *A functional approach to the analysis of millimetre wave and infrared astronomical instruments*. PhD thesis, University of Cambridge.

[44] Saklatvala, G., Withington, S., and Hobson, M. P. (2007). Coupled-mode theory for infrared and submillimeter wave detectors. *JOSA A*, 24(3):764–775.

[45] Saklatvala, G., Withington, S., and Hobson, M. P. (2008). Simulations of astronomical imaging phased arrays. *JOSA A*, 25(4):958–967.

[46] Senior, T. (1979). Backscattering from resistive strips. *IEEE Transactions on Antennas and Propagation*, 27(6):808–813.

[47] Smith, D. H., Gillett, G., de Almeida, M., Branciard, C., Fedrizzi, A., Weinhold, T. J., Lita, A., Calkins, B., Gerrits, T., and Wiseman, H. M. (2011). Conclusive quantum steering with superconducting transition edge sensors. *arXiv preprint arXiv:1111.0829*.

[48] Swetz, D. S., Bennett, D. A., Irwin, K. D., Schmidt, D. R., and Ullom, J. N. (2012). Current distribution and transition width in superconducting transition-edge sensors. *Applied Physics Letters*, 101(24):242603.

[49] Thomas, C. N. (2012). *Theoretical, numerical and experimental studies of the optical behaviour of few-mode power detectors for submillimetre and far-infrared astronomy*. PhD thesis, University of Cambridge.

[50] Thomas, C. N. and Withington, S. (2010). Electromagnetic simulations of the partially coherent optical behavior of resistive film tes detectors. In *Proceedings of the 21st International Symposium on Space Terahertz Technology*, pages 23–25.

[51] Thomas, C. N., Withington, S., Chuss, D. T., Wollack, E. J., and Moseley, S. H. (2010). Modeling the intensity and polarization response of planar bolometric detectors. *JOSA A*, 27(5):1219–1231.

[52] Twerenbold, D., Vuilleumier, J.-L. . L., Gerber, D., Tadsen, A., van den Brandt, B., and Gillevet, P. M. (1996). Detection of single macromolecules using a cryogenic particle detector coupled to a biopolymer mass spectrometer. *Applied physics letters*, 68(24):3503–3505.

[53] Ventura, G., Barucci, M., Gottardi, E., and Peroni, I. (2000). Low temperature thermal conductivity of kevlar. *Cryogenics*, 40(7):489–491.

[54] Walton, A. J., Parkes, W., Terry, J. G., Dunare, C., Stevenson, J. T. M., Gundlach, A. M., Hilton, G. C., Irwin, K. D., Ullom, J. N., and Holland, W. S. (2004). Design and fabrication of the detector technology for scuba-2. *IEE Proceedings-Science, Measurement and Technology*, 151(2):110–120.

[55] Werner, M. W., Roellig, T. L., Low, F. J., Rieke, G. H., Rieke, M., Hoffmann, W. F., Young, E., Houck, J. R., Brandl, B., and Fazio, G. G. (2004). The spitzer space telescope mission. *The Astrophysical Journal Supplement Series*, 154(1):1.

[56] Withington, S. (2004). Terahertz astronomical telescopes and instrumentation. *Philosophical Transactions of the Royal Society of London A: Mathematical, Physical and Engineering Sciences*, 362(1815):395–402.

[57] Withington, S., Campbell, E. S., and Hobson, M. P. (2005). A numerical procedure for simulating the behavior of multimode, bolometric, astronomical interferometers. *Journal of applied physics*, 97(12):124909.

[58] Withington, S. and Saklatvala, G. (2007). Characterizing the behaviour of partially coherent detectors through spatio-temporal modes. *Journal of Optics A: Pure and Applied Optics*, 9(7):626.

[59] Withington, S., Saklatvala, G., and Hobson, M. P. (2006). Partially coherent analysis of imaging and interferometric phased arrays: noise, correlations, and fluctuations. *JOSA A*, 23(6):1340–1348.

[60] Withington, S., Saklatvala, G., and Hobson, M. P. (2007). Theoretical analysis of astronomical phased arrays. *Journal of Optics A: Pure and Applied Optics*, 10(1):015304.

[61] Withington, S., Tham, C., and Yassin, G. (2003). Theoretical analysis of planar bolometric arrays for thz imaging systems. In *Astronomical Telescopes and Instrumentation*, pages 49–62. International Society for Optics and Photonics.

[62] Withington, S. and Thomas, C. N. (2009). Optical theory of partially coherent thin-film energy-absorbing structures for power detectors and imaging arrays. *JOSA A*, 26(6):1382–1392.

[63] Withington, S. and Thomas, C. N. (2010). Analysis of far-infrared horns, lightpipes, and cavities containing patterned conductive films. *JOSA A*, 27(11):2354–2364.

[64] Withington, S., Thomas, C. N., and Goldie, D. J. (2013). Partially coherent optical modelling of the ultra-low-noise far-infrared imaging arrays on the spica mission. *arXiv preprint arXiv:1307.7278*.

[65] Woodbury, M. A. (1950). Inverting modified matrices. *Memorandum report*, 42(106):336.

[66] Young, N. (1988). *An introduction to Hilbert space*. Cambridge university press.